UNDERSTANDING THE DEFORMATION BEHAVIOR OF METALLIC AND NANOGLASSES THROUGH INDENTATION

Ph.D. Thesis

By

ABHINAV SHARMA

DEPARTMENT OF METALLURGY ENGINEERING AND MATERIALS SCIENCE

INDIAN INSTITUTE OF TECHNOLOGY INDORE

JULY 2022

UNDERSTANDING THE DEFORMATION BEHAVIOR OF METALLIC AND NANOGLASSES THROUGH INDENTATION

A THESIS

Submitted in partial fulfillment of the requirements for the award of the degree

of

DOCTOR OF PHILOSOPHY

By

ABHINAV SHARMA

DEPARTMENT OF METALLURGY ENGINEERING AND MATERIALS SCIENCE

INDIAN INSTITUTE OF TECHNOLOGY INDORE

JULY 2022

INDIAN INSTITUTE OF TECHNOLOGY INDORE

CANDIDATE'S DECLARATION

I hereby certify that the work which is being presented in the thesis entitled "**Understanding the Deformation Behavior of Metallic and Nanoglasses through Indentation"** in the partial fulfillment of the requirements for the award of the degree of **DOCTOR OF PHILOSOPHY** and submitted in the **Department of Metallurgy Engineering and Materials Science, Indian Institute of Technology Indore**, is an authentic record of my own work carried out during the time period from July 2018 to July 2022 under the supervision of **Dr. Eswara Prasad Korimilli, Asst. Prof., IIT Indore.**

The matter presented in this thesis has not been submitted by me for the award of any other degree of this or any other institute.

3/10/2022

Signature of the student with date
(ABHINAV SHARMA)

This is to certify that the above statement made by the candidate is correct to the best of my/our knowledge.

3/10/2022
Signature of Thesis Supervisor with date

(Dr. ESWARA PRASAD KORIMILLI)

ABHINAV SHARMA has successfully given his Ph.D. Oral Examination held on **30/09/2022**

3/10/2022
Signature of Thesis Supervisor with date

(Dr. ESWARA PRASAD KORIMILLI)

ACKNOWLEDGEMENT

"The best teachers are those who show you where to look but don't tell you what to see."

-Alexandra K. Trenfor

To begin with, I would like to express my sincere gratitude to my supervisor Dr. Eswara Prasad Korimilli, for considering me as his Ph.D. student. I am highly obliged to him for providing me with continuous support, advice, and guidance during the Ph.D. I've gained a lot of knowledge from him, like how to critically review a paper and write a scientific article with a proper approach to literature. And what can I say about his presentation skill? He is an artist in explaining things with his presentation while keeping the audience intact and engaged the whole time. Frankly speaking, I've met a lot of dynamic professors in my life during the journey, but Dr. Eswara sir is far different from them. I mean, earlier, I used to see myself as an allrounder since, apart from academics, I have an interest in sports, cooking, politics, gadgets, etc. But, after meeting him, I understood the exact definition of an all-rounder. He is a person who is skilled, capable, and knowledgeable in a lot of different things. He is one of a kind, and I am so fortunate that he is my Ph.D. supervisor. If given a chance, I would love to work under him for my entire life. He is and will always remain a role model in my life. Thank you so much for everything.

I am also grateful to Prof. Horst Hahn and Dr. Sree Harsha Nandam, Karlsruhe Institute of Technology (KIT), Germany, for collaborating with us and providing the nanoglass and metallic glass samples. Your continuous advice, insights, and comments on the outcomes of the experiments have helped me a lot.

I am highly indebted to Dr. Abhishek Chaturvedi, Indian Institute of Science (IISc), Bangalore, and Prof. Upadrasta Ramamurty, Nanyang Technological University (NTU), Singapore, for providing access to the nanoindenter facility.

I am very thankful to Mr. Sai Ram and Dr. Rajesh Kumar, Indian Institute of Technology Hyderabad, for letting us access the nanoindentation and scanning electron microscopy. I am glad that I met Mr. Sai Ram during this journey. He is the person who always tells me, while joking around, "Think big, do big." The countless nights we spent in the lab to polish the samples will always remain one of the most memorable moments of my Ph.D. He treated me like a brother. He let me stay in his hostel room (even though I had never met him) and provided me with all the support I needed during my visit to IIT Hyderabad. I wish to work with him in the future.

I am highly grateful to Ms. Ananya Tripathi and Dr. Praveen Kumar, Indian Institute of Science (IISc), Bangalore, for providing access to the nanoindenter facility. I would like to thank Mr. Rainish for providing all the hospitality during my stay in IISc Bangalore. He is one of the nicest juniors I have met during my Ph.D. journey.

I would like to acknowledge my PG student progress committee (PSPC) members, Dr. Satyajit Chatterjee, Department of Mechanical Engineering, and Dr. Pankaj Sagdeo, Department of Physics, IIT Indore, for their valuable comments and suggestions to enhance the quality of my research work.

I would like to thank present and past Directors of IIT Indore, Prof. Suhas S. Joshi, Prof. Neelesh Kumar Jain, and Prof. Pradeep Mathur, for providing a conducive environment for research and the opportunity to explore my research capabilities at IIT Indore. I extend my gratitude to the present and past Head of Department (HOD) – MEMS, Dr. Vinod Kumar, and Dr. Parasharam Shirage, for providing all the technical and official support required to carry out the project efficiently and successfully. My sincere gratitude to present and past Departmental Post Graduate conveners (DPGC) Dr. Sumanta Samal, Dr. Rupesh Devan, and Dr. Mrigendra Dubey for their continuous help during my Ph.D. Research work.

I want to thank lab technicians Mr. Mayur Dhake, Mr. Shubham Kumar, and Mr. Deepak Rathore for aiding with the lab work. Mayur sir has helped me every time whenever I got stuck with any of the experimental work. He is always available with just one call away.

I would like to thank my present and past lab mates for providing pleasant company and constant support during my entire time in the Mechanics of Materials (MOM) lab. The discussions and suggestions from Tulika and Vaibhav were very helpful in improving the research work. I have learned a lot from both of them. Tulika and I started the journey together at IIT Indore. She helped with the experimental work during my Ph.D. The short, cheerful discussions with her on different topics made my stay much more pleasant in the lab. It’s always great to have a friend like her around. I also thank Vaibhav for the discussions we had on different topics, especially nanoindentation. His discipline and dedication to research are unmatchable. I am still learning a lot from him.

It is very difficult to express in words how much I owe to all my friends, juniors, and seniors at IIT Indore. I especially want to thank Vishal sir, Pravin sir, Mahendra (Bahu), Vivek, Siddarth sir, Sourabh sir, Vibhum sir, Mohit sir, Siddhartha Sir, Vikesh, Vinod, and Manish for their unconditional love and support during my entire journey. The time I've spent with Vishal sir, Pravin sir, Bahu, and Vivek in Unit no. 204 (HJB Hostel) will forever remain close to my heart. I cannot mention the support and favor I've received from Janmejai. He is the person who always stands by me every time, doesn't matter what the situation is. I am grateful and lucky to have a friend like him.

Lastly, I would like to thank my family and my parents. They have always supported me whenever I struggled with my studies. My father has provided me with everything since my childhood. I would like to acknowledge especially my mom for her regular prayers, blessings, support, and encouragement. Without her, I might not be running on this road. She is my life. I owe my entire journey to her.

Dedicated to

my family, my guide,

and my country

SYNOPSIS

Metallic glasses (MGs) are amorphous alloys produced by the rapid quenching of liquid alloys at high cooling rates by melt spinning technique. They first came into the picture when Klement and Duwez were trying to quench Au-Si eutectic alloy at very high cooling rates and ended up discovering a new material known as metallic glass [Klement et al., 1960]. Over the past few decades, many experimental and simulation studies have been conducted, discovering metallic glasses with novel compositions, and investigating their mechanical and functional properties. It has been observed that MGs exhibit high yield strengths (~ 2 GPa), large yield strains (~ up to 2%) along with excellent formability at high temperatures, good corrosion, and wear resistance, making them potentially suitable for electronic, bio-medical applications [Telford, 2004]. One of the major drawbacks of MGs is their poor room temperature tensile ductility as they fail catastrophically after the elastic limit due to the plastic flow localization into narrow shear bands [Schuh et al., 2007]. Extensive literature studies have been focused on improving the plasticity of MGs by altering their internal microstructure with an aim (*i*) to reduce the plastic strain localization (distribution of plastic strain into multiple shear bands) or (*ii*) mitigating the unhindered propagation of shear bands by having a crystalline phase in the amorphous matrix. In the former one, the surface of the MGs is severely deformed to create more free volume or shear transformation zones (the fundamental units of plastic flow carriers of MGs), thereby leading to profuse shear banding during the deformation. While the latter is more effective in increasing the ductility of the glasses with a reduction in strength. Both the methods suffer from certain disadvantages. For example, the severe plastic deformation due to shot peening is only limited to the surface layers, with the core of MG still comprising the original structure. Similarly, the BMG composites contain a significant volume fraction of the crystalline phases leading to a reduction in fatigue strength and other properties (e.g., corrosion resistance, conductivity, etc.) that are unique to a completely amorphous structure. These studies illustrate that enhancing the plasticity of binary glasses is still an alluring issue as obtaining a fully amorphous structure with uniformly distributed free volume at different regions of the samples is challenging.

With this motivation, Gleiter and co-workers have proposed a concept to obtain a dense amorphous material by compacting amorphous nanoparticles under high pressure, called nanoglass (NG). NGs represent a novel modification in the structure of amorphous material, displaying different properties and structural details than those observed in MGs prepared by rapid quenching. They have shown improved plasticity at room temperature compared to their

MG counterpart, which is attributed to their unique microstructure containing glass interfaces (GIs) between the glassy grains (GGs) [Ivanisenko et al., 2018]. These GIs, akin to grain boundaries in crystalline material, are characterized by high free volume and low density [Ritter et al., 2011]. In general, the areas of high free volume are assumed to be the potential nucleating sites for the activation of shear transformation zones (STZs), a cluster of atoms that undergo cumulative shearing under the influence of external load. In NGs, STZs are nucleated in both the GGs and GIs, with GIs being the preferential sites, leading to numerous shear bands (SBs) dispersed homogeneously throughout the sample. Recent indentation and in-situ micromechanical testing experiments have shown that NGs exhibit very high tensile elongation (up to a plastic strain of ~17%) in comparison to MGs of identical composition [Wang et al., 2016]. Further, nanoindentation studies on various NGs showed less or no noticeable serrations in the loading portion of indentation load, *P*, vs. penetration depth, *h*, curves, unlike their binary MG counterparts. This atypical behavior of NGs is attributed to the presence of GIs though there is no direct experimental evidence to understand the exact reason. However, there are few Molecular Dynamics (MD) simulation studies to understand the deformation behavior of NGs, which show that the plastic flow occurs by multiple shear bands and is sensitive to the volume fraction of interfaces, topological order of amorphous clusters in the interfaces, and the free volume content of GIs and GGs [Adibi et al., 2016; Adjaoud et al., 2019]. The limited experimental indentation studies conducted to date reveal the presence of few or no SBs at the periphery of the imprint in NGs while many SBs in MGs. It is interesting to examine the shear band characteristics directly underneath the indenters as they affect the serrated flow rather than the ones around the indenter impression. Understanding the shear band flow underneath the indentation is impossible by constraint indentation as the deformation features get lost during sectioning and polishing the specimen. Therefore, bonded interface indentation (BII) technique is employed to investigate the SB morphology, their density, spatial distribution, etc., in detail, as shown in Figure 1.

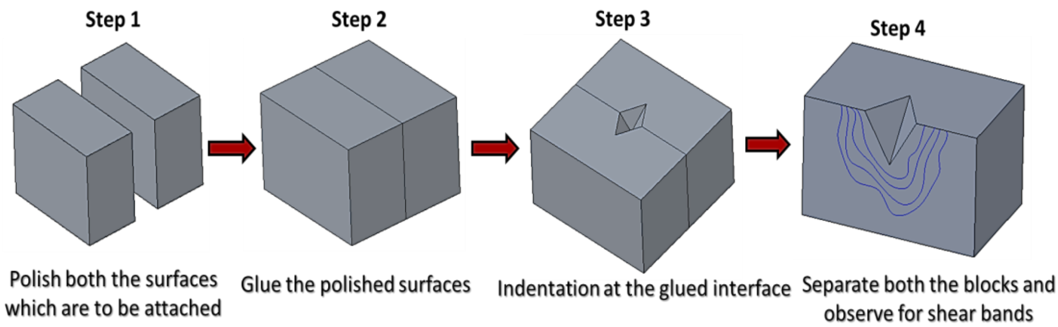

Figure 1. Steps involved in a Bonded interface indentation (BII) technique.

The results demonstrate the differences in the shear band characteristics between MG and NG (Fig.2). It is evident from Fig.2 that the plastic strain in the subsurface deformation region of MG (Figure 2a) is mainly accommodated by primary shear bands (PSBs) whereas, in NG (Figure 2b), many fine secondary shear bands (SSBs) are embedded in between the PSBs, suggesting that both PSBs and SSBs accommodate the plastic strain. In fact, NG also exhibits a higher subsurface deformation zone, which is associated with the more uniform distribution of free volume and increased propensity for SB formation even for a small increase in load, *P* leading to near homogeneous plastic flow.

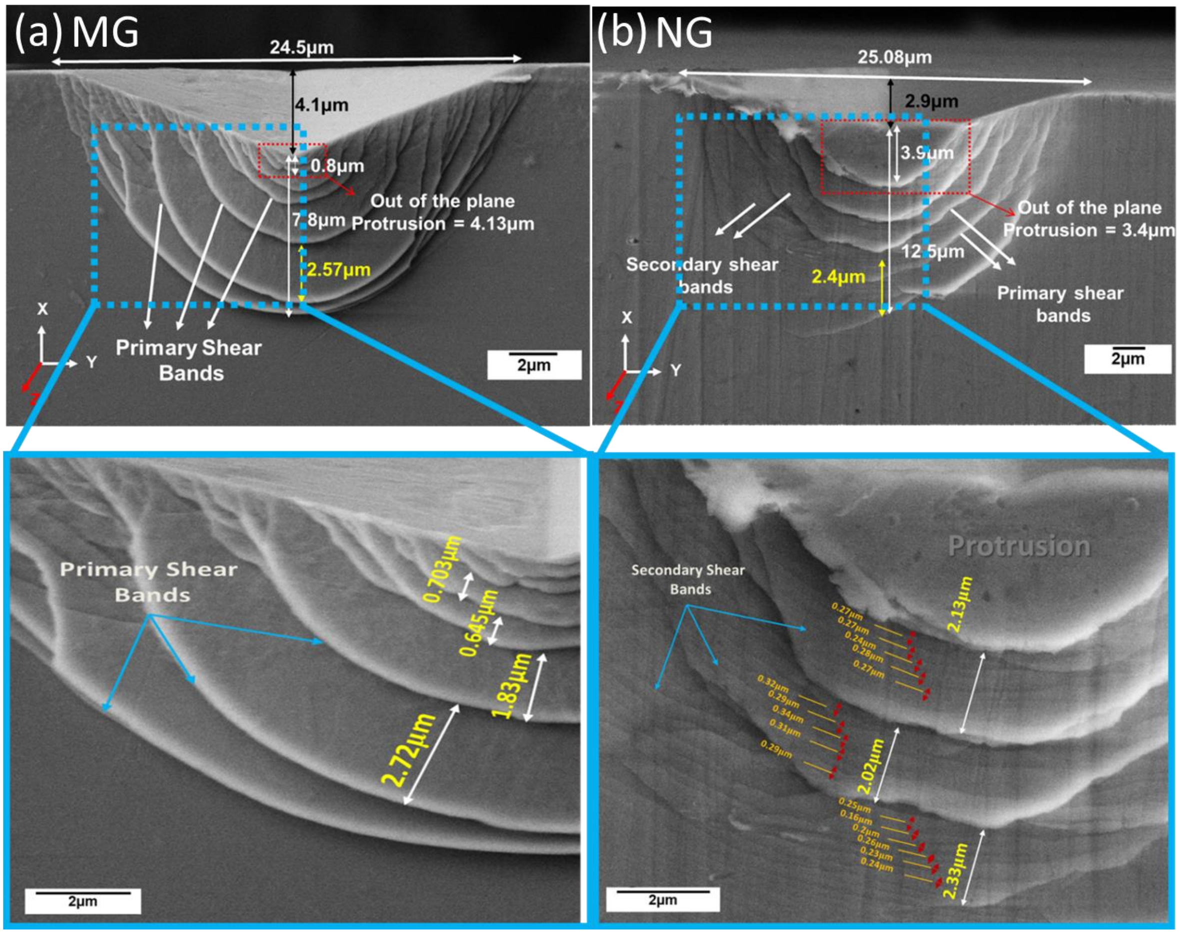

Figure 2. Subsurface SEM images of a $Pd_{80}Si_{20}$ for a) MG and b) NG at an indentation load of 100gf.

Although, a considerable number of extensive studies have been conducted on NGs to investigate their functional and mechanical properties using experiments and simulations. A limited number of studies are available in understanding the deformation behavior of structurally relaxed (SR) NGs. It is very important to understand whether a SR NG will deform in a ductile or brittle manner. The recent MD simulations of Cu-Zr NGs illustrate that structural relaxation causes an increase in the volume fraction of fully icosahedron (FI) Cu ⟨0 0 12 0⟩ clusters [Ritter et al., 2011; Adjaoud et al., 2021]. The fraction of FI Cu ⟨0 0 12 0⟩ clusters at the GIs increases significantly during the annealing process while they change little in the interior of GGs. Moreover, Nandam et al., 2017 have reported the absence of pop-ins in the *P-h* curves and SBs at the imprint edges of an annealed Cu–Zr NG, contrary to the MD results, which predict SB-mediated plastic flow. So, it would be interesting to see if relaxing the NG at high temperatures (nearly at the T_g) has any effect on the nature of the plastic flow. Therefore, nano and micro-indentation experiments are carried out at different loads on AP and SR Cu-Zr-based NG. The results reveal that annealing has a marked influence on the SB behavior and properties of SR NG. The *P-h* curves, which generally display a smooth behavior in NG, exhibit discrete displacement bursts in SR NG, indicating that the plastic deformation is heterogeneous, which is also supported by the shear bands at the periphery of the imprint in the micro-indentation (Figure 3a). SR NG displays higher hardness than MG, which is attributed to the FI clusters and the annihilation of free volume (Figure 3b).

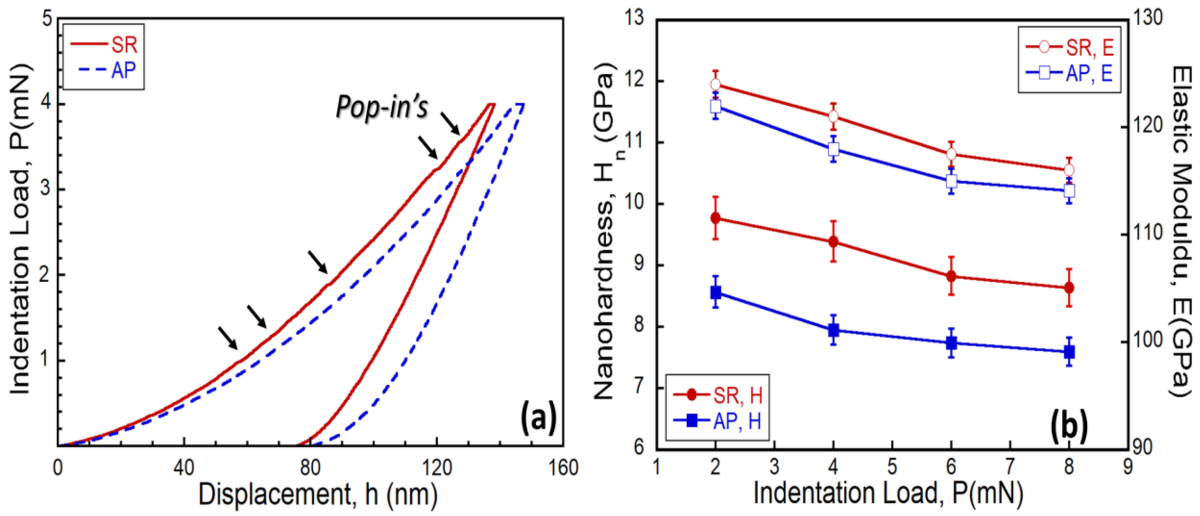

Figure 3. (a) Representative indentation load, *P*, vs. penetration depth, *h*, curves of the SR and AP NGs obtained at a P_{max} of 4 mN. (b) Variation of nanohardness, H_n, and elastic modulus, *E*, with maximum indentation load, P_{max}, of both SR and AP NGs.

Further, the *H* decreases with increasing *P* in both the nano- and micro-indentation regimes, showing an indentation size effect. The increase in free volume generation in the subsurface deformation zone and the increase in deformation volume underneath the indentation with indentation load appear to be the reasons for the ISE.

Apart from the recent research on understanding the origins and kinetics of SBs, one of the important aspects of plastic flow has received very less attention in NGs, which is strain rate sensitivity (SRS). SRS provides useful information about the mechanism of plastic flow. It has been shown that SRS can also be obtained from the indentation experiments as $m = dlogH/dlog\dot{\varepsilon}_i$, where H and $\dot{\varepsilon}_i$ represents the indentation hardness and indentation strain rate, respectively. In this regard, several studies have been conducted on BMGs to investigate the m value of BMGs, and most of the studies have reported report negative m, except a few. It has been argued that the positive m values are due to the experimental artifact, and the possible reason for this is the overestimation of H without considering the pile-up around the impression, particularly at high indentation loads [Bhattacharya et al., 2015]. Unlike the deformed MGs and BMGs, where the free volume is heterogeneously distributed, the NGs have a more uniformly distributed defect structure. Hence, in the context of NGs, it is very important to understand: (a) What is the effect of loading rate on NG and MG load vs. displacement response having identical composition? (b) How does the hardness vary with the loading rate? (c) What is the role of NG microstructure on m? and (d) How do m values of NGs fare with the MGs of an identical composition? To address the above questions, nanoindentation experiments are carried out on a binary $Cu_{60}Zr_{40}$ MG and NG at different loading rates. Results show that the *P*-*h* curves of MG exhibited noticeable displacement bursts at low loading rates, which gradually decreased with increasing loading rate suggesting a transition from more to less severe heterogeneous plastic flow (Figure 4a). While in the case of NG, no noticeable displacement bursts are present at any of the loading rates suggesting a near homogeneous plastic flow (Figure 4b). The hardness of both the NG and MG decreases with increasing loading rate implying negative strain rate sensitivity, m, which is attributed to the increase in free volume due to the increase in indentation load. The m values of NG are observed higher than the MG, indicating a tendency towards the near homogeneous plastic flow. To understand the trend observed in m values between the NG and MG interface, micro-indentation experiments are performed by utilizing the bonded interface technique. The results indicate that the primary shear bands (PSBs) are the main carriers of plastic flow in MG, while in NG, owing to the high free volume, it is by secondary shear bands (SSBs). The high value of m in NG compared to the MG is attributed to a large number of fine shear bands and near homogeneous plastic deformation.

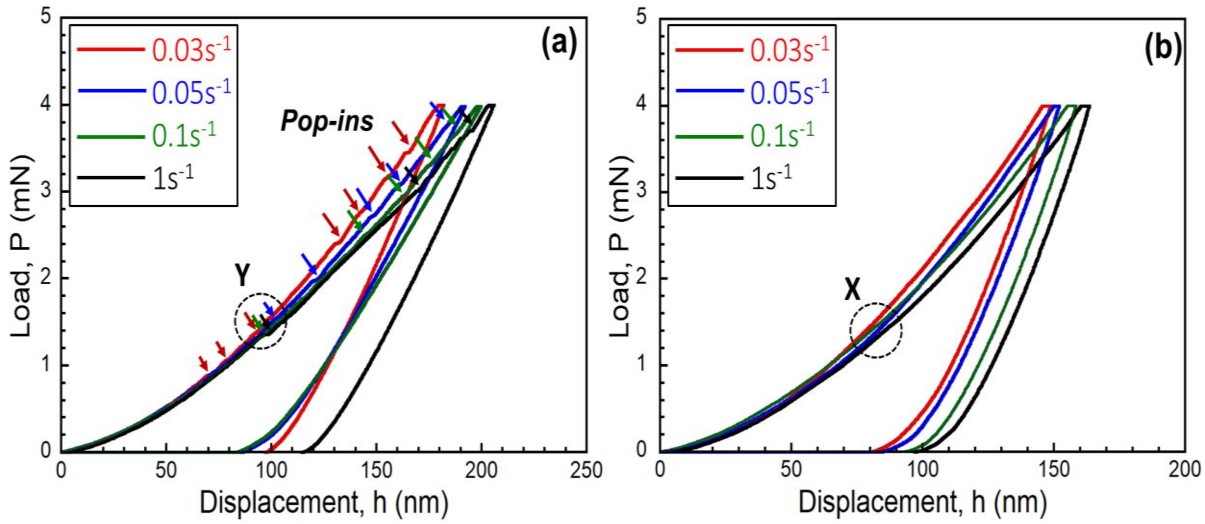

Figure 4. Representative indentation load, *P* vs. penetration depth, *h* curves obtained under different loading rates for (a) NG and (b) MG at a P_{max} of 4 mN, respectively.

Among the available nanoindentation technique, the use of a three-sided Berkovich pyramid tip as an indenter has become a standard in conventional hardness tests because of the possibility of formulating sharper tips with small tip rounding. However, a much sharper indenter travels a much larger depth inside material for a given load due to the generation of high-local stresses beneath the tip. The sharper the angle, the greater the strain generated beneath the tip. Jang et al., 2007 utilized Berkovich and cube-corner indenters to observe the deformation behavior and concluded that the serrated flow behavior observed in the *P*-*h* curves depends not only on the instrument's resolution but also on the indenter geometry. They reported that the sharp cube-corner indenter produces more significant pop-ins in *P*-*h* curves and a larger proportion of permanent plastic deformation after unloading. Thus, it is crucial to understand the dependency of indenter geometry on the mechanical properties of amorphous material. Nevertheless, most of the studies conducted hitherto are on binary MGs or multicomponent BMGs, but limited, or no attention has been given till now to understanding the effect of indenter geometry on the deformation behavior of NGs. Therefore, a series of nanoindentation experiments are conducted between a binary $Pd_{80}Si_{20}$ metallic glass (MG) and nanoglass (NG) using Berkovich and cube-corner indenters having different centreline-to-face angles. The results show a strong dependence of serrated flow behavior on the indenter angle observed in MG and NG. The sharp cube-corner indenter displaces a greater volume of material for a given load (more than three times the Berkovich indenter), and the material deforms by a cutting mechanism, resulting in prominent serrations in the loading curves and higher pile-up.

For a given geometry of the indenter, NG displays lower hardness than MG owing to the lower segregation effect, and the hardness decreases with the increase in maximum indentation load, which signifies the indentation size effect (ISE). The rise in the deformation volume underneath the tip due to an increase in free volume content with indentation load appears to be the reason for the ISE. A useful parameter, discrete plasticity ratio, Ψ is utilized to estimate the influence of serrations on the total plastic deformation. It is observed that Ψ does not change significantly with the load (Figure 5), indicating that the deformation mode remains the same with either indenter in both MG and NG (i.e., heterogeneous in MG and homogeneous in NG. The results are explained in terms of primary concepts to examine the deformation behaviors in the MG and NG with different indenter geometry.

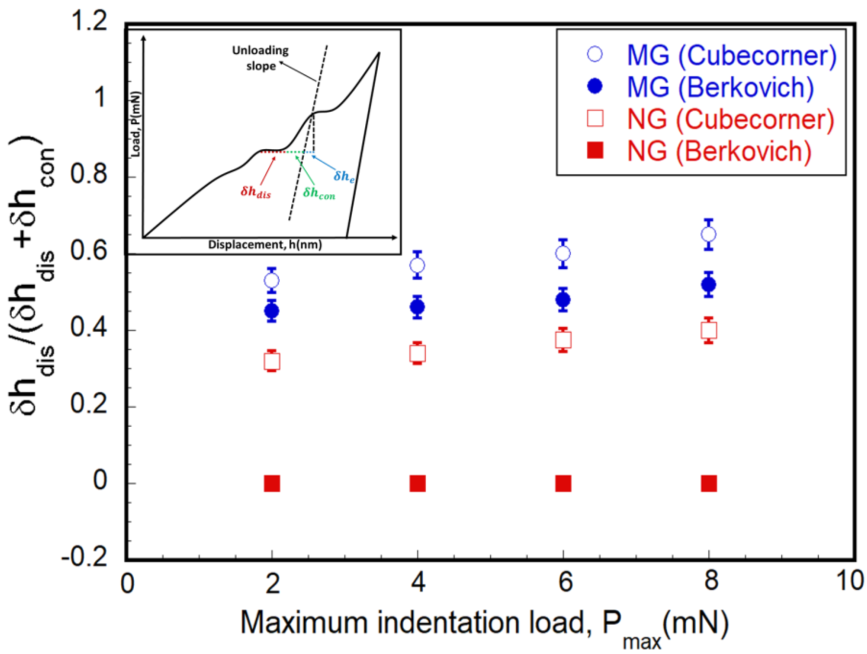

Figure 5. Plot showing the variation in the discrete plasticity ratio, Ψ with the maximum indentation load, P_{max} for MG and MG with Berkovich and cube-corner indenter (The inset image displays the method to calculate Ψ)

In summary, the present thesis is focused on understanding the deformation behavior and plastic flow of SBs in binary MGs and NGs by utilizing nanoindentation, micro-indentation, and bonded-interface indentation techniques. The findings will help us shed new light on understanding the deformation mechanisms of MG and NG and provide novel guidelines for designing the amorphous alloys with improved ductility, for the desired engineering applications.

The organization of the present thesis is as follows:

In chapter 1, the introduction of MG and NG, along with their deformation theories, are discussed. Further, the different indentation techniques along with the pertinent literature of MG and NG on those techniques, are discussed in detail. The motivation and objective of the thesis are also presented.

In chapter 2, Bonded interface indentation (BII) technique is employed to understand the differences in the shear band characteristics between a binary Pd-Si MG and NG.

In chapter 3, The effect of structural relaxation on the deformation behavior of NG is studied by employing the nanoindentation and micro indentation techniques. The role of free volume on the Indentation size effect and deformation behavior is examined.

In chapter 4, the strain rate sensitivity, m, of a binary $Cu_{60}Zr_{40}$ NG and MG is investigated using nanoindentation. Indentations were performed at different loading rates in the range of 0.26 to 8 mN/s, which gives equivalent indentation strain rates over three decades. Further, the BII method is used to explain the variation in the values of m among MG and NG.

In chapter 5, the role of indenter geometry on the deformation behavior in a PdSi MG and NG is investigated by using Berkovich and cube-corner indenters. A useful parameter, discrete plasticity ratio, Ψ is utilized to estimate the influence of pop-ins on the total plastic deformation.

In chapter 6, the conclusion from the present work is summarized, and directions for future work is proposed.

List of publications from the present thesis work:

Sharma A., Nandam S. H., Hahn H., Prasad K. E. (2021), On the difference in shear band characteristics between a binary Pd-Si metallic and nanoglass, *Scripta Materialia*, 191, 17-22 (doi.org/10.1016/j.scriptamat.2020.09.009).

Sharma A., Nandam S. H., Hahn H., Prasad K. E. (2021), Effect of structural relaxation on the indentation size effect and deformation behavior of Cu-Zr- Based Nanoglasses, *Frontiers in Materials*, 8, 1-10 (doi.org/10.3389/fmats.2021.676764).

Sharma A., Hirmukhe S. S., Nandam S. H., Hahn H., Singh I., Narayan R. L., Prasad K. E. (2022), Strain rate sensitivity of a $Cu_{60}Zr_{40}$ metallic and nanoglass, *Journal of Alloys and Compounds*, 921, 165991 (doi.org/10.1016/j.jallcom.2022.165991).

Sharma A., Tripathi A., Nandam S. H., Hahn H., Prasad K. E. (2022), Role of Indenter geometry on the deformation behavior in a Pd-Si metallic and nanoglass, (Under Review- *JALCOM*).

List of publications out of present thesis work:

Hirmukhe S. S., **Sharma A.**, Nandam S. H., Hahn H., Prasad K. E., Singh I. (2021), Investigation of softening induced indentation size effect in nanoglass and metallic glass, *Journal of Non-Crystalline Solids*, 577, 121316 (doi.org/10.1016/j.jnoncrysol.2021.121316).

Sharma A., Sharma J., Singh I., Prasad K. E. (2022), Experimental assessment on the validity of Interface Indentation technique using Spherical Indenter, (To be submitted).

List of conferences/oral presentations from present thesis work:

1. **Sharma A.**, Prasad K. E. On the differences in the shear band characteristics between a binary Pd-Si metallic glass and nanoglass. *Indian Institute of Metals 75th Annual technical meeting (IIM ATM 2021)*, held online on 13 to 15 November 2021.
2. **Sharma A.**, Prasad K. E. Effect of structural relaxation on the indentation size effect and deformation behavior of CuZr-based nanoglasses. *International conference on advanced materials and mechanical characterization* (ICAMMC 2021-VIRTUAL) on 2-4 December 2021.

TABLE OF CONTENTS

LIST OF FIGURES

APPENDIX A

LIST OF TABLES

APPENDIX A

NOMENCLATURE

ABBREVATIONS AND GREEK SYMBOLS

T_g	Glass transition temperature
T_x	Crystallization temperature
ϑ	Free volume
ϑ_f	Average free volume
ϑ^*	Critical volume
γ	Geometrical factor
k_f	Temperature dependent rate constant
Ω	Atomic volume
K_B	Boltzmann constant
σ	Applied Stress
T	Temperature
V_0	Volume of the defect
c_f	Flow defect concentration
τ	Shear stress
P	Indentation load
P_{max}	Maximum indentation load
h	Penetration depth or Displacement
h_f	Final indentation depth
h_c	Indentation size or Contact depth
h_s	Sink-in depth
h_{max}	Maximum penetration depth
H	Hardness

H_d	Dynamic hardness
H_n	Nano-hardness
H_m	Mirco-hardness
E	Young's modulus or Elastic modulus
E_i	Elastic modulus of indenter
E_s	Elastic modulus of specimen
S	Stiffness
a	Contact Radius
A_c	Projected area of contact
ν	Poisson's ratio
μ	Geometry constant
α, β	Fitting constants obtained from the Oliver and Pharr method
ΔG	Activation barrier energy
Δf	Volume fraction of material with potential-jump sites
m	Strain rate sensitivity
Ψ	Shear band density
δ	Inter-band spacing
r_d	Distance from the tip of the indentation impression
λ	Subsurface deformation zone size
χ	Normalized subsurface deformation zone size
I	Current
$\dot{\varepsilon}$	Strain rate
$\dot{\varepsilon}_i$	Indentation strain rate
ε_r	Representative strain

$\dot{\gamma}$ Shear strain rate

C Temperature dependent material constant

h_{pop-in} Pop-in length or pop-in width

dP/dt Loading rate

φ Semi-apex angle

ACRONYMS

MG	Metallic glass
BMG	Bulk metallic glass
BMGMC	Bulk metallic glass matrix composite
MSR	Melt spun ribbon
SRO	Short range order
MRO	Medium range order
SB	Shear band
STZ	Shear transformation zone
GG	Glassy grain
GI	Glassy interface
NG	Nanoglass
TEM	Transmission electron microscopy
SEM	Scanning electron microscopy
XRD	X-ray diffraction
SAED	Selective area electron diffraction
IGC	Inert gas condensation
GNP	Glassy nanoparticle
MD	Molecular dynamics
AFM	Atomic force microscopy
DSC	Differential scanning calorimeter
ISE	Indentation size effect
RISE	Reverse indentation size effect
BII	Bonded interface indentation
PSB	Primary shear band

SSB	Secondary shear band
AP	As-prepared
AC	As-cast
SR	Structurally relaxed
FI	Fully Icosahedron
SLM	Selective laser melting
CSM	Cooperative shearing model
SP	Shot-peened
FEA	Finite element analysis

CHAPTER 1

INTRODUCTION

1.1. Metallic glasses: History, Kinetics, and Applications

Metallic glasses (MGs) are amorphous alloys fabricated by the rapid cooling of liquid alloys. In general, when the liquid alloy is rapidly cooled to a temperature lower than the meting point, it freezes to form a glass at a temperature called glass transition temperature (T_g) (refer to Fig. 1.1). Kauzmann, 1948 was the first scientist who gave the concept of the glass transition phenomenon according to which when the entropy of the liquid is extrapolated to a temperature below the melting point, the entropy of the liquid becomes equal to the entropy of the solid, which is not feasible. Thus, the liquid melt can no longer sustain in that metastable condition and freezes to form a glass at a temperature known as Kauzmann temperature (T_k) or glass transition temperature (T_g). It is important to observe from Fig. 1.1 that there is no change in the molar volume at T_g, implying no shrinkage in the melt during rapid quenching. Another important information that can be inferred from figure 1.1 is that the T_g depends on the rate of cooling, and the stability of the glass increases with decreasing cooling rate.

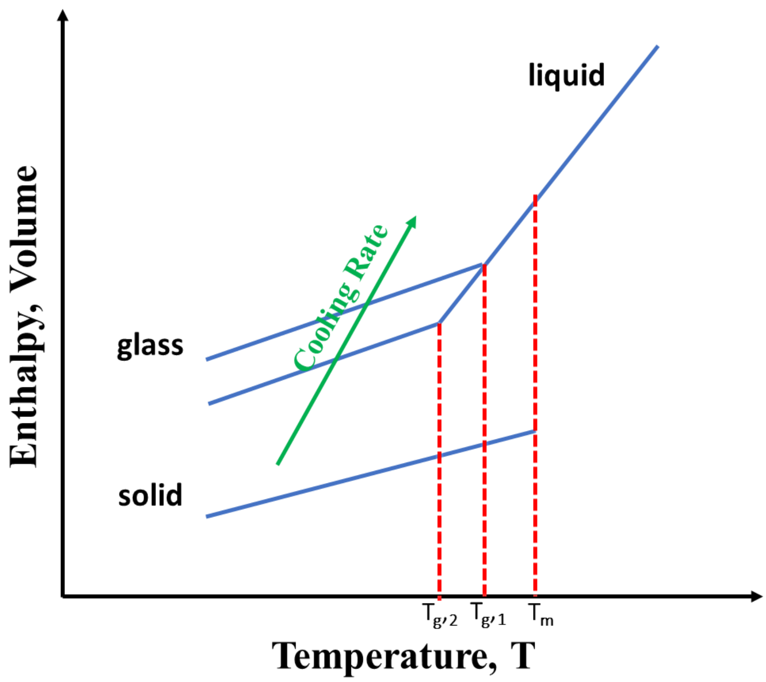

Figure 1.1 Representative plot displaying a variation of molar volume or enthalpy with temperature during the transition of liquid melt into an amorphous glass. The Tg increases with an increase in cooling rate. [Image inspired from the work of Kauzmann, 1948]

The very first MG came into the picture when Klement and co-workers tried to quench AuSi-based liquid alloy at very high cooling rates and discovered a new amorphous material named metallic glass (Klement et al., 1960). They utilized the "Splat quenching" technique to rapidly cool the liquid alloy at a cooling rate of around 10^5- 10^6 K/s. As it is not possible to achieve such high cooling rates on thick (or bulk) samples, the MGs, initially, are limited to only thin flakes or ribbons (typically < 1 mm), usually referred to as melt-spun ribbons. So, in the early days, the primary objective of the researchers was to fabricate the MGs in the bulk form, also referred to as bulk metallic glasses (BMGs). BMGs are multicomponent alloys, unlike binary MGs, and have thickness or diameter greater than 1 mm. Peker et al. 1993, successfully synthesized the BMGs up to a thickness of 14 mm by employing cooling rates even less than 10K/s. Inoue et al. 1995 made a pioneering contribution to the field of BMGs by introducing the empirical rules for the fabrication of BMGs, which are as follows:

i. The overall composition should comprise more than three elements.
ii. The three main elements should have an atomic size difference of 12%.
iii. The heat of mixing should be negative among the main elements.

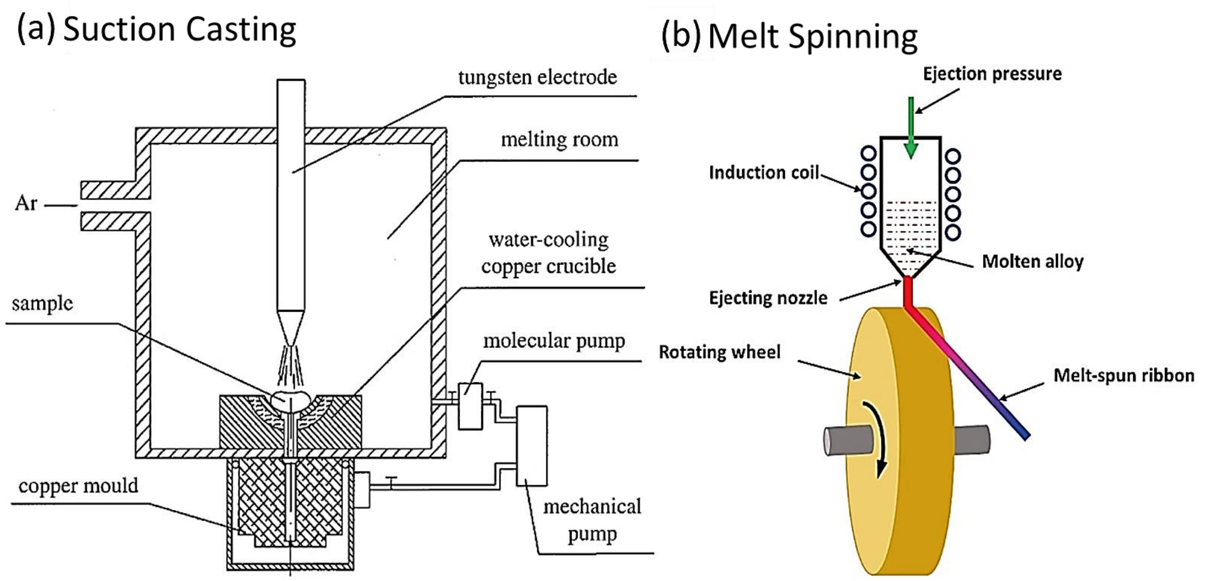

Figure 1.2 Schematic displaying the process of (a) Suction casting and (b) Melt spinning used to fabricate MGs [Adopted from Huang et al., 2006; Rong et al., 2018]

Following the above rules, different compositions of BMGs were synthesized to date using methods (refer to Figure 1.2a) like suction casting (Shen et al., 2005; Xia et al., 2007; Xu et al., 2010).

Since the MGs are formed by rapid quenching of liquid alloy, their atomic structure is similar to a frozen liquid. Unlike crystalline materials, they do not have a long-range periodic arrangement of atoms, and the atomic order is categorized into short-range order (SRO) and medium-range order (MRO). This has a marked influence on the defect structure of MGs and their structural and functional properties. MGs exhibit high hardness, wear resistance, high yield strength, resilience, low mechanical damping, excellent corrosion resistance, high magnetic permeability, and resistivity, which is nearly independent of temperature (Ashby and Greer, 2006). A combination of the above properties makes them promising materials for sports, electrical, aesthetics, medical, and space applications, and some of the components made of glasses are displayed in Fig. 1.3a. (Suryanarayana and Inoue, 2000).

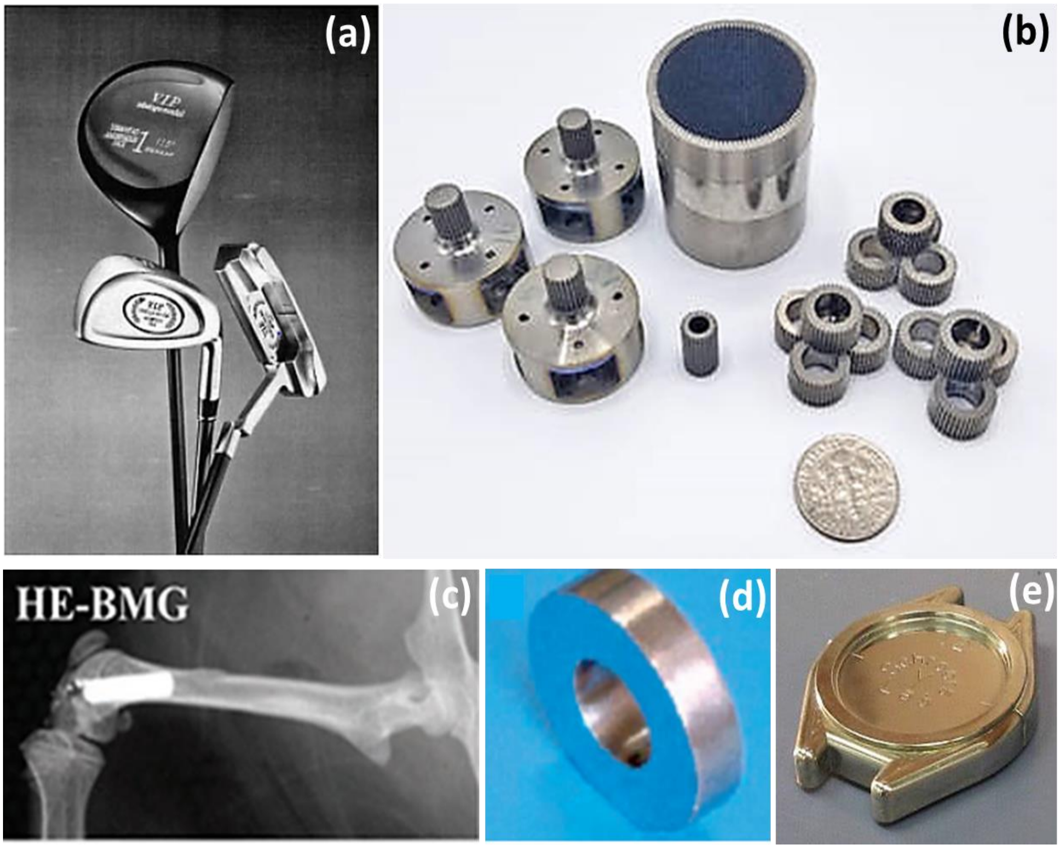

Figure 1.3 Typical application of BMGs (a) Sports (Golf sticks), (b) Automobile (Gears and Gearboxes), (c) Biomedical implants, (d) Electrical (Magnetic core), and (e) Watch cases [Adopted from Suryanarayana and Inoue, 2000; nasa.gov; Sharma and Inoue., 2010; Meagher et al., 2016; Schroers et al., 2011]

Another excellent and intriguing feature of MGs is the absence of volume shrinkage at T_g, which helps in making intricate net-shaped objects like gears, gearboxes, etc. (Wang et al., 2004). Recently, the National Aeronautics and Space Administration (NASA) has been exploring the possibility of miniature gears using BMGs, which can survive in cryogenic environments without the need for lubrication (nasa.gov). BMG gears and gearboxes with superior wear and corrosion resistance are capable of operating at very low temperatures and hence can be of help for in-space missions (refer to Fig. 1.3(b)). It is seen that Co- and Fe-based BMGs have shown good magnetic properties and hence have potential applications in the transformer core and magnetic shields. Compared to conventional transformers, the power transformers with MGs as a core are found to help in reducing core losses (Sharma and Inoue., 2010). Titanium-based BMGs have shown low density, excellent biocompatibility, and corrosion resistance and are considered ideal materials for biomedical applications (Meagher et al., 2016). Even the Nickel (Ni) watch cases are also replaced with BMGs with the help of the blow molding technique to prevent skin allergic reactions (Schroers et al., 2011).

These attractive attributes of MGs are offset by the lack of good tensile ductility at room temperature. They fail catastrophically in the form of shear bands (SBs) due to plastic strain localization (Schuh et al., 2007), preventing their widespread usage as a structural material.

1.2. Deformation theories of MGs

The deformation behavior of crystalline materials is explained by the dislocation theory, which is well supported by strong experimental evidence. The dislocation motion during the deformation can be well traced by experimental techniques such as transmission electron microscope (TEM) and high-resolution TEM. Unlike crystalline materials, the deformation behavior of MGs is difficult to comprehend due to the presence of SRO and MRO. The exact nature of local atomic motion during the plastic flow of MGs is not fully resolved by experimental methods. However, the consensus is that the strain is accommodated by the local rearrangement of a cluster of atoms in the less densely packed regions. The deformation behavior of MGs is often described by (a) Free volume theory and (b) shear transformation zone theory proposed by Spaepen, 1977 and Argon, 1979, respectively.

1.2.1. Free volume theory:

The original free volume model was proposed by Cohen and Turnbull,1959 in which the free volume ϑ of an atom is defined as the volume of the cage enclosed by the first nearest neighbor atoms, less the average volume of an atom. The probability, $p(\vartheta)d\vartheta$, of finding an atom with the free volume ϑ and $\vartheta + d\vartheta$ in (liquid/glass) is calculated to be:

$$p(\vartheta)d\vartheta = \left(\frac{\gamma}{\vartheta_f}\right) exp\left(\frac{\gamma\vartheta}{\vartheta_f}\right) d\vartheta$$

Where γ is the geometrical factor between 0.5 and 1, and ϑ_f is the average free volume of an atom. Free volume theory relies on the existence of voids whose volume is greater than critical volume ϑ^*. Spaepen (1977) used free volume theory and developed constitutive equations to describe the plastic flow in MGs. The plastic flow rate is calculated as the product of a fraction of potential jump sites and the net number of forward jumps per second in the shear direction.

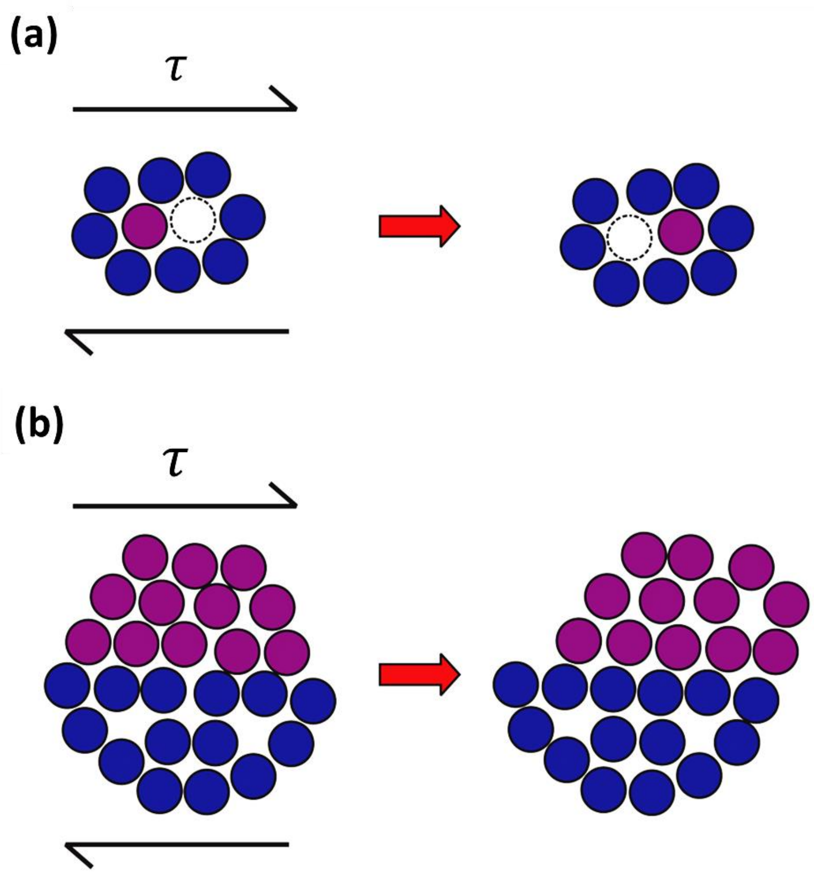

Figure 1.4 Schematic displaying the deformation theories proposed for MG. (a) Free volume (Spaepen, 1977) and (b) Shear transformation zone (STZ) theories (Argon, 1979).

The general constitutive equation is given as, $\frac{d\varepsilon}{dt} = 2c_f k_f \frac{\varepsilon_0 V_0}{\Omega} sinh\left(\frac{\varepsilon_0 V_0 \sigma}{2kT}\right)$ where k_f is the temperature-dependent rate constant, Ω atomic volume, k is the Boltzman constant, σ is the applied stress, T is the temperature, ε_0 is the strain, V_0 is the volume of defect, and c_f is the flow defect concentration. Spaepen used the above constitutive equation on the creep data and found that the critical defect (also known as flow defect) size is about 3-4 Å. Spaepen also proposed that the plastic deformation of MGs is characterized by the creation and annihilation of free volume. At high temperatures and low stresses, the plastic flow is Newtonian with constant viscosity and is classified as homogeneous deformation. While at low temperatures and high stresses, free volume is created due to squeezing of atoms into void size less than the ϑ^* causing a reduction in local viscosity leading to heterogeneous deformation. When a load is applied on MG, the atom jumps from its position to the immediate neighboring place, having a vacant space, leading to the creation of excess free volume, as shown in Figure 1.4a. The jumps are favorable to the nearby sites, which can easily accommodate the atom, and the model is also known as the local jump phenomenon. The steady-state plastic flow is achieved when the free volume creation rate is equal to the annihilation of free volume.

1.2.2. Shear transformation zone theory

Argon (1979) proposed that the free volume model based on the single atomic jump cannot describe the deformation. Instead, a cluster of atoms must be needed to accommodate the plastic deformation. According to this theory, under the application of stress in MG, a local cluster of atoms (~30-100 atoms) experiences an inelastic transition from one low energy configuration to another low energy configuration, passing transiently a stimulated configuration of high energy and volume, as shown in Figure 1.4b. Such clusters of atoms are known as shear transformation zones (STZs), and the simultaneous operation of several STZs contributes to the total inelastic strain during the deformation of MGs. Unlike dislocations, the STZs are transience can not be traced by experimental techniques. The computer simulations show that the number of STZs are limited at room temperature, and their density increases with increasing temperature. It is also observed that STZs are transformed in a given direction (in the direction of applied stress) and cannot be further transformed in the same direction as dislocations of crystalline materials.

At room temperature and high stresses, the limited number of STZs present at different locations of MGs coalesce and tends to form shear bands (SBs). Due to the paucity of STZs, the total plastic strain gets localized into one or few of the SBs, leading to catastrophic failure of MG, and the deformation, in this case, is deemed as heterogeneous (refer to Figure 1.5a-d). With the increase in temperature, the density of STZs increases leading to more uniform plastic flow and a change in the deformation mechanism from heterogeneous to homogeneous. The operation of STZs also requires significant dilatation of the matrix surrounding it, thus causing the plastic deformation of MGs sensitive to mean pressure or hydrostatic stress (Patnaik et al., 2004; Narasimhan, 2004). There have been several efforts to investigate the SB characteristics during the deformation of MGs, and indentation is one of the useful techniques to comprehensively characterize them, which will be discussed in detail in the subsequent sections of the chapter.

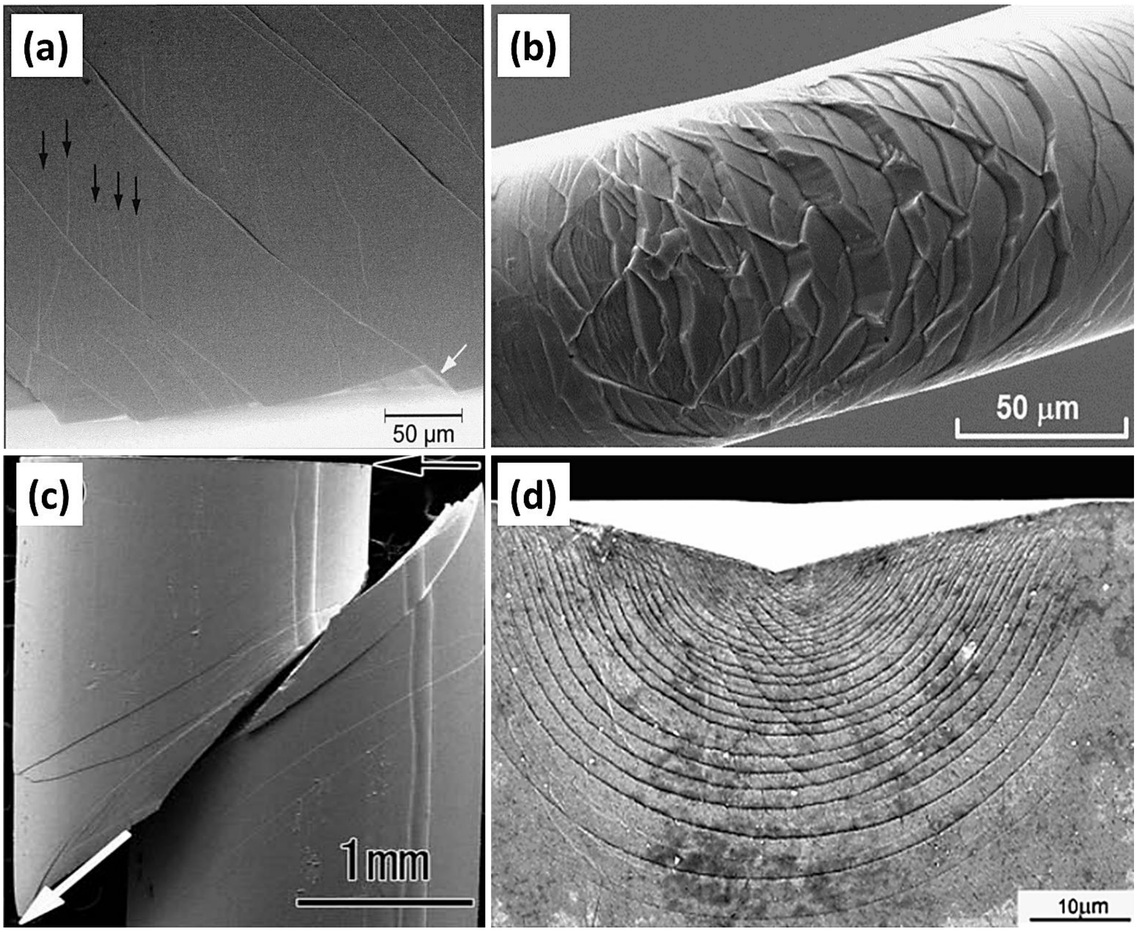

Figure 1.5 Shear bands observed in MGs at room temperature under different testing conditions (a)3-point bending, (b)In-situ Tensile, (c)In-situ Compression, and (d) Vickers Indentation. [Adopted from Hufnagel et al., 2000; Greer et al., 2013; Zhang et al., 2010; Xie et al., 2008]

1.3. Ductility improvement in MGs

The catastrophic failure of MGs due to localized shear deformation in the form of SBs at room temperature restricts their usage in several structural applications. Extensive literature studies have been focused on improving the plasticity of MGs by altering their internal microstructure of which the following are notable:

(i) Increase the free volume and STZ of as-cast glasses so as to increase the shear band density and reduce the plastic strain localization (distribution of plastic strain into multiple shear bands). This is often achieved by subjecting the as-cast samples to severe plastic deformation (Wang et al., 2012) using shot or laser shock peening

(ii) Providing selective obstacles to the rapidly propagating shear bands by having a crystalline phase in the amorphous matrix, also known as bulk metallic glass matrix composites (BMGMCs) (refer to Fig. 1.6) (Das et al., 2003; Hajlaoui et al., 2007; Eckert et al., 2011; Hofmann et al., 2008; Hays et al., 2000; Narayan et al., 2012; Qiao et al., 2016).

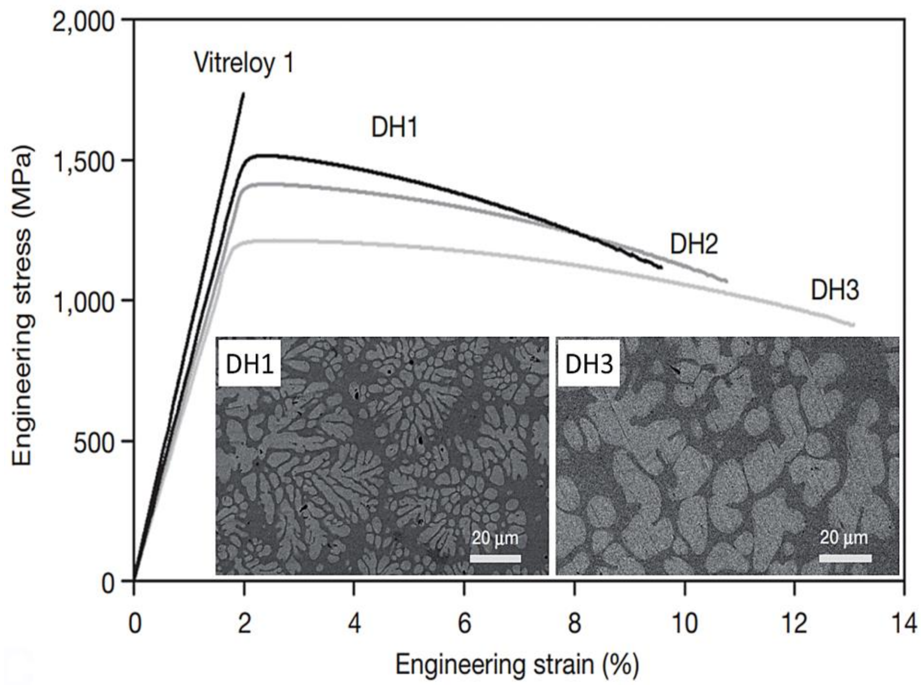

Figure 1.6 Engineering stress-strain curve of the different types of Zr-based BMG and its composites, along with inset images displaying their SEM micrographs. DH1, DH2, and DH3 refer to the different compositions of BMG matric composite [Adopted from Hofmann et al., 2008]

Although they reduced the shear localization to some extent, both the above methods suffer from certain disadvantages. For example, the severe plastic deformation due to shot or laser peening is only limited to the surface layers, with the interior of samples still comprising the original structure. Similarly, the BMG composites contain a significant volume fraction of crystalline phases leading to a reduction in fatigue strength and other properties (e.g., corrosion resistance, conductivity, etc.) that are unique to a completely amorphous structure. These studies illustrate that enhancing the plasticity of binary glasses is still an alluring issue as obtaining a fully amorphous structure with uniformly distributed free volume at different regions of the samples is very challenging.

1.4. Nanoglass: A new amorphous material

The limitations of the above two methods can be overcome if the amorphous alloys are designed in such a way to contain uniformly distributed free volume throughout the bulk sample without any crystalline phases. Gleiter and co-workers have proposed a concept to develop a dense amorphous alloy containing glassy grains (GGs) surrounded by glassy interfaces (GIs) (akin to nanocrystalline materials), both having different free volume content. Such glass can be fabricated if the amorphous nanoparticles are compressed at high pressures to achieve a dense amorphous alloy, with both the grains and interfaces being amorphous. The central theme of designing such material is to check if the differential free volume present in GGs and GIs can improve the ductility of the glasses. The molecular dynamic simulations of such an amorphous alloy reveal the presence of profuse shear bands throughout the volume of the sample during deformation and thus avoiding plastic flow localization arising from a single shear band. Hahn and co-workers have fabricated such glass using the inert gas condensation (IGC) technique. The fundamental principle of IGC involves the evaporation of atoms, which collide with inert gas atoms in the chamber, lose their energy, and nucleate as small powder particles close to the evaporation crucible. These nanoparticles subsequently grow in the chamber and are carried to the cold finger by the convection current of the inert gas. There are several ways to evaporate the material in IGC, like thermal evaporation, laser ablation, sputtering, plasma heating, and electric arc discharge. Among these, thermal evaporation is the most popular because of its flexibility in preparing nanoparticles. The primary problem with making metallic amorphous nanoparticles in the thermal evaporation technique is the different vapor pressure of the constituent elements. Since metallic glasses form only in specific composition ranges, it is of utmost importance to have elements that have similar vapor pressures. So, to overcome this difficulty for other material systems, magnetron sputtering is employed instead of thermal evaporation in IGC. The NGs are prepared using direct current magnetron sputtering in an inert gas condensation (IGC) system. The nano-amorphous particles generated are collected in a powder collection cup and following the identical route of fabricating nanocrystalline materials by compacting and sintering nanoparticles (refer to Fig1.7a). These amorphous nanoparticles are then consolidated under high uniaxial pressure (~3-6 GPa) to obtain a structure consisting of GGs and GIs in bulk form, which is referred to as nanoglass (NG) (refer to Fig.1.7b) (Jing et al., 1989; Ivanisenko et al., 2018).

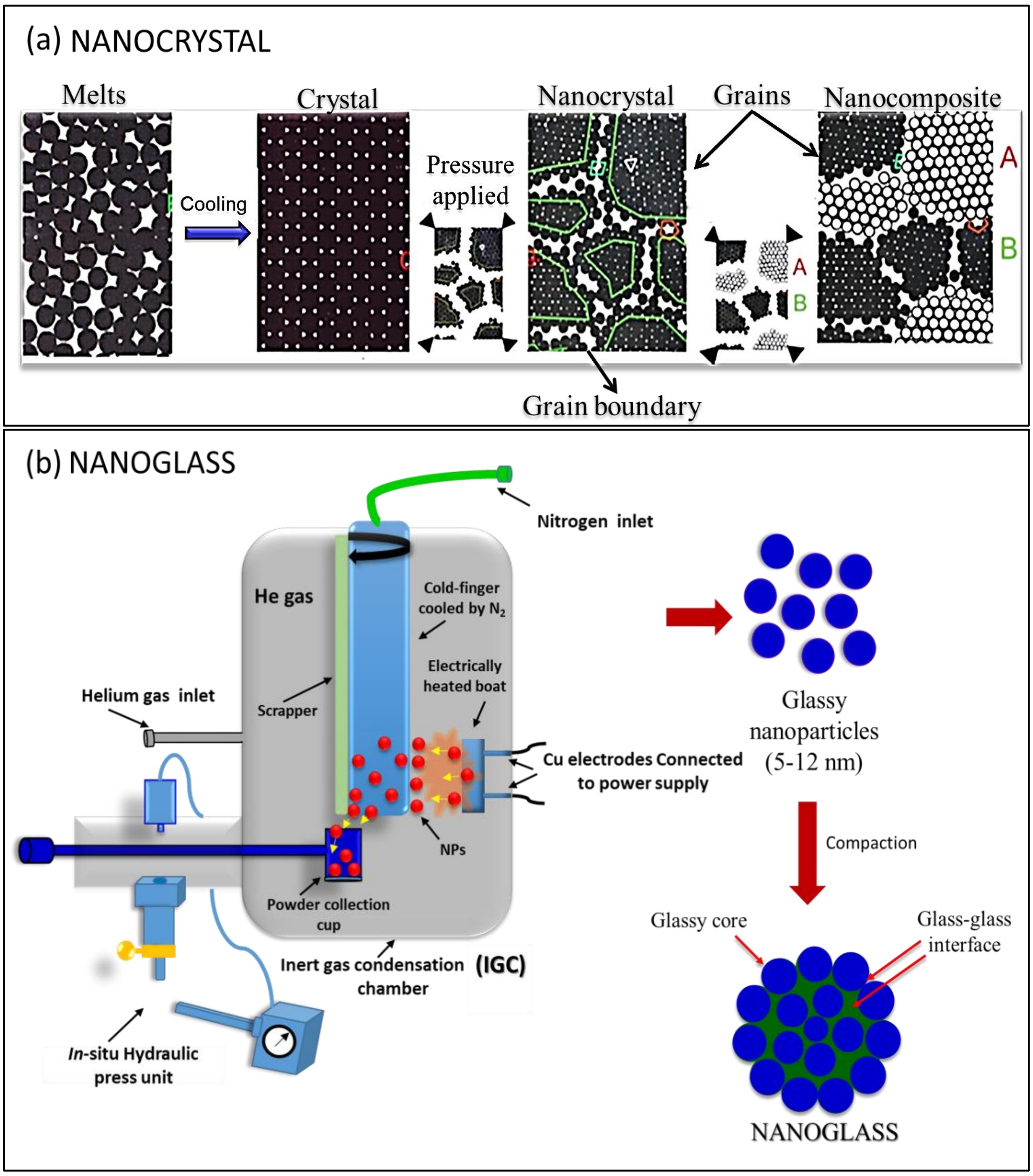

Figure 1.7 Figure displaying the analogy of the synthesis route of a (a) Nanocrystal and (b) Nanoglass. Schematic of IGC is also presented in (b) [Adopted from Gleiter, 2013; Singh et al., 2020]

Mossbauer spectroscopy of NGs reveals that the GIs are relatively less dense compared to the GGs, i.e., they are characterized by high free volume (Jing et al., 1989). Transmission electron microscope (TEM) investigations of NGs show that both the GGs and GIs are amorphous in nature with no signatures of crystalline phases (refer to Fig. 1.8a and b). The very first NG having a composition of $Pd_{70}Fe_{3}Si_{27}$ was fabricated in an inert gas condensation chamber (IGC) using the thermal evaporation technique. Later on, several other methods, such as magnetron sputtering (Chen et al., 2013; Nandam et al., 2017, 2020), multi-phase electron deposition (Guo et al., 2017, 2019; Li et al., 2018), and cold compaction (Fang et al., 2012; Nandam et al., 2017, 2020) were also explored. The average size of GGs and GIs in a NG is reported to be in the range of ~5-20 nm and ~1-2 nm, respectively (Ivanisenko et al., 2018). Several experimental and simulation studies on the morphology of a NG have reported an excess free volume and defective SRO in the GIs (Sopu et al., 2009; Ritter et al., 2011; Fang et al., 2012). Interestingly, it is observed that there is chemical segregation of elemental constituents occurring between the GGs and GIs.

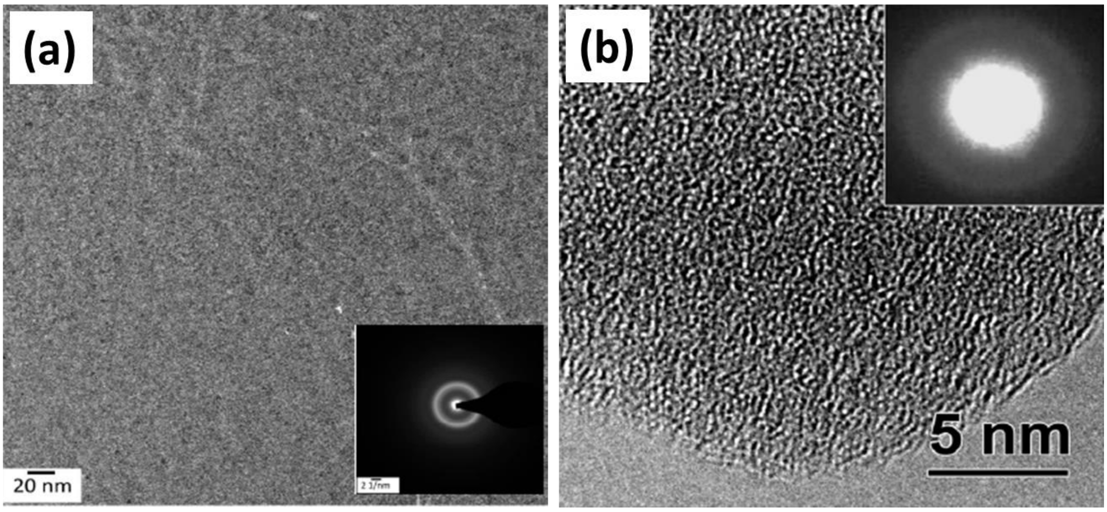

Figure 1.8 (a)TEM image of a Cu-Zr-based NG. (b) High-resolution TEM image of an Au-based NG. The inset displays the corresponding SAED patterns. [Adopted from Nandam et al., 2017; Wang et al., 2014].

Wang et al., 2017 utilized the X-ray scattering technique to study the atomic structure of a $Fe_{90}Sc_{10}$ glassy nanoparticle (GNP) and NG. The results indicate that the electron density of the surface shell is lower than the core of the GNP due to the segregation of Fe to the surface, leading to a lower atomic packing density. During the compaction of these GNPs into a NG, the extra free volume and SRO present in the core gets percolated to the interfaces. Ritter et al., 2011 utilized molecular dynamics (MD) simulations on a Cu-Zr-based NG and observed a defective SRO in the GIs along with an increase in free volume content of around ~1-2% compared to the GGs. Adjaoud et al., 2016, 2017 reported the surface segregation of Pd and Cu to the interfacial regions of $Pd_{80}Si_{20}$ and $Cu_{64}Zr_{36}$ NG, respectively, which has a significant influence on the structure of GGs and GIs (refer to Fig. 1.9). Nandam et al., 2017, 2020 observed high free volume in the GIs along with elemental segregation of 10% and 3-4% in $Cu_{60}Zr_{40}$ and $Pd_{80}Si_{20}$ NGs. It is evident that, besides the free volume, chemical segregation also has a marked influence on the physical properties of NG.

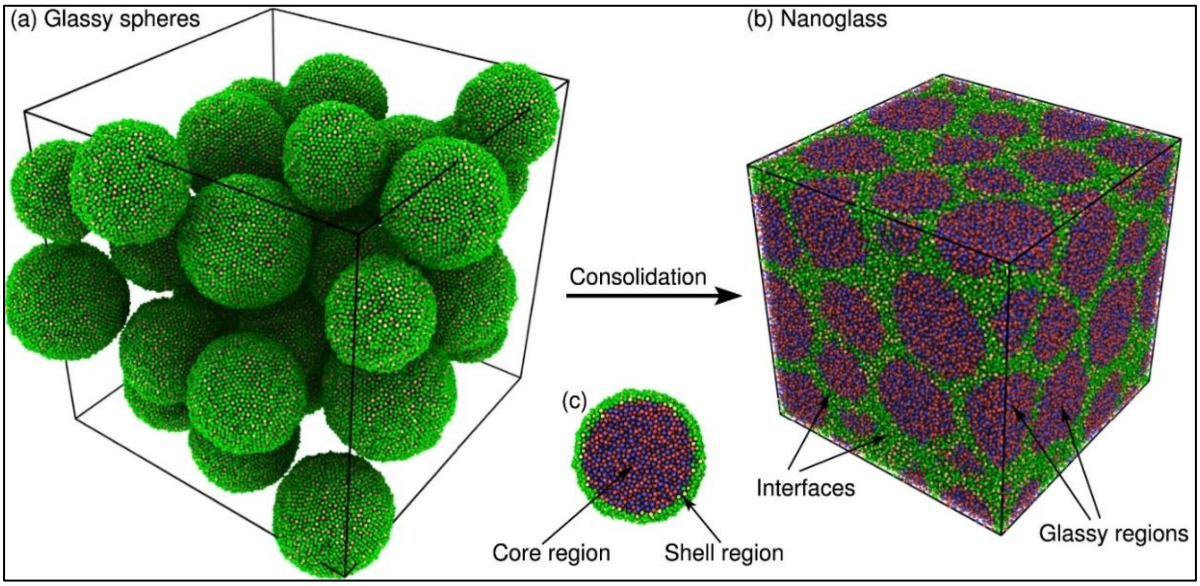

Figure 1.9 Figure displaying the processing route of Cu64Zr36 using MD simulation. Green and yellow colors represent the Cu and Zr atoms in the shell region, whereas red and blue colors show Cu and Zr atoms in the core region. The shell region has a different composition than the core due to surface segregation [Adopted from Adjaoud et al., 2017]

1.4.1. Attractive attributes of NGs over MGs

Unlike MGs, which fail in a brittle manner at room temperature, the NGs have shown remarkable improvement in ductility. Several MD simulations and limited experimental studies on different compositions of NGs have shown that NGs exhibit good ductility, and the deformation appears to be homogenous. Sopu et al. 2011 compared the deformation response of $Cu_{64}Zr_{36}$ MG and NG using MD simulations and observed that plastic strain gets accommodated in multiple shear bands in NGs while in very few shear bands in MGs. Besides this, they have also investigated the deformation response of a homogeneous and inhomogeneous NG, which differ from each other in terms of SRO, surface segregation, and free volume. Their observations reveal an increased SB activity in the inhomogeneous NGs as compared to the homogeneous NGs and MGs of identical composition (refer to Fig. 1.10). Albe et al., 2013 have observed that the deformation in NG changes from homogeneous to heterogeneous with the increase in grain size. The strength and elastic modulus also increase with the increase in grain size.

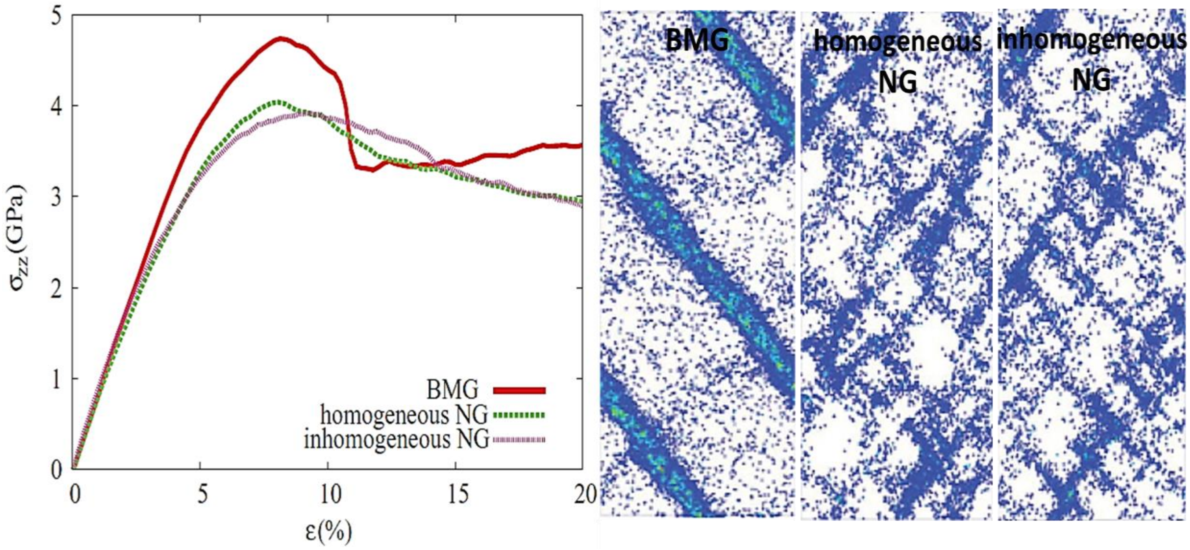

Figure 1.10 Stress-strain curves for CuZr BMG and homogeneous and inhomogeneous NG with corresponding simulation plots at 16% applied strain. [Adopted from Sopu et al., 2011].

Wang et al., 2015 performed uniaxial in-situ compression and tension experiments on $Sc_{75}Fe_{25}$ NG and MG and reported a tensile plastic strain of ~17% in NG while MG failed at about ~2%. The tensile samples showed necking features similar to the ductile metals, while the cross-section view of compressed samples showed signatures of multiple SBs in NGs single macroscopic SB in MG (refer to Fig. 1.11). Further, they also investigated the effect of specimen size on the strength and deformation behavior of NG and MG by varying the pillar diameter from 2 µm to 95 nm. The results showed that strength is independent of specimen size for MGs while it exhibits strong dependence for NG [Wang et al., 2016]. The deformation mode remains nearly homogenous in the case of NG at all the pillar sizes, whereas a transition in deformation mode is observed in MG with decreasing pillar size (refer to Fig. 1.12). Though uniaxial micro and macro compression experiments are helpful in understanding the deformation behavior of NGs, they are expensive and time-consuming and often fail to capture SB characteristics completely. In this regard, indentation is an extremely useful technique for characterizing the deformation behavior of amorphous alloys.

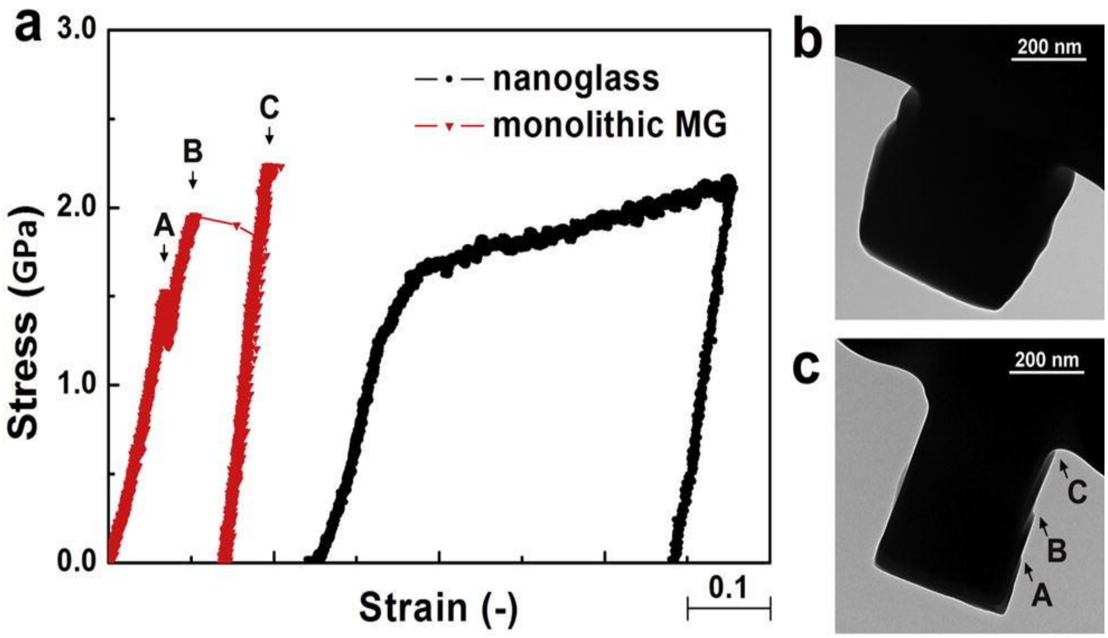

Figure 1.11 (a) Representative Stress-strain curves for MG and NG along with post-deformation TEM images of (b) MG and (c) NG. [Adopted from Wang et al., 2015]

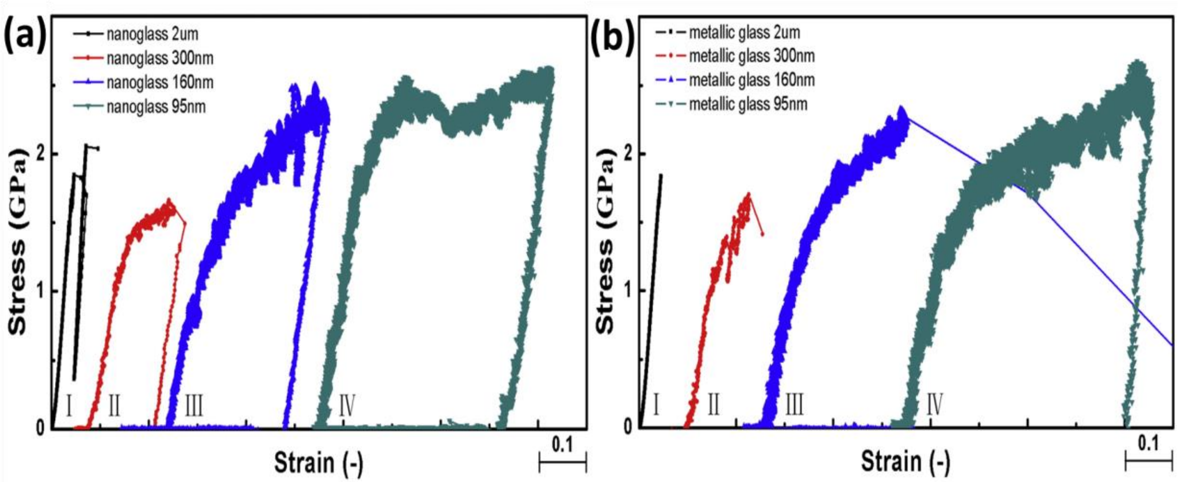

Figure 1.12 Stress-strain curves for (a) NG and (b) MG for different pillar diameters. [Adopted from Wang et al., 2016]

1.5. Indentation as a tool to characterize the deformation behavior of amorphous alloys

The indentation technique is one of the oldest methods to characterize the material's mechanical strength by means of hardness. This technique has certain advantages as compared to the conventional uniaxial compression: (i) It requires a small sample size, (ii) Experiments can be performed in quick time (iii) It involves constrained loading conditions. The constrained loading is particularly helpful in characterizing the deformation response of behavior of brittle materials as the large elastic continuum surrounding the indentation impression will resist the unhindered propagation of cracks. With the advent of instrumented indentation, it is possible to determine the elastic modulus of materials in addition to the indentation hardness.

1.5.1. Nanoindentation

Among the available instrumented indentation techniques, nanoindentation is found to be more effective due to its ability to apply indentation loads as small as *nN* and measure the penetration depths with a resolution of *nm*. During nanoindentation, the indentation load, *P*, and penetration depth or displacement, *h*, are continuously recorded to yield *P* vs. *h* curves, and a typical P vs. *h* curve of an elastoplastic material is shown in Fig. 1.13a. The hardness and elastic modulus are indirectly computed from the unloading portion of the *P*-*h* curve using the analysis proposed by Oliver and Pharr, 1994, popularly known as the O&P method. According to the O&P analysis, the relation between the *P* and *h* of the loading and unloading curves are described by equations 1 and 2 presented below:

$$\boldsymbol{P = \alpha h^{q}} \tag{1}$$

$$\boldsymbol{P = \beta\left(h - h_f\right)^{r}} \tag{2}$$

where $\alpha, q,$ are the fitting constants of the loading curve while β, r are fitting constants obtained from the unloading curves, h and h_f indicate the instantaneous and final penetration depth of the indenter, respectively.

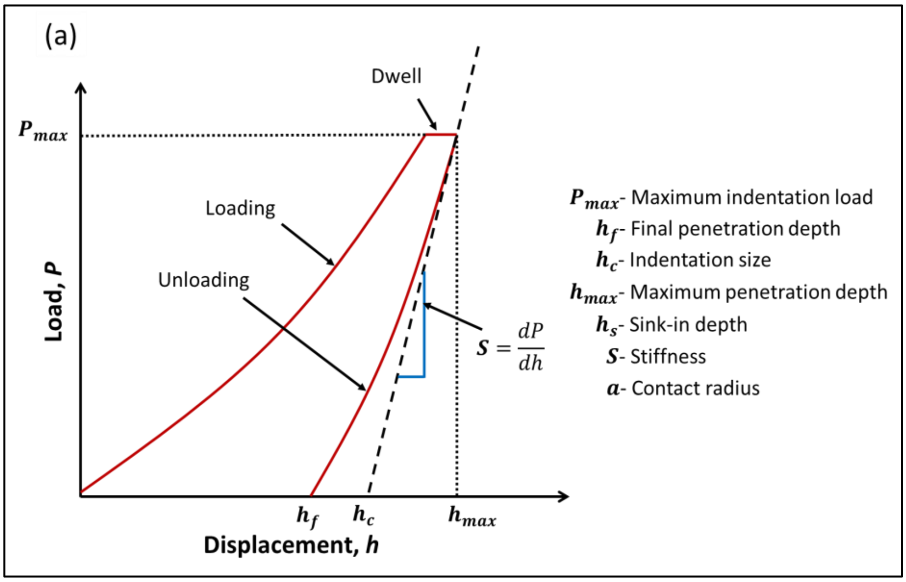

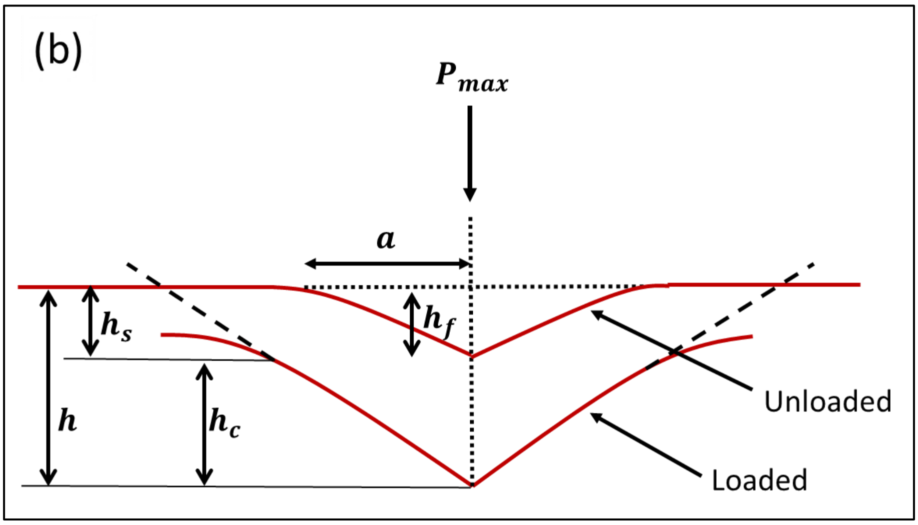

Figure 1.13 Schematic illustration of the (a) indentation load, P vs. displacement, h curves, and (b) unloading process displaying the important parameters used for the calculation of different properties. [Adopted and redrawn from Oliver and Pharr, 1992, 2004].

The values of q and r depend on the indenter geometry, and q lies in the range of 1.2 - 1.6, whereas r is in the range of 1.2 - 2. In the case of flat punch, both take a value equal to 1. The hardness, H, determined using the O&P method, is given as,

$$\boldsymbol{H = \frac{P_{max}}{A_c}} \tag{3}$$

Where P_{max} is the maximum indentation load, A_c is the contact area, which is a function of contact depth, h_c. As per the O&P method, the h_c is given by equation (2)

$$\boldsymbol{h_c = h_{max} - \mu \frac{P_{max}}{S}} \tag{4}$$

Here, h_{max} is the maximum penetration depth, μ is the geometry constant (~ 0.75, for Berkovich and cube-corner indenter), and S is the stiffness computed from the upper part of the unloading curve (refer to Fig. 1.13) as $S = dP/dh$. Finally, the effective modulus, E_s, is obtained from the equation (5):

$$\boldsymbol{E_s = (1 - \nu_s^2)\left[\left(\frac{2\sqrt{A_c}}{S\sqrt{\pi}}\right) - \left(\frac{1-\nu_i^2}{E_i}\right)\right]^{-1}} \tag{5}$$

where E and ν represent the elastic modulus, and Poisson's ratio and the subscripts i and s refer to the indenter and specimen, respectively. Before proceeding with any experiment, the area function of the indenter tip is calibrated with the help of a standard quartz sample by performing a series of indentations at different indentation depths and the relation between A_c

and h_c are obtained which is used in equations 3 and 5 to determine H and E_s. Berkovich and cube-corner indenters are the most commonly used indenters for nanoindentation, and they differ in the centre to face line angles (refer to Fig. 1.14). Cube corner, a sharper indenter, is often used to measure the indentation fracture toughness of brittle solids. Besides the hardness and elastic modulus, the *P*-*h* curves also provide information about the dislocation nucleation stresses in crystalline materials, shear bands in amorphous alloys, cracking events in ceramics, and phase transformation in materials (refer to Fig. 1.15).

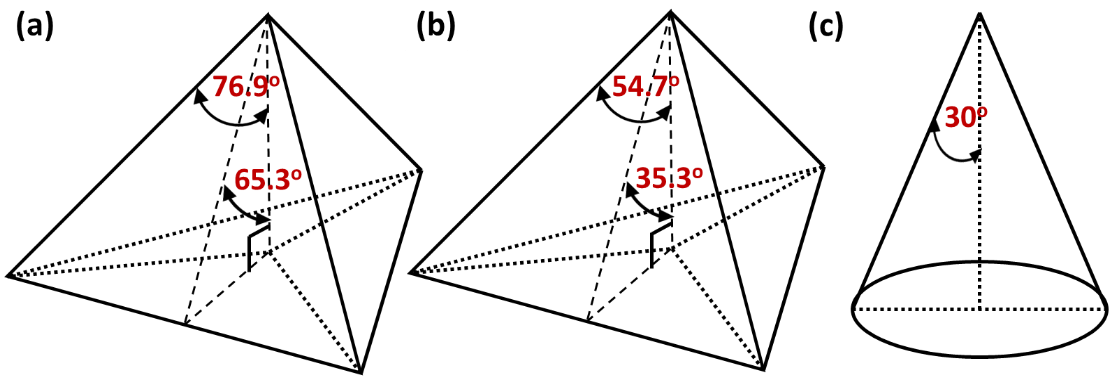

Figure 1.14 Schematic representing the shape and geometry (a) Berkovich, (b) Cube-corner, and (c) Conical tip.

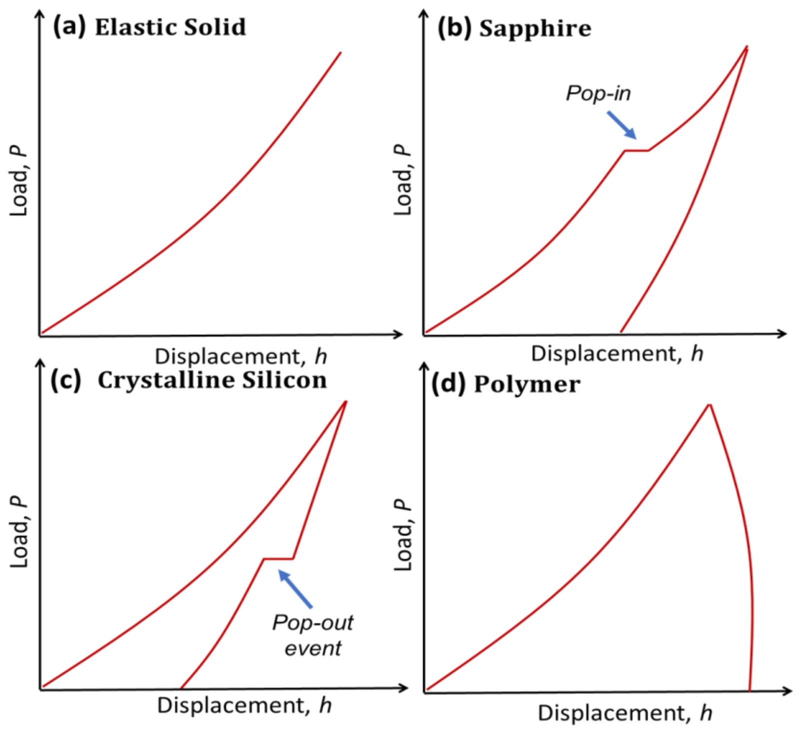

Figure 1.15 Schematic illustration of the *P* vs. *h* curve responses obtained for different materials. [Adopted and redrawn from Oliver and Pharr, 1992, 2004].

1.5.1.1. Nanoindentation studies on MGs

1.5.1.1.1. Serrated flow behavior in the *P-h* curves

It is well known that the plastic deformation of MGs occurs by nucleation and propagation of shear bands. Interestingly this is manifested as discrete displacement bursts (also called as pop-ins or displacement bursts) in the loading part of the *P-h* curves. Schuh and co-workers carried out nanoindentation experiments on Pd and Zr-based BMGs and observed a large number of pop-ins (refer to Fig. 1.16) in the loading curves. They concluded that each pop-in event possibly corresponds to the nucleation and activation of an individual SB. The propensity of SBs depends upon the indentation loading rate and temperature. They observed that pop-in width decreases with increasing loading rate suggesting that the deformation mechanism changes from heterogeneous to homogeneous. The threshold strain rate where the pop-ins are absent depends on the composition of the alloy and the local arrangement of atoms. Due to the kinetic limit of the SB, a single SB cannot accommodate the plastic strain at higher loading rates, thus leading to multiple SBs. (Schuh et al., 2002, 2003, 2004).

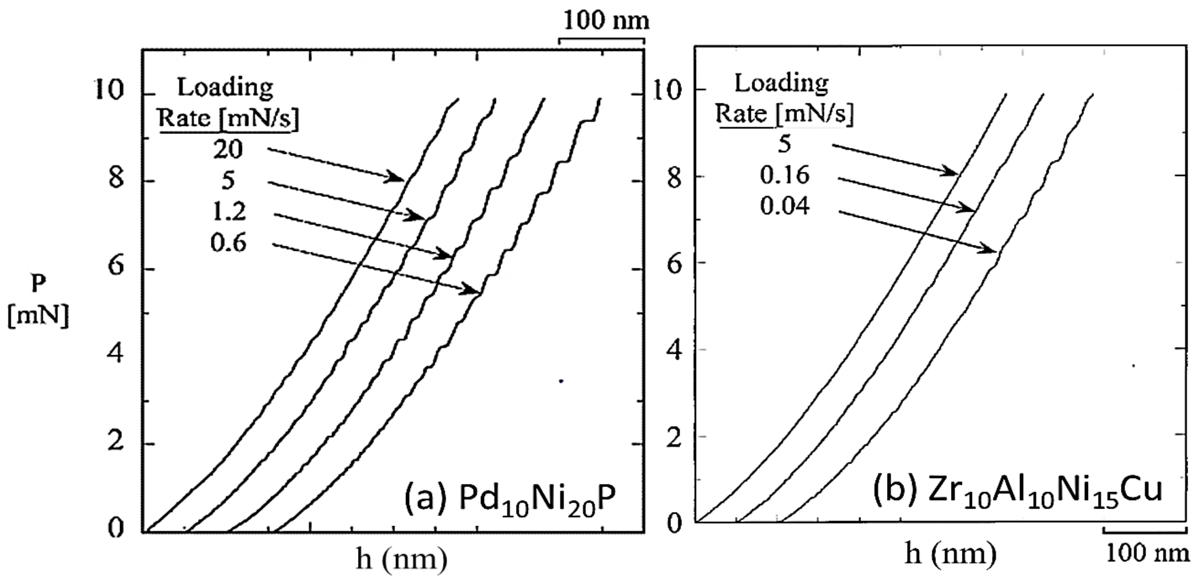

Figure 1.16 Representative $P - h$ curves displaying the loading portion of the nanoindentation tests for Pd and Zr-based BMGs [Adopted from Schuh et al., 2003]

Further, Jiang and Atzmon, 2003 and Greer et al. 2004 analyzed the indentation imprints of $Al_{90}Fe_5Gd_5$ and $Ni_{79}Ta_{14}C_7$ MGs (obtained at high loading rates) using atomic force microscopy (AFM) and observed shear bands on the slanting faces of the impression despite the absence of pop-ins in the *P-h* curves (refer to Fig. 1.17). The absence of serrated flow in the *P-h* curves could be due to the limitations of the resolution of the instrument. Jang et al., 2007 carried out indentation experiments using Berkovich and cube-corner indenters and showed that indenter geometry also has a marked influence on the serrated flow. At any given loading rate, the MG, which does not exhibit serrated flow using the Berkovich indenter, exhibits severe pop-ins with cube-corner indenters suggesting that the propensity of SBs depends on the plastic strain imposed by the indenter in the subsurface deformation zone.

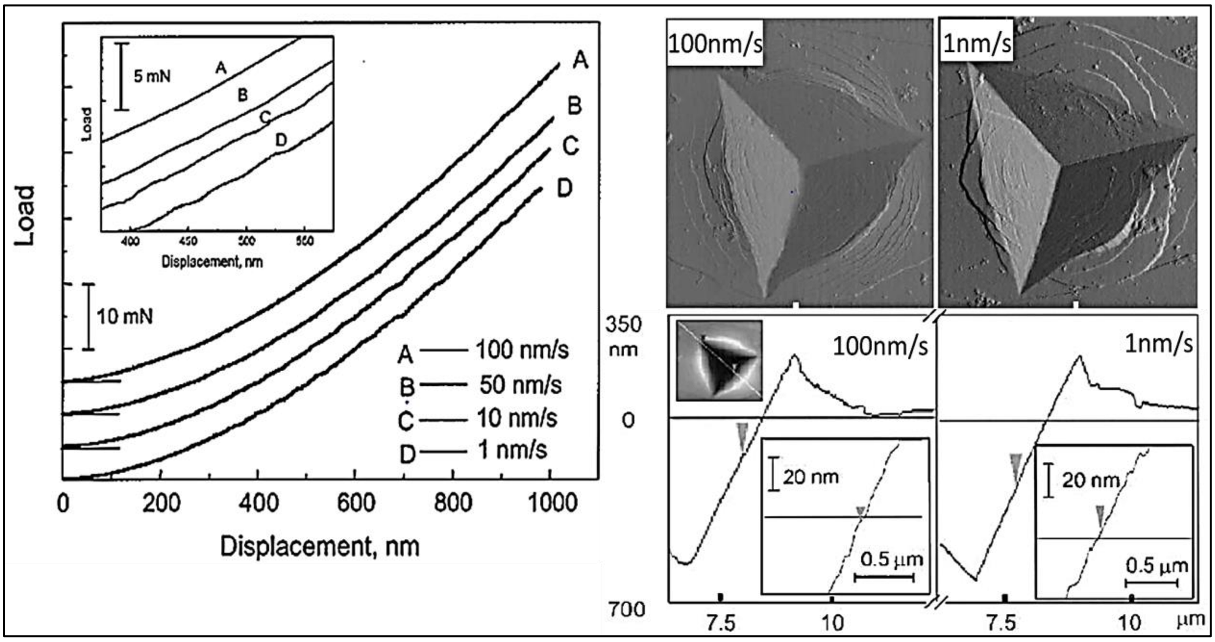

Figure 1.17 Representative $P - h$ curves, AFM illumination images with corresponding depth profiles of Al90Fe5Gd5 MG [Adopted from Jiang and Atzmon, 2003]

Ramamurty and co-workers 2005 investigated the role of structural relaxation on the P vs. h curves, hardness, and embrittlement of a Zr-based BMG. The as-cast glasses annealed below the T_g for different time intervals, and the differential scanning calorimetry (DSC) analysis of the samples shows that the free volume decreases with increasing annealing temperature or time. The nanoindentation *P-h* curves show pop-ins in both as-cast and annealed glasses, with the pop-in width slightly higher for the annealed glasses (refer to Fig. 1.18), which is attributed to the annihilation of free volume due to structural relaxation and thus leading to increased heterogeneous plastic flow. The macro-indentation *P-h* curves do not show serrations which may be due to the resolution of the instrument. The interesting observation is that the annealed glass shows a lower nanohardness (vis-à-vis large penetration depths) and higher microhardness as compared to as-cast BMGs. The trends in microhardness are concomitant with the reduction in free volume in the annealed BMG, but observations in nanohardness are conspicuous, which could be an experimental artefact or issues with the metallographic sample preparation. Later studies by the same group and others show that the hardness of the glasses increases with structural relaxation (Ramamurty et al., 2005; Zhang and Xie, 2005; Jiang et al., 2007; Yoo et al., 2009, 2011; Gu et al., 2013; Chen et al., 2019; Shi et al., 2021).

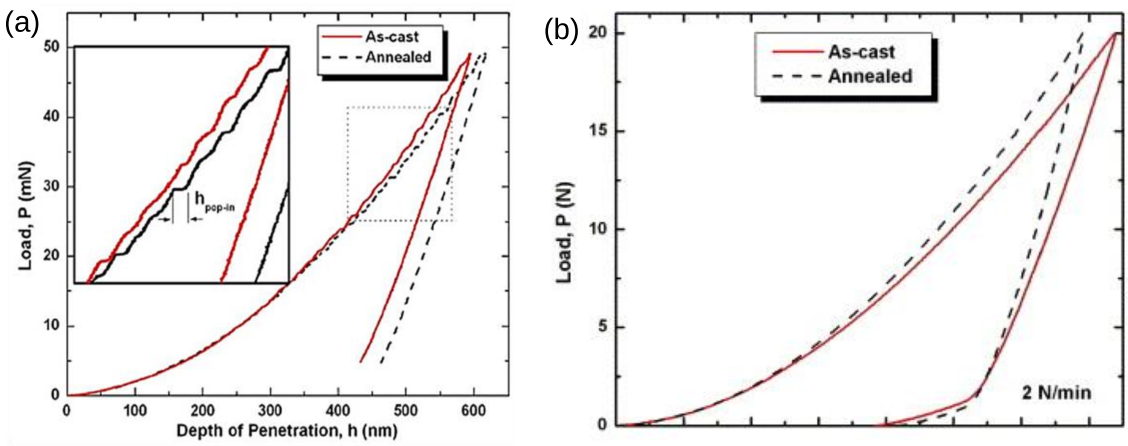

Figure 1.18 Representative (a) nano (b) micro-indentation P-h curves of as-cast and annealed Zr41.2Ti13.75Cu12.5Ni10Be22.5 BMG [Adopted from Murali and Ramamurty, 2005].

1.5.1.1.2. Indentation size effect

Apart from the serrated flow in the *P-h* curves, it is observed that the hardness of BMGs decreases with increasing in indentation load, commonly known as the indentation size effect (ISE) (Wright et al., 2001; Lam and Chong, 2001; Ramamurty et al., 2005; Yang et al., 2007; Steenberge et al., 2007; Huang et al., 2010; Xu et al., 2014; Xue et al., 2016; Li et al., 2017; Zhou et al., 2019). Wright et al., 2001 attributed the ISE in hardness to the material's ability to nucleate more SBs with increasing load due to an increase in deformation volume. Lam and Chong, 2001 developed an analytical model analogous to the Nix-Gao model and showed that geometrically necessary flow defects decreased with increasing indentation load. Later, Steenberge et al. 2007argued that the ISE observed is a consequence of the generation and annihilation of free volume in the subsurface deformation zone and proposed a relation between the hardness and free volume as per the following equation:

$$H \approx A \sinh^{-1}\left[\frac{\dot{\gamma}\Omega}{Bc_f} exp\left(\frac{\Delta G}{kT}\right)\right] \quad \textbf{(6)}$$

where constants A and B incorporate the activation volume of the flow event and material undergoing plastic shear, $\dot{\gamma}$ is the plastic shear rate, Ω is the atomic volume, c_f is the concentration of free volume which evolves during the deformation, k is the Boltzmann constant, T is the temperature, and ΔG is the activation barrier energy for defect migration.

According to the relation, the hardness inversely varies with the amount of free volume, which increases with an increase in indentation load resulting in ISE. The structurally relaxed BMG exhibit higher hardness (at all the indentation loads) compared to the as-cast due to the low free volume content (refer to Fig. 1.19). Huang et al. 2010 attributed the ISE to the pileup of material around the indenter, which appears to be more pronounced at low indentation loads and thus leads to the overestimation of O&P hardness (refer to Fig. 1.20).

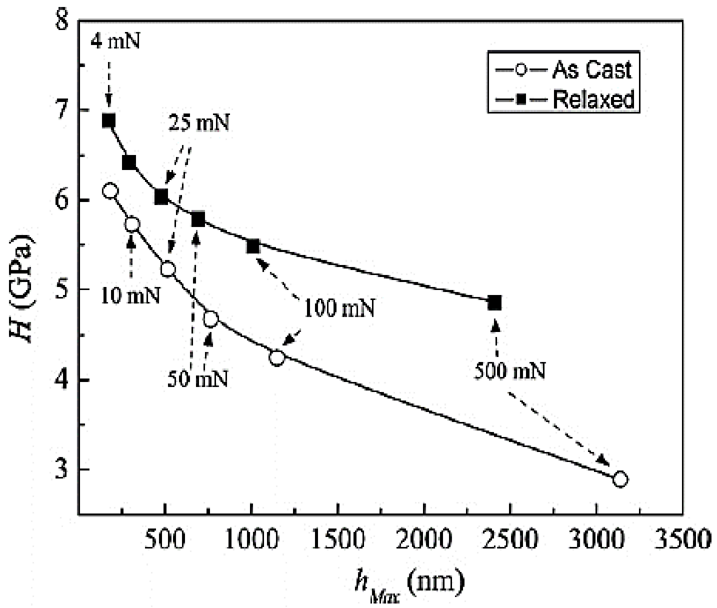

Figure 1.19 Hardness vs. maximum penetration depth plot for the as-cast and structurally relaxed sample. [Adopted from Steenberge et al., 2007]

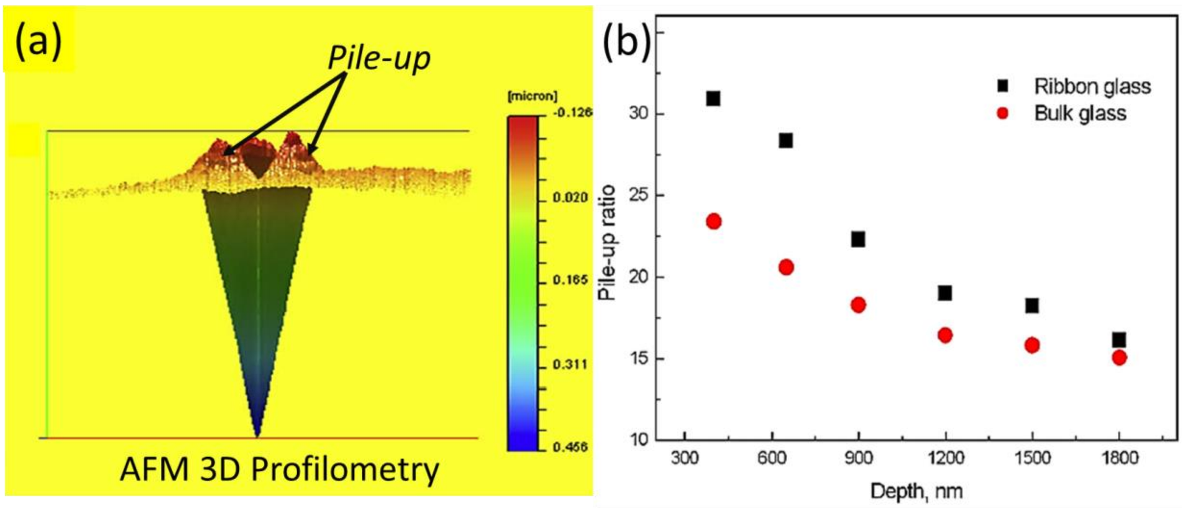

Figure 1.20 (a) Profile image of the indent using the atomic force profilometry (AFM) technique, (b) Plot representing the variation of pile-up ratio with the indentation depth. [Adopted from Huang et al., 2010].

1.5.1.1.3. Strain rate sensitivity

One of the key characteristics of plastic deformation of materials is the strain rate sensitivity, m, as it provides useful information about the mechanisms of plastic flow. Conventionally, m is determined from the strain rate jump tests under uniaxial loading conditions, and recently it has been shown that m can also be obtained from the indentation experiments as $m = dlogH/dlog\dot{\varepsilon}_\iota$, where H and $\dot{\varepsilon}_\iota$ represents the indentation hardness and indentation strain rate, respectively. Several studies (Dalla Torre et al., 2006; Jiang et al., 2007; Mukai et al., 2002; Dubach et al., 2009a; Gonzalez et al., 2011; Li et al., 2020; Wang et al., 2021; Ma et al., 2020; Pan et al., 2008; Boltynjuk et al., 2018; Bhattacharyya et al., 2015; Sort et al., 2019; Sahu et al., 2019; Zhao et al., 2021; Gunti et al., 2022) have been conducted to investigate the *m* value of BMGs, and most of the studies have reported negative *m*, except a few (Li et al., 2020; Wang et al., 2021; Ma et al., 2020; Pan et al., 2008; Boltynjuk et al., 2018). Pan et al., 2008 performed indentation strain rate jump experiments and observed that the *H* increases with loading rate, indicating positive *m* values. The micromechanics theory of deformation of materials suggests that the heterogeneous deformation results in negative *m* as observed in crystalline materials when the deformation occurs by luder bands. It is puzzling as to why the BMGs exhibit positive *m* despite the SB-mediated plasticity. Bhattacharya et al. 2015 have carried out rigorous experimental investigations on as-cast, structurally relaxed, and shot-peened BMG to check if the positive *m* is due to the material's response or any experimental artefact. Their experimental results show that *m* is negative, independent of the structural state of the BMG (refer to Fig. 1.21). A thorough analysis of the indentation impressions using AFM and SEM reveals a significant pile-up at the edges of the imprint, which increases with loading rate leading to overestimation of hardness. The possible reasons for this could be due to the lack of sufficient time (at high loading rates) for the material to relax the structure in the subsurface deformation zone. A slightly lower *m* for SP samples is due to the deformation-induced free volume with a concomitant increase in the number of STZs. Apart from the pile-up, Sort et al., 2019 have argued that the negative *m* could be due to the generation and accumulation of free volume at high loading rates leading to a decrease in hardness. In another study, Zhao et al., 2021 reasoned that the negative *m* values arise due to the differences in diffusion relaxation processes at different loading rates. Recently, Gunti et al. 2021 also observed a negative *m* and attributed it to increased activation of STZs at high loading rates.

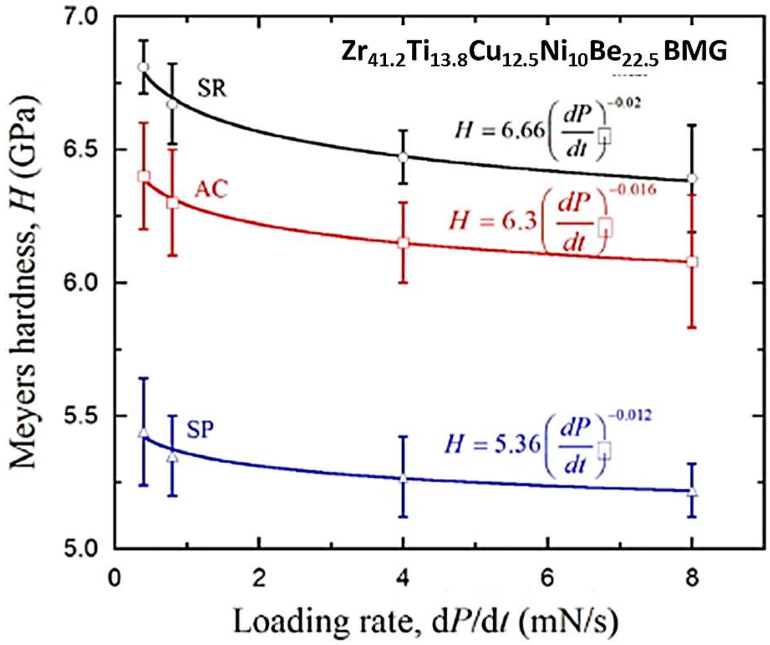

Figure 1.21 Variation of Hardness, H with loading rate dP/dt for $Zr_{41.2}Ti_{13.8}Cu_{12.5}Ni_{10}Be_{22.5}$ BMG [Adopted from Bhattacharya et al., 2015]

1.5.1.2. Nanoindentation studies on NGs

In line with the indentation studies on MGs and BMGs, micro and nanoindentation experiments, albeit limited, are conducted on NG primarily to understand the deformation behavior. Franke et al., 2014 carried out nanoindentation experiments on Scandium rich ($Fe_{28}Sc_{72}$) and Iron rich ($Fe_{90}Sc_{10}$) NGs and MGs and observed a higher hardness and modulus for Iron rich NG as compared to MG with no significant difference in $Fe_{90}Sc_{10}$ glasses. The reasons for the high hardness of Scandium-rich NG are attributed to the oxidation of NG as the scandium (Sc) has a high affinity to react with oxygen. Nandam et al., 2017 carried out nano and micro-indentation experiments on $Cu_{60}Zr_{40}$ NG and MG and observed no noticeable pop-ins P vs. h curves in NG while the MG counterparts exhibit pronounced pop-ins. The periphery of micro-indents in MG shows large SBs, while no SBs are observed in NG (refer to Fig. 1.22). NG exhibits a higher hardness and elastic modulus as compared to the MG because of the segregation of Cu atoms to the interfacial regions of Zr-rich dense cores. In another followed this, Nandam et al. 2020 observed a similar deformation response for $Pd_{80}Si_{20}$ NG and MG, with both the glasses exhibiting serrations in the P-h curves. A similar observation was reported for Ni-P thin film NG by Guo et al. 2019.

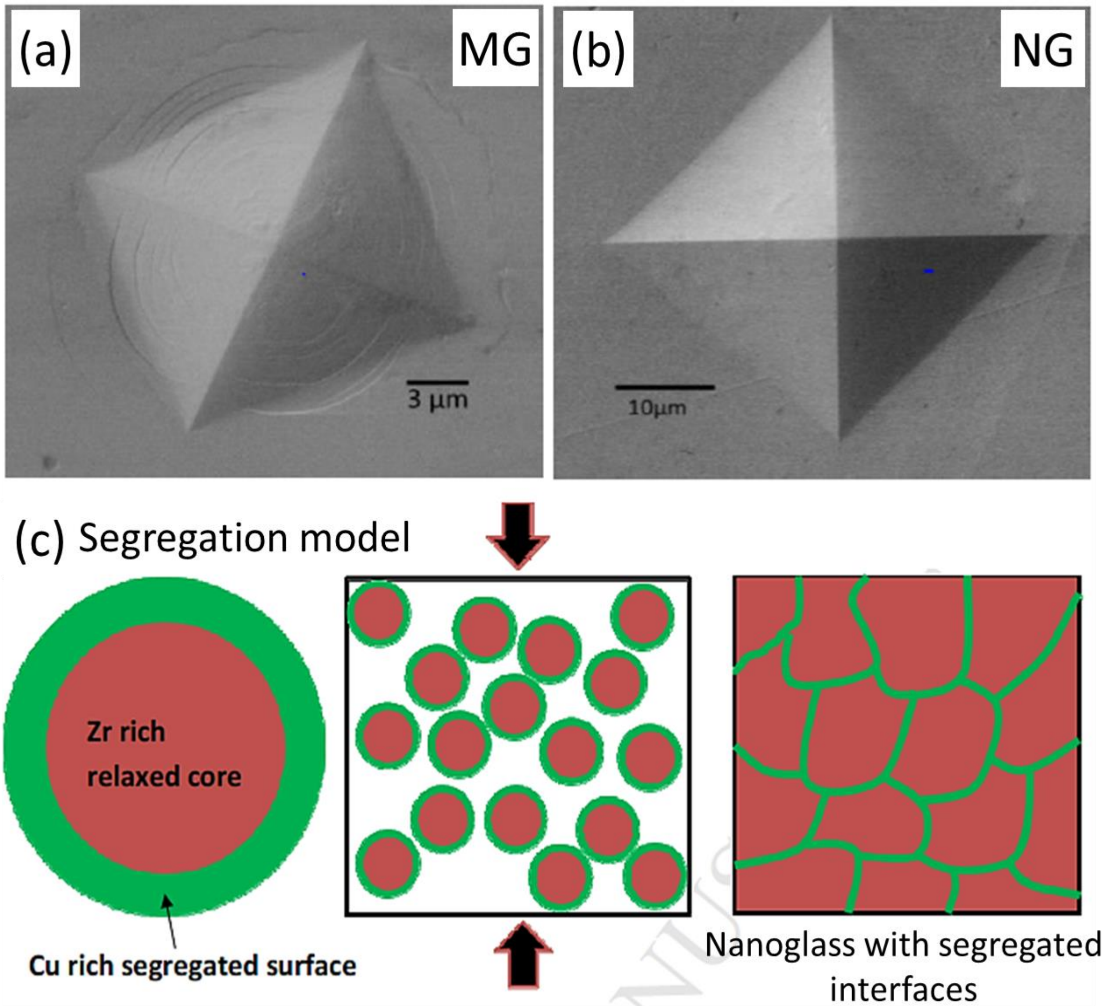

Figure 1.22 SEM images of the micro-indents in (a) NG and (b) MG, along with the proposed segregation model, are displayed in (c). [Adopted from Nandam et al., 2017].

Unlike Cu-Zr glass, a lower hardness is observed for Pd-Si NG, and the possible reason for this is the absence of segregation in Pd-Si NG. The MD simulations suggest the presence of icosahedral clusters in the interfacial regions of Cu-Zr NG causes an increase in hardness.

Often, most experimental studies link the serrated flow in MGs and NGs to the SBs around the indenter impression. But this could not be a good correlation as the number of SBs around the indentation imprint is far less than the number of pop-ins observed on the *P*-*h* curves. Probably, this could be due to the pop-ins recorded in the *P*-*h* curves stemming from the SB nucleation and propagation occurring underneath the indenter, and only a few of these SBs are extended to the indentation surface. Also, the SBs emanating from the sample's surface are flattened by the slanting faces of the indenter during the loading process. Hence, a detailed statistical analysis of the first, second, and subsequent pop-ins in the *P*-*h* curves and related them to the SB kinetics is still an open question and actively pursued research topic to date. Using constrained indentation, it is not directly possible to visualize the SB kinetics underneath the indentation. Therefore, alternate methods of visualizing the SBs underneath the indentation are needed, of which bonded interface indentation (BII) technique was found to be an important method.

1.5.2. Bonded interface indentation

The bonded interface indentation (BII) technique was initially used for investigating the subsurface deformation events (e.g., cracks) and deformation zone of brittle and ductile materials. In this method, two rectangular samples of similar dimensions are bonded together with a strong adhesive. Before bonding the samples, the inner and top surfaces are polished to a 0.25 µm surface finish by utilizing the standard metallographic techniques. The specimens are then cold mounted in such a way that the bonded interface is on the top of the mold, and the top surface is again polished up to a surface finish of 0.25 µm. Following this, the Vickers indentations are performed in such a way that one of the diagonals of the imprint lies along the interface (refer to Fig. 1.23). Subsequently, the bonded interface is opened by keeping the bonded samples in acetone for about 30 min, and the subsurface deformation zones are then further examined using the scanning electron microscope.

Mulhearn and co-workers (1957, 1959) carried out BII experiments (also referred to as the composite block technique) on copper and brass samples and compared the shape and size of a subsurface deformation zone to constrained indentations performed under similar loading conditions. Their studies revealed that the shape of the deformation zone of BII and constrained indentation samples are similar, but the size of the BII samples is shallower due to the relaxation of plastic constraints. Later this technique is successfully employed for BMGs to resolve the subsurface deformation zone and SB characteristics underneath the indenter.

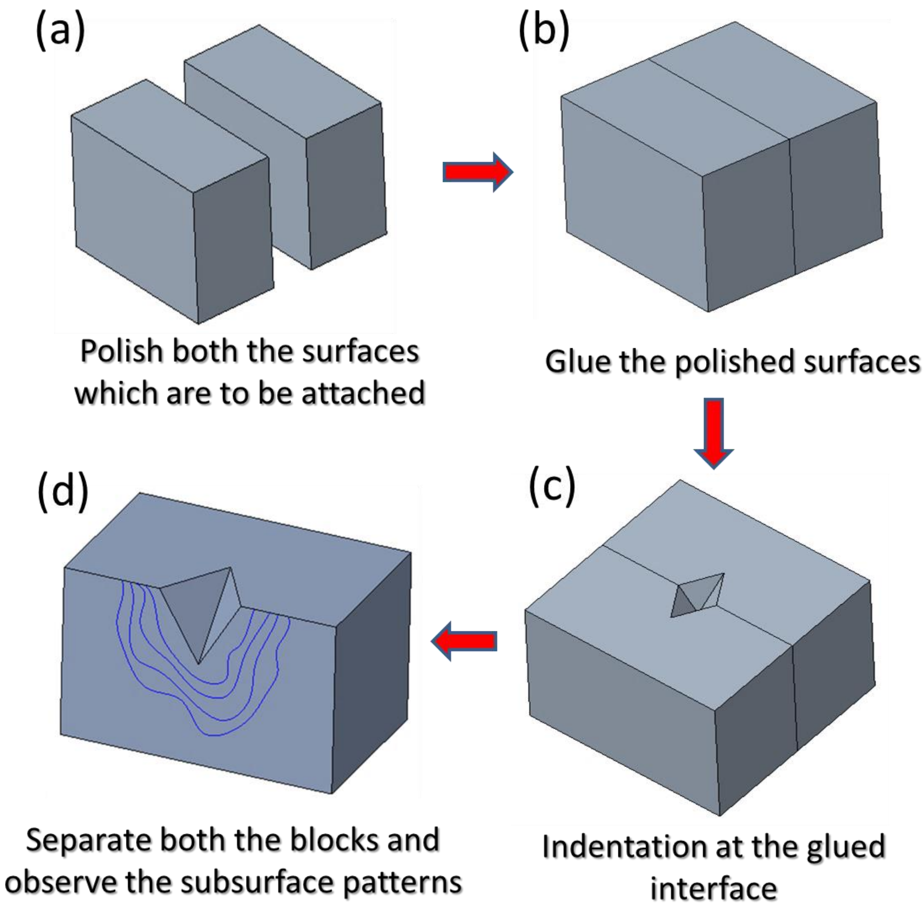

Figure 1.23 Schematic of the various steps involved in a Bonded-interface indentation (BII) technique.

1.5.2.1. Bonded interface indentation studies on MGs

Different researchers have utilized the BII technique to examine the subsurface deformation behavior in several BMGs (Jana et al., 2004; Ramamurty et al., 2005; Zhang et al., 2005; Bhowmick et al., 2006; Subhash and Zhang, 2007; Xie and George, 2008; Yoo et al., 2009). Jana et al., 2004 performed BII on Pd and Zr-based BMGs and observed profuse shear bands in the subsurface deformation zone. Two types of SBs (semi-circular and radial) were reported (refer to Fig.1.24), with semi-circular being more dominant in the Pd-based BMG and radial in Zr-based BMG. They attributed the presence of dendrite-like crystallites in Zr-based BMG is possibly responsible for the observed different morphology. The normalized deformed zone sizes are independent of the applied load for both bulk and interface indentation. The inter-band spacing is independent of the location and increases with applied load.

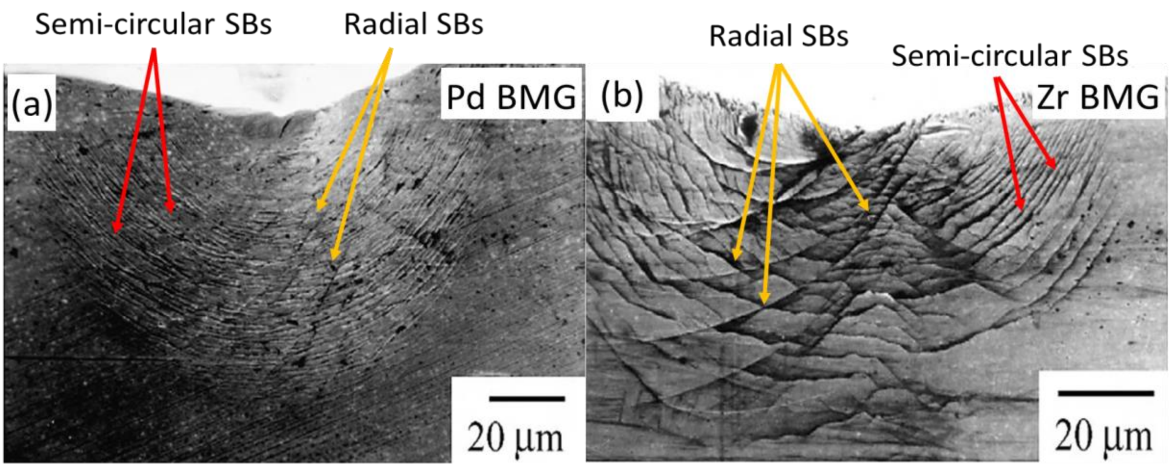

Figure 1.24 Representative images displaying the SEM micrographs of the subsurface deformation zone for Pd and Zr-based BMG. [Adopted and modified from Jana et al., 2004].

To understand the role of excess free volume on the strain softening in MGs, Bhowmick et al., 2006 employed the BII technique and then performed a series of nanoindentations in the subsurface deformation zone. The *P-h* curves of the deformed zone were characterized by several pop-ins as compared to the *P-h* curves of the undeformed zone (refer to Fig1.25). Similarly, the hardness values just beneath the indenter were found to be lower than the region away from the indenter, indicating a gradient in the strain softening behavior.

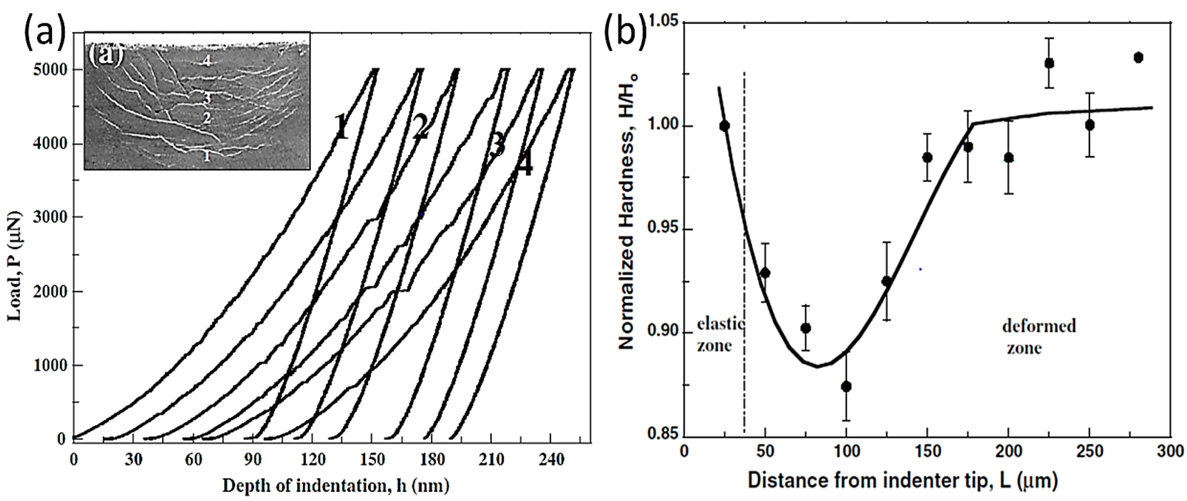

Figure 1.25 Representative *P-h* curves and hardness variation in the subsurface with respect to the distance from the indenter tip [Bhowmick et al., 2006].

Xie and George, 2008 employed the BII on (i) as-cast, (ii) pre-strained, and (iii) pre-strained plus annealed BMG to understand the differences in SB characteristics. The SBs of as-cast and pre-strained plus annealed BMG are similar while they are completely different in pre-strained samples (as displayed in Fig. 1.26). The differences in SB morphology among the samples is attributed to the differences in free volume. Also, the formation of semi-circular and radial SBs is due to the different components of stress acting in the subsurface deformation zone.

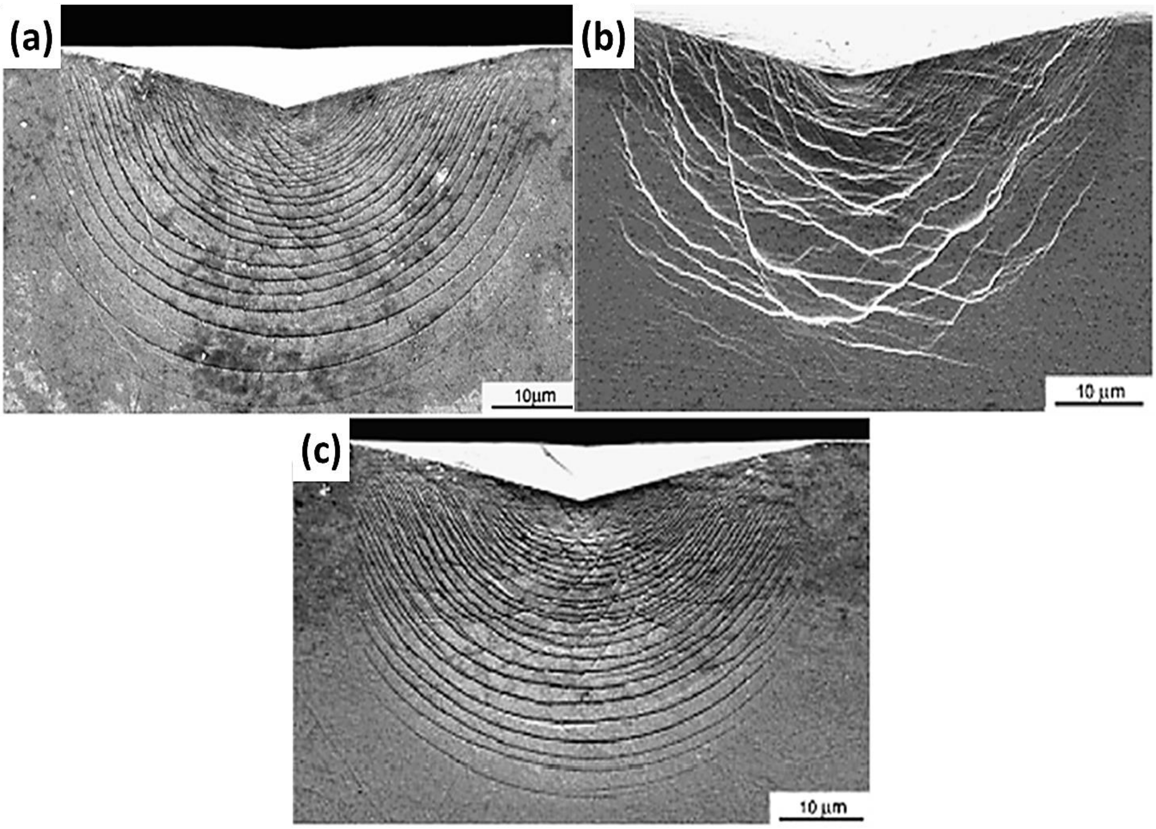

Figure 1.26 Representative subsurface SEM micrographs of (a)as-cast, (b)pre-strained, and (c) pre-strained plus annealed Zr-based BMG [Adopted from Xie and George, 2008].

Later, Yoo et al. 2009 performed a series of nanoindentations (as displayed in Fig. 1.27a and b) on the subsurface deformation zone after gently polishing the interface indented samples. They managed to perform indentations in the deformed regions between the SBs as well as including SBs. The *P-h* curves of these regions are then compared with the undeformed region, as shown in Fig. 1.27c. Their studies reveal that the hardness of the shear banded regions is the lowest, followed by the deformed region (between the bands) and the undeformed region. This is expected as the three regions contain different magnitudes of free volume. Though a good number of studies have been carried out on BMGs, no such studies are available to characterize the SB characteristics in the subsurface deformation zone of NGs. It would be interesting to examine the SB morphology in NGs as there are no direct experimental studies on this front. This will surely provide insights into the nature shear banding in the subsurface deformation zone.

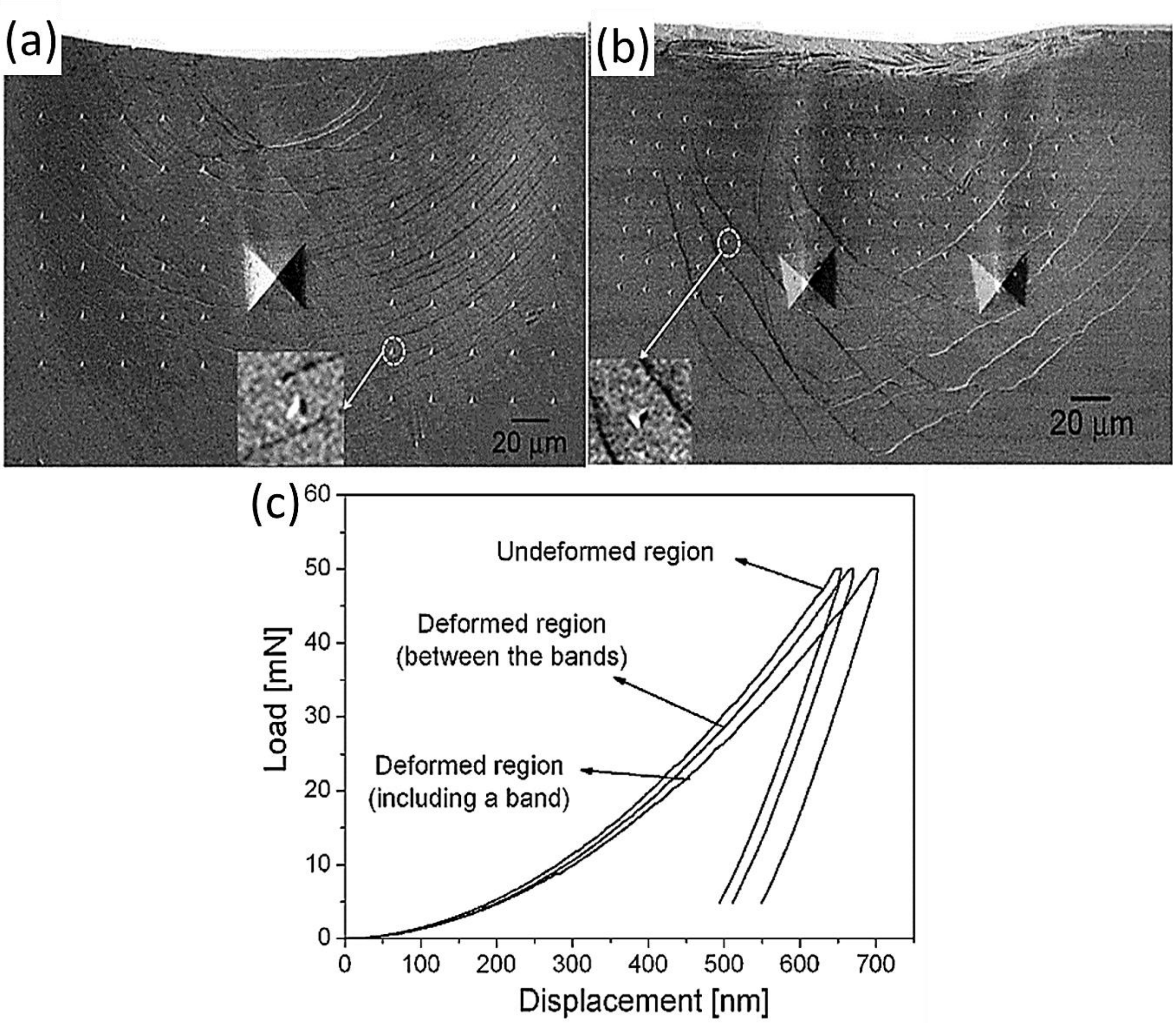

Figure 1.27 Representative subsurface SEM micrographs of (a)as-cast and (b)annealed Zr-based BMG along with (c) P-h curves for different deformed regions [Adopted from Yoo et al., 2009]

1.6. Summary of the literature studies and issues for investigation

In summary, the limited experimental studies conducted on identical NG and MG leads to the following important observations: (i) NGs exhibit considerable tensile ductility as compared to MGs (ii) NGs do not fail catastrophically like MGs although the macroscopic plasticity is mediated by SBs (ii) The *P-h* curves of NGs do not show noticeable pop-ins in the loading curves (iv) the periphery of the indentation imprint of NGs do not show any SBs. Though the absence of serrated flow indicates the near homogeneous deformation of NGs, no direct experimental evidence exists to characterize the SBs underneath the indentation. Therefore, it would be interesting to examine the shear band characteristics in the subsurface deformation zone of NGs and compare them with the MG of identical composition. Similarly, the effect of structural relaxation on the deformation response of NGs is not well investigated. Nandam et al., 2017 conducted the micro- and nanoindentation experiments on as-prepared and structurally relaxed (annealed at 0.9 T_g for 3 h) Cu-Zr NG and observed the absence of pop-ins in the *P*-*h* curves of both the NGs. Commensurate with this, the indentation imprint edges in both the NGs did not show any SBs. Very recently, Yang et al., 2021 have observed that annealing of NGs causes an increase in the size of GGs and a decrease in the characteristic length of GIs to ~ 3 nm. However, no comprehensive experimental studies on the deformation response of structurally relaxed NGs are available in the literature. Similarly, the effects of indentation load on the hardness and plastic flow characteristics are not well investigated. Both glasses are expected to exhibit differences in indentation size effect (ISE) in hardness due to the differences in their microstructure. The ISE in hardness of NGs is also not investigated, and it would be interesting also to investigate the effect of structural relaxation on the ISE of NGs. Another important parameter that influences the plastic deformation of materials is the strain rate sensitivity, *m*. The only study available in the open literature on strain rate sensitivity of NGs is by Nandam et al. 2017 who observed a positive *m* though the mechanistic reasons for this are not well discussed. Since the plastic flow in NGs occurs by SBs, it is expected that *m* should be negative. Another research problem of interest in the NG literature is the strain rate sensitivity of NGs. As discussed in the earlier section, the indenter geometry has a marked influence on the serrated flow in BMGs. It is observed that a much sharper cube-corner indenter leads to an increased heterogeneous deformation as compared to the Berkovich or Vickers indenters. However, few studies on this front are available for BMGs, and no studies in the open literature investigate the effect of indenter geometry on the deformation of NGs. In this context, it would be interesting to examine the effect of indenter geometry on the (*i*) serration flow of NGs, (*ii*) indentation size effect (*iii*) SB evolution around the indentation imprint.

1.7. Scope and Objective of the thesis

Based on the above-identified issues for investigation, the thesis is aimed to accomplish the following objectives.

- To characterize the differences in SB morphology and the nature of plastic flow in the subsurface deformed zone of a binary Pd-Si, Cu-Zr NG, and MG using the BII technique.
- To study the effect of structural relaxation on the deformation behavior and ISE of Cu-Zr NG.

- To determine the strain rate sensitivity of NGs and compare it with the MGs of identical composition using nanoindentation experiments at different indentation loading rates.
- To examine the role of indenter geometry on the deformation behavior and ISE in Pd-Si NG and MG using Berkovich and Cube-corner indenters.

1.8. Organization of the thesis

Following the above objectives, the thesis is organized in the following manner.

Chapter 2 presents the micro-indentation and BII experiments to characterize the differences in SB morphology between the binary $Pd_{80}Si_{20}$ NG and MG and the subsurface deformed zone between the two glasses.

In Chapter 3, the effect of structural relaxation on the ISE and the deformation Behavior of Cu-Zr-Based NG is explored. The NG samples are annealed just below and above the glass transition temperature (i.e., $0.98T_g$ and $1.2T_g$) to obtain samples having different defect structures. Both nano- and micro-indentation experiments are performed on the as-prepared and structurally relaxed NGs to determine the variation in hardness with indentation load. The indentation imprints are characterized using AFM and SEM, and the pile-up corrected hardness is determined. The results are explained by considering the evolution of the deformation zone with indentation load.

In Chapter 4, the strain rate sensitivity, *m*, of a binary $Cu_{60}Zr_{40}$ NG and MG is investigated by performing nanoindentations over 3 decades of indentation strain rates. The differences in *m* between the NG and MG are explained by closely examining the SB characteristics in the subsurface deformation zone.

In Chapter 5, the role of indenter geometry on the deformation behavior in a Pd-Si MG and NG is investigated using Berkovich and cube-corner indenters. The differences in hardness between the two indenters are explained by considering the plastic strain exerted by the indenters in the subsurface deformation zone and the nature of flow (compression vs. cutting) exerted by the indenters. The serrated flow and the influence of pop-ins on the total plastic deformation are characterized by the parameter discrete plasticity ratio, Ψ.

Chapter 6 presents key conclusions from the present thesis work and along with the providing certain directions for future scope.

CHAPTER 2

On the differences in the shear band characteristics between a Pd-Si binary metallic and nanoglass

Abstract: This work investigates the Shear band morphology of a binary $Pd_{80}Si_{20}$ nanoglass (NG) and metallic glass (MG) using bonded interface indentation technique. The results clearly indicate that the plastic strain in the subsurface deformation zone in NG is accommodated by very fine secondary shear bands in addition to fewer primary shear bands, while in MG, it is mainly by primary shear bands. Furthermore, at any given indentation load, the size of the normalized subsurface deformation zone, χ, is found to be higher for NG compared to MG, suggesting that the deformation of $Pd_{80}Si_{20}$ NG is more pressure sensitive and softer than MG. These differences in deformation characteristics between the NG and MG are closely related to the intrinsic differences in the glass structure*.

2.1. Introduction

Nanoglasses (NGs) are a new class of binary amorphous alloys that exhibit high strength and good ductility, unlike their metallic glass (MG) counterparts, i.e., melt spun ribbons [Jing et al., 1989]. The enhanced plasticity of NGs is attributed to their unique microstructural architecture containing few nanometers (nm) thick amorphous interfaces between the amorphous grains [Gleiter, 2013; Wang et al., 2014; Chen et al., 2013]. This peculiar microstructural architecture of NGs is achieved by cold compaction of fine amorphous nanoparticles (with an average size of 10 nm) obtained by inert gas condensation (IGC) followed by high-pressure consolidation [Gleiter, 2008]. In IGC, thermal evaporation [Fang et al., 2012], magnetron sputtering [Hahn and Averback, 1990], and laser ablation [Bag et al., 2019] can be used for the formation of amorphous nanoparticles.

---

*The work presented in this chapter is based on the following publication:

A. Sharma, S. H. Nandam, H. Hahn., K. E. Prasad. On the Differences in Shear Band Characteristics between a Binary Pd-Si Metallic and Nanoglass, *Scripta Materialia*, 191 (2021), 17–22 (doi: 10.1016/j.scriptamat.2020.09.009).

To date, NGs with a variety of binary compositions have been synthesized using IGC (e.g., Pd-Si, Cu-Zr, Fe-Sc, Ni-Ti, Ni- P, Ni-Nb, etc.), and their mechanical properties have been investigated by various means [Kushima et al., 2011; Chen et al., 2011; Wang et al., 2015, 2016; Nandam et al., 2017, 2020; Ivanisenko et al., 2018; Pang et al., 2012; Rauf et al., 2018]. Wang et al., 2015, 2016 have carried out nanoindentation and in-situ micromechanical testing experiments on $Sc_{75}Fe_{25}$ NGs and MGs and observed that NGs exhibit very high tensile elongation (up to a plastic strain ~17%) while MGs failed catastrophically. This improved ductility of NGs has been attributed to the presence of amorphous interfaces leading to homogeneous deformation. Furthermore, nanoindentation studies on various NGs [Nandam et al., 2017; Pang et al., 2012; Rauf et al., 2018; Guo et al., 2019] showed less or no noticeable serrations in the indentation load, P, vs. penetration depth, h, curves, unlike their binary MG counterparts. This atypical behavior of NGs is attributed to the presence of glassy interfaces (GIs), a potential host of STZs and shear band nucleation sites, though the exact reasons are not well understood. Albe and co-workers [Albe et al., 2013; Sopu and Albe 2015; Adjaoud and Albe, 2019], and Adibi et al., 2014 have employed Molecular Dynamics (MD) simulations and showed that the deformation behavior of NGs is sensitive to the volume fraction of interfaces, the topological order of the amorphous clusters present in the interfaces, and free volume content of GIs and glassy grains (GGs). They demonstrated that the presence of GIs promotes the formation of multiple shear bands (SBs) and hence increased plasticity. The limited experimental studies conducted to date did not show any direct evidence of profuse shear bands during the deformation of NGs. However, the only difference observed between MGs and NGs is that the indentation impression of NGs shows few or no SBs at the periphery of the imprint. Few interesting questions to pose at this juncture are: Why does the P vs. h curves of NGs show a limited number of serrations in nanoindentation as compared to MGs? Similarly, why does the periphery of indentation impression in NGs exhibit no or limited number of SBs in contrast to the MGs? As these observations are direct consequences of deformation events taking place underneath the indentation, it is important to investigate the plastic flow behavior beneath the indenter. Consequently, the objectives of this study are to investigate the SB characteristics underneath the indentation and characterize the subsurface deformation zone of a binary NG in comparison with MG of identical composition.

Of the several ways to characterize the subsurface deformation zone, bonded interface indentation (BII) technique in particular, has been very effective in studying the effect of temperature, indentation rate, and structural relaxation on the SB characteristics underneath indentation [Jana et al., 2004a, 2004b; Ramamurty et al., 2005; Bhowmick et al., 2006; Zhang et al., 2005; Xie and George, 2008; Subhash and Zhang, 2007; Chen and Lin, 210; Narasimhan, 2004]. However, to the authors' knowledge, no such studies have been performed on binary MGs and NGs (having identical compositions) to understand the differences in deformation behavior. Therefore, in the current study, BII experiments are performed on $Pd_{80}Si_{20}$ NG and MG, and the SB morphology, their density, spatial distribution, and subsurface de- formation zone are investigated in detail.

2.2. Materials and Experiments

$Pd_{80}Si_{20}$ and $Cu_{60}Zr_{40}$ MGs are produced by melt spinning technique while the NG samples are synthesized using magnetron sputtering in an inert-gas condensation (IGC) system with binary $Pd_{80}Si_{20}$ alloy as the sputtering target and for more details, the reader is referred to the works of Nandam et al. [Nandam et al., 2017, 2020]. As prepared NG and MG samples are characterized using X-ray diffraction (XRD) and differential scanning calorimetry (DSC) clearly shows the amorphous nature of the samples [Nandam et al., 2020]. Then the samples are taken for micro-indentation and BII experiments. To perform BII, two cuboidal specimens were used with one side of the specimens being polished to a 0.25 μm surface finish. The polished surfaces of the specimen are then bonded together with the help of a strong adhesive ("super glue") and allowed to dry for 6 hrs. The specimens are then cold mounted in such a way that the bonded interface is perpendicular to the mold surface and polished upto a surface finish of 0.25 μm. Following this procedure, Vickers indentations are performed on the interfaces in the load range of 25 to 300 gf in such a way that the diagonal of the imprint lies along the interface. The spacing between the successive indents was kept far enough so that their strain fields do not interact. Subsequently, the bonded interface was opened by dissolving the adhesive in acetone for 1 hr and the subsurface deformation zones were examined using scanning electron microscope (SEM) to characterize the shear band morphology underneath indentation.

2.3. Result and Discussion

The Vickers indentation imprints of $Cu_{60}Zr_{40}$ and $Pd_{80}Si_{20}$ glasses presented in Fig. 2.1(a)-(d) along with a representative image of the imprint obtained from interface indentation shown in Fig. 2.1e. It is evident from Fig. 2.1a and c that both the MGs shows SBs at the imprint edges and no SBs are observed in $Cu_{60}Zr_{40}$ NG (Fig. 2.1 b) while fewer of SBs are noticed in $Pd_{80}Si_{20}$ NG (Fig. 2.1d). The differences SB densities between the two NGs may arise due to the differences in their topological order [Nandam et al., 2020; Ivanisenko et al., 2018]. However, in both the cases, a higher density of SBs is observed around the imprint of MGs (Fig. 2.1 a and c) as compared to NGs (Fig. 2.1 b and d). Representative top view SEM image of an interface indentation imprint of a MG at P of 200 gf is shown in Fig. 2.1e do not show SBs at the edges unlike Fig. 2.1c. This is expected as the soft adhesive relaxes the indentation strain and does not offer any constraint to the P which is also consistent with the BII experiments on BMGs [Zhang et al., 2005; Xie and George, 2008; Subhash and Zhang, 2007]. Moreover, the presence of a soft adhesive layer causes plastic displacement of material normal to the P, thereby leading to a protrusion in the

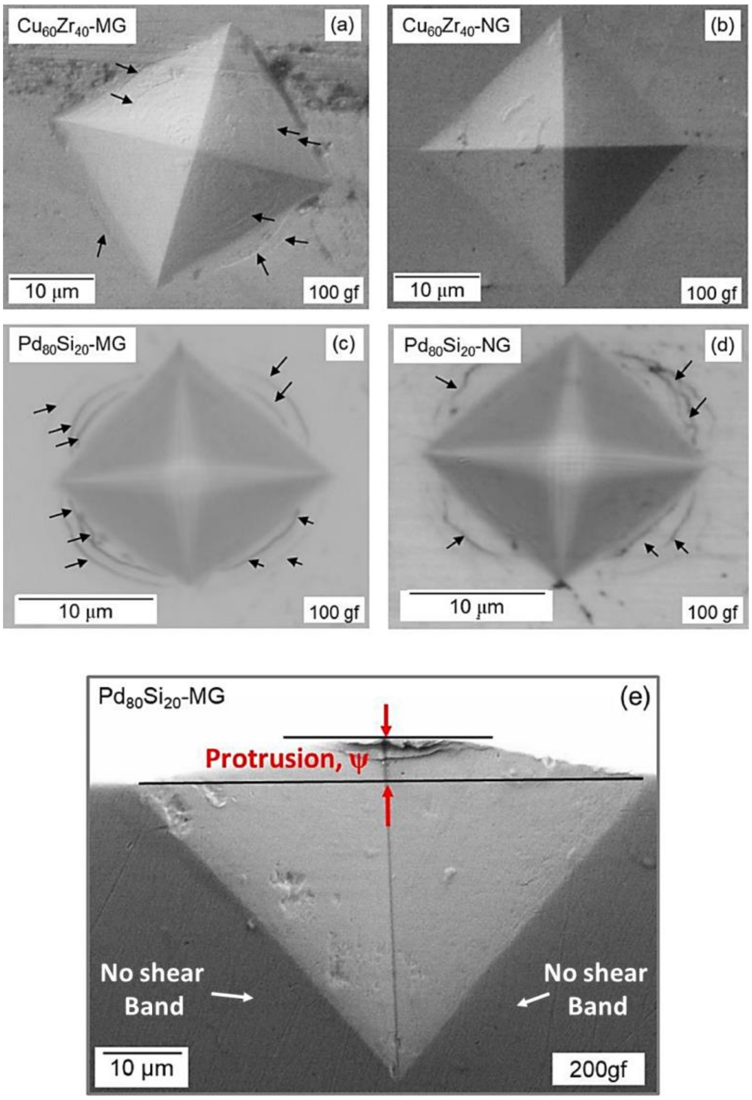

Figure 2.1 Representative SEM (a, b) and Optical (c, d) images of Vickers indentation imprints: (a) $Cu_{60}Zr_{40}$ MG (b) $Cu_{60}Zr_{40}$NG (c) $Pd_{80}Si_{20}$ MG (d) $Pd_{80}Si_{20}$ NG, and (e) the interface indentation imprint of a $Pd_{80}Si_{20}$ MG. The arrows indicate the shear band fronts around the imprint.

impression. For a given indenter geometry, the thickness of the protrusion, ψ, depends on P, nature of the material, interface width, thickness and properties of adhesive layer. It is observed that the value ψ is found to in-crease with increasing, P. The value ψ for MG and NG is measured to be ~7.0 ±0.3 and 6.5±0.3 μm, respectively at P of 200 gf and such small differences in ψ values between the two is due to the differences in interface width. In case of Zr- based BMG (Vitreloy 106), Zhang et al., 2005 have observed ψ to be 3 μm for a P of 200 gf and interface width of 6 μm. A slightly higher ψ is due to the increased interface width present in the current experiment.

Figs. 2.2 and 2.3 illustrate the subsurface deformation zones of interface indentation regions of MG and NG, respectively. It is evident from Fig. 2.2 that the plastic strain in the subsurface deformation region of MG is mainly accommodated by large shear bands (hereafter referred to as primary shear bands (PSBs)), which appear to be semi-circular in shape with no waviness at SB front. At the termination points of the impression in MGs, a negligible number of fine SBs different from PSBs are noticed. While in the case of NGs (Fig. 2.3), a large number of fine SBs (also referred to as secondary shear bands (SSBs)) are embedded between the PSBs, suggesting that the plastic strain underneath the indentation in NGs is accommodated by both PSBs and SSBs. The PSB front in NGs, unlike MGs, is wavy, which may be due to the multiple SB interaction. Chen and Lin, 2010 performed a rigorous analysis of the SBs underneath indentation in a BMG and observed that both the PSBs and SSBs are semi-circular in shape and expand as concentric circles with increasing P. Further, the SSBs in BMGs are formed orthogonal to the PSBs and the radius of which is found to be √2 times the PSBs. Zhang et al., 2005 have argued that normal radial stresses are responsible for the formation of PSBs while SSBs are formed due to the maximum shear stresses. However, in the current study, we define the fine shear bands located between the PSBs as SSBs, which also appear to be the precursors to the fully grown PSBs. So, the mechanistic arguments proposed for the formation of SSBs in BMGs are not valid to explain the origin and nature of SSBs in NGs, which must be associated with the unique microstructural architecture of NGs comprising of GGs and GIs. The spectroscopic measurements [Jing et al., 1989; Gleiter, 2008] indicate that GIs contain higher free volume (about 1–2%) and different topological order compared to the GGs. This promotes easy nucleation of SBs, and with increasing P, both nucleation and propagation events happen simultaneously, leading to the formation of SSBs and PSBs, as noticed in Fig. 2.3. Another interesting observation is that the number density of PSBs in MG is near twice the PSBs in NG while the deformation volume (computed assuming the elliptical shape of the deformation

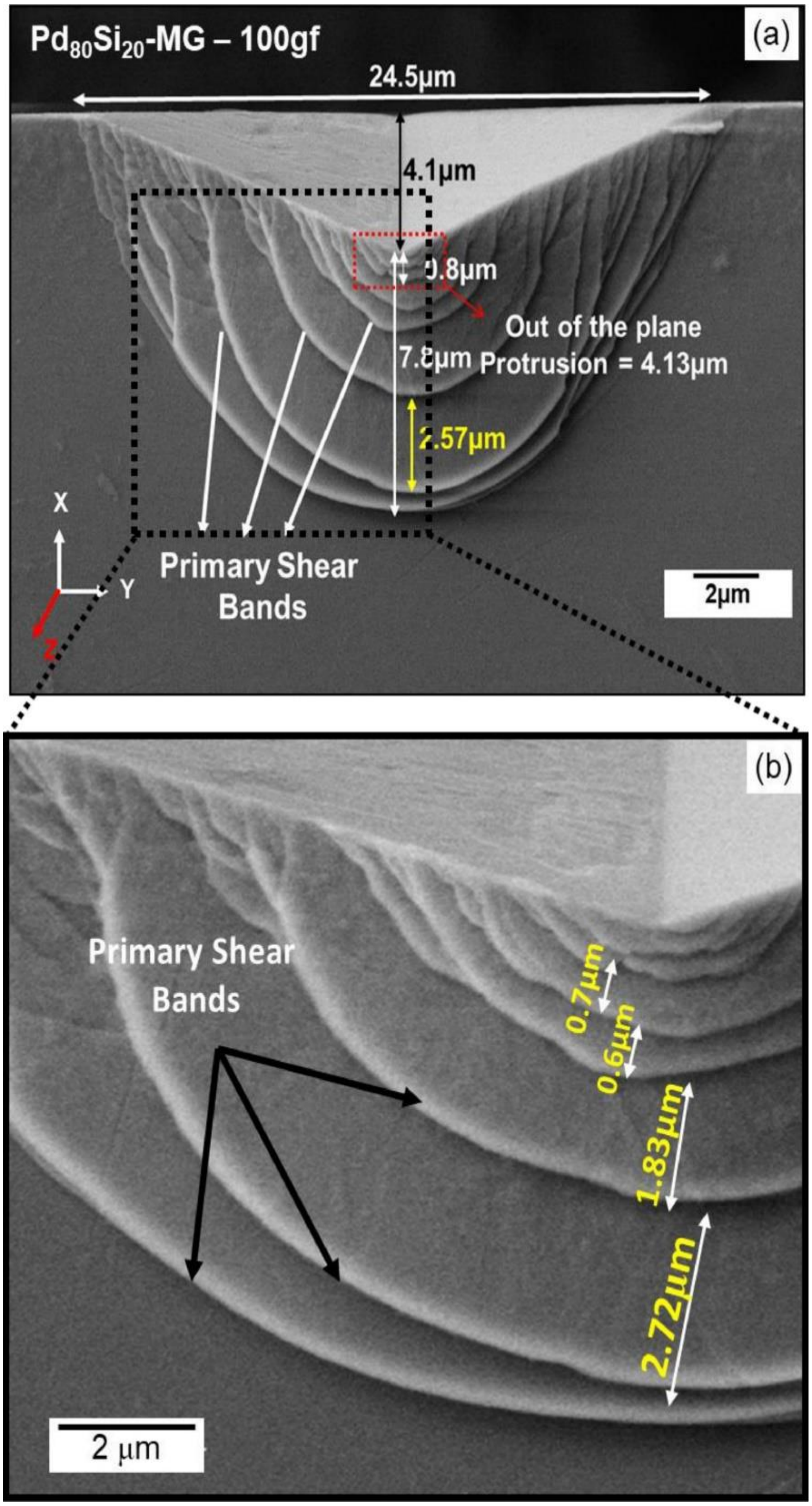

Figure 2.2 Subsurface deformation zone of a $Pd_{80}Si_{20}$ MG at indentation load of 100 gf indicating (a) complete deformation zone and (b) a high magnification image of the highlighted region clearly describing that the deformation is accommodated mainly by primary shear bands.

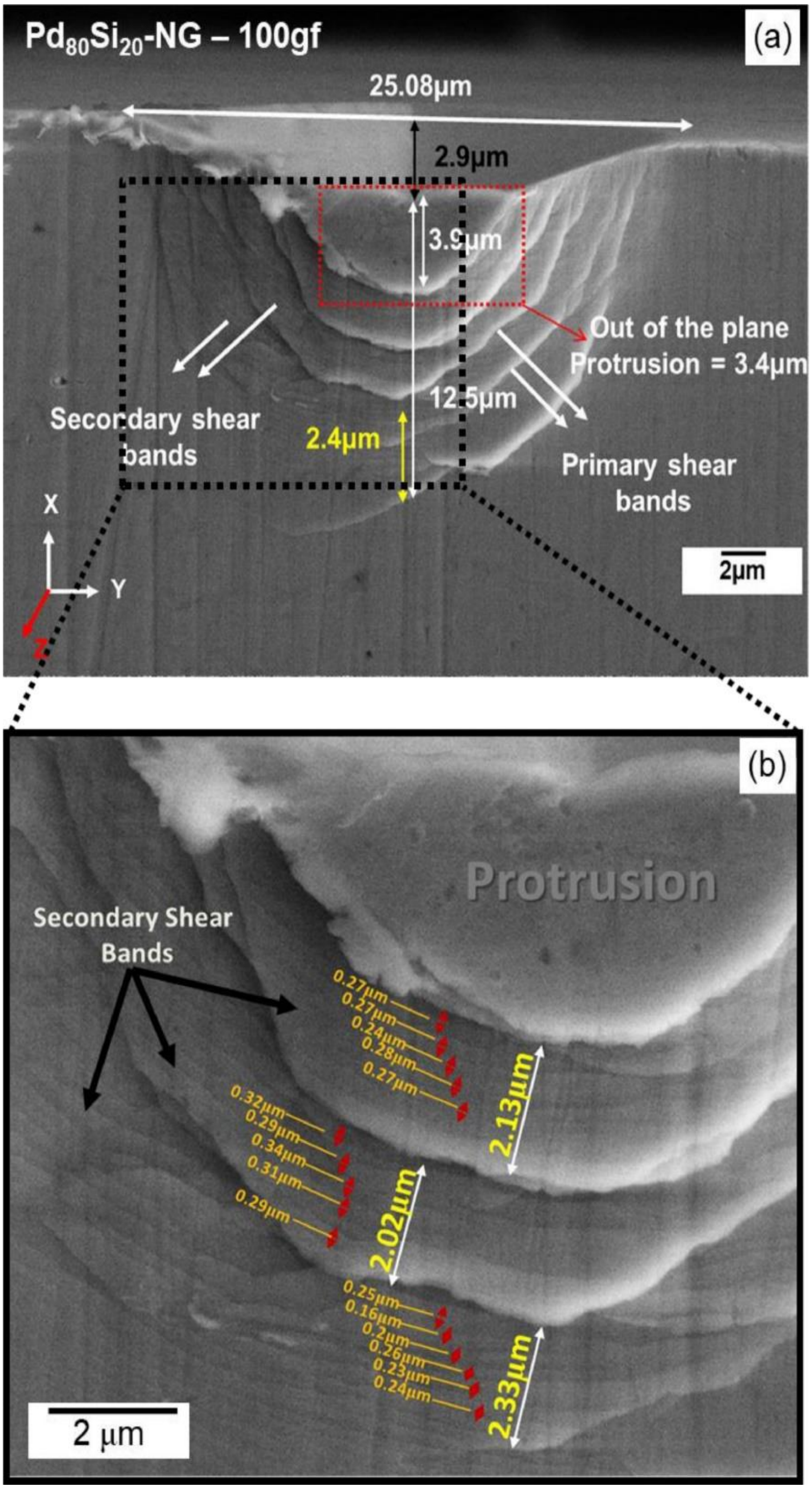

Figure 2.3 Subsurface deformation zone of a $Pd_{80}Si_{20}$ NG at an indentation load of 100 gf indicating (a) the full view of subsurface deformation zone and (b) a high magnification image of the highlighted region of (a) describing a profuse density of fine shear bands besides the primary shear bands.

zone) of MG is ~nearly 10 to 12% lower than the NG at P of 100 gf. This clearly shows that the net plastic strain carried by the PSBs of NG is much smaller than the PSB of MGs and hence SSBs can accommodate significant amount of plastic flow leading to plastic strain delocalization. By simultaneous measurement of penetration depth, h, and electrical current, I, during the nanoindentation of a BMG, Singh et al., 2016 have shown that the pop-ins in the loading curve and surges in I are directly correlated to the shear offsets (due to the nucleation and propagation of SBs) taking place underneath the indentation. Schuh and co-workers [Schuh et al., 2002, 2003, 2004] have also observed that the occurrence of profuse shear banding (due to high indentation rates) underneath indentation leads to the absence of serrations in the loading curves. Therefore, high density of SSBs (vis-à-vis small inter-band spacing) observed in NGs demonstrate the reasons for less noticeable pop-ins in NGs. The topological order present in the interfaces [Nandam et al., 2017, 2020; Ivanisenko et al., 2018], size of the GGs, thickness of the GIs, and free volume distribution may have a marked influence on the nucleation kinetics of SBs and their propagation dynamics which warrant a detailed experimental study. A close examination of high magnification images (Fig. 2.3b) of subsurface deformation zone shows that the SSBs are less wavy than the PSBs indicating easy percolation of SBs across the GGs and GIs.

To further understand the SB morphology in subsurface deformation zone, we have computed the inter SB spacing, δ, the distance between the two adjacent SBs in the plane view of SEM images and plotted it as a function of distance from the tip of indentation impression, r_d, in Fig. 2.4a. It is evident from Fig. 2.4a that inter PSB spacing, δ_{PSB} in MG increases with r_d consistent with the literature observations reported for BMGs. Unlike MG, δ_{PSB} and inter SSB spacing, δ_{SSB} in NG remain invariant with r_d and δ_{SSB} is found to be 0.26±0.04 μm, which is an order of magnitude lower than δ_{PSB} ~1.95±0.19 μm. In case of BMGs, Ramamurty et al., 2005 have observed that the variation of δ with r_d depends on the amount of free volume and its distribution in the starting material: δ is unchanged with r_d for as-cast BMGs containing higher free volume while it increases with r_d for annealed BMGs containing lower free volume (indicating plastic strain localization into few dominating SBs). The differences observed in δ_{PSB} between the NG and MG can be attributed to the differences in free volume content, which is generally higher for NG than the MG [Wang et al., 2015, 2016; Nandam et al., 2017, 2020]. The subsurface deformation zone, λ, is measured as the distance from the tip of the indentation impression to the farthest SB and normalized with the total distance from the specimen surface, D (which is also referred to as normalized deformation zone, χ). The χ is plotted against the indentation load, P in Fig. 2.4b leads to the following important observations: (i) χ is nearly independent of P in MG (ii) at any given P, NG shows a higher χ than MG (iii) χ increases with increase in P for NG. Ramamurty and co-workers [Jana et al., 2004a, 2004b; Ramamurty et al., 2005; Bhowmick et al., 2006; Prasad and Ramamurty, 2012] have shown that χ increases with an increase in pressure-sensitive plastic flow which is indirectly measured by the pressure sensitive index, α. Narasimhan, 2004 modified the spherical expanding cavity model to suit

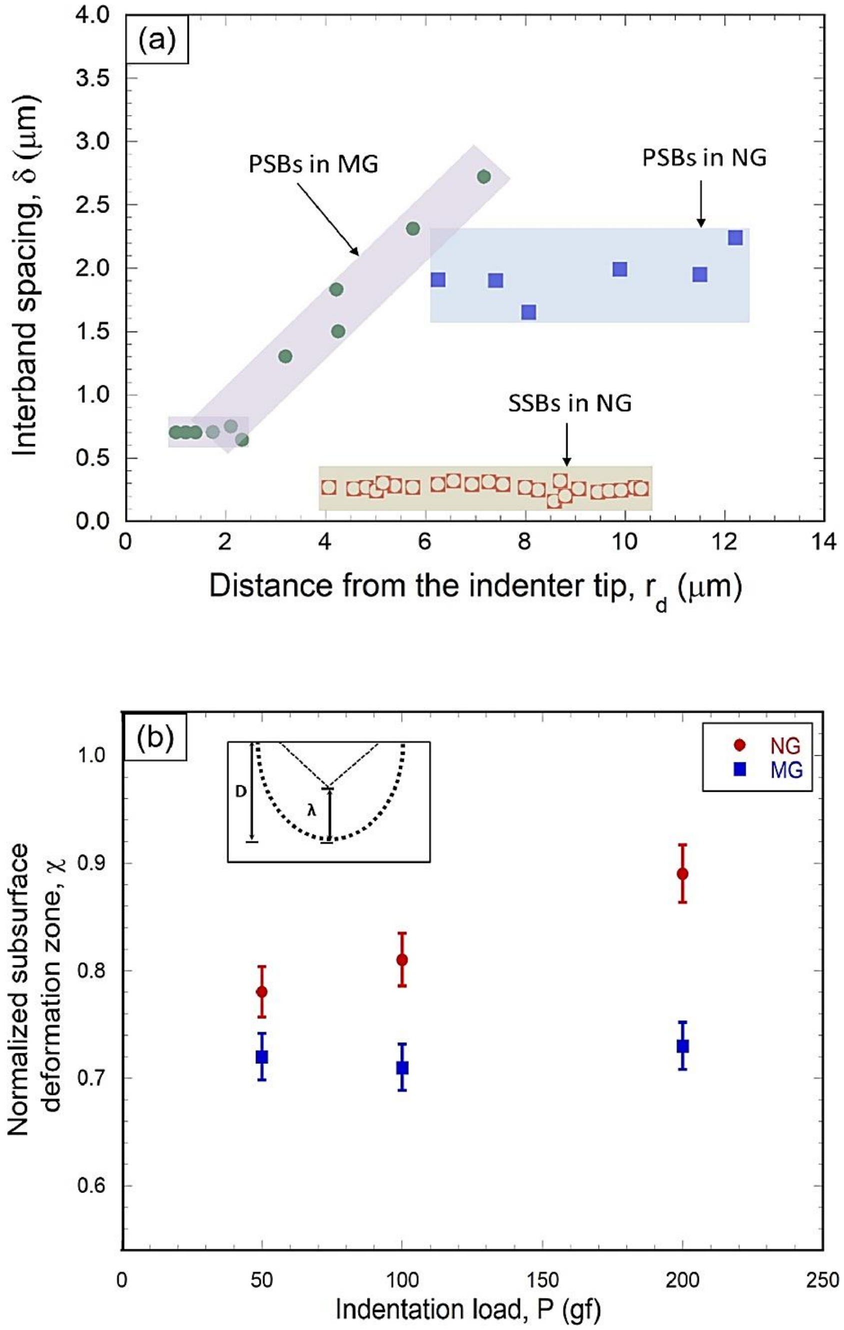

Figure 2.4 Plots showing the variation of (a) inter-shear band spacing, δ, with the distance from the tip of the indentation impression, r_d and, (b) normalized subsurface deformation zone size, χ with indentation load, P for MG and NG.

for pressure dependent solids and shown that χ increases with increasing pressure sensitivity index, α, which is attributed to the increased magnitude of axial stresses underneath indentation. Prasad and Ramamurty, 2012 have proposed that χ comprises of both SB mediated (heterogeneous) and STZ mediated (homogeneous) deformation regions between which the latter one is sensitive to hydrostatic pressure. Recent finite element simulation studies of Cu-Zr based NG and MG show that NG exhibit a higher χ compared to MG [Hirmukhe et al., 2020].

The individual α values of GGs and GIs obtained from fitting the P vs. h curve shows a higher α for GIs compared to GGs which was attributed to higher free volume of GIs. The variation of χ with P is governed by the relative increase in λ and D with increase in P. In case of NG, a small increase in penetration depth leads to a rapid increase in λ as compared to D suggests easy nucleation and propagation of SBs. One of the possible reasons for this is attributed to more uniform distribution of free volume and increased propensity for SB formation even for a small increase in P leading to homogeneous plastic flow. However, understanding free volume evolution and plastic strain distribution using subsurface indentation experiments provide more insights about subsurface deformation zone and the contribution of GIs (and SSBs) to the total deformation.

2.4. Summary

In summary, the present chapter demonstrates the differences in shear band characteristics between the MG and NG in the subsurface deformation zone. The plastic strain in a NG is accommodated by finer multiple secondary shear bands besides coarser fewer primary shear bands unlike a MG where the strain accommodation completely occurs by primary shear bands. These fine secondary shear bands observed in the NG is due to the presence of glassy interfaces which leads to nearly homogeneous deformation as compared to the MG counterparts. NG also exhibit a higher subsurface deformation zone compared to MG, which is associated with the uniform distribution of free volume leading to easy SB nucleation and propagation.

CHAPTER 3

Effect of Structural relaxation on the Indentation Size effect and Deformation Behavior of Cu-Zr-Based Nanoglasses

Abstract: In this work, the deformation behavior of as-prepared (AP) and structurally relaxed (SR) Cu–Zr–based nanoglasses (NGs) are investigated using nano- and micro-indentation. The NGs are subjected to structural relaxation by annealing them close to the glass transition temperature without altering their amorphous nature. The indentation load, P vs. displacement, h, curves of SR samples are characterized by discrete displacement bursts, while the AP samples do not show any of them, suggesting that annealing has caused a local change in the amorphous structure. In both the samples, hardness (at nano- and micro-indentation) decreases with increasing P, demonstrating the indentation size effect. The micro-indentation imprints of SR NGs show evidence of shear bands at the periphery, indicating a heterogeneous plastic flow, while AP NG does not display any shear bands. Interestingly, the shear band density decreases with p, highlighting the fact that plastic strain is accommodated entirely by the shear bands in the subsurface deformation zone. The results are explained by the differences in the amorphous structure of the two NGs[*].

3.1. Introduction

At room temperature, conventional amorphous alloys such as bulk metallic glasses and melt-spun ribbons (MSR) exhibit limited plasticity as deformation gets localized into one dominant shear band, leading to catastrophic failure [Schuh et al., 2007]. While the same materials can show extensive plasticity at elevated temperatures (near and above the glass transition temperature) due to change in the plastic deformation mechanism from the shear band (SB) mediated to STZ-mediated flow [Prasad and Ramamurty, 2012].

---

[*]The work presented in this chapter is based on the following publication:

A. Sharma, S. H. Nandam, H. Hahn., K. E. Prasad. Effect of structural relaxation on the indentation size effect and deformation behavior of Cu-Zr-based nanoglasses, *Frontiers in Materials*, 8 (2021), 676764 (doi.org/10.3389/fmats.2021.676764).

STZs are the fundamental carriers of plasticity (akin to dislocations in crystalline materials) in amorphous materials, comprising a cluster of atoms undergoing inelastic deformation beyond critical applied stress. STZs, unlike dislocations, are nearly impossible to observe directly using experiments, but the molecular dynamic studies show that they occur in the vicinity of regions containing high free volume. Consequently, it seems that one of the ways to increase the plasticity of amorphous alloys is to produce a structure containing areas of high free volume. With this motivation, Gleiter and co-workers [Jing et al., 1989; Gleiter, 2008; Gleiter, 2009; Gleiter, 2013; Gleiter, 2016] proposed the concept of nanoglasses (NGs) consisting of glassy grains (GGs) separated by glassy interfaces (GIs) of higher free volume, and later, several researchers have successfully fabricated NGs using different manufacturing routes [Gleiter et al., 2014; Nandam et al., 2017; Ivanisenko et al., 2018; Nandam et al., 2020]. Extensive studies have been conducted on NGs to investigate their mechanical and functional properties using both experiments and simulations [Chen et al., 2011; Ritter et al., 2011; Sopu et al., 2011; Wang et al., 2011; Ritter and Albe, 2012; Adibi et al., 2013; Albe et al., 2013; Witte et al., 2013; Wang et al., 2014; Adjoud and Albe, 2016; Sniadecki et al., 2016; Nandam et al., 2017; Hirmukhe et al., 2019; Arnold et al., 2020; Singh et al., 2020a; Singh et al., 2020b; Hirmukhe et al., 2020; Katnagallu et al., 2020; Nandam et al., 2020]. A series of MD simulation studies have been performed on NGs with different GG sizes and observed that the plasticity increases with the decreasing size of the GGs. The increase in plasticity is attributed to the increased number of GIs, which are the potential sites of STZs due to high free volume. Sopu et al.,2011 and Sopu and Albe, 2015 have shown that annealing of NGs causes a change in the deformation mechanism from STZ to shear band dominated due to the annihilation of free volume and increase in GG size. The simulations are complemented by the limited number of experimental studies (primarily using micro-compression or nano-indentation) using a small volume of materials [Fang et al., 2012; Wang et al., 2015; Wang et al., 2016]. Wang et al. (2015), Wang et al. (2016) carried out in situ micro-compression of NGs and MSR and observed extensive plasticity in a binary Fe–Sc NG compared to MSR of identical composition.

The indentation (both micro- and nano-indentation) method is a viable technique to understand the deformation behavior of glasses as the deformation mechanisms taking place underneath the indenter gets reflected in the indentation load, P, vs. displacement, h, curves as well as the residual impression of the indentation imprint. Unlike MSR and BMGs, Cu–Zr-based NGs do not exhibit any noticeable displacement bursts (also known as pop-ins) in the loading portion of P vs. h curves, indicating that the flow is homogeneous [Pang et al., 2012; Nandam et al., 2017; Rauf et al., 2018] which is also supported by the absence of shear bands at the imprint edges of a micro-indent. The pop-ins in the loading curves correspond to nucleation and propagation of shear bands beneath the indentation [Singh et al., 2012; Singh et al., 2016]. Recently, Sharma et al., 2021 have carried out bonded interface indentation experiments and observed that the subsurface deformation in a Pd–Si NG is accommodated by a large number of very fine secondary shear bands (SSBs) contrary to the few numbers of large primary shear bands (PSBs) in MSR of identical composition, suggesting that the absence of noticeable pop-ins in NGs could be due to the near homogeneous flow underneath the indentation. A good agreement is found between the experiments and simulations regarding the deformation mechanisms of the as processed (AP) NGs. However, limited experimental studies are available in understanding the deformation of structurally relaxed (SR) NGs, despite several simulation studies, and there appears to be some discrepancy between the two. For example, Nandam et al., 2017 have reported the absence of pop-ins in the loading curves and SBs at the imprint edges of an annealed (at 0.9 T_g for 3 h) Cu–Zr NG, contrary to the MD results (though the exact annealing temperature is not well-described in the literature), which predicts SB-mediated plastic flow. So, it would be interesting to see if relaxing the NG at high temperatures (nearly at the T_g) has any effect on the nature of plastic flow. Apart from this, the role of P on the hardness, H; elastic modulus, E; and deformation mechanisms of AP and SR NGs is not studied in detail, at least experimentally. In the case of BMGs, it is observed that H decreases with increasing P, showing an indentation size effect (ISE). It would be interesting to examine the ISE on H and E in AP and SR NGs. Following this, the present work aims at 1) understanding the role of annealing (or structural relaxation) on the deformation behavior of NGs, 2) investigating the effect of indentation load/or size on H and E of AP and SR NGs, and 3) examining the evolution of shear bands with p around the indentation imprint.

3.2. Material and Experiments

$Cu_{50}Zr_{50}$ and $Cu_{60}Zr_{40}$ NGs are synthesized using magnetron sputtering in an inert gas condensation (IGC) system, and the processing details have been reported in detail by Nandam et al.,2017. Since the deformation behavior of both $Cu_{50}Zr_{50}$ and $Cu_{60}Zr_{40}$ NG is very similar in terms of plasticity, we have used AP $Cu_{60}Zr_{40}$ NG and SR $Cu_{50}Zr_{50}$ NG for our present evaluation. We will also make a comparison with the previously published results of $Cu_{50}Zr_{50}$ NG to give a more detailed analysis. Since the glass transition temperature, T_g, of the $Cu_{50}Zr_{50}$ NG is not clearly visible, we will consider the T_g of the MSR as the reference, that is, 410 °C [Nandam et al., 2017]. The AP NG was annealed at 400 °C (about 0.98 T_g) for 90 min as the sub-T_g annealing promotes structural relaxation. Both the AP and SR NGs are characterized using Mo Kα X-ray diffraction (XRD), as shown in Figure 3.1, which does not display any crystallization peaks in the diffraction spectrum of both the samples, confirming the amorphous nature of samples. In order to check the thermal stability, the NG samples are annealed slightly above the T_g (1.2 T_g) for 2 h and the XRD spectrum of which presented in Appendix A1 Figure A1. Appendix A1 Figure A1 shows small additional peaks in addition to the amorphous hump, suggesting that NGs are no longer fully amorphous, and the structural relaxation at this temperature leads to the formation of small crystallites. The sample surfaces for micro- and nanoindentation experiments are then polished to 0.25 μm surface finish using standard metallographic sample preparation. Nanoindentation was carried out at room temperature in a load-controlled mode using a Berkovich three-sided pyramidal shaped indenter tip. Before the experiment, the tip area function is calibrated using a standard quartz sample by making a series of indentations in the depth range of 80–200 nm. Nano-indentation experiments are conducted in the load range of 2-8 mN at a constant loading rate of 1 mN/ s. For all the indentations, the thermal drift was kept under ±0.05 nm/s. Micro-indentation experiments are carried out using a Vickers (four-sided) diamond indenter in the load range of 0.25–10 N with a loading and unloading segment of 10 s and a holding segment of 15 s at peak load. A minimum of ten indentations are performed at P to obtain statistically significant data. The indentation imprints and deformation morphology around the imprints are analyzed using scanning electron microscopy (SEM) and atomic force microscopy (AFM).

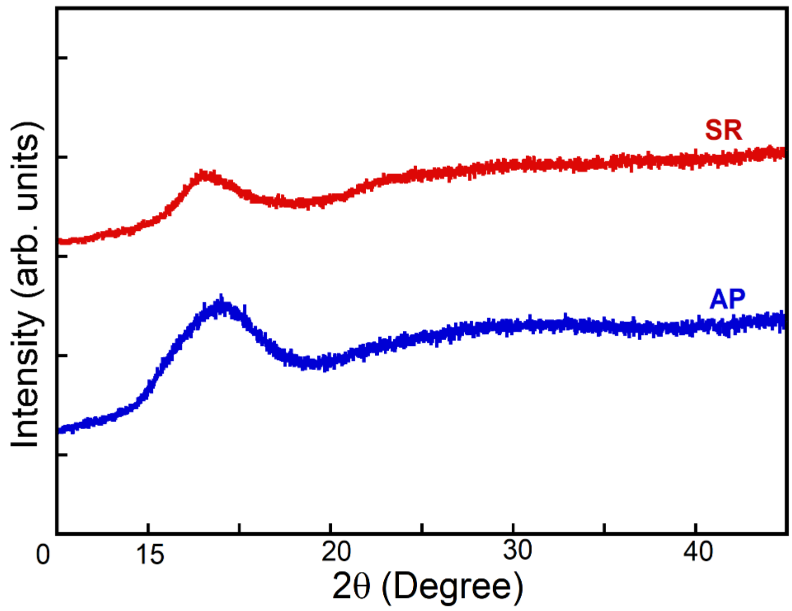

Figure 3.1 X-ray diffraction patterns of the SR and AP NGs displaying the amorphous nature of the samples.

3.3. Results

3.3.1. Indentation Load, *P*, vs. Penetration Depth, h, Curves

Representative P vs. h curves of AP and SR NGs are shown in Figure 3.2. The loading curves of AP samples do not show any noticeable pop-ins, suggesting the homogeneous nature of plastic flow during the indentation, consistent with the literature [Pang et al., 2012; Nandam et al., 2017; Rauf et al., 2018]. Unlike AP samples, the loading curves for the SR samples are characterized by a serrated flow, manifested by noticeable pop-ins (as indicated by the arrows). The serrations in the loading curves are attributed to nucleation and propagation of shear bands underneath the indentation, indicating that the plastic deformation is heterogeneous [Schuh and Nieh, 2003; Schuh et al., 2004; Greer et al., 2004; Yang et al., 2007a].

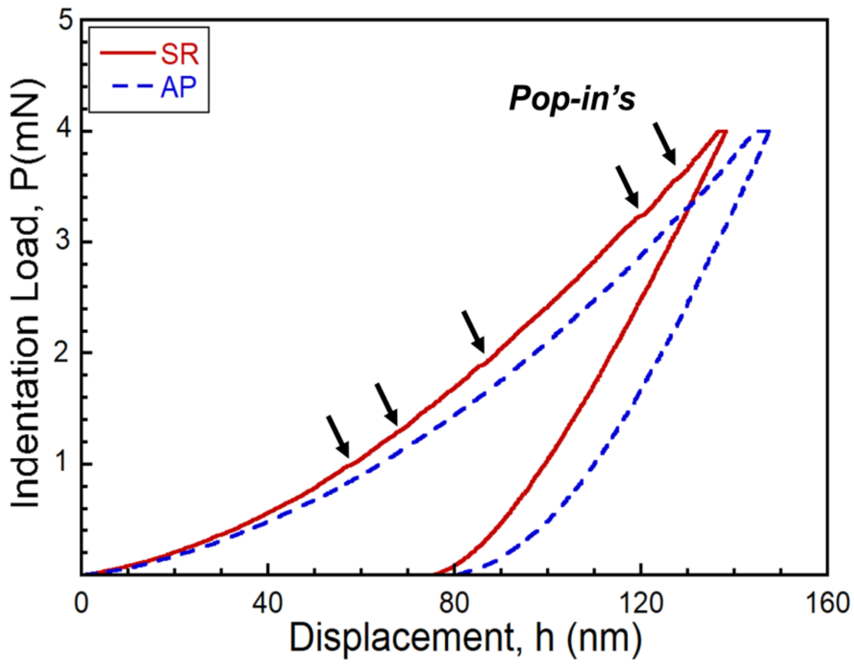

Figure 3.2 Representative indentation load, P, vs. penetration depth, h, curves of the SR and AP NGs obtained at a Pmax of 4 mN.

Interestingly, Nandam and co-workers did not observe any pop-ins in SR NGs, annealed at 350 °C (0.9 Tg) for 2 h, indicating that the deformation is still homogeneous. The indentation data were then analyzed using the Oliver and Pharr (O&P) method [Oliver and Pharr, 1992], according to which P and h are related for loading and unloading curves by Eq. 1 and Eq. 2, respectively:

$$\boldsymbol{P = \alpha h^n} \tag{1}$$

$$\boldsymbol{P = \beta(h - h_f)^m} \tag{2}$$

where α, β, n and m are fitting constants, which depend on the material under indentation; and h and h_f are the instantaneous and final penetration depth of the indenter, respectively. Higher values of α for SR samples indicate increased resistance to plastic flow as compared to AP NGs. The reasons for the increased H in SR samples will be discussed in the subsequent sections.

3.3.2. Variation of Nanohardness with the Indentation Load

The variation in nanohardness, H_n, and elastic modulus, E, with the P_{max}, plotted in Figure 3.3, clearly shows that both H_n and E decrease with increasing P_{max}. The decrease in H_n with P_{max} is referred to as the indentation size effect (ISE) and has been observed even in other metallic glasses, such as MSR and BMGs [Steenberge et al., 2007; Li et al., 2008; Li et al., 2009a; Huang et al., 2010; Jang et al., 2011; Xu et al., 2014; Xue et al., 2016]. In the case of crystalline materials, the ISE is attributed to the presence of geometrically necessary dislocations (due to high plastic strain gradients) at low P [Nix and Gao, 1998; Pharr et al., 2010; Prasad and Ramesh., 2019; Kathavate et al., 2021]. However, owing to the amorphous nature, the ISE in metallic glasses cannot be explained by the dislocation theory and is often attributed to the shear band nucleation and propagation characteristics underneath the indentation [Li et al., 2009b] and evolution of free volume during indentation [Yang and Nieh, 2007b].

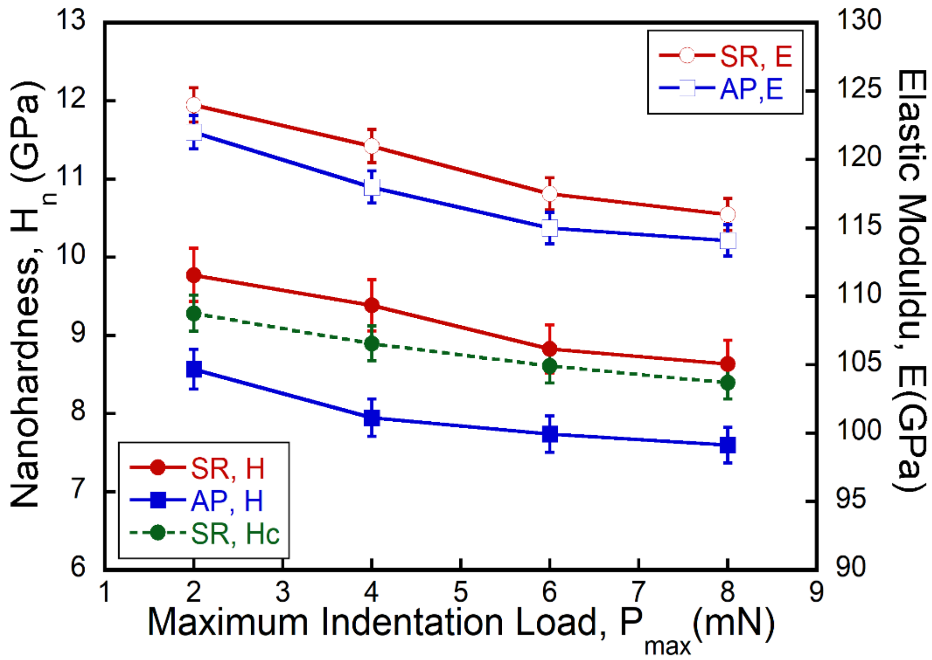

Figure 3.3 Variation of nanohardness, H_n, and elastic modulus, E, with maximum indentation load, P_{max}, of both SR and AP NGs indicating the ISE.

Huang et al., 2010 attributed the ISE in BMGs to the pileup of shear bands at the periphery of the imprint, which appears to be more pronounced at low indentation loads (due to the tip bluntness), thereby overestimation of hardness using the O&P method. However, the blunt tip theory cannot satisfactorily describe the ISE in NGs as the plastic flow under a blunt indenter is compressive in nature and transitions to cutting mechanism with a decreasing indenter angle. Therefore, pileup should be more pronounced for sharp indenters (or geometrically self-similar indenters) due to the large plastic strain gradients directly underneath the indenter. So, the blunt tip theory cannot definitely be used to explain the ISE, and the plastic flow characteristics of the material underneath the indenter will also contribute to the degree of pileup. Further, the pileup of shear bands does not appear to be the main reason for the ISE in AP NGs, at least as the imprint edges in SR NGs are free from shear bands (as shown in Figure 3.3, and Figure 3.4). Jang et al., 2011 also argued that the ISE in BMGs could be associated with the deformation mechanisms (rather than the overestimate in H), such as the occurrence of STZs in the subsurface indentation zone.

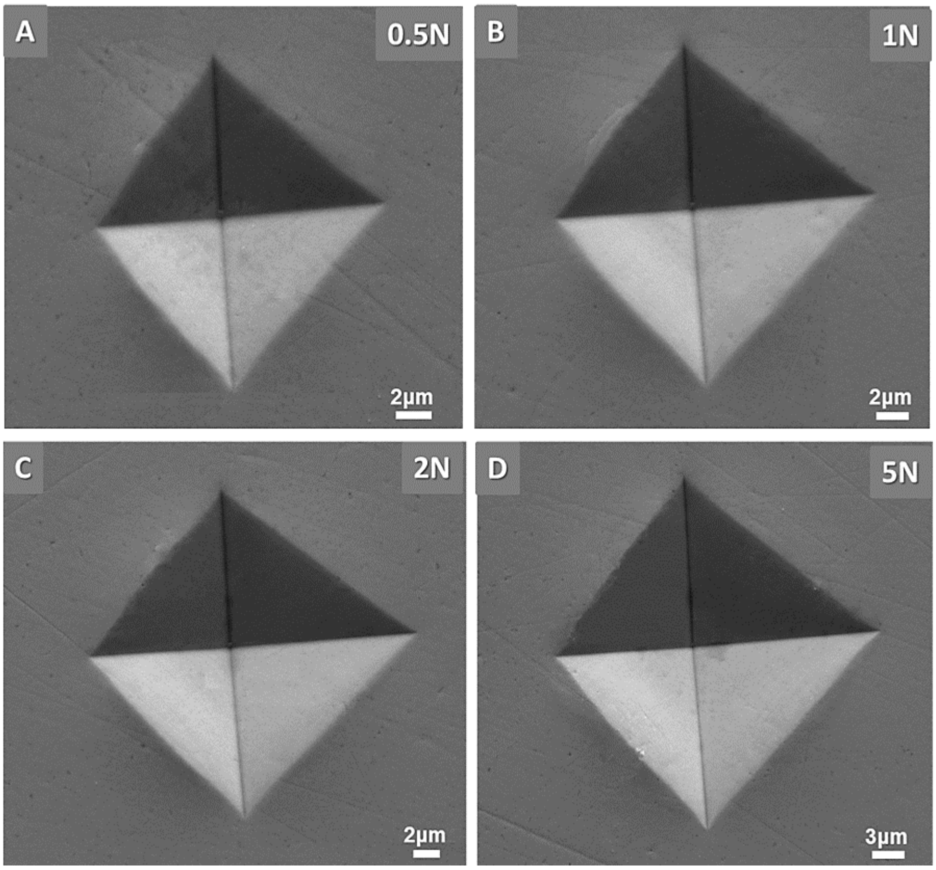

Figure 3.4 Representative SEM images of Vickers indentation imprints of AP NGs maximum indentation load, P_{max}, of (A) 0.5 N, (B)1 N, (C)2 N, and (D) 5 N.

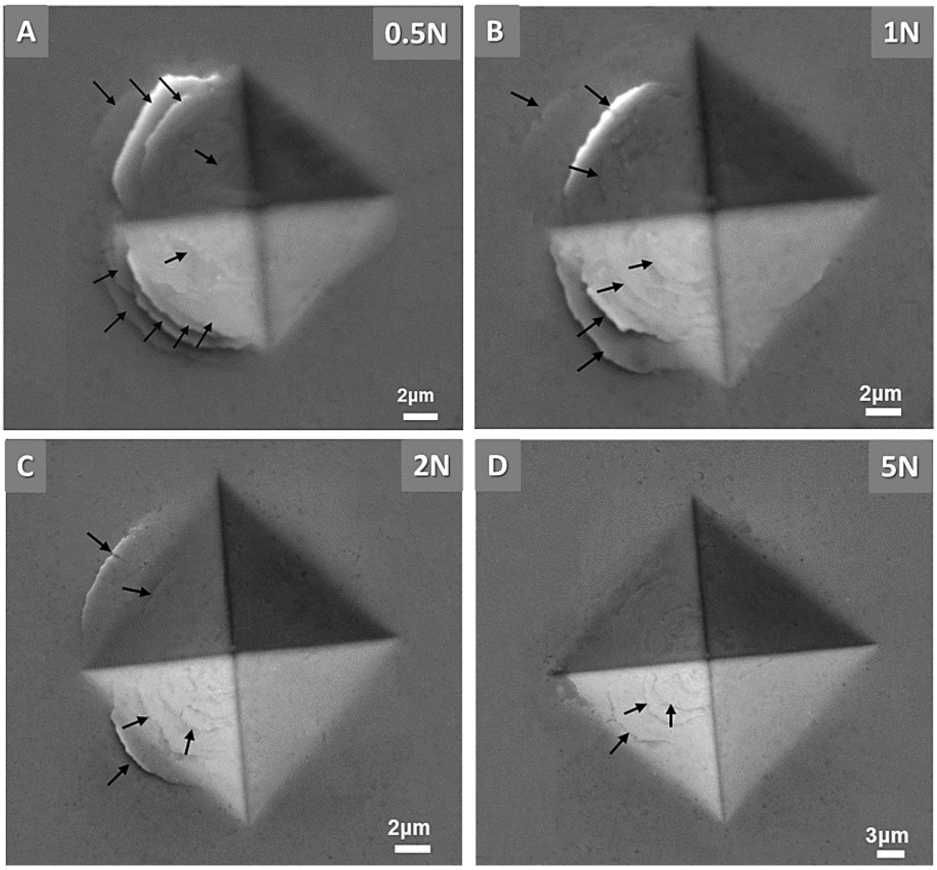

Figure 3.5 Representative SEM images of Vickers indentation imprints of SR NGs maximum indentation load, P_{max}, of (A) 0.5 N, (B)1 N, (C)2 N, and (D) 5 N.

3.3.3. Microhardness and Deformation Morphology Around the Imprint

To further understand the role of SR on deformation morphology and H, micro-indentation experiments are performed. The SEM images of micro-indentation imprints of AP and SR NGs are presented in Figure 3.4, and Figure 3.5, respectively. The imprints of AP NGs do not show any noticeable shear bands, while the SR NGs have profuse shear bands at the periphery of the imprint. The absence of shear bands at the imprint edges is generally attributed to homogeneous flow in metallic glasses, which is typically observed near the T_g [Prasad et al., 2007]. Nandam et al., 2017 also did observe shear bands in NG samples annealed at 350 °C for 2 h, consistent with the current results. The AFM images and the profilometry across the imprints of AP and SR samples (indented at P_{max} ~ 0.5 N), as shown in Figures 3.6 A, B, respectively, further confirm the observations made by SEM. Interestingly, the pileup height (of the shear bands in SR NGs) at the imprint edges reaches as high as 310 nm (1/3rd of the penetration depth), suggesting that the plastic strain cannot be accommodated by the material in the subsurface deformation zone.

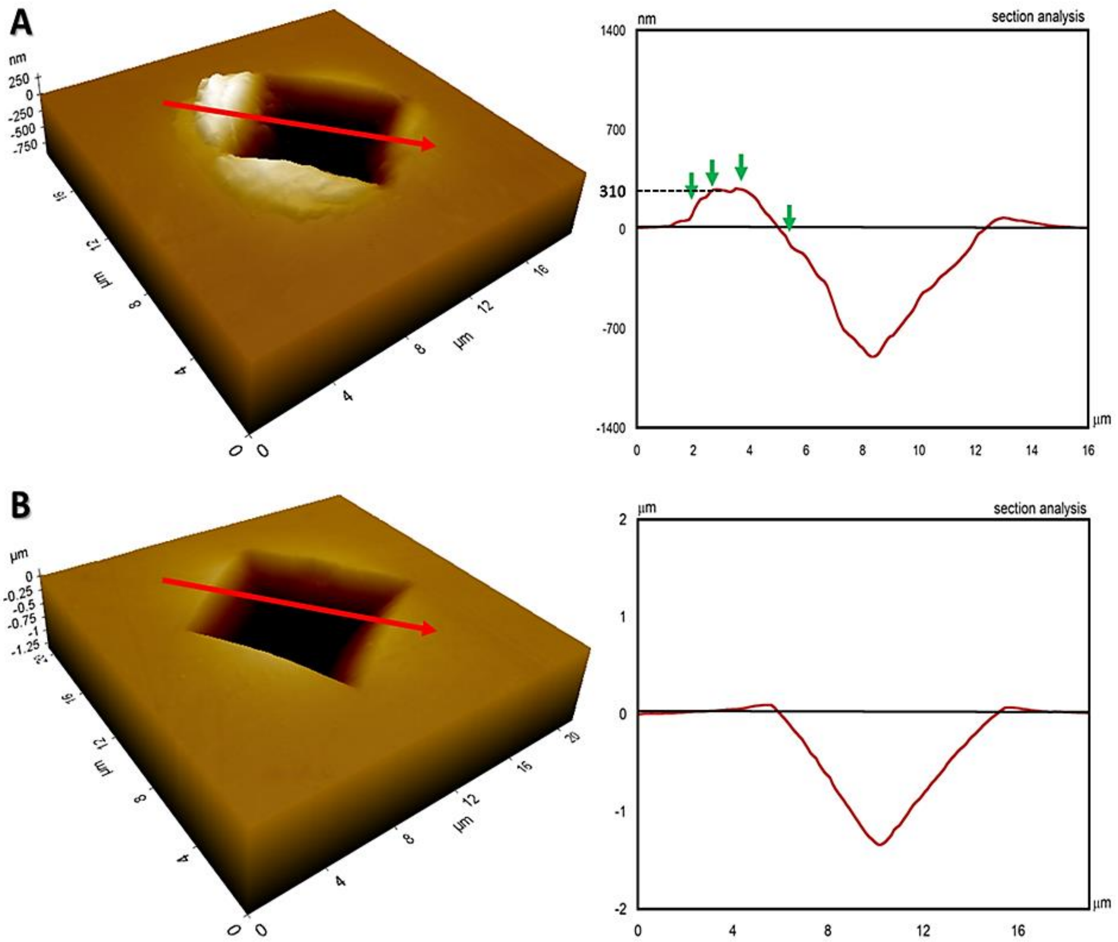

Figure 3.6 AFM images of the residual imprint along with the corresponding line scans taken across the edge of the imprint of (A) SR and (B) AP NGs obtained at a P_{max} of 0.5 N.

The microhardness, H_m, of AP and SR samples is determined from the projected area of the impression and plotted against P_{max}, as shown in Figure 3.7, which also clearly shows ISE. Similar observations were made by Ramamurty and co-workers [Jana et al., 2004; Ramamurty et al., 2005] in the case of BMGs who attributed the ISE in H_m to the roundness of the indenter at low indentation loads. The saturation H_m values of AP and SR NGs are 4.9 ± 0.03 and 5.9 ± 0.05 GPa, respectively, while for H_n, they were observed to be 7.6 and 8.6 GPa, respectively. A similar trend was observed in BMGs where the SR samples have shown higher H_m than the AP samples [Steenberge et al., 2007; Li et al., 2008; Xue et al., 2016]. The number of SBs at the imprint edges (defined as SB density, ψ) is computed and plotted against P_{max}, as shown in Figure 3.8. ψ is zero in AP NGs and independent of P_{max}, while ψ decreases with increasing P_{max} in SR NGs. The absence of SBs at high P_{max} indicates that the plastic flow is fully accommodated by the subsurface deformation zone underneath the indentation without any pileup of SBs at the imprint edges.

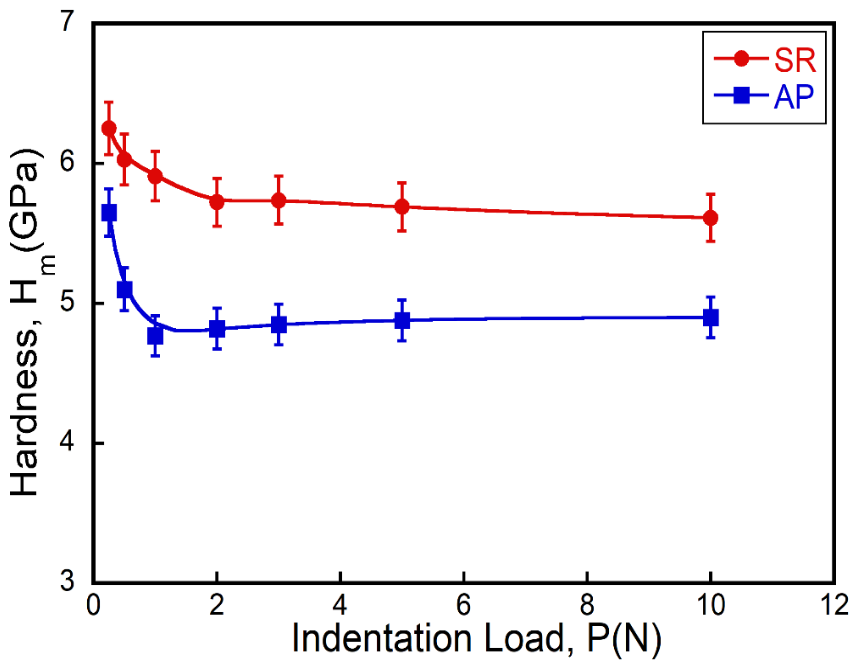

Figure 3.7 Plot showing the dependence of microhardness, H_m, on maximum indentation load, P_{max}, for the SR and AP NGs.

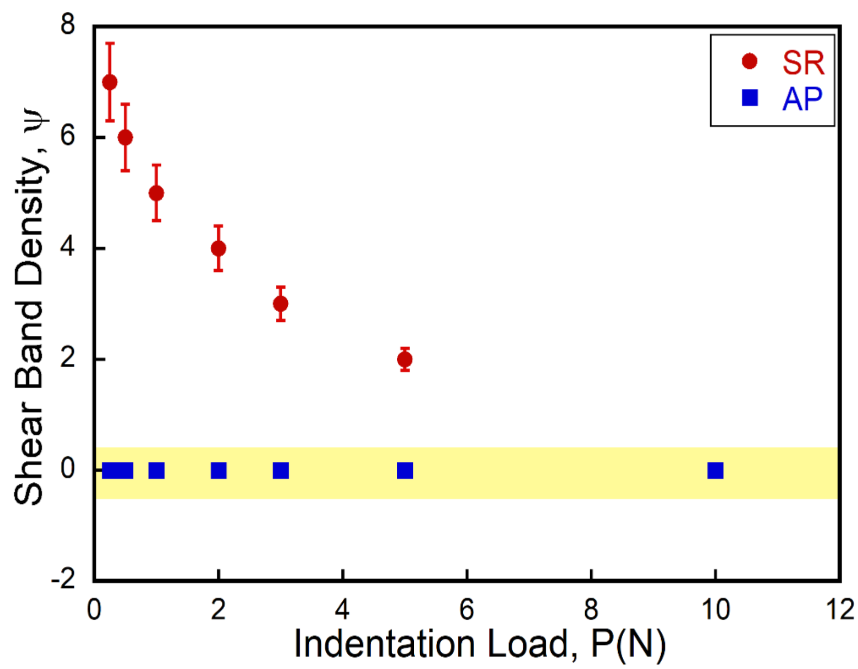

Figure 3.8 Variation of the shear band density, ψ (number of shear bands on the indented surface), with maximum indentation load, P_{max}, for both the SR and AP NGs.

The indentation imprints of above-T_g annealed NGs, as presented in Appendix A1 Figure A2, also shows the presence of SBs at the periphery of the impression, indicating that the deformation in these samples is also mediated primarily by SBs but slightly to a lesser degree than that of sub-T_g annealed samples. The shear band density, ψ, of the above-Tg annealed samples along with the AP and sub-T_g annealed samples, as plotted in Appendix A1 Figure A3, confirms that ψ decreases in these samples.

3.4. Discussion

It is well-established that sub-T_g annealing of BMGs leads to structural relaxation, thereby decreasing the free volume content of BMGs [Slipenyuk and Eckert, 2004]. One of the consequences of this is the embrittlement of BMG, leading to an increase in *H* [Murali and Ramamurty, 2005; Ramamurty et al., 2005]. In addition to the annihilation of free volume, the structural relaxation of NGs also promotes the formation of full icosahedron (FI) clusters, which may influence the mechanical properties. MD simulations of Cu–Zr NGs illustrate that structural relaxation causes an increase in the volume fraction of FI Cu ⟨0 0 12 0⟩ clusters. More importantly, the fraction of FI Cu ⟨0 0 12 0⟩ clusters at the GIs increases significantly during the annealing process while they change little in the interior of GGs [Ritter et al., 2011; Adjoud and Albe, 2021]. The increase in volume fraction of FI clusters in the interfacial region tends to increase the strength of SR NGs [Park et al., 2007; Cheng et al., 2008; Cheng and Trelewicz, 2019]. This could be one reason for an increase in H and E of SR NGs compared to AP NG.

Furthermore, the free volume content and its evolution during plastic deformation influence H as per the following equation [Hey et al., 1998; Steenberge et al., 2007; Xue et al., 2016]:

$$\mathrm{H} \approx \mathrm{A} \sinh^{-1}\left(\frac{\dot{\gamma}\Omega}{\mathrm{B}c_f} \exp\left(\frac{\Delta\mathrm{G}}{\mathrm{kT}}\right)\right) \tag{3}$$

where constants A and B incorporate the activation volume of the flow event and material undergoing plastic shear, $\dot{\gamma}$ is the plastic shear rate, Ω is the atomic volume, c_f is the concentration of free volume which evolves during the deformation, k is the Boltzmann constant, T is the temperature, and ΔG is the activation barrier energy for defect migration. The free volume evolution during indentation can be computed from the flow equation, the shear strain rate ($\dot{\gamma}$) in metallic glass can be expressed as [Spaepen, 1977]:

$$\dot{\gamma} = 2\nu\Delta f c_f \sinh\left(\frac{\tau\Omega}{2K_BT}\right) exp\left(\frac{-\Delta G}{K_BT}\right) \tag{4}$$

where ν is the frequency of atomic vibration (i.e., the Debye frequency), Δf is the fraction of the sample volume in which potential-jump sites can be found, c_f is the defect concentration which exponentially decays with inverse of reduced free volume, x by $\exp(-1/x)$, τ is the shear stress related to the indentation hardness by $H = 3\sqrt{3}\tau$, Ω is the atom volume, K_B is the Boltzmann constant, T is the test temperature, and ΔG is the activation barrier energy for defect migration [Steenberge et al., 2007]. Assuming that the changes in Δf and ΔG are less significant during nanoindentation, the above equation (4) can be re-written as:

$$Kc_f \approx \frac{1}{H} \tag{5}$$

where $K = \frac{\sqrt{3}}{9}\nu\Delta f\frac{\Omega}{K_B T\dot{\gamma}}\exp\left(-\frac{\Delta G}{K_B T}\right)$ can be approximated to constant [Li et al., 2009] and using equation (3), Kc_f is plotted against P_{max} in Figure 3.9 to understand the evolution of free volume which shows the free volume generation increases with the increase in P_{max} in both AP and SR NGs. The high H of SR NGs as compared to the AP NGs can also be attributed to lower c_f. During nano-indentation, with the increase in the load, the higher amount of free volume generation leads to the activation of more STZs, thereby leading to the mechanical softening of the material and ISE in H.

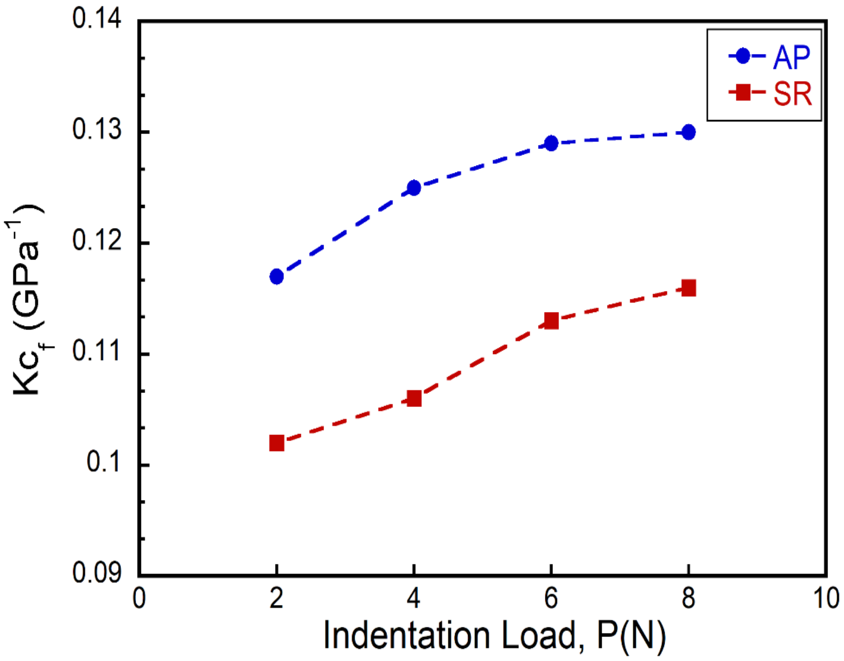

Figure 3.9 Variation of free volume with maximum indentation load, P_{max}, for AP and SR samples.

Another possible reason for the ISE in SR-NGs could also be attributed to the overestimation of H at low indentation loads due to the pileup. The pileup is not significant in nano-indentation, and the differences in pileup are corrected, and Oliver–Pharr hardness is not substantial and differs by less than 5% (as shown in Appendix A1 Figure A4). Therefore, the ISE observed in SR NGs is indeed the response of the material not an experimental artifact. Unlike nanohardness, the microhardness values presented in Figure 3.7 are computed from the projected area of the impression and hence are corrected for pileup. It is also observed from Figure 3.7 that the ISE is more pronounced in microhardness than nanohardness. The ISE is mainly connected to the plastic zone size underneath the indentation, rather than the over- or underestimate of hardness due to the pileup. In the case of nano-indentation, the size of the plastic zone at the lowest and peak loads is not significant, and hence, the observed differences are smaller, while in the case of micro-indentation, the difference in indentation depths (and thus the size of the plastic zone sizes) between the smallest and highest loads is quite significant, thereby resulting in large ISE. A similar argument can be made to describe the ISE in NGs with increasing load. The interesting question here is how does the increased plastic zone size lead to a reduction in hardness and increase pileup? We seek to explain this with the help of a model presented in Figures 3.10 A–D. Figures 3.10 A, B show the deformation morphology at low and high indentation loads for AP NGs, respectively, while Figures 3.10 C, D represent the morphology of low and high indentation loads for SR NGs, respectively. We have considered the following facts while developing this model: 1) Structural relaxation leads to a decrease in free volume and STZ density, which is manifested in a reduction in the interface width and an increase in local atomic density inside the GGs (following MD simulations by Able and co-workers) and 2) the subsurface deformation volume increases with increasing indentation load (although the representative strain, ε_r, is nearly a constant for geometrically self-similar indenters) implying that a larger volume of the material beneath the indenter undergoes plastic deformation.

In the case of AP NGs, both at low and high indentation loads (Figures 3.10 A, B), the plastic flow gets completely confined to subsurface deformation regions owing to the presence of a large number of STZs (displayed as red atoms) and high free volume present in the GG and GI which arrests the shear band pileup at the imprint edges. The increased contribution of free volume and STZs to the total deformation with an increase in indentation load also results in a decrease in H. In the case of SR NGs, at low indentation loads (Figure 3.10 C), the plastic flow cannot be completely accommodated by the region underneath the indentation (owing to the low free volume and STZ density in the subsurface deformation zone), causing the upward flow of material (vis-à-vis shear bands) between the indenter and material, thereby leading to pileup of shear bands at the periphery of the imprint.

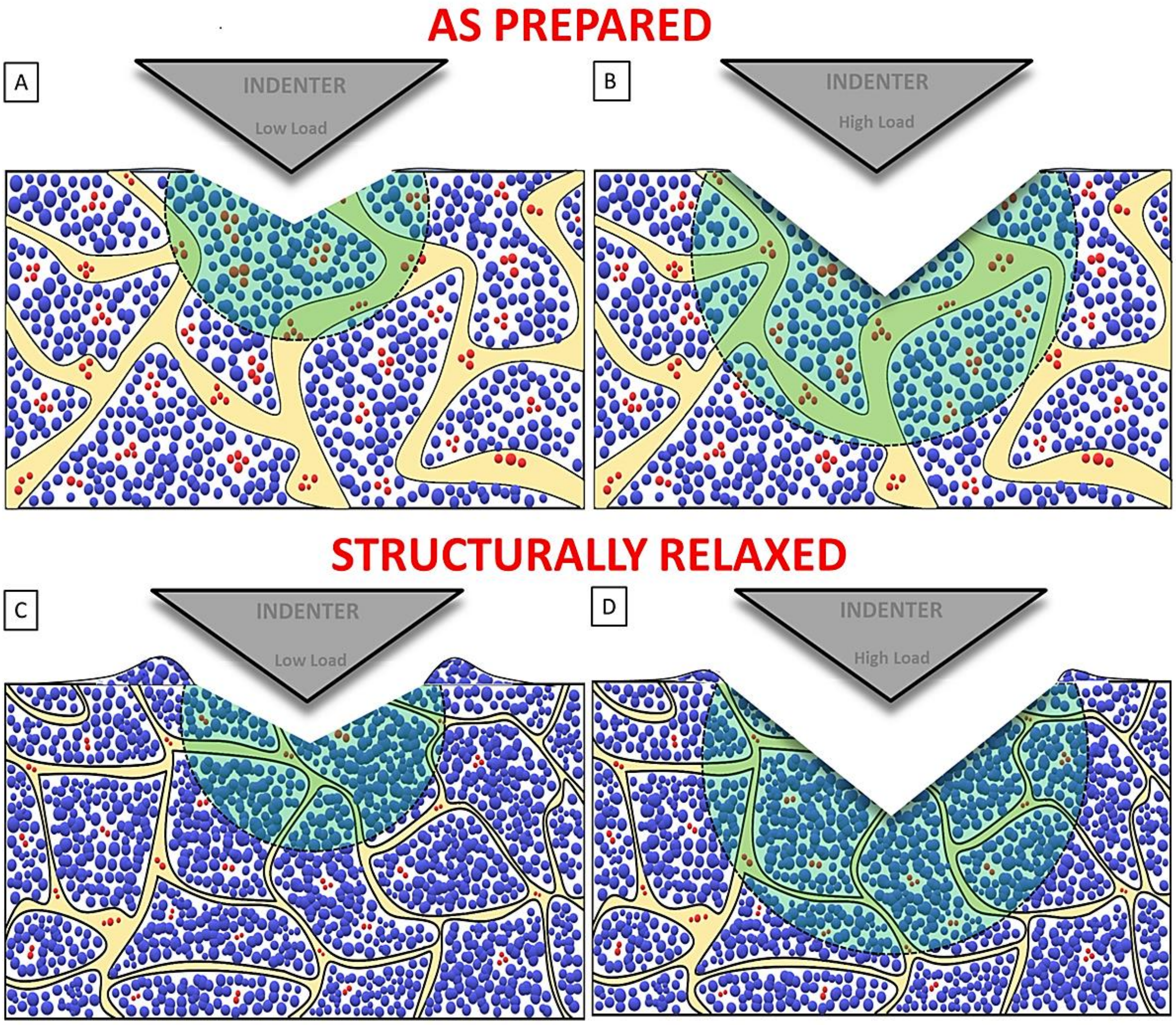

Figure 3.10 Schematic illustrating the differences in microstructure and deformation morphology between AP and SR NGs. (A, B) represents the deformation morphology at low and high indentation loads of AP NGs, respectively, while (C, D) for low and high indentation loads for SR NGs, respectively.

On the other hand, the deformation volume increases with increasing indentation load (as shown Figure 3.10D), facilitating the increased contribution of free volume to the total plastic flow under the indentation arresting the pileup of shear bands. Another possibility that prevents the shear band pileup is the frictional forces between the indenter and specimen interface, which increases with increasing load leading to their flattening on the slanting faces of the impression. However, a detailed study is warranted to investigate the friction effects, the evolution of free volume, and shear band characteristics in the subsurface deformation zone.

3.5. Summary

In summary, it is observed in the present chapter that the free volume has a marked influence on the deformation behavior of Cu–Zr NGs, with structurally relaxed (SR) NGs exhibiting a higher H than the as-prepared (AP) NGs. The loading curves of the SR NGs, in contrast to AP NGs, exhibit discrete displacement bursts, indicating that the plastic deformation is heterogeneous, which is also supported by the shear bands at the periphery of the imprint in the micro-indentation. The increase in H and serrated flow of the loading curves is attributed to the FI clusters and reduction in free volume due to the annealing, respectively. Further, the H decreases with increasing P in both the nano- and micro-indentation regimes, showing an indentation size effect. The increase in free volume generation in the subsurface deformation zone and the increase in deformation volume underneath the indentation with indentation load appear to be the reasons for the ISE.

CHAPTER 4

Strain rate sensitivity of a $Cu_{60}Zr_{40}$ metallic and nanoglass

Abstract: In this work, the strain rate sensitivity, m, of a binary $Cu_{60}Zr_{40}$ nanoglass (NG) and metallic glass (MG) are investigated using nanoindentation. Indentations were performed at different loading rates in the range of 0.26–8 mN/s, which gives equivalent indentation strain rates over three decades. The load vs. displacement curves of MG exhibited noticeable displacement bursts at low loading rates, which gradually decreased with increasing loading rate suggesting a transition from more to less severe heterogeneous plastic flow. While in the case of NG, no noticeable displacement bursts are present at any of the loading rates suggesting a near homogeneous plastic flow. In both NG and MG, the hardness decreases with increasing loading rate, resulting in negative strain rate sensitivity, m. The m for NG is higher than the MG, indicating a more homogeneous flow underneath the indentation. Interface indentation experiments and subsequent analysis of the deformation zone showed a larger number of fine secondary shear bands (SSBs) in NG as compared to the primary shear bands (PSBs), while the plastic flow in MG is accommodated mostly by the PSBs. The findings of the current study will help improve the understanding of the plastic deformation behavior of NGs and provide insights for designing the novel microstructural architecture of amorphous alloys with improved ductility*.

4.1. Introduction

Amorphous alloys, such as metallic glasses (MGs) and bulk metallics glasses (BMGs), exhibit an interesting combination of mechanical properties such as high yield strengths (~ 1 GPa) and large yield strains. However, these advantages are overshadowed by their poor room temperature ductility due to the plastic flow localization into thin shear bands, thereby leading to catastrophic failure [Falk and Langer, 1998; Schuh et al., 2007; Song et al., 2009].

*The work presented in this chapter is based on the following publication:

A. Sharma, S. S. Hirmukhe, S. H. Nandam, H. Hahn., I. Singh, K. E. Prasad. Strain rate sensitivity of $Cu_{60}Zr_{40}$ metallic and nanoglass, *Journal of Alloys and Compounds*, 921 (2022), 165991 (doi:10.1016/j.jallcom.2022.165991).

When deformed at elevated temperatures (near the glass transition temperature, T_g), the same glasses exhibit extensive plastic flow, which is attributed to the strain partitioning into multiple fine shear bands [Prasad and Ramamurty, 2012]. To date, different methods have been proposed to improve the room temperature ductility of MGs, of which the notable ones include the fabrication of (i) bulk metallic glass matrix composites (BMGMCs) [Hays et al., 2000] and (ii) Nanoglasses (NGs) [Gleiter, 2013; Ivanisenko et al., 2018]. BMGMCs comprise of crystalline phases embedded in an amorphous matrix which appears to resist the unhindered propagation of shear bands in the matrix regions, thereby avoiding catastrophic failure and thus increasing the ductility. However, due to the presence of crystalline phases, the key attributes of a fully amorphous structure cannot be completely exploited. Recently, it was shown that BMGs could also be fabricated using the selective laser melting (SLM) process, which offers distinct shear band characteristics compared to the conventional BMGs but exhibits lower strength and ductility due to the presence of large porosity [Deng et al., 2021].

Unlike BMGMCs, the newly developed NGs contain a fully amorphous structure with glassy grains (GGs) separated by glassy interfaces (GIs). Similar to the MGs, the fundamental units of plastic deformation in NGs are the shear transformation zones (STZs) which are a cluster of atoms that undergo cumulative shearing under the influence of external load and nucleate in the regions of high free volume [Ritter et al., 2011; Adjaoud and Albe, 2016, 2019]. In NGs, both the GIs and GGs are the sources of free volume, and hence the probability of finding STZs is much higher than the MG counterparts. NGs are fabricated using bottom-up approaches like magnetron sputtering, electroplating, and inert gas condensation [Chen et al., 2011; Witte et al., 2013; Sniadecki et al., 2016]. The preliminary deformation experiments conducted on NGs show reasonably good plasticity compared to the MGs of identical composition [Nandam et al., 2017, 2020, 2021; Sharma et al., 2021a, 2021b; Wang et al., 2015, 2016]. The reason is attributed to the unique microstructure of NGs, which promotes nucleation of multiple shear bands, leading to strain partitioning and consequently avoiding plastic flow localization. Although there have been experimental studies characterizing the plastic flow characteristics of NGs, limited attention was given to investigating the effect of loading rate (or the strain rate) on the deformation behavior of NGs. One of the key characteristics of plastic deformation of materials is the strain rate sensitivity, m, as it provides useful information about the mechanisms of plastic flow.

The dependence of flow stress, σ, on the strain rate, $\dot{\varepsilon}$, is expressed by the power-law relation $\sigma = C\dot{\varepsilon}^m$where C is a temperature-dependent material constant and m is strain rate sensitivity. The positive m values indicate homogeneous deformation, while the negative m indicate heterogeneous deformation. Besides qualitatively describing the nature of deformation, m is also used to quantify the activation volume needed for the plastic deformation. Conventionally, m is determined from the strain rate jump tests under uniaxial loading conditions, and recently it has been shown that m can also be obtained from the indentation experiments as $m = \frac{dlogH}{dlog\dot{\varepsilon}_i}$, where H and $\dot{\varepsilon}_i$ represents the indentation hardness and indentation strain rate, respectively. The $\dot{\varepsilon}_i$ is expressed as $\frac{\dot{P}}{2P_{max}}$, where $\dot{P}$ is the indentation loading rate and P_{max} is the maximum indentation load [Dieter, 1986]. At room temperature, most of the engineering alloys display positive m values ranging between 0 and 0.1.

Several studies [Dalla Torre et al., 2006; Jiang et al., 2007; Mukai et al., 2002; Dubach et al., 2009a; Gonzalez et al., 2011; Li et al., 2020; Wang et al., 2021; Ma et al., 2020; Pan et al., 2008; Boltynjuk et al., 2018; Bhattacharyya et al., 2015; Sort et al., 2019; Sahu et al., 2019; Zhao et al., 2021; Gunti et al., 2022] have been conducted to investigate the m value of BMGs, and most of the studies, except a few [Li et al., 2020; Wang et al., 2021; Ma et al., 2020; Pan et al., 2008; Boltynjuk et al., 2018], report negative m, while limited studies are available on MGs and NGs. Pan et al., 2008 performed indentation strain rate jump experiments and observed that the H increases with loading rate, indicating positive m values. Using m values and the cooperating shearing model (CSM), they have determined the STZ volume, which is in the range of 2–7 nm^3 (containing a few 100′s atoms) for most BMGs. Recently, Boltynjuk et al., 2018 observed a higher m in severely deformed Zr- based BMG than the as-cast BMG and attributed the positive m values to high STZ sites. Bhattacharyya et al., 2015 argued that the positive m values are due to the experimental artifact and the possible reason for this is the overestimation of H without considering the pile-up around the impression, particularly at high indentation loads. Further, they argued that the negative m values are due to the lack of time (with increasing loading rate) for the material to relax the structure. Sort et al., 2019 reasoned that the negative m values are due to the generation and accumulation of free volume at high loading rates. Recently, Sahu et al., 2019 reported a negative m value for Ni_{60} Zr_{40} thin-film MG (containing fine crystals of 2–3 nm in size) and attributed it to a decrease in STZ size at high loading rates and relaxation mechanisms prevalent at low loading rates. In another study, Zhao et al., 2021 reasoned that the time available for relaxation or diffusion is less at a higher loading rate, making the material softer, resulting in negative m. Recently, Gunti et al., 2022 have also argued that higher loading rates caused significant activation of

STZs and accredited the difference in the deformation behavior in mode to the strain rate fluctuations observed with increasing indentation depth. The negative m obtained from various literature studies is summarized and presented in Table 4.1. Most of the studies conducted to date are on the as-cast or deformed MGs and BMGs, but limited attention was given to understanding the strain rate sensitivity of NGs. Unlike the deformed MGs and BMGs, where the free volume is heterogeneously distributed, the NGs have a more uniformly distributed defect structure. Hence, it is interesting to investigate the strain rate sensitivity of NGs. This will not just only provide the key findings but will help us shed new light on understanding the deformation mechanisms of NG and provide novel guidelines for designing amorphous alloys with improved ductility.

Therefore, the current study is performed with the following objectives: (a) What is the effect of loading rate on NG and MG load vs. displacement response having identical composition? (b) How does the hardness vary with the loading rate? (c) What is the role of NG microstructure on m? and (d) How do m values of NGs fare with the MGs of an identical composition? To address the above questions, we have carried out nanoindentation experiments on a binary $Cu_{60}Zr_{40}$ MG and NG at different loading rates. In order to understand differences in shear band characteristics and the trend observed in m values between the NG and MG interface, micro- indentation experiments are performed as it is difficult to characterize the same using nanoindentation due to the limitations of maximum indentation load.

4.2. Material and experiments

$Cu_{60}Zr_{40}$ NG samples are produced in an inert-gas condensation (IGC) system, using binary $Cu_{60}Zr_{40}$ alloy as the sputtering target, while the binary $Cu_{60}Zr_{40}$ MG are synthesized using the melt-spinning technique. Both the NG and MG used in the current experiments are in as-processed condition without any subsequent annealing after their fabrication. The NG is disc-shaped with a thickness of ~0.3 mm and a diameter of 8 mm, and MG has a thickness of 30–40 μm, a width of ~1 mm, and a length of 10–20 mm. The amorphous nature of NG and MG is confirmed using X-ray diffraction (XRD). XRD was conducted using Cu-Kα radiation within the range of 2–70°. The surface of the samples is subsequently polished to a surface finish of 0.25 μm using the standard metallographic sample preparation method and then taken for indentation experiments.

Table 4.1 Summary of the m values reported for glasses in various literature

Material	Structural state	Nature of test (Strain rate range, s^{-1})	Strain Rate Sensitivity, *m*
$Zr_{52.5}Ti_5Cu_{17.9}Ni_{14.6}Al_{10}$ (Vitreloy105) (Dalla Torre et al., 2006)	As-cast	Compression 3.3×10^{-3} - 3.7×10^{-4}	- 0.001 ± 0.0005
Vitreloy 105 (Jiang et al., 2007)	As-cast	Compression test 2.34×10^{-3} - 1.87×10^{-1}	- 0.0026
$Pd_{40}Ni_{40}P_{20}$ (Mukai et al., 2002)	As-cast	Compression $3.3 \times 10^{-5} – 2 \times 10^{3}$	Negative
Vitreloy 105 (Dubach et al., 2009)	As-cast	Compression $3.33 \times 10^{-3} – 2 \times 10^{-1}$	-0.002
$Zr_{65}Cu_{20}Fe_5Al_{10}$ (Gonzalez et al., 2011)	As-cast	Compression tests $5 \times 10^{-3} – 5 \times 10^{-2}$	- 0.0026
$Zr_{41.2}Ti_{13.8}Cu_{12.5}Ni_{10}Be_{22.5}$ Vitreloy 1 (Bhattacharyya et al., 2015)	As-cast	Indentation tests @ P_{max} of 9 mN $2.22 \times 10^{-2} – 4.4 \times 10^{-1}$	-0.0166 ± 0.001
	Structurally relaxed		-0.0201 ± 0.001
	Shot peened		-0.0128 ± 0.001
	As-cast	Indentation tests @ P_{max} of 250 mN $3.33 \times 10^{-3} – 2 \times 10^{-1}$	-0.0137 ± 0.001
	Structurally relaxed		-0.0106 ± 0.001
	Shot peened		-0.008 ± 0.001
$Ti_{40}Zr_{25}Ni_8Cu_9Be_{18}$ BMG (Sort et al., 2019)	As-cast	Indentation $2.5 \times 10^{-3} – 1.25 \times 10^{-1}$	-0.063
$Ni_{60}Zr_{40}$ amorphous NG thin film (Sahu et al., 2019)	As-deposited	Indentation tests 0.01, 0.1 and 1 s^{-1}	-0.032 to -0.057 (300 K)
			-0.021 to-0.039 (600 K)
$Pd_{40}Cu_{30}Ni_{10}P_{20}$ $Zr_{48}Cu_{32}Ni_4Al_8Ag_8$ $Zr_{48}Cu_{34}Pd_2Al_8Ag_8$ (Zhao et al., 2021)	As-cast	Indentation tests @ P_{max} of 50, 100, 200 mN $5 \times 10^{-3} – 2.5 \times 10^{-1}$	Negative
Vitreloy 1 Vitreloy 105 $Zr_{58.5}Cu_{15.6}Ni_{12.8}Al_{10.3}Nb_{2.8}$ (Vitreloy 106A) $Zr_{55}Cu_{30}Ni_5Al_{10}$ (ZR55)	As-cast	Indentation tests @ P_{max} of 500 mN $1 \times 10^{-3} – 1$	Negative

Nanoindentation experiments are performed at room temperature using a Hysitron Triboindenter with a Berkovich three side pyramidal-shaped diamond indenter. The experiments are conducted in a load-controlled mode at a maximum applied load of 4 mN. The indentations are performed at different loading rates in the range of 0.26 mN/s to 8 mN/s, which corresponds to 3 decades of indentation strain rates. A minimum (4 ×4) array of 16 indents is taken at each load to obtain precise and reliable statistical data. The distance between the successive indents is kept about ten times the maximum indentation depth to circumvent the strain field interaction. The hardness, H, is determined using the Oliver and Pharr (O&P) method [Oliver and Pharr, 1992] as

$$\boldsymbol{H} = \frac{\boldsymbol{P_{max}}}{\boldsymbol{A_c}} \tag{1}$$

where P_{max} is the maximum indentation load, and A_c is the contact area, which is a function of contact depth, h_c. As per the O&P method, the h_c is given by Eq. (2):

$$\boldsymbol{h_c} = \boldsymbol{h_{max}} - \boldsymbol{\mu}\frac{\boldsymbol{P_{max}}}{\boldsymbol{S}} \tag{2}$$

Here, h_{max} is the maximum penetration depth, μ is the geometry constant which depends upon the power law exponent m obtained from the unloading slope (μ ~ 0.75 is recommended for Berkovich indenter), and S is the stiffness which is obtained from the slope of the unloading part of P vs. h curve as $S = dP/dh$. Finally, the modulus, E, is obtained using the equation (3):

$$\boldsymbol{E_s} = (\boldsymbol{1} - \boldsymbol{\nu_s^2})\left[\left(\frac{2\sqrt{A_c}}{S\sqrt{\pi}}\right) - \left(\frac{1-\nu_i^2}{E_i}\right)\right]^{-1} \tag{3}$$

where E and ν represent the elastic modulus, and Poisson's ratio and the subscripts i and s refer to the indenter and specimen, respectively. The berkovich diamond indenter tip is used having an elastic modulus, $E = 1140\ GPa$ and a poisson ratio, $\mu = 0.04$. Before starting the experiment, the area function of the indenter tip is calibrated with the help of a standard quartz sample by performing a series of indentations at different indentation depths.

Bonded interface indentation (BII) experiments are performed to qualitatively compare the differences in deformation characteristics beneath the indenter for both the NG and MG samples as they may provide reasons for the differences in m. Two specimens are taken with one of their surfaces polished up to 0.25 μm surface finish to perform the BII experiment. The polished surfaces are then bonded together by applying a strong adhesive ("super glue") and allowed to dry for 5 h. The specimens are then cold mounted in such a way that the bonded interface is on the top surface of the mould, which is again polished up to a surface finish of 0.25 µm. Following this, Vickers indentation is performed on the interface at a P_{max} of 3 N. The indentations are made in such a way that the diagonal of the imprint lies along with the interface. Subsequently, the bonded interface is opened by dissolving the super glue in acetone for 1-2 h and examined using a scanning electron microscope (SEM) to characterize the differences in shear band morphology underneath the indentation between the two glasses. Although we have used nanoindentation experiments to compute the m values, the micro-indentation was used for BII experiments due to the limitations of P_{max} in nanoindentation. Nevertheless, the BII experiments are performed under similar loading conditions (with the same load, loading rate, and indenter geometry) on both NG and MG to compare the shear band characteristics effectively.

4.3. Results

The XRD patterns of the as-prepared MG and NG samples are presented in Fig. 4.1, which shows a broad characteristic diffraction hump with no signatures of crystalline phases, confirming the presence of an amorphous structure. Fig. 4.2a and b show the typical P vs. h curves of NG and MG corresponding to different loading rates, i.e., 0.26, 0.4, 0.8, and 8 mN/s.

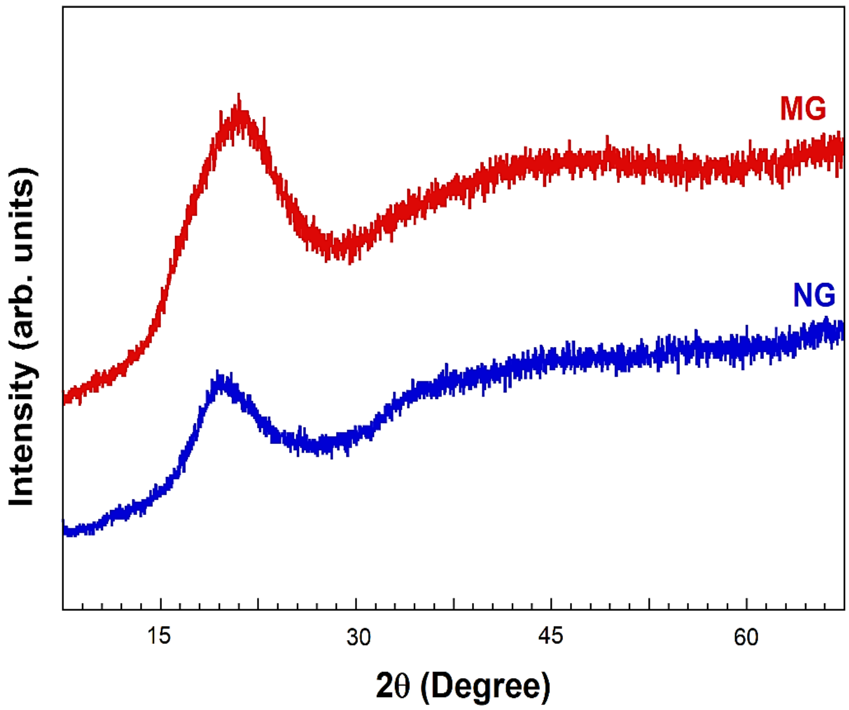

Figure 4.1 X-ray diffraction spectra of the MG and NG samples.

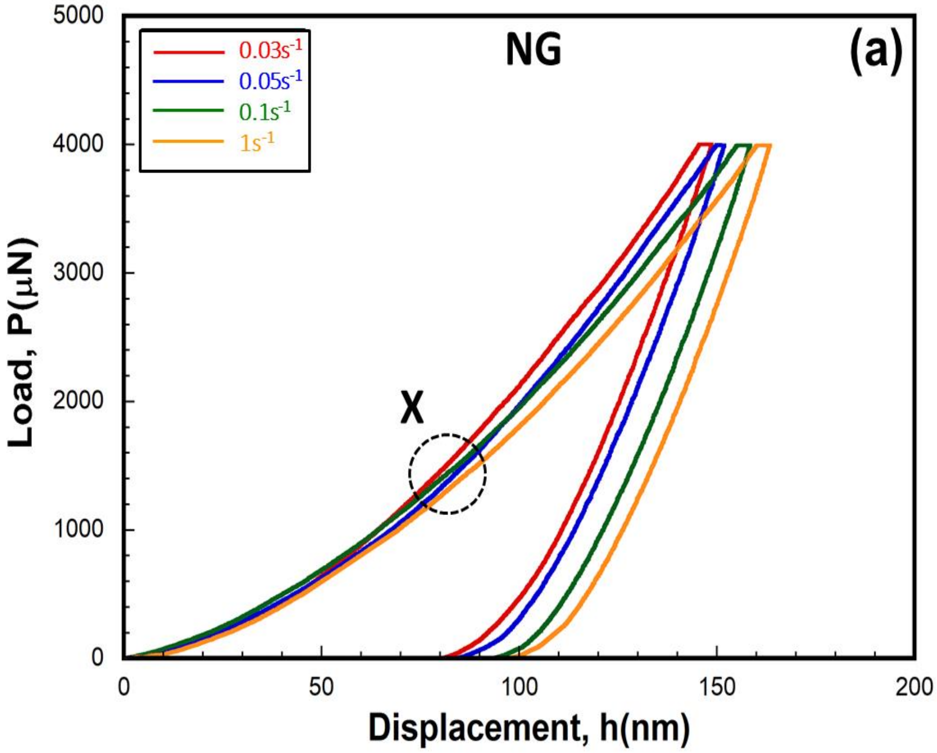

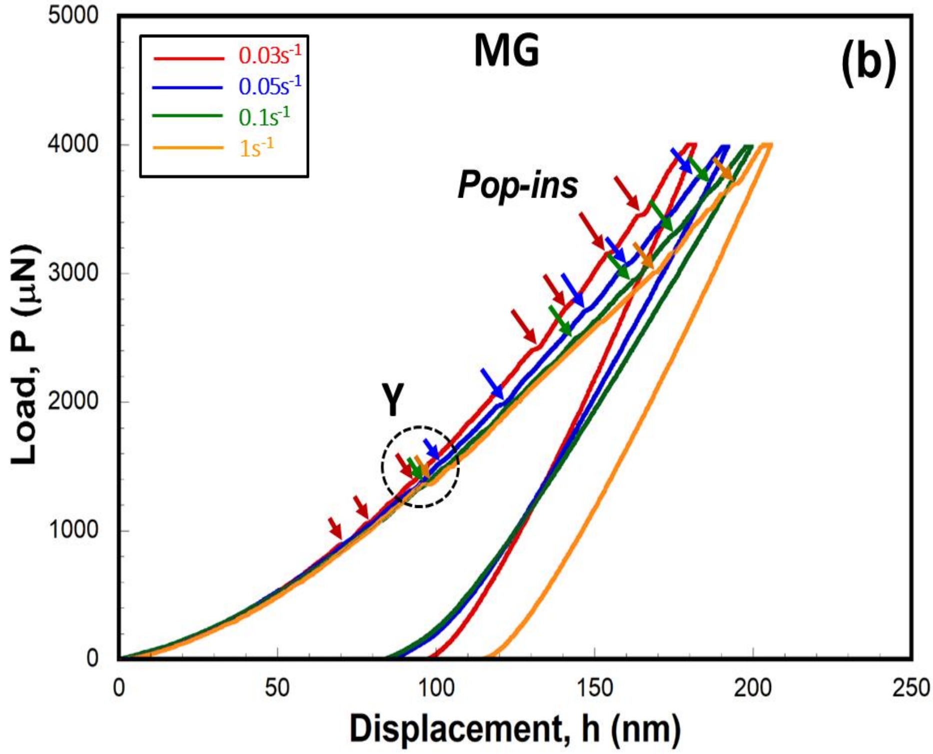

Figure 4.2 Representative indentation load, P vs. penetration depth, h curves obtained under different loading rates for (a) NG and (b) MG at a P_{max} of 4 mN, respectively.

The indentation imprints of NG and MG show no significant pile-up at the imprint edges, indicating that the O&P analysis can be suitably employed to determine the H [Nandam et al., 2017; Sharma et al., 2021b]. According to the O&P analysis, the relation between the P and h of the loading and unloading curves are described by the equations 4 and 5 presented below:

$$\boldsymbol{P = \alpha h^q} \tag{4}$$

$$\boldsymbol{P = \beta\left(h - h_f\right)^r} \tag{5}$$

Where fitting constants α and β represent the resistance to indentation, and the elastic recovery of the material, $q,$ and r represent the power-law exponents of loading and unloading curves, which depend on the indenter geometry, while h and h_f indicate the instantaneous and final penetration depth of the indenter, respectively. The loading and unloading curves of both NGs and MGs are well described by the equations (4) and (5) (as presented in Figures A5 and A6 of Appendix A1) with the regression coefficient values, R^{2}, close to ~ 0.999. All the P vs. h curves (at different loading rates) yield similar power-law exponents approving a high level of reproducibility and repeatability of the nanoindentation results. The loading curves of NG (as presented in Fig. 4.2a) exhibit smooth behaviour (characterized by the absence of displacement bursts or "*pop-ins*"), suggesting homogeneous plastic deformation. This observation is consistent with previous experimental studies reported for NGs [Nandam et al., 2017, 2020; Sharma et al., 2021a, 2021b; Li et al., 2017; Hirmukhe et al., 2022; Pang et al., 2012; Rauf et al., 2018]. Another interesting observation from Fig. 4.2a is the increase in penetration depth with loading rate suggesting softening of the material, and the reason for this behavior is discussed in detail in the subsequent sections. Contrastingly, the loading curves of MG samples (Fig. 4.2b) are characterized by a serrated flow, manifested by a large number of pop-ins (indicated by arrows), indicating the inhomogeneous nature of the deformation of MGs. A close examination of the loading segments reveals that the *pop-in* width decreases with an increase in loading rate for the MG, as shown in the magnified view in Fig. 4.3. Further, derivative technique is employed on the loading curves to characterize the pop-in behavior in detail as shown in figure Fig. A7 of Appendix A1 [McGurk et al., 1999; Malzbender et al., 2001]. The plots dP/dh vs. h and $dP\ /\ dh^2$ vs. h^2 for MG are presented in Fig. A7a and b, while for NG in c and d, respectively. The significant spikes observed in the horizontal line of Fig. A7 indicate the pop-ins occurring due to the nucleation of shear bands in MG. The intensity of spikes decreases with increasing strain rate, indicating the absence of severe flow localization. Such spikes are not observed in NG at all the strain rates suggesting a near homogeneous deformation. Further, the displacement bursts are quantified by measuring the *pop-in* width,

$h_{\text{pop-in}}$, at different loading rates, and their average values are plotted as a function of the loading

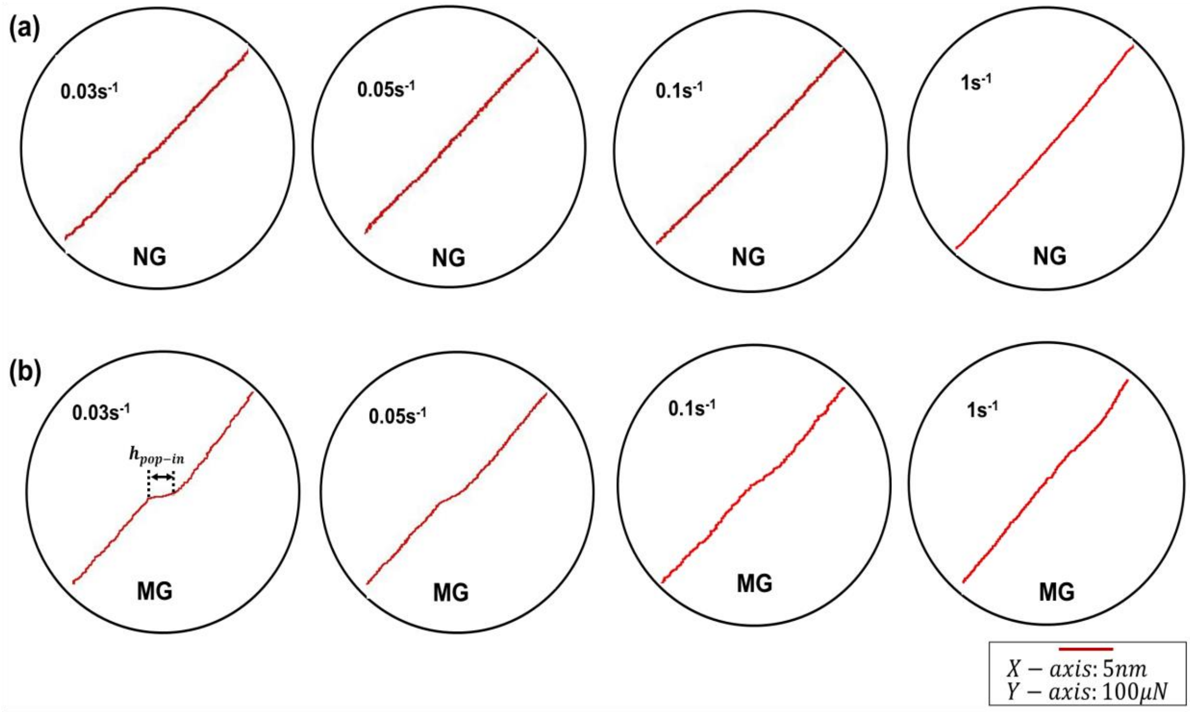

Figure 4.3 Enlarged view of the loading portion of the *P* vs. *h* curves from regions X and Y at different loading rates for (a) NG and (b) MG respectively, describing the pop-in behaviour.

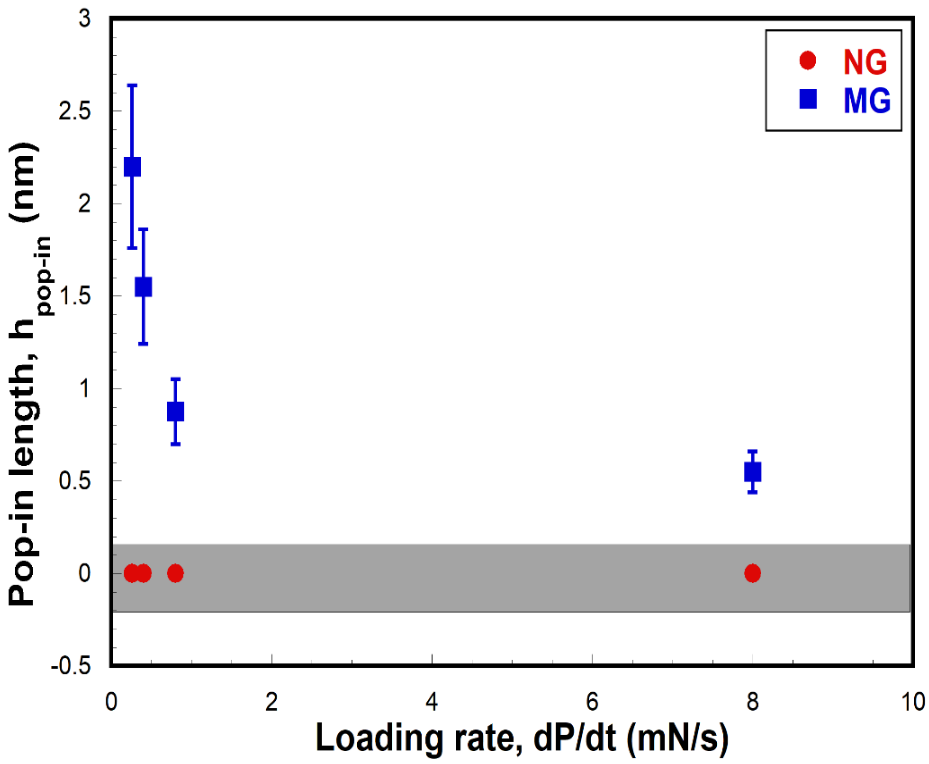

Figure 4.4 Plot representing the variation of pop-in length, $h_{pop\text{-}in}$, with loading rate for NG and MG.

rate for NG and MG, as shown in Fig. 4.4. In order to determine the pop-in width, $h_{\text{pop-in}}$, the loading portion curves are magnified in the regions where there is a deviation from the power law. The horizontal distance between the start and end points from such regions yields, $h_{\text{pop-in}}$. The penetration depth corresponding to pop-ins are clearly identified from figure Fig. A7 in the Appendix A1. It is evident from Fig. 4.4 that for MGs, the $h_{\text{pop-in}}$ decreases with an increase in loading rate. A similar trend is reported for MGs and BMGs in the previous literature studies [Sort et al., 2019; Zhao et al., 2021; Schuh et al., 2002, 2003, 2004], which is attributed to the change in deformation mechanism from heterogeneous to homogeneous with an increase in loading rate. Interestingly, $h_{\text{pop-in}}$ remains nearly zero for NG, suggesting no substantial change in the deformation mechanism with increasing loading rate. The variation of H with the loading rate for both NG and MG obtained at P_{max} of 4 mN is plotted in Fig. 4.5a. It can be noticed from the figure that, at all the loading rates, NG exhibits a higher H than the MG, consistent with the previous experimental and simulation studies [Nandam et al., 2017; Sharma et al., 2021a, 2021b; Hirmukhe et al., 2020; Franke et al., 2014; Adjaoud and Albe, 2021; Xie and George, 2008]. Besides this, the H decreases with an increased loading rate for both the NG and MG samples. The m values are obtained from the slope of H vs. equivalent strain rate plotted in the log-log scale (Fig. 4.5b) and are presented in Table 4.2. In both the glasses, the m value is found to be negative, but interestingly, its value for NG is towards more positive than the MG.

Table 4.2 Values of m obtained in present study for NG and MG.

Glass	Strain rate sensitivity, m @ P_{max} of 4mN
$Cu_{60}Zr_{40}$-NG	-0.028 ± 0.002
$Cu_{60}Zr_{40}$-MG	-0.037 ± 0.003

Further, the reasons for the observed differences in m values are examined using subsurface deformation zones of MG and NG as presented in Figs. 4.6 and 4.7, respectively. It is observed from Fig. 4.6 that the plastic strain in the subsurface deformation region of MG is mainly accommodated by large shear bands, known as primary shear bands (PSBs). The PSBs appear to be semi-circular in shape with no waviness at the shear band front having small and large curvatures. The shear bands having smaller curvature at their front are much sharper suggesting unhindered propagation during the deformation, while the one with large curvature has a wavy front indicating their interaction with other bands during their propagation. The differences in

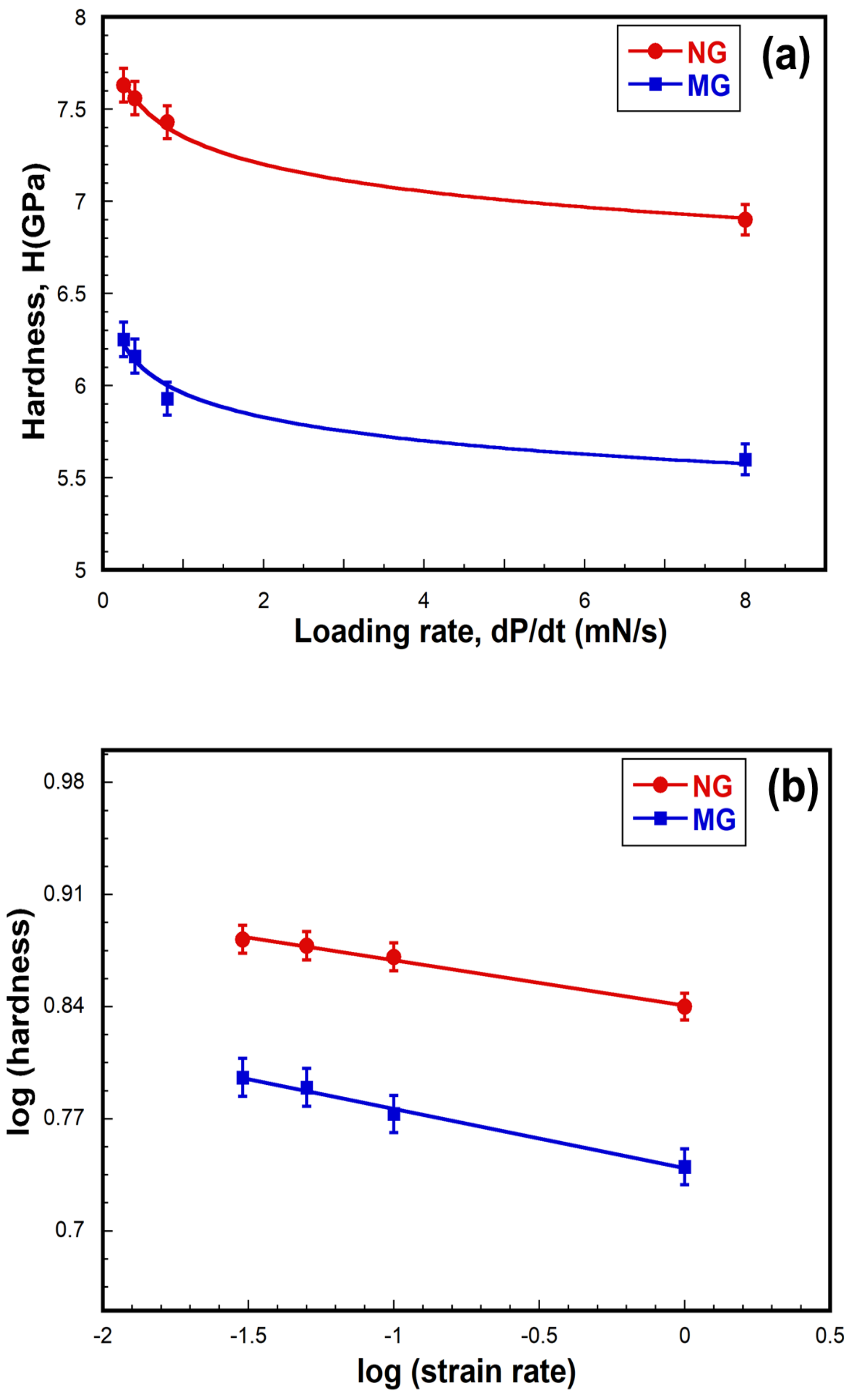

Figure 4.5 Plot representing (a) the variation of hardness, H, with loading rate, dP/dt and (b) strain rate, $\dot{\varepsilon}$, plotted on log scale for NG and MG.

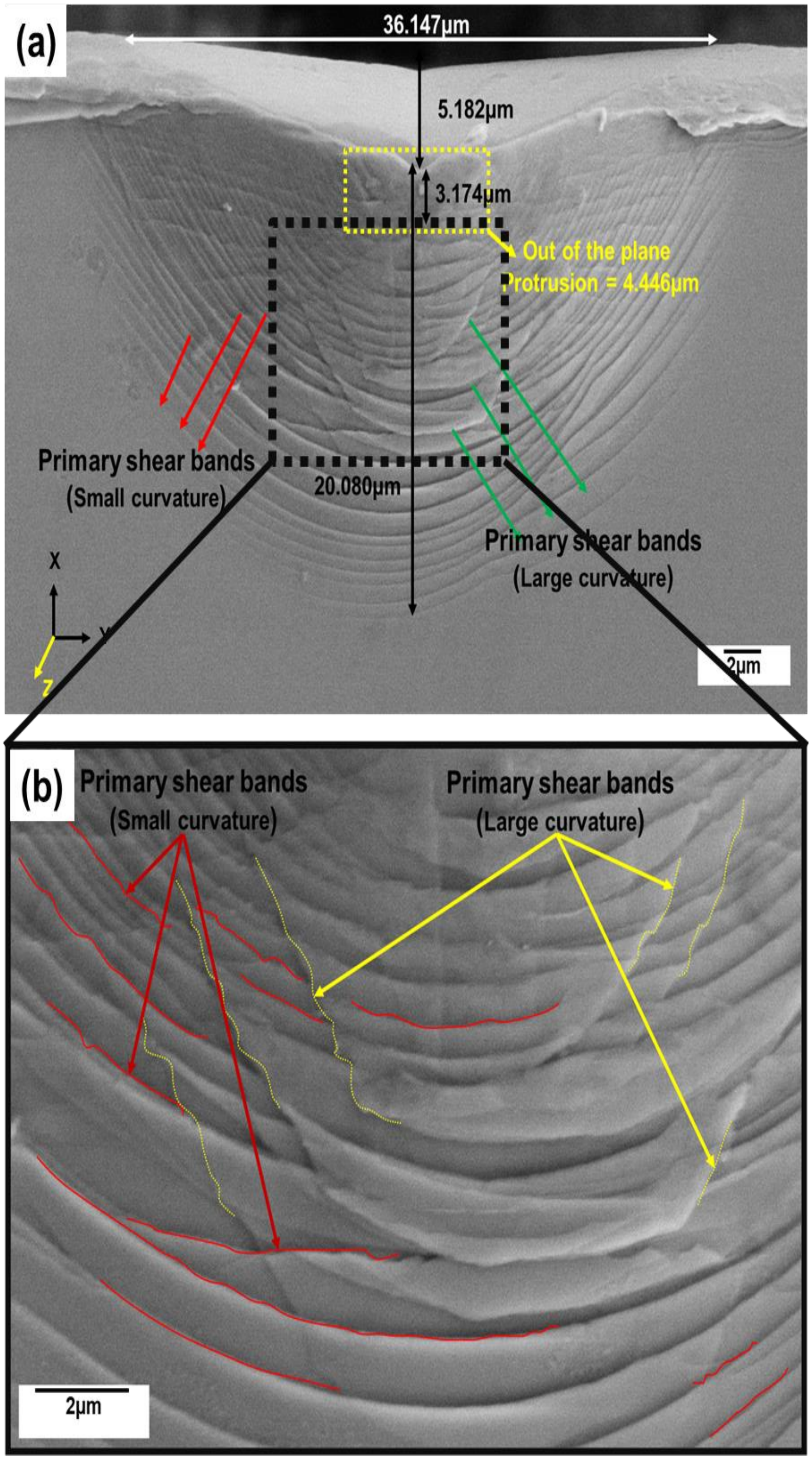

Figure 4.6 Subsurface deformation zone of a $Cu_{60}Zr_{40}$ MG at a Pmax of 3 N obtained at a loading rate of 0.3 N/s (an equivalent strain rate of 0.1 s-1) indicating (a) complete deformation zone and (b) a high magnification image of the highlighted region of (a).

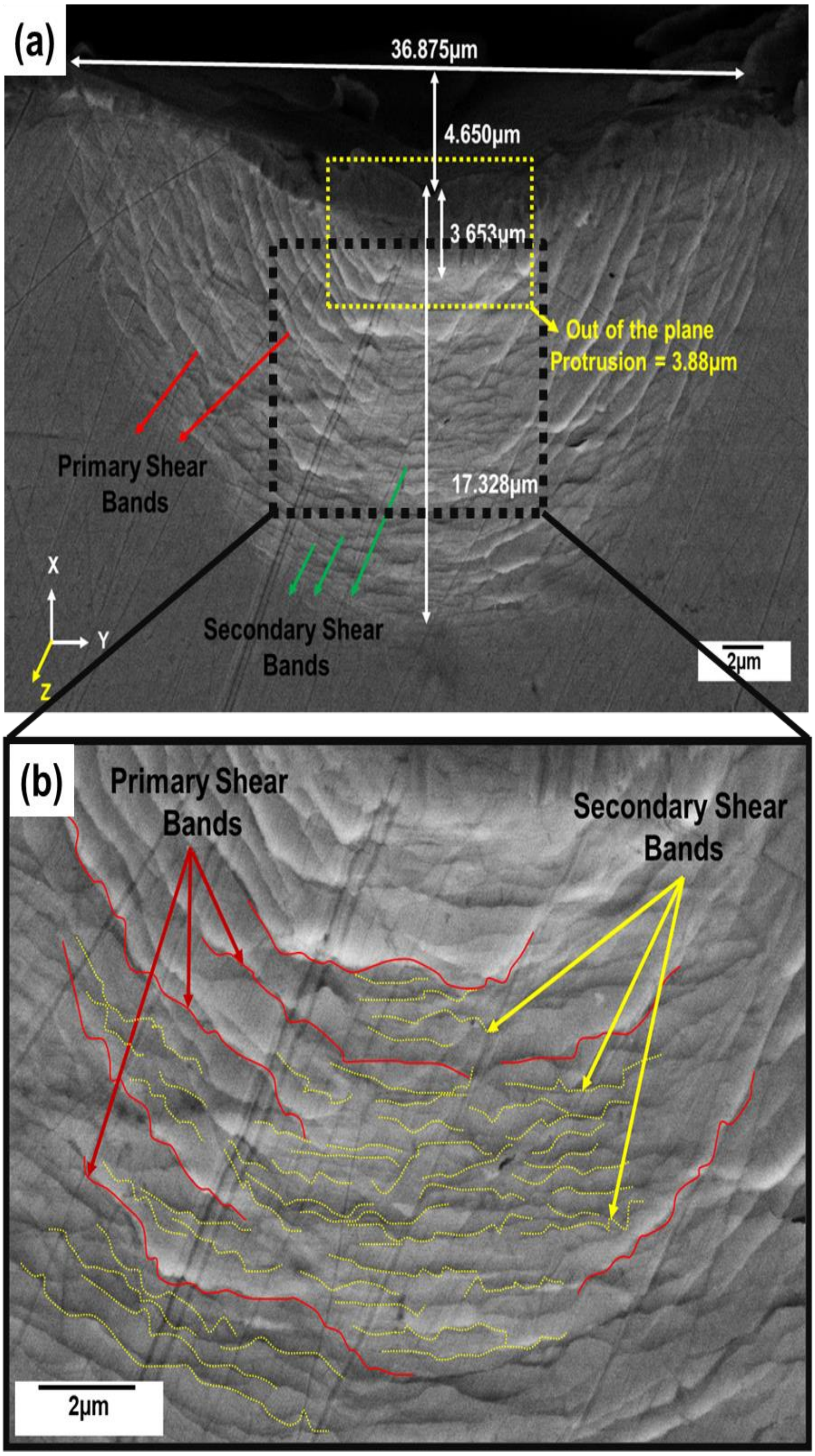

Figure 4.7 Subsurface deformation zone of a $Cu_{60}Zr_{40}$ NG at a Pmax of 3 N obtained at a loading rate of 0.3 N/s (an equivalent strain rate of 0.1 s-1) indicating (a) complete deformation zone and (b) a high magnification image of the highlighted region of (a).

curvatures of the shear bands possibly appeared due to diverse stress fields generated beneath the indenter during indentation [Subhash et al., 2007; Xie and George, 2008]. Contrastingly, in the case of NGs, a large number of very fine shear bands, referred to as secondary shear bands (SSBs), are formed in between PSBs (Fig. 4.7). Unlike MGs, the shear bands front in NGs is wavy, which may be due to the multiple shear band interactions. The bands are diffused and thus making it difficult to differentiate the primary and secondary shear bands (SSBs). Similar observations have been reported in the case of binary Pd-Si MG and NG [Sharma et al., 2021b]. The primary and secondary shear bands are discernible in Pd-Si NGs, unlike the Cu-Zr NGs. In summary, the following observations can be made from the experimental results (a) The Cu-Zr NG shows a higher H as compared to the MG, having the identical composition (b) The pop-ins in the loading portion of P vs. h curves are dependent on the loading rate in MG while it has a no effect in NG (c) The penetration depth is found to increase with the increase in loading rate for both MG and NG indicating that both the glasses become softer with increasing loading rates. (d) The m computed from the nanoindentation data clearly shows a negative value for both MG and NG, albeit slightly more positive in NG than the MG. (e) The subsurface deformation zone in NG comprises several fine shear bands compared to the large shear bands in MG.

4.4. Discussion

In the following discussion and subsequent analysis, the effect of loading rate on the P vs. h response, H, and strain rate sensitivity is analyzed in light of STZ activity and the differences in shear band characteristics in the subsurface deformation zone between the two glasses.

4.4.1. Analysis of *P* vs. *h* curves: effect of loading rate

The loading part of the P vs. h curve provides insights into the deformation events taking place underneath the indenter, and the smoother curve (i.e., the absence of pop-ins) indicates near homogeneous plastic flow. It has been observed in BMGs that temperature, strain rate, and structural state of the glass govern the pop-in behavior. Ramamurty and co-workers [Yoo et al., 2009; Raghavan et al., 2008; Bhowmick et al., 2006; Dubach et al., 2009b; Ramamurty et al., 2005] carried out experiments on as-cast (AC), structurally relaxed (SR), and shot-peened (SP) BMGs and observed that SP BMG exhibited the lowest number of pop-ins in the loading curves, which was attributed to the presence of high free volume and nucleation of a large number of STZs. Schuh and co-workers [Schuh et al., 2002, 2003, 2004] have developed a deformation mechanism map based on the indentation experiments with indentation strain rate and temperature as the abscissa and ordinate. According to this map, BMGs exhibit near homogeneous flow at high temperatures and high strain rates because of the dynamic relaxation processes prevalent under these experimental conditions. The post deformation images of the indentation imprints did not show any shear bands at the periphery of the impression confirming that the flow is homogenous. Jang et al., 2007 have repeated indentation experiments under similar conditions (with T and $\dot{\varepsilon}$) with a cube-corner indenter and reported shear bands at the periphery of the imprint. They argued that the stress state underneath the indenter, besides the temperature and strain rate, also has a marked influence on the nature of deformation. One of the possible reasons for this could be the *cutting* type of plastic flow mechanism observed under the cube corner indenter in contrast to the *compression* type of mechanism in a Berkovich indentation. The absence of pop-ins in NGs at all the indentation loading rates is attributed to the high free volume containing regions and abundance of STZ nucleation sites [Ritter et al., 2011]. In contrast, the decrease in the number of pop-ins in MGs with increasing loading rate is attributed to the difference in the dynamic relaxation processes around the indentation. Under low indentation loading rates, there is sufficient time for the material around the indenter to relax the structure in MG, which necessitates the nucleation of new shear bands or propagation of existing bands leading to pop-ins in the loading curve. Lack of time for the structural relaxation at high loading rates causes a local increase in free volume around the indenter, eventually leading to an absence of pop-ins in the loading curve.

4.4.2. Variation of hardness between the NG and MG

It is observed that the annealed (or structural relaxed) BMGs exhibit a higher H than the as-cast and shot-peened BMGs due to the presence of low free volume [Raghavan et al., 2008; Bhowmick et al., 2006; Dubach et al., 2009b]. Following this, it is expected that Cu-Zr NGs should exhibit a lower H as compared to MGs, contrary to the current experimental results (Table 4.3) observed in the current study. The possible reasons for this could be attributed to the (i) compositional segregation prevalent in the nanoparticles during their fabrication in NGs, (ii) increased pressure sensitivity of NGs and (iii) presence of icosahedra clusters in the interfacial regions. In $Cu_{60}Zr_{40}$ NG, a higher T_g and T_x are observed due to the segregation of Cu to the interfacial regions of GGs with the core rich in Zr [Ritter et al., 2011; Adjaoud and Albe, 2016, 2019, 2021; Nandam et al., 2017]. These Cu particles are prone to form icosahedra clusters leading to an increase in medium-range ordering (MRO) in the interfacial regions. These clusters offer greater resistance to plastic deformation, thereby increasing the H of NGs.

Recently, it has been observed that the number of clusters and their size can be varied by thermal annealing, which influences the β-relaxation kinetics and mechanical properties [Sharma et al., 2021b; Sopu et al., 2011, 2015]. Further, the high free volume present in the GIs also causes an increase in pressure sensitivity index during the plastic deformation, thereby leading to an increase in the hardness of NGs [Hirmukhe et al., 2020]. With the help of a modified expanding cavity model applicable, Narasimhan, 2004 has observed higher H in materials having higher pressure sensitivity index due to the large elasticity continuum surrounding the indentation zone.

4.4.3. Strain rate sensitivity of NGs and MGs and its structural dependence

The negative m for both the NGs and MGs shows that the deformation is heterogeneous in both the glasses, consistent with the observations reported for BMGs [Dalla Torre et al., 2006; Jiang et al., 2007; Mukai et al., 2002; Dubach et al., 2009a; Gonzalez et al., 2011]. Between the two, NGs exhibit more positive m values as compared to the MGs, and these differences in m are attributed to the variation in the internal microstructures. In both NG and MG, the fundamental carriers of plasticity are STZs, but they differ in their number density, and the volume (number of atoms present in the STZ). Pan et al., 2008 have measured the STZ volume and number of atoms present in the STZ for a number of BMGs using the co-operative shearing model (CSM). For a $Cu_{60}Ti_{25}Hf_{15}$ (which is stoichiometrically closer to the glasses used in the current study), the STZ volume is 4.23 nm^3 with 359 atoms. After rigorous evaluation of the indentation impressions, Bhattacharya et al., 2015 noticed that the positive m in BMGs is indeed an experimental artifact due to the pile-up of the material around the impression. Choi et al., 2012 have later computed the STZ volume for an as-cast and annealed Zr-based BMG (Vit 105), considering the first pop-in load which is found to be 0.347 and 0.464 nm^3, respectively, suggesting that structural relaxation increases the size of STZ. Using the same procedure, Tao et al., 2021 analyzed the STZ size in a $Zr_{50}Cu_{40}Al_{10}$ BMG in three different structural states (as-cast, annealed, and plastically deformed) and observed it to be 0.43, 0.55, and 0.34 nm^{3,} respectively. These studies clearly show that STZ size depends on the structural state, which decreases with decreasing free volume content. Nandam et al., 2017 have also computed the STZ volume in $Cu_{50}Zr_{50}$ NG and MG as 7.41 and 1.93 nm^3, respectively, based on the positive m value, which are much higher than the predictions of BMG. One of the possible reasons for this could be due to the high nanoindentation load (25 mN) and the use of

Table 4.3 Summary of nanomechanical properties and elastic recovery obtained from the analysis of load, *P* vs. displacement, *h* curves

Strain rate, s^{-1}	Nanohardness, *H* (GPa)		Elastic modulus, *E* (GPa)	
	NG	MG	NG	MG
0.03	7.63 ± 0.10	6.25 ± 0.12	109 ± 1.8	91.8 ± 1.5
0.05	7.56 ± 0.15	6.16 ± 0.10	112 ± 1.0	92.6 ± 1.2
0.1	7.43 ± 0.12	5.93 ± 0.12	112 ± 2.5	91.3 ± 2.2
1	6.90 ± 0.15	5.60 ± 0.11	112 ± 1.5	94.5 ± 1.0

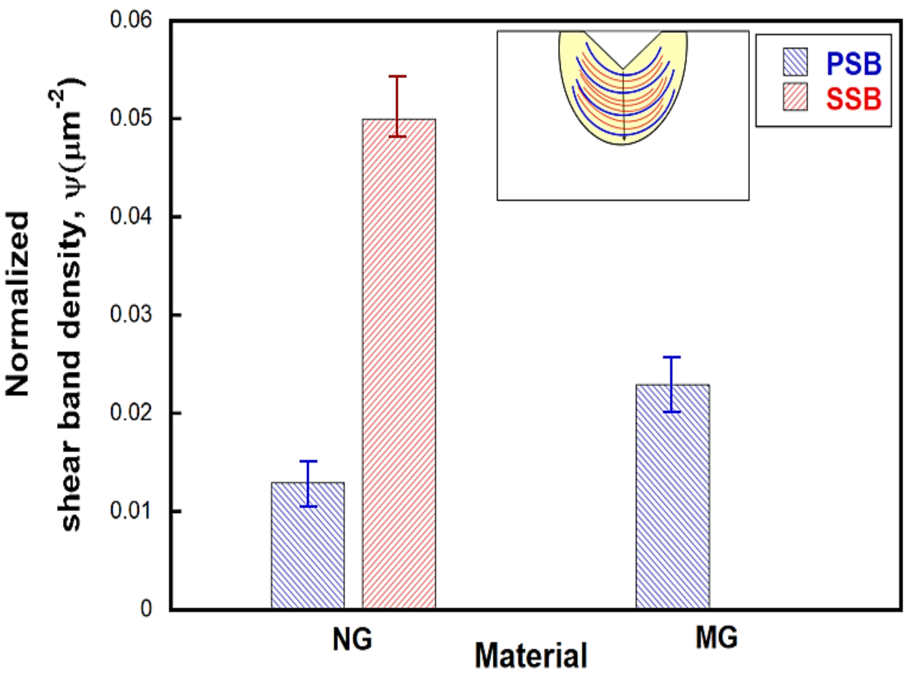

Figure 4.8 Variation of normalized primary and secondary shear band density, Ψ, in the subsurface deformation zone for NG and MG.

H not corrected for *pile-up*. Since the NGs do not contain *pop-ins* in the loading curve, it is impossible to compute the STZ volume based on the first pop-in load, which also implies that the STZ volume in NGs must be much smaller than the ones predicted for severely deformed BMG. The subsurface deformation zone presented in Figs. 4.6 and 4.7 (performed under identical loading conditions) highlights the relative difference in shear band characteristics between the MGs and NGs, although it is not a true representation of constrained indentation based on which the m values are computed. The shear band density, Ψ, is calculated as the number of primary and secondary shear bands (PSBs and SSBs, respectively) per unit deformation area and plotted for NG and MG in Fig. 4.8. It is observed that the Ψ of PSBs in NG, unlike MGs, is very small compared to the SSBs. The increased Ψ of SSBs is indicative of a large number of STZ nucleation sites, thereby reducing the propensity of heterogeneous deformation. In a nutshell, the less negative m values of NG indicate an increased tendency for homogeneous nature deformation, which could be attributed to the high free volume (and concomitant availability of a large number of STZs). A detailed investigation of the STZ size in NGs is warranted to understand the origins of reduced m values further. Advanced characterization techniques are needed to resolve further the STZ volume in NGs, which may provide further insights into the deformation behavior of NGs and ways to enhance the plasticity of glasses.

4.5. Summary

$Cu_{60}Zr_{40}$ nano- and metallic glasses are synthesized using IGC and melt spun technique, respectively, and their strain rate sensitivity over three decades of strain rates is investigated using nanoindentation. Further, the deformation characteristics in the subsurface deformation zone are analyzed using bonded interface indentation. The following conclusions can be drawn from the current results:

- The serrated flow in the loading curves of MGs decreases with an increase in loading rate while it does not have any effect on the NGs. NGs do not exhibit serrated flow at any indentation loading rate.
- The hardness of both the NG and MG decreases with increasing loading rate implying negative strain rate sensitivity, m. The m values of NG are higher than the MG, indicating a tendency towards the near homogeneous plastic flow. Despite the high hardness in NGs, the high free volume is due to icosahedra clusters present at the interfaces.
- The primary shear bands (PSBs) are the main carriers of plastic flow in MG, while in NG, owing to the high free volume, it is by secondary shear bands (SSBs). The relatively positive m in NG compared to the MG is attributed to a large number of fine shear bands and near homogeneous plastic deformation.

CHAPTER 5

Role of Indenter geometry on the deformation behavior in a PdSi metallic and nanoglass

Abstract: In this work, a series of nanoindentation experiments were conducted between a binary PdSi metallic glass (MG) and nanoglass (NG) using Berkovich and cube-corner indenters having different centreline-to-face angles. A strong dependence of serrated flow behavior on the indenter angle is observed in MG and NG. The sharp cube-corner indenter displaces a greater volume of material for a given load (more than three times the Berkovich indenter), and the material deforms by a cutting mechanism, resulting in prominent serrations in the loading curves and higher pile-up. For a given geometry of the indenter, NG displays lower hardness than MG owing to the lower segregation effect, and the hardness decreases with the increase in maximum indentation load, which signifies the indentation size effect (ISE). The rise in the deformation volume underneath the tip due to an increase in free volume content with indentation load appears to be the reason for the ISE. A useful parameter, discrete plasticity ratio, Ψ is utilized to estimate the influence of serrations on the total plastic deformation. It is observed that Ψ does not change significantly with the load, indicating that the deformation mode remains the same with either of the indenters in both MG and NG (i.e., heterogeneous in MG and homogeneous in NG. The results are explained in terms of primary concepts for enlightening the examination of the deformation behaviors in the MG and NG with different indenter geometry*.

5.1. Introduction

The deformation behavior of crystalline materials is controlled by dislocations and the presence of which contributes to an increase in plasticity but substantially reduces the strength of the crystalline materials. With this consideration Klement et al. 1960 have developed metallic glasses (MGs) by rapidly cooling the alloys so that their crystallization kinetics gets arrested and thus leading to amorphous structure.

*The work presented in this chapter is submitted in the following publication:

A. Sharma, A. Tripathi, S. H. Nandam, H. Hahn, K. E. Prasad. Role of Indenter geometry on the deformation behavior in a PdSi metallic and nanoglass (Under Review- *Journal of Alloys and Compounds*).

These MGs exhibit strength values an order of higher than the crystalline alloys of identical composition, high hardness, wear resistance, excellent corrosion resistance (due to the absence of grains and grain boundaries) and magnetic permeability [Schuh et al., 2007; Inoue et al., 2003; Ashby and Greer, 2006]. However, these alloys suffer from room temperature ductility due to the absence of dislocations although they exhibit super plastic behavior (showing extensive elongations) at temperatures close to glass transition temperature [Prasad et al., 2007, 2012; Singh et al., 2012]. This atypical behavior of MGs is attributed to the fundamental units of plastic flow carriers which are typically referred to as shear transformation zones (STZs). The STZs are a cluster of atoms that accommodate shear strain by atomic shuffling rather than the linear motion (contrary to the dislocation motion) in the direction of applied shear stress [Spapepen 1977; Argon 1979]. At room temperature and high applied stresses, the deformation (at the macroscopic level) occurs by nucleation and propagation of shear bands with the failure taking place via a dominant shear band. The unhindered propagation of shear bands can be controlled if the plastic strain is allowed to distribute in multiple shear bands. This can be achieved by increasing the free volume and distributing it in the entire volume of the sample. Nanoglasses comprising of glassy grains (GIs) separated by glass interfaces (GIs) appears to provide extensive tensile elongations [Gleiter, 2013]. The limited experimental results show that profuse secondary shear bands in NGs compared to the MGs of identical compositions and the molecular dynamic (MD) simulations shows that the presence of GIs will enable increased nucleation sites for shear bands [Adjaoud et al., 2016, 2019; Ivanisenko et al., 2018; Hirmukhe et al., 2020, 2022; Guo et al., 2019; Nandam et al., 2017, 2020; Sharma et al., 2021, 2022]. A detailed experimental investigation of the effect of temperature, stress state, and strain rate on the mechanical behavior of NGs under various external conditions will provide further insights in understanding the differences in deformation mechanisms in NG and MGs.

Sharma et al. 2022 investigated the effect of strain rate on the deformation behavior of NGs and MGs and observed that the strain rate sensitivity of NGs is more positive than the MGs of identical composition. Another important factor that influences the deformation mechanisms is the stress state and strain distribution underneath the indenter which strongly depends on the indenter geometry. Mulhearn, Tabor, and co-workers [Tabor 1951, Mulhearn 1959] have conducted indentation experiments with indenters having different apex angles, α and studied plastic flow mechanisms underneath them. Their observation suggests that the plastic flow mechanism changes from compressive to cutting nature for α glower than 55°. Jang and co-workers [Jang et al., 2007; Yoo et al., 2007] have carried out the nanoindentation experiments on Zr-based BMG at different strain rates using Berkovich and cube-corner indenters and showed that the indentation load, *P* vs. penetration depth, *h* curves of cube-corner indentations show *pop-ins* at all the strain rates which is the not the case with Berkovich indenter. The possible reason for this was attributed to the high indentation pressure under the cube-corner indenter as compared to the Berkovich indenter. However, the effect of compression and cutting mechanisms on the flow mechanisms around the indenter for amorphous alloys such as BMGs and MGs was not highlighted and discussed in detail. Even the experimental studies conducted on NGs are also limited only to Berkovich and Vickers indenters which exhibit a compressive flow mechanism. It would be interesting to examine the plastic deformation behavior of NGs using a cube-corner indenter and characterize the *P-h* curves, indentation size effect, and pile-up around the indentation. Therefore, in the current study, we have carried out nanoindentation experiments on a binary MG and NG (having identical composition) using Berkovich and cube-corner indenters and studied the effect of indenter geometry on the characteristics of the *P-h* curves, differences in indentation size effect in hardness between the two indenters as well as the samples, the effect of plastic flow mechanisms on the pile-up around the indenter.

5.2. Material and experiments

$Pd_{80}Si_{20}$ NG samples are prepared by magnetron sputtering technique in an inert-gas condensation (IGC) chamber, whereas the MG samples are synthesized using melt spinning technique with binary $Pd_{80}Si_{20}$ alloy as a sputtering target. The NG and MG samples used in the current experiments are in an as-prepared state without prior annealing after their fabrication. The NG samples are disc-shaped with a thickness of ~0.4 mm and a diameter of 8 mm while the MG samples have a thickness of 30-40 μm, a width of ~1 mm, and a length of 10-20 mm. X-ray diffraction (XRD) analysis confirms the amorphous nature of the glasses (as shown in Fig. 5.1a) while the glass transition temperature is obtained by performing differential scanning calorimetry (DSC) analysis and a representative DSC scan is presented in Fig. 5.1b. Before proceeding with the indentation experiments, the surface of the samples is polished to a mirror finish by utilizing the standard metallographic technique. Nanoindentation tests are conducted at room temperature on NG and MG using a Hysitron Triboindenter. Two different types of indenters Berkovich and Cube-corner are used for the nanoindentation experiments. The included between the centerline-to-face angles for Berkovich and cube-corner indenters are 65.3^{o} and 35.3^{o}, respectively resulting in different indenter strains in the subsurface deformation zone. The area function of both the indenter tips is calibrated using the standard sample of quartz, and the thermal drift is maintained at 0.05 nm/s. The indentations are performed within the load range of 2 to 8 mN in a load-controlled mode.

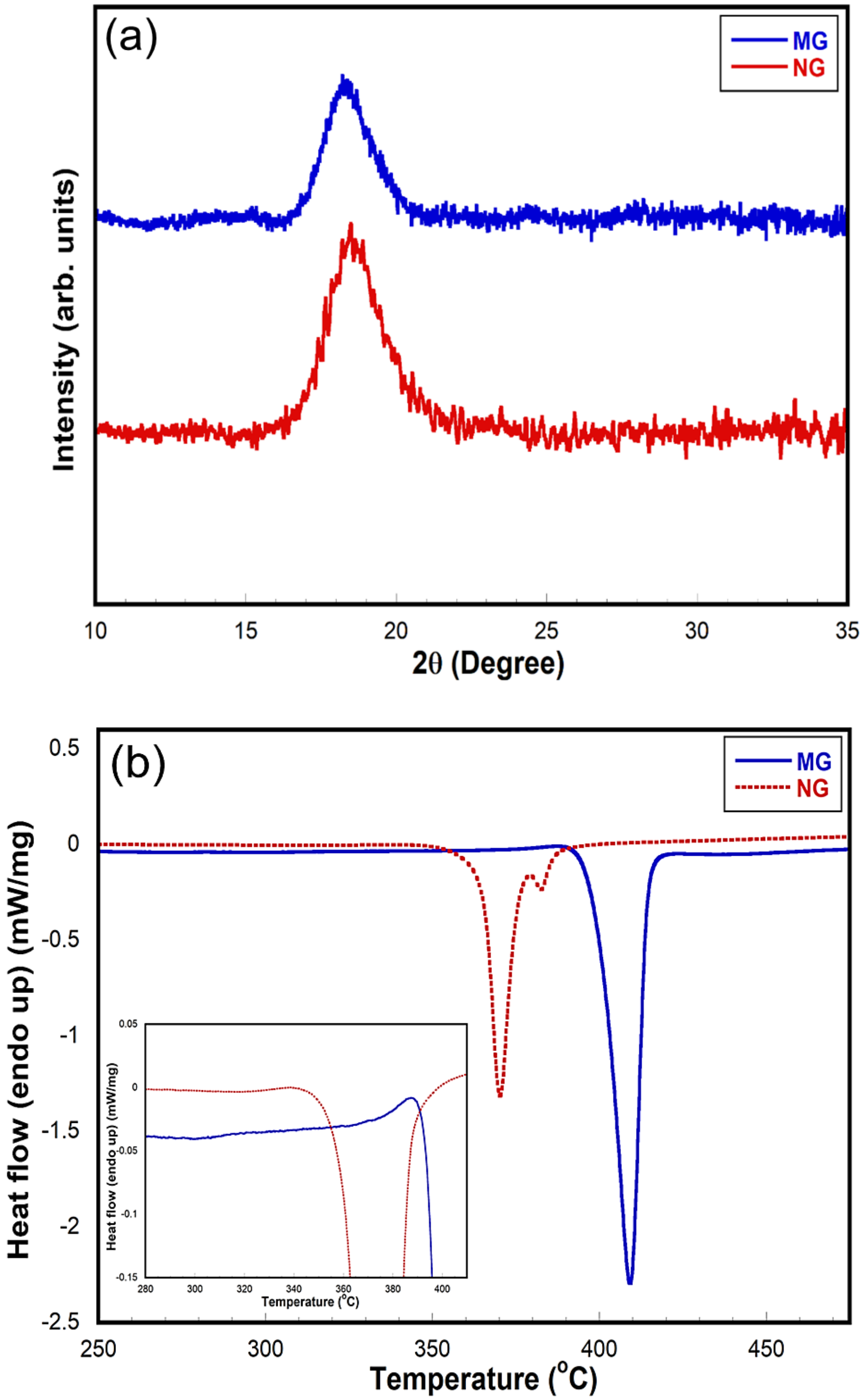

Figure 5.1 (a) X-ray diffraction spectra, and (b) DSC curves of the MG and NG samples (The inset figure in DSC displays the magnified image of the glass transition region).

The loading and unloading rates are kept constant at around 1mN/s, and with a dwell time of 2 s at maximum indentation load, P_{max}. A minimum of (3 x 3) array of 9 indents is made at each P_{max} to obtain reliable data. To prevent the strain filed interaction, a distance of ten times the maximum indentation depth is kept between the successive indents. The hardness, *H*, is determined with the help Oliver and Pharr (O&P) method given by the following equation [Oliver and Pharr 1992, 2004]:

$$H = \frac{P_{max}}{A_c} \qquad (1)$$

where P_{max} is the maximum indentation load, and A_c is the projected area of contact, which is a function of contact depth, h_c. As per the O&P method, the h_c is calculated as:

$$h_c = h_{max} - \mu \frac{P_{max}}{S} \qquad (2)$$

Here, h_{max} is the maximum penetration depth, μ is the geometry constant (~0.75, for Berkovich and Cube-corner indenter), and S is the stiffness computed from the slope of the unloading part of the *P* vs. *h* curve. The elastic modulus, E, of the samples is obtained using the equation (3):

$$E_s = (1 - \nu_s^2)\left[\left(\frac{2\sqrt{A_c}}{S\sqrt{\pi}}\right) - \left(\frac{1-\nu_i^2}{E_i}\right)\right]^{-1} \qquad (3)$$

where *E* and ν represent the elastic modulus, and Poisson's ratio and the subscripts i and s refer to the indenter and specimen, respectively. Scanning electron microscopy (SEM) and atomic force microscopy (AFM) are used to examine the indentation imprints and their deformation morphology.

5.3. Results

5.3.1. Indentation load, *P* vs. displacement, *h* curves

The representative *P vs. h* curves for MG and NG obtained using Berkovich indenter are displayed in Figs. 5.2a and b respectively. The loading curves performed at different indentation loads agree well with each other confirming the homogeneity of the material (refer to Supplementary data). The loading curves obtained using Berkovich indentation exhibit contrasting behavior between MG and NG with the loading curves of MG (Fig. 5.2a) exhibiting serrated flow manifested by large number of *pop-ins*, while no noticeable *pop-ins* in NG curves. These observations are consistent with the literature studies reported on MGs and NGs with the Berkovich indenter [Nandam et al. 2017, 2020; Sharma et al. 2020, 2022].

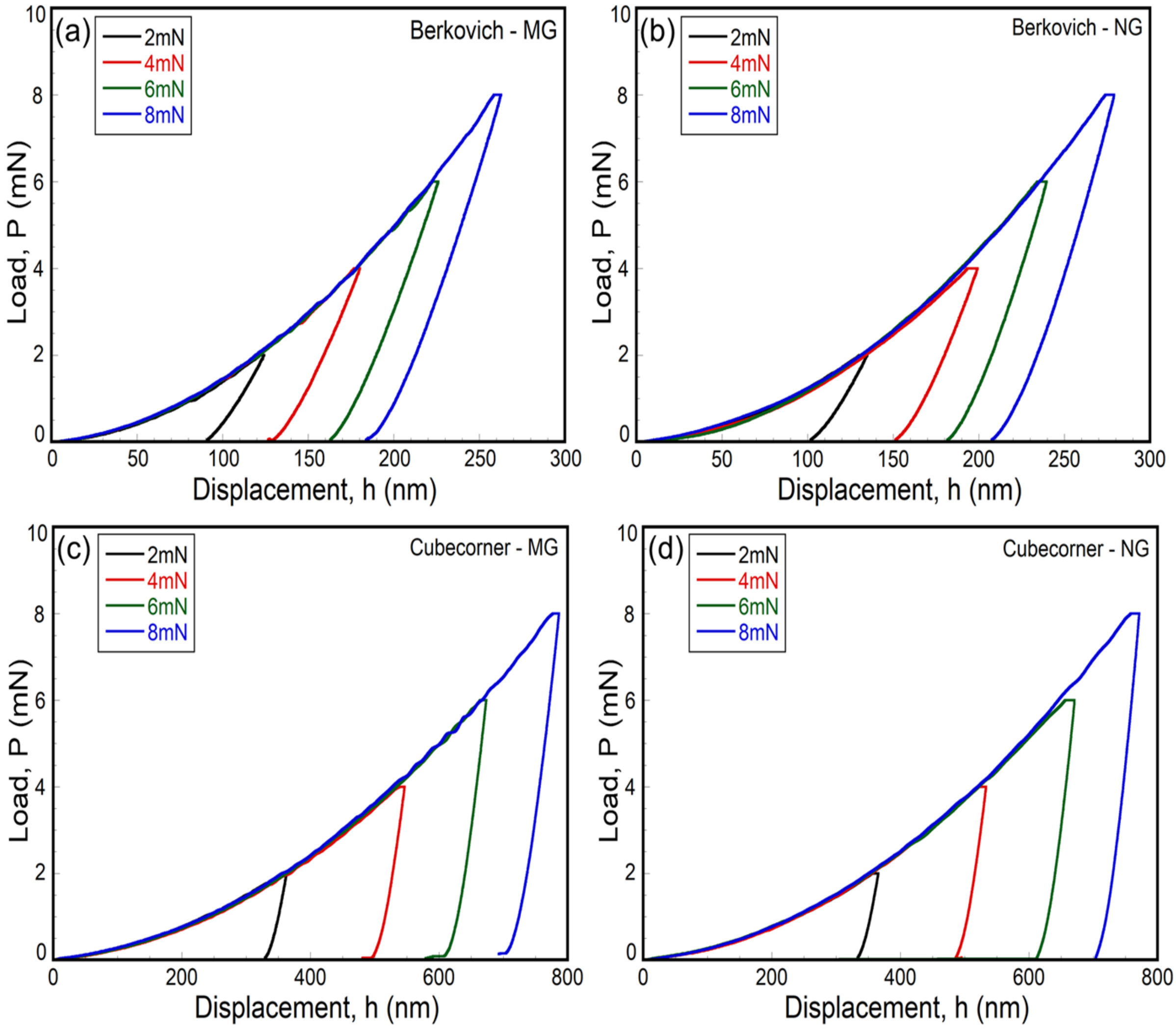

Figure 5.2 Typical load, *P* vs. displacement, *h* curves obtained with Berkovich and cube-corner indenters at different peak loads for (a, c) MG and (b, d) NG, respectively.

The absence and presence of pop-ins can directly be attributed to the nature of SBs in the subsurface deformation zone. Sharma et al. 2021 have carried out bonded interface indentation experiments on a Pd-Si MG and NG and observed that the plastic deformation underneath the indenter in MG is accommodated by primary shear bands having a large interband spacing while for NGs, it is predominantly by fine secondary shear bands (SSBs) having small interband spacing. It appears that the presence of PSBs leads to serrated flow in *P-h* curves while the machine is unable to capture the *pop-ins* occurring due to SSBs. The *P-h* curves for MG and NG generated with Cube-corner indenters are shown in Figs. 5.2c and d, respectively. Interestingly, unlike Berkovich indenter, the *P-h* curves obtained using the Cube-corner indenter show serrated flow even for NGs. Besides this, the h_{max} at any given *P* for the cube-corner indenter is nearly 3 times higher than that observed for Berkovich indenter. One of the possible reasons for this could be due to the increase in stress intensity ahead of the Cube-corner indenter tip as compared to the Berkovich indenter which will be discussed in detail in the next section. To visualize the pop-ins more clearly, the loading curves corresponding to P_{max} of 8 mN is plotted for Berkovich and Cube corner indenters in Figs. 5.3a and b respectively along with the corresponding dP/dh with h in Figs. 5.3c and d.

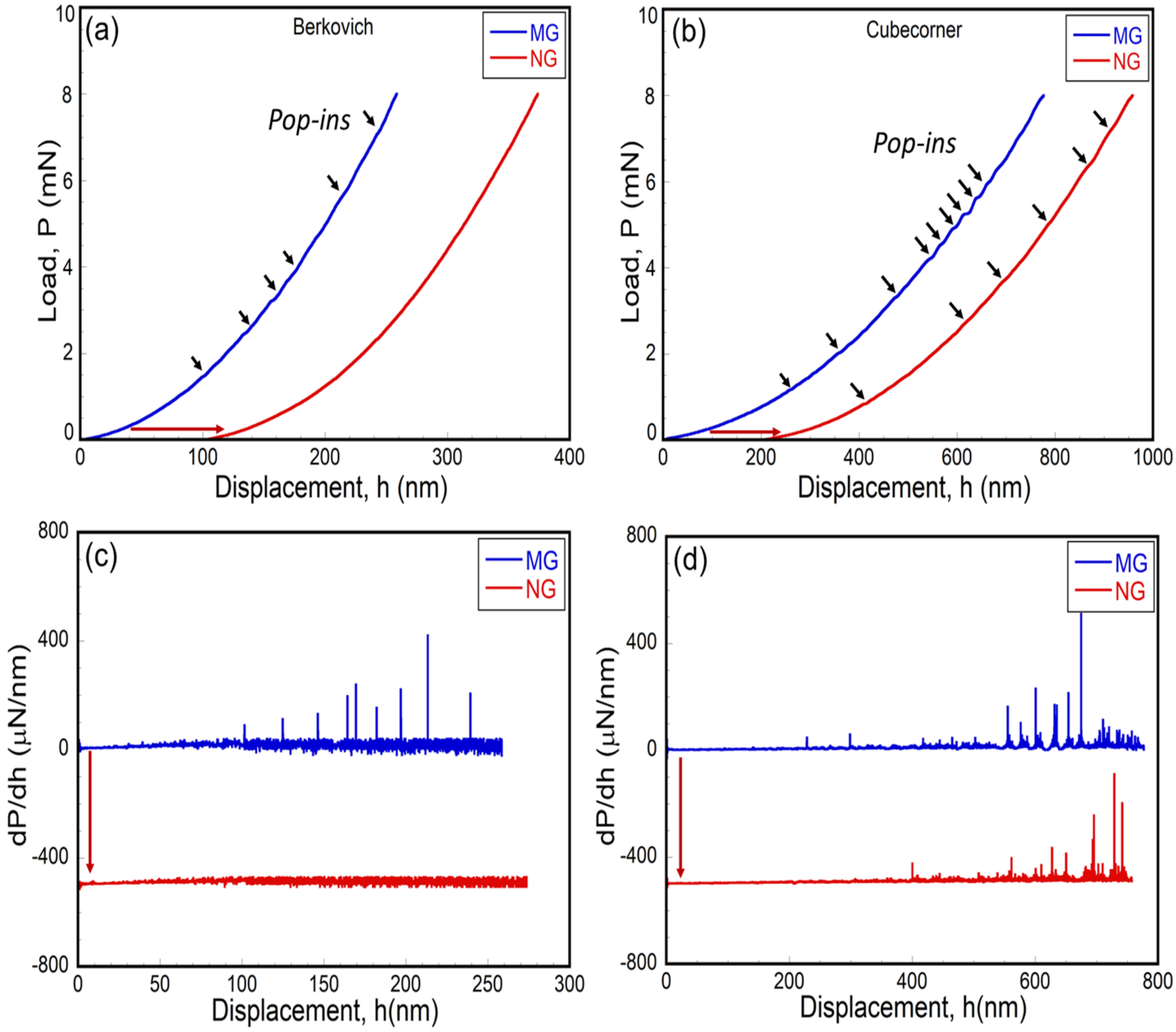

Figure 5.3 Representative loading portion of the $P - h$ curves obtained at P_{max}=8mN and corresponding derivative plots representing the variation of dP / dh with h for MG and NG with (a, c) Berkovich and (b, d) cube-corner indenter, respectively.

The loading curves of the NG are displaced along *x-axis* while the dP/dh of MG along the *y-axis* for clarity. The following observations can be made from these Figs. 5.2 and 5.3: (i) The number of *pop-ins* and *pop-in* width of MG is higher for Cube-corner than the Berkovich indentation (ii) The significant spikes observed dP/dh with h plots indicate the increase *pop-in* width (vis-à-vis SB nucleation and propagation) which is more pronounced in the Cube-corner indentation (iii) The loading curves of Berkovich indentation made with NG do not clearly shows any *pop-ins* concomitant with no noticeable spikes in dP/dh vs. h plots. (iv) The intensity of spikes in the dP/dh vs. h plots increases in the Cube-corner indentations which appears to be more pronounced at large penetration depths.

5.3.2. SEM and AFM analysis of indentation imprints

Figs. 4a and b illustrate the SEM images of the Berkovich indentation imprints of MG and NG, respectively while Figs. 5.4c and d of MG and NG shows the imprints made of cube-corner indenter. The SBs are observed at all the edges of Berkovich indentation imprints for MG (Fig. 5.4a) while one of the edges of the imprint shows signatures of SBs in the case of NG.

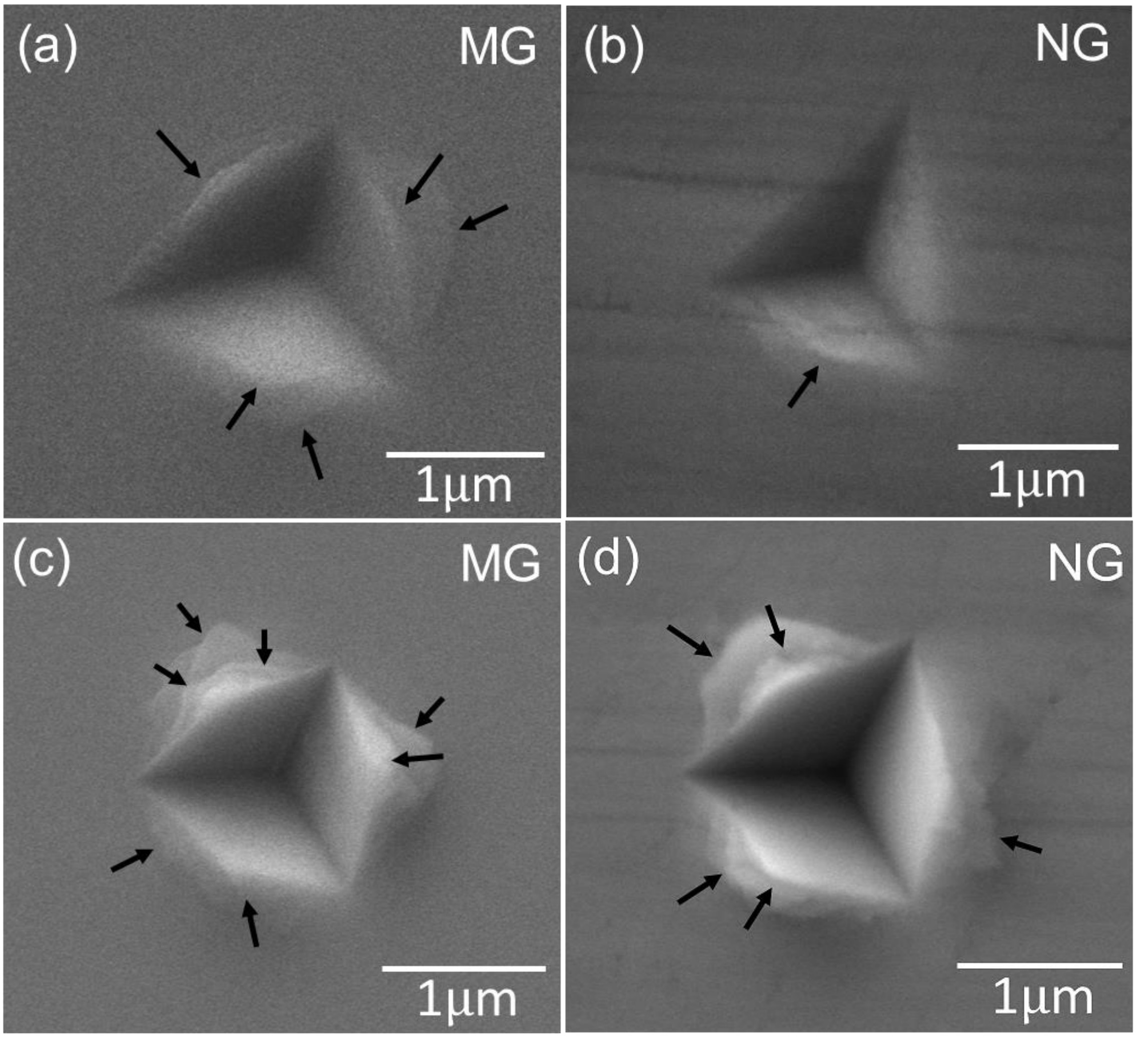

Figure 5.4 Representative SEM images of nanoindentation imprints for MG and NG with (a, b) Berkovich and (c, d) cube-corner indenter, respectively.

These observations are consistent with the indentation studies performed on PdSi MG and NG [18-19]. On the other hand, profuse number of SBs are observed in MG and NG around the periphery of the cube-corner indent imprint (Fig. 5.4c, d). AFM and profilometry analysis are conducted on the Berkovich and Cube-corner indentation imprints (obtained at P_{max} of 8 mN) to characterize *pile-up* height and the depth of penetration and is displayed in Figs. 5.5 and 5.6.

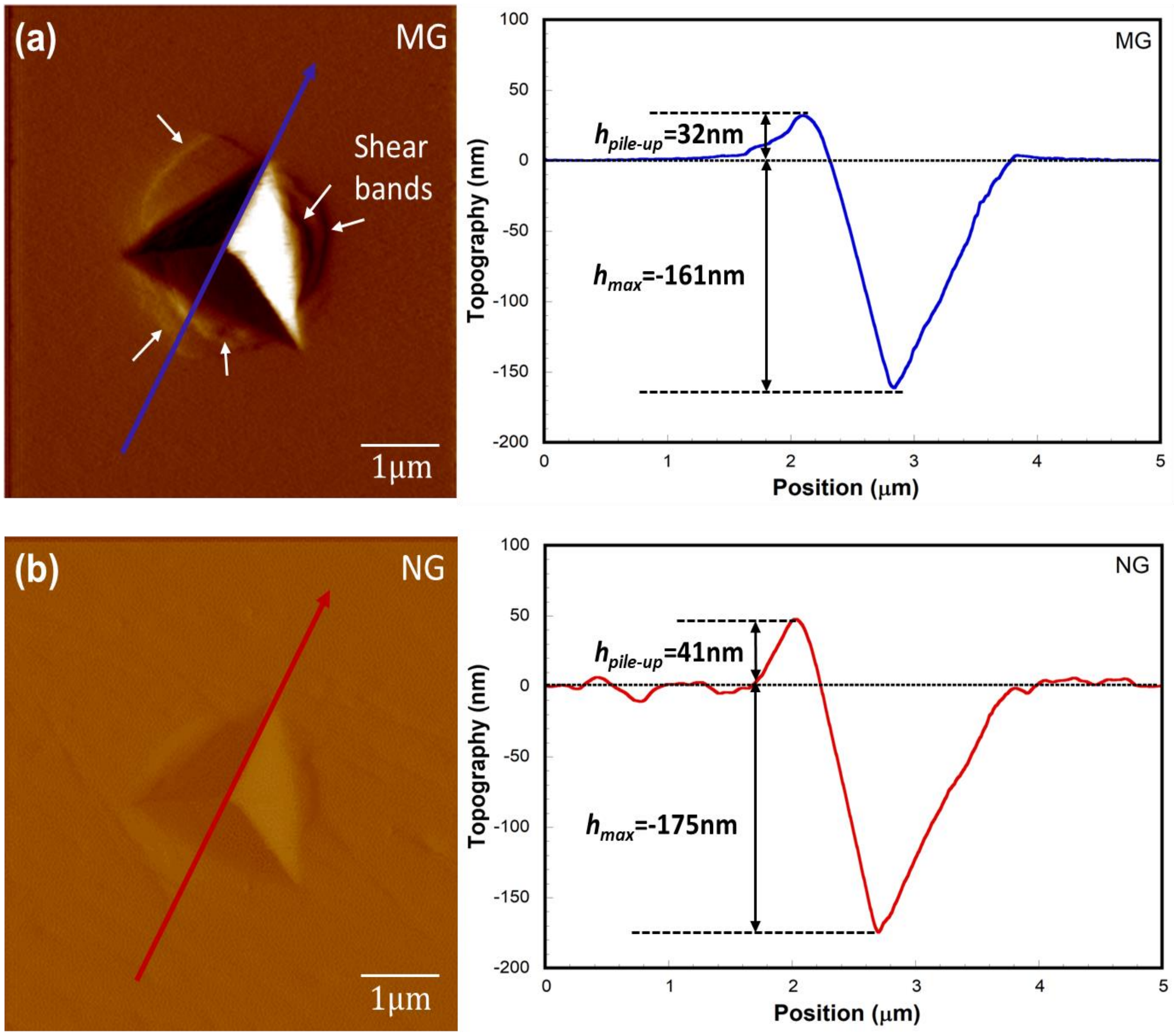

Figure 5.5 AFM images of the Berkovich indentation imprints and the corresponding line scans taken across the edge of the imprint of (A) MG and (B) NG obtained at a P_{max} = 8 mN.

The AFM images of the Berkovich indentation imprints for MG and NG (Figs. 5a and b, respectively) agree with SEM images and the profilometer analysis shows that the pile-up height ($h_{pile-up}$) is about 32 nm and 41 nm for MG and NG, respectively. The h_{max} for MG and NG is reported to be 161 nm and 175 nm, respectively (which is nearly 4-5 times the $h_{pile-up}$) indicating that the latter is relatively softer than the former. The AFM images of the Cube-corner indentation imprint (Fig. 5.6) displays large number of SBs at the periphery of the impression. The $h_{pile-up}$ of MG and NG in this case are about 246 nm and 265 nm with the corresponding h_{max} as 518 and 533 nm (which is nearly 2 times the $h_{pile-up}$), respectively. A comparison of $h_{pile-up}$ and h_{max} of Berkovich and Cube-corner indenters shows that the increase in $h_{pile-up}$ is significantly high (about 6 – 7 times) in contrast to the increase in h_{max} which is only about 3 times.

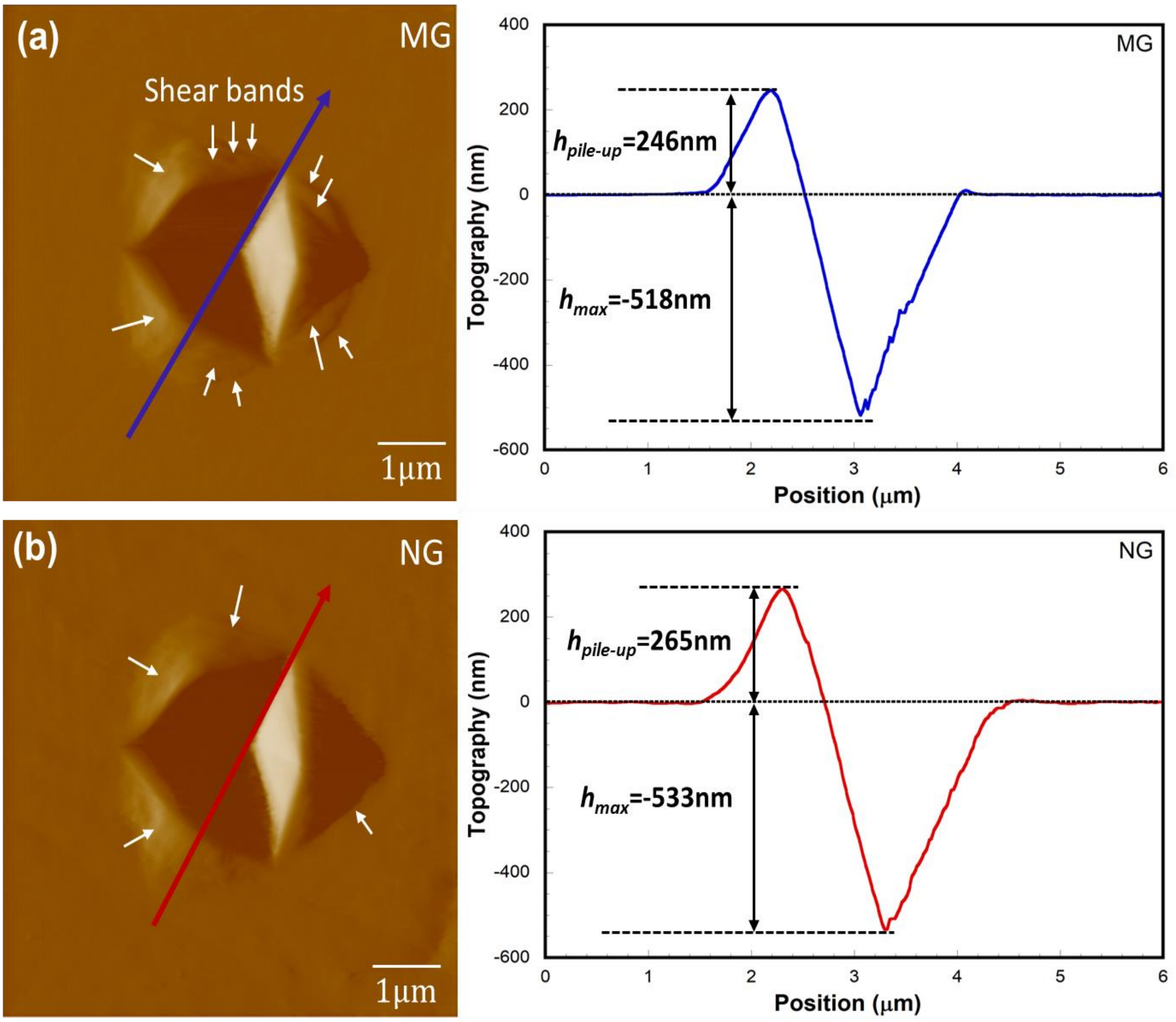

Figure 5.6 AFM images of the Cube-corner indentation imprints and the corresponding line scans taken across the edge of the imprint of (A) MG and (B) NG obtained at a P_{max} = 8 mN.

5.3.3. Effect of indenter geometry on the hardness

Figures 5.7a and b represent the variation of nano-hardness of MG and NG with P_{max} for Berkovich, and Cube-corner indenter, respectively. The hardness calculated with the O&P method is shown by dotted lines. Due to the pile-up observed around the indent imprint (Fig. 5.5, 5.6) O&P method overestimates the hardness and it needs to be corrected for pile-up. The pile-up corrected hardness is computed as the ratio of indentation load and projected area of the impression (which is obtained from the indentation imprint). The pile-up corrected hardness is plotted against the P_{max} and is shown in Figs. 5.7a and b as the solid lines.

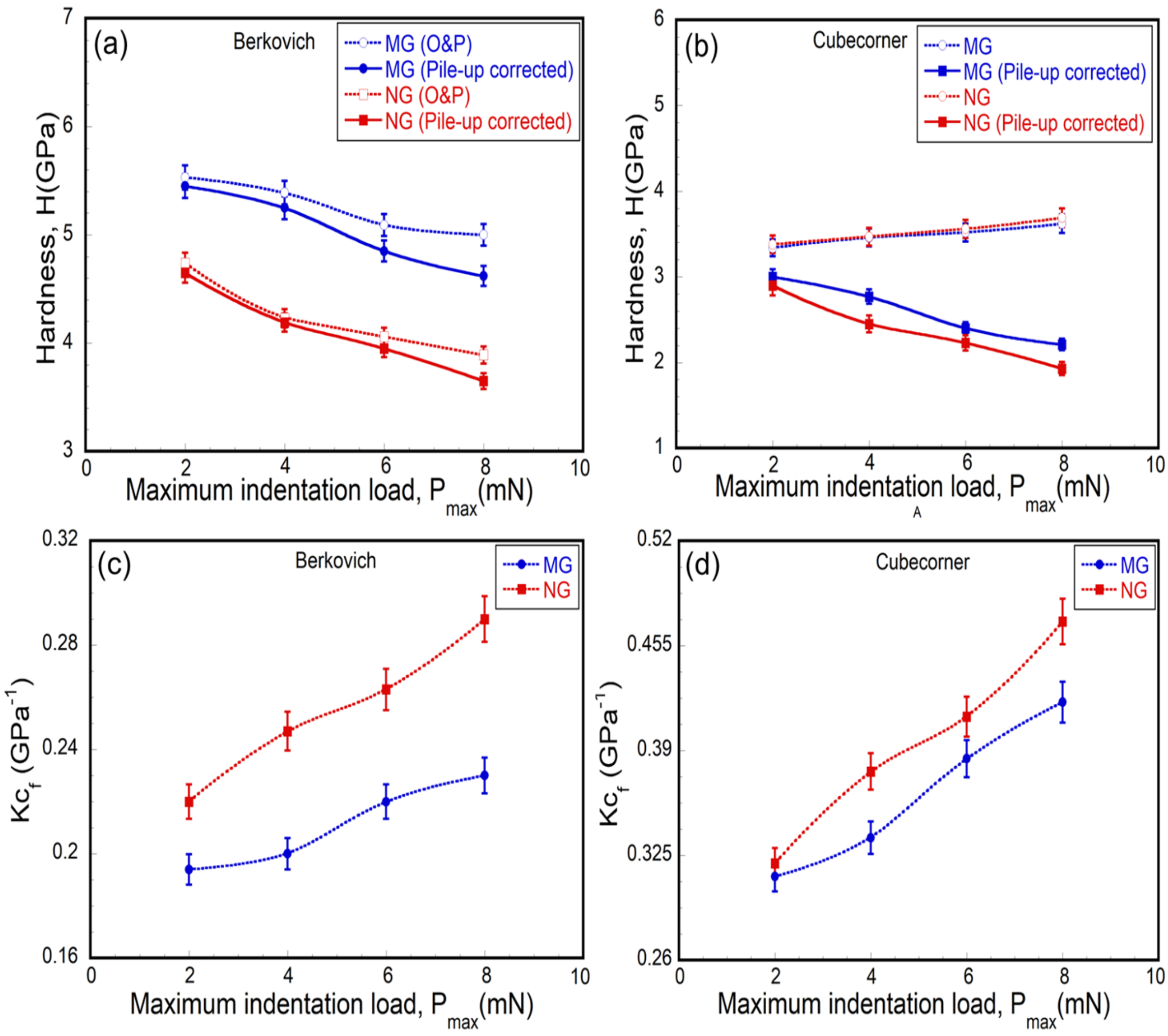

Figure 5.7 Plot showing the variation of (a, b) hardness, H, and (c, d) free volume, Kcf, with maximum indentation load, Pmax for MG and NG with Berkovich and cube-corner indenter, respectively.

It is evident from Fig. 5.7a that the hardness of MG is higher than the NG for Berkovich indentation. The results are in concurrence with the observations of Nandam et al. 2020 on Pd-Si glass having identical composition. Both the glasses display indentation size effect (ISE) in hardness and the reasons for this could be attributed to the ease of SB nucleation with increasing P_{max} due to the increase in indentation volume. Unlike Berkovich indenter, the O&P hardness (not corrected for pile-up) of cube-corner indentations displays similar hardness for both MG and NG. Besides this, the O&P hardness also increases with increase in P_{max} as shown in Fig.

5.7b (with dotted lines) which could be due to the increase in pile-up with indentation load. The hardness corrected by taking the *pile-up* into consideration and is plotted with P_{max} in Fig. 5.7b as displayed by solid lines. The *pile-up* corrected hardness shows a higher hardness in MG than NG and also the ISE is observed in both glasses consistent with the trend observed Berkovich indentations.

5.4. Discussion

5.4.1. Analysis of *P-h* curves, serrated flow, and Pile-up around the indenter

The deformation events taking place beneath the indenter during the application of load is manifested as *pop-ins* in the loading curves and the presence of which is related to the nucleation and propagation of SBs of noticeable size while their absence to the fine or no SBs. The presence of large number of STZs in the GIs and GGs (in the case of NGs) offers more SB nucleation sites leading to the formation of fine SBs (and the absence of pop-ins) under Berkovich indenter which is not the case with Cube-corner indenter. *The interesting question here as to why there is an increased propensity of pop-ins in cube-corner indenter as compared to the Berkovich indenter?* The stress state ahead of the indenter, pressure distribution underneath the indenter, and the plastic flow mechanisms taking place in the subsurface deformation zone play a vital role in controlling the *pop-in* characteristics. Sneddon 1965 has proposed that the pressure distribution under a rigid conical indenter is given by:

$$p(r) = \frac{E}{2(1-\nu^2)} \frac{\cosh^{-1}(a/r)}{\tan\varphi}, \quad 0 \le r \le a \qquad (4)$$

where E and ν are the Young's modulus and Poisson's ratio of the material, φ is the semi-apex angle of the indenter, r is the radial coordinate on the surface, and a is the contact radius. The equation shows for any a and r, a higher pressure is generated for the indenter having a smaller φ as compared to the indenter having a larger φ. Prasad et al. 2011 investigated the effect of φ on the subsurface deformation and observed that the subsurface deformation zone is elliptical at φ ~ 55° and tends to hemispherical with increasing φ. Their results also reveal that, for any given indentation load, the material just underneath the indenter experiences a higher plastic strain at low φ as compared to high φ. From the indenter geometry, the Cube-corner indenter having a lower φ as compared to the Berkovich indenter and hence records a greater penetration depth for a given indentation load. This is the possible reason for both the glasses exhibiting a lower hardness with the Cube-corner as compared to the Berkovich indenter. Similarly, the volume of material just beneath the indenter experiences a greater plastic strain under the Cube-corner indenter than the Berkovich leading to an increased SB activity in subsurface deformation zone and thus causing serrated flow in the loading curves.

Estimating the contribution of serrated to flow to the total plastic deformation will provide insights into the nature of plastic flow which is expressed by the discrete plasticity ratio (Ψ). Ψ is defined as the ratio of pop-in displacement, Δh_{dis} to the total displacement, h_{tot} which is obtained by the summation of Δh_{dis} and continuous displacement, Δh_{con}.

$$\Psi = \frac{\Delta h_{dis}}{\Delta h_{con} + \Delta h_{dis}} \qquad (5)$$

Fig. 5.8 represents the variation of Ψ with maximum indentation load. Schuh and Nieh 2002, 2003, 2004 performed nanoindentation experiments on various BMGs and showed that Ψ decreases with indentation loading rate from 0.9 to nearly "zero" indicating absence of serrated flow with loading rate. Later Jang et al. [Jang et al., 2007; Yoo et al., 2007] have shown that this is an experimental artefact and serrated flow depends on the indenter geometry and sharpness of the indenter. For a Zr-based BMG, they observed Ψ is independent of loading rate and is in the range of 0.4-0.7 for Berkovich and 0.75-0.95 for a cube-corner indenter.

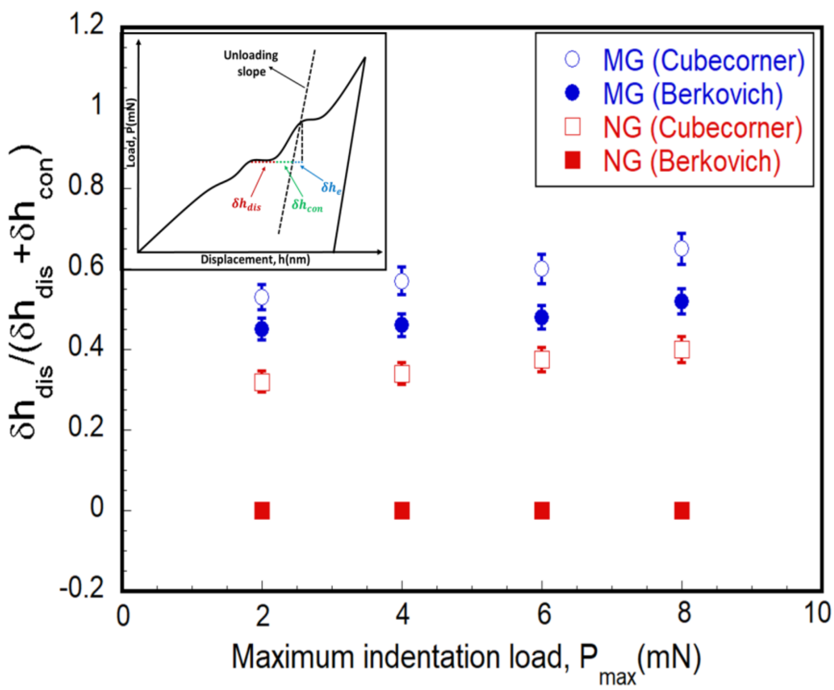

Figure 5.8 Plot showing the variation in the discrete plasticity ratio, Ψ with the maximum indentation load, Pmax for MG and MG with Berkovich and cube-corner indenter.

The Ψ values for MG computed in the current study lie in the range of 0.53-0.61 for cube-corner indentation and 0.45-0.50 for Berkovich indentation indicating that under both the indenters, the deformation is largely accommodated by the PSBs and the intensity of PSBs increases with cube-corner indentations. While for NG, Ψ is in the range of 0.32-0.40 for cube-corner indentation and almost negligible for Berkovich indentation suggesting that the deformation under cube-corner indentation is more heterogeneous and is likely to be accommodated in PSBs. A detailed experiments characterizing the subsurface deformation zone under sharp indenters as well as hardness mapping of underneath the indentation provide more insights about the shear band characteristics and free volume evolution underneath the sharper indenters.

The *pile-up* around the indentation impression is significantly influenced by the strain hardening characteristics of the material and the nature of plastic flow under the indenter which in turn is governed by the indenter geometry. In case of highly strain hardened materials (with very low strain hardening exponent), the material in the subsurface deformation zone (in the elastic continuum) cannot accommodate the plastic flow and thus leading to escape of the materials between the indenter and sample surface resulting in pile-up. Mulhearn and co-workers [Mulhearn 1959] and recently Prasad et al. 2011 have shown that the plastic flow mechanism underneath the indenter changes from compression to cutting mechanism with decreasing φ (particularly when $\varphi < 55°$). Both the mechanisms are explained with the help of a schematic as shown in Fig. 5.9.

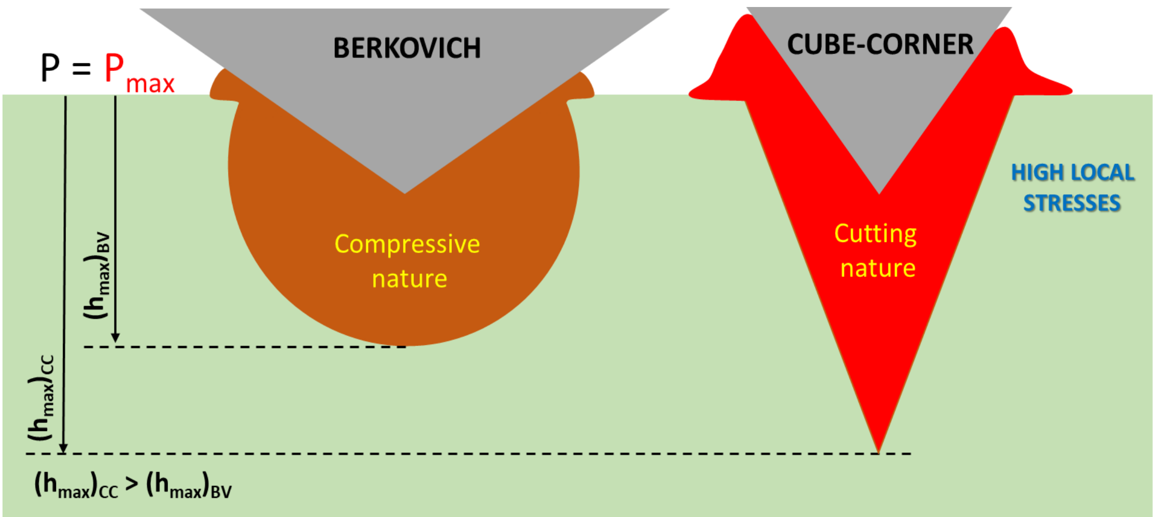

Figure 5.9 Schematic of nanoindentation-probed volume, pile-up effect and deformation mechanism for Berkovich and cube-corner indentation.

In the compressive mechanism (typically observed in Berkovich, Vickers, spherical, and other blunt indenters), the material displaced by the indenter gets either accommodated by the radial expansion of elastic continuum (for high strain hardening materials) surrounding the plastic zone or by means of pile-up of material around the indenter (for low strain hardening materials). In case of Berkovich indenter, most of the plastic flow underneath the indenter gets accommodated by radial displacement of material during indentation resulting in negligible pile-up of material in comparison to the h_{max}. Contrary to this, significant pile-up is observed during Cube-corner indentation due to the *cutting mechanism* prevalent underneath the indentation. In the cutting mechanism, irrespective of the strain hardening characteristics, the material in the subsurface deformation zone tends to flow around the indenter rather than the radial expansion and hence causing a significant pile-up.

5.4.2. Indentation size effect (ISE) in hardness.

The hardness of NG, unlike the MG of identical composition, depends on factors such as the effective free volume present in the microstructure and the segregation of certain elements to the interface forming icosahedral clusters at the interface. The former decreases the hardness of the glass while the latter increase it. The Cu-Zr and Scandium rich NGs exhibit a higher hardness as compared to the MGs of identical composition due to the presence of icosahedral clusters at the interfaces and the segregation of elements to the interface [Nandam et al., 2017, 2021]. The Pd-Si NGs does not show the presence of such clusters and hence exhibiting a lower hardness as compared to MGs [Nandam et al., 2020]. Another trend that is observed in both the glasses is the occurrence of ISE in hardness which is intimately connected to the evolution of free volume with the indentation load (vis-à-vis indentation volume). The Free volume evolution during the plastic deformation related to the Hardness by the following equation [Spapepen 1977; Argon 1979]:

$$H = \frac{6\sqrt{3}K_B T}{\Omega} \sinh^{-1}\left[\frac{\dot{\varepsilon}}{2\upsilon \Delta f c_f} exp\left(\frac{\Delta G}{K_B T}\right)\right] \quad (6)$$

where, K_B is the Boltzmann constant, Ω is the atomic volume, T is the temperature, $\dot{\varepsilon}$ is the shear strain rate, υ is the frequency of atomic vibration, Δf is the volume fraction of material having potential-jump sites, c_f is the concentration of free volume evolved during deformation, and ΔG is the activation barrier energy. Since all the tests are conducted at constant $\dot{\varepsilon}$ and T. Assuming that the changes in Δf and ΔG are less significant during nanoindentation. The equation (6) can be further simplified to estimate the free volume generation as [Steenberge et al., 2007]:

$$Kc_f = \left(\frac{v\Delta f\left(\frac{\Omega}{K_B T}\right)exp\left(\frac{-\Delta G}{K_B T}\right)}{3\sqrt{3}\dot{\varepsilon}}\right)c_f \approx \frac{1}{H} \quad (7)$$

The Kc_f vs. H plots for Berkovich and cube-corner indenters are displayed in Figure 7c and d, respectively. It is evident from the Figures that the free volume evolution is (i) higher in NG as compared to MG, (ii) higher in cube-corner indenter than the Berkovich, thereby resulting in lower hardness. The H and Kc_f values obtained with the Berkovich and cube-corner indenters are presented in Table1 and Table 2. The higher free volume in case cube-corner is related to the high indentation pressure ahead of the indenter, and larger indentation strain underneath the indentation.

Table 5.1 Summary of hardness, *H* values (corrected) obtained with Berkovich and cube-corner indenter at different maximum indentation loads for MG and NG, respectively.

$P_{max}(mN)$	**Hardness, $H(GPa)$**			
	Berkovich		**Cube corner**	
	MG	**NG**	**MG**	**NG**
2	5.45	4.65	3.01	2.89
4	5.25	4.19	2.77	2.45
6	4.85	3.95	2.40	2.23
8	4.62	3.65	2.21	1.93

Table 5.2 Summary of free volume generation, Kc_f values obtained with Berkovich and cube-corner indenter at different maximum indentation loads for MG and NG, respectively.

$P_{max}(mN)$	**Free volume, $Kc_f(GPa^{-1})$**			
	Berkovich		**Cube corner**	
	MG	**NG**	**MG**	**NG**
2	0.19	0.22	0.31	0.32
4	0.20	0.25	0.34	0.38
6	0.22	0.26	0.38	0.41
8	0.23	0.29	0.42	0.47

5.5. Summary

The shear band governed deformation behavior of PdSi metallic- and nanoglasses is explored with the help of the nanoindentation technique by utilizing two geometrically different pyramidal indenters, i.e., Berkovich and cube-corner indenter. Further, a discrete plasticity ratio is used to examine the transition and the contribution of serrations to the total plastic deformation. The following conclusions are drawn from the current results:

- A significant dependence of serrated flow behavior on the indenter angle is observed in MG and NG. The sharp cube-corner indenter displaces a greater volume of material for a given load (almost three times the Berkovich indenter), and the material deforms by a cutting mechanism, resulting in prominent serrations in the loading curves and higher pile-up.
- NG displays lower hardness than MG owing to the lower segregation, high free volume and absence of icosahedral clusters.
- For a given geometry of the indenter, the hardness of the material decreases with the increase in maximum indentation load, which signifies ISE. The rise in the deformation volume underneath the tip due to an increase in free volume content with indentation load appears to be the reason for the ISE.
- The discrete plasticity ratio, Ψ values computed are higher in case of a cube-corner indentation than the Berkovich signifies that the deformation under cube-corner indentation is more heterogeneous and is likely to be accommodated in PSBs.

CHAPTER 6
Conclusions and Future Scope

Abstract: This chapter summarizes the important results and key conclusions from the present thesis. The scope for future work based on the experiments performed and proposed mechanisms is mentioned in the last part of the chapter.

6.1. Summary and Conclusions

This thesis presents a systematic investigation on understanding the deformation behavior of MGs and NGs using indentation technique. Although a considerable amount of simulation work describing the microstructural features and deformation behavior of NG is available. But, limited number of experiments are conducted to date to ascertain the role of such unique microstructure of NG on its mechanical properties. In this context, Nanoindentation and Bonded interface indentation (BII) technique is utilized to understand the SB characteristics, effect of structural relaxation, strain rate sensitivity, and the role of indenter geometry in binary MGs and NGs. The above-mentioned objectives are reported in Chapter 2-4 and the following conclusions are drawn:

- Plastic strain in the NG is accommodated by very fine secondary shear bands (SSBs) and fewer primary shear bands (PSBs) whereas in case of MGs, it is mainly by PSBs. These fine SSBs observed in the NG is due to the presence of glassy interfaces which leads to nearly homogeneous deformation as compared to the MG counterparts. At any given indentation load, the size of the normalized subsurface is found to be higher in NG compared to the MG, which is associated with the uniform distribution of free volume leading to easy SB nucleation and propagation.
- The results from the micro- and nano-indentation experiments of the as-prepared (AP) and structurally relaxed (SR) NG reveal that the free volume has a marked influence on the deformation behavior of NG, with SR NG exhibiting a higher H than the AP NG. The loading curves of the SR NGs, in contrast to AP NGs, exhibit discrete displacement bursts, indicating that the plastic deformation is heterogeneous, which is also supported by the shear bands at the periphery of the imprint in the micro-indentation. The increase in H and serrated flow of the loading curves is attributed to the fully icosahedron (FI) clusters and reduction in free volume due to the annealing, respectively. Further, the H

decreases with increasing p in both the nano- and micro-indentation regimes, showing an indentation size effect. The increase in free volume generation in the subsurface deformation zone and the increase in deformation volume underneath the indentation with indentation load appear to be the reasons for the ISE.

- The results from the investigation of the strain rate sensitivity on the MGs and NGs illustrates that the serrated flow in the loading curves of MGs decreases with an increase in loading rate while it does not have any effect on the NGs. NGs do not exhibit serrated flow at any indentation loading rate. The hardness of both the NG and MG decreases with increasing loading rate implying negative strain rate sensitivity, m. The m values of NG are higher than the MG, indicating a tendency towards the near homogeneous plastic flow. Despite the high hardness in NGs, the high free volume is due to icosahedra clusters present at the interfaces. The BII tests conducted to understand the higher value of m in NG reveal that the primary shear bands (PSBs) are the main carriers of plastic flow in MG, while in NG, owing to the high free volume, it is by secondary shear bands (SSBs). The relatively positive m in NG compared to the MG is attributed to a large number of fine shear bands and near homogeneous plastic deformation.
- A strong dependence of serrated flow behavior on the indenter angle is observed in NG and MG. A useful parameter, discrete plasticity ratio, Ψ is utilized to estimate the influence of serrations on the total plastic deformation. It is observed that Ψ does not change significantly with the load, indicating that the deformation mode remains the same with either of the indenters in both MG and NG (i.e., heterogeneous in MG and homogeneous in NG.

6.2. Directions for Future Work

The present study attempts to understand the deformation behavior of MGs and NGs through indentation technique. In this regard, the SB characteristics along with the role of structural relaxation, strain rate sensitivity and indenter geometry are explored in details. However, there are certain tests or characterization to be conducted to establish any assumptions used to explain the behaviour.

- Transmission electron microscopy (TEM) can be utilized to observe the formation of SBs and STZs clusters. Further, Atomic probe topography (APT) can be used to understand the segeragation behavior of NG.

- Micro-tensile and compression testing can be conducted to understand and establish a correlation on the deformation behavior of NG between the indentation and conventional testing method.
- Nanoscratch experiments can be conducted on NG to explore the tribological applications.
- High temperature indentation experiments on BMGs have shown a transition in the deformation mode [Prasad et al. 2007; 2011]. Therefore, it would be very interesting to examine the nature of plastic flow in NGs when subjected to high temperature surroundings.
- The hardness mapping of the subsurface zone in BMGs have shown a significant variation in the serrations of the *P-h* curves. Moreover, a difference in the hardness of the deformed (including SB) and undeformed zone were reported [Yoo and Jang 2008]. Since, we observed with the help of BII technique that NGs deform by PSBs and SSBs. Therefore, by performing the hardness mapping of the subsurface deformation zone will help in providing some new insights about the homogeneous deformation in NG.
- The indentation creep experiments conducted at different loading rates and temperature on several BMGs have shown that the viscoelastic or viscoplastic characteristics are strongly dependent on the loading rate and temperature. Thus, it would be very interesting to examine the creep deformation in NGs.
- Only limited number of studies have reported the influence of high strain rate and dynamic failure in BMGs whereas to date no such studies have been conducted on NGs. This is one of the important open problems which can be explored by conducting high strain rate experiments on NGs with the help of Split Hopkinson pressure bar (SHPB) or Kolsky bar.

APPENDIX A

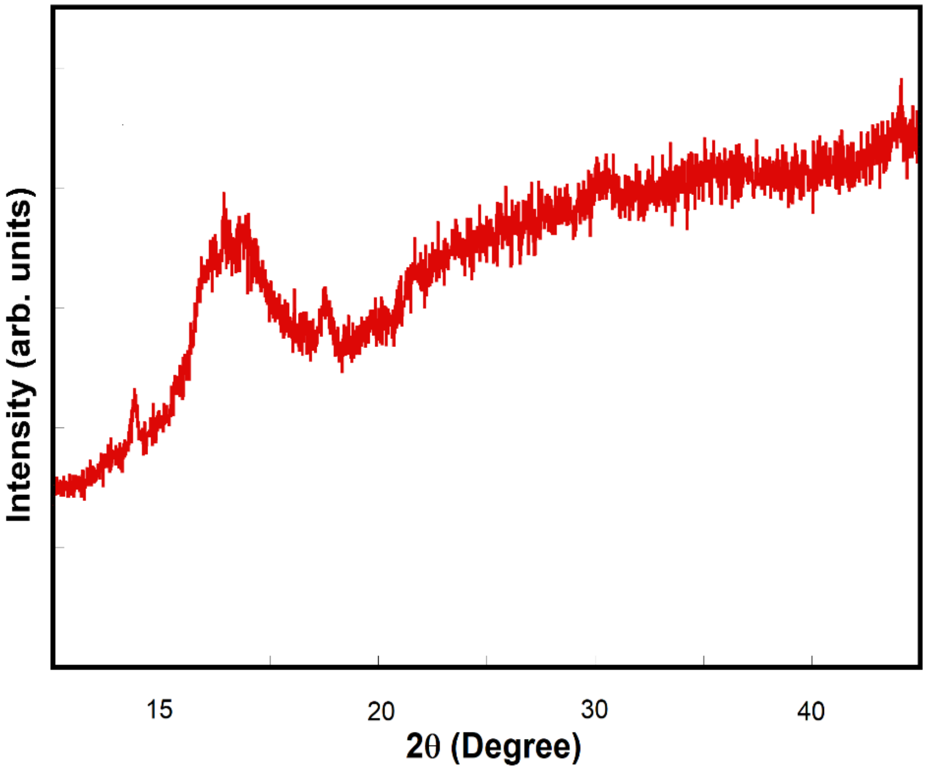

Figure A.1 X-ray diffraction of the above T_g annealed samples showing the presence of small crystalline peaks in addition the amorphous hump, confirming its crystalline nature.

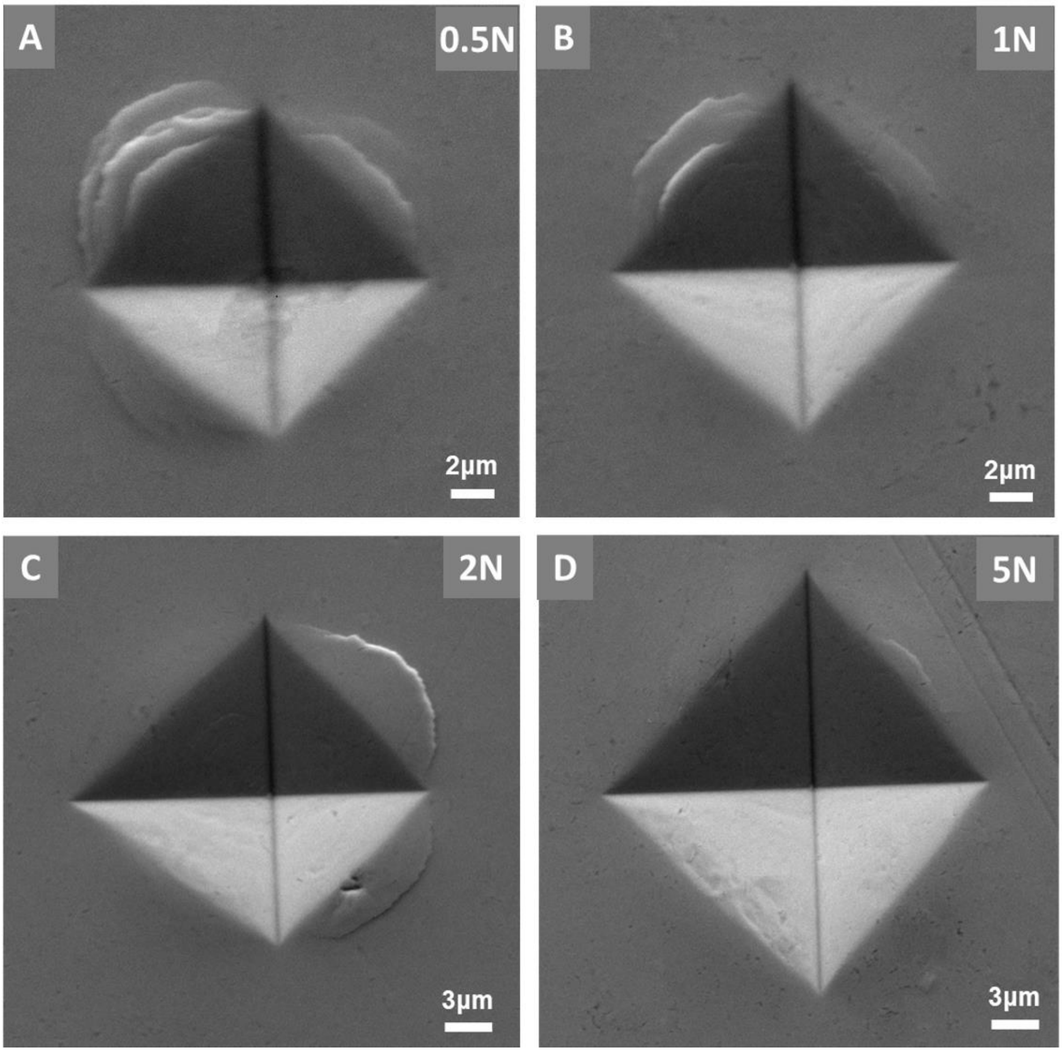

Figure A.2 Vickers indentation imprints of above T_g annealed samples showing the shear bands at the periphery of the imprint.

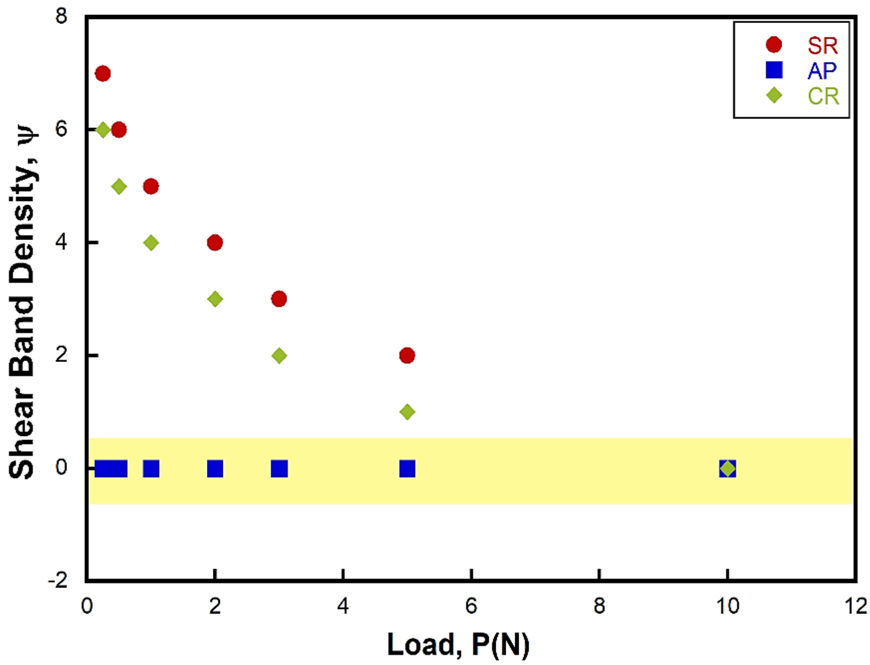

Figure A.3 Variation of the shear band density, ψ (Number of shear bands on the indented surface) with the indentation load, *P* for SR, AP and crystallized (CR) NGs.

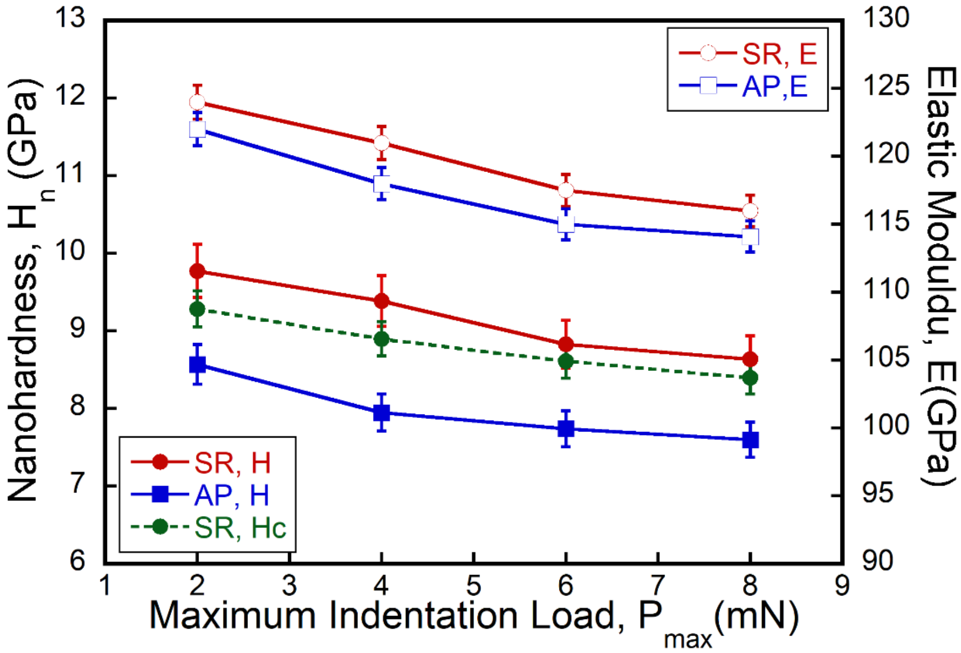

Figure A.4 Variation of nanohardness, H_n, and elastic modulus, E, with maximum indentation load, Pmax, of both SR and AP NGs indicating the ISE. Corrected nanohardness, H_c is plotted for the SR NG due to the pile-up generated around the indent imprint.

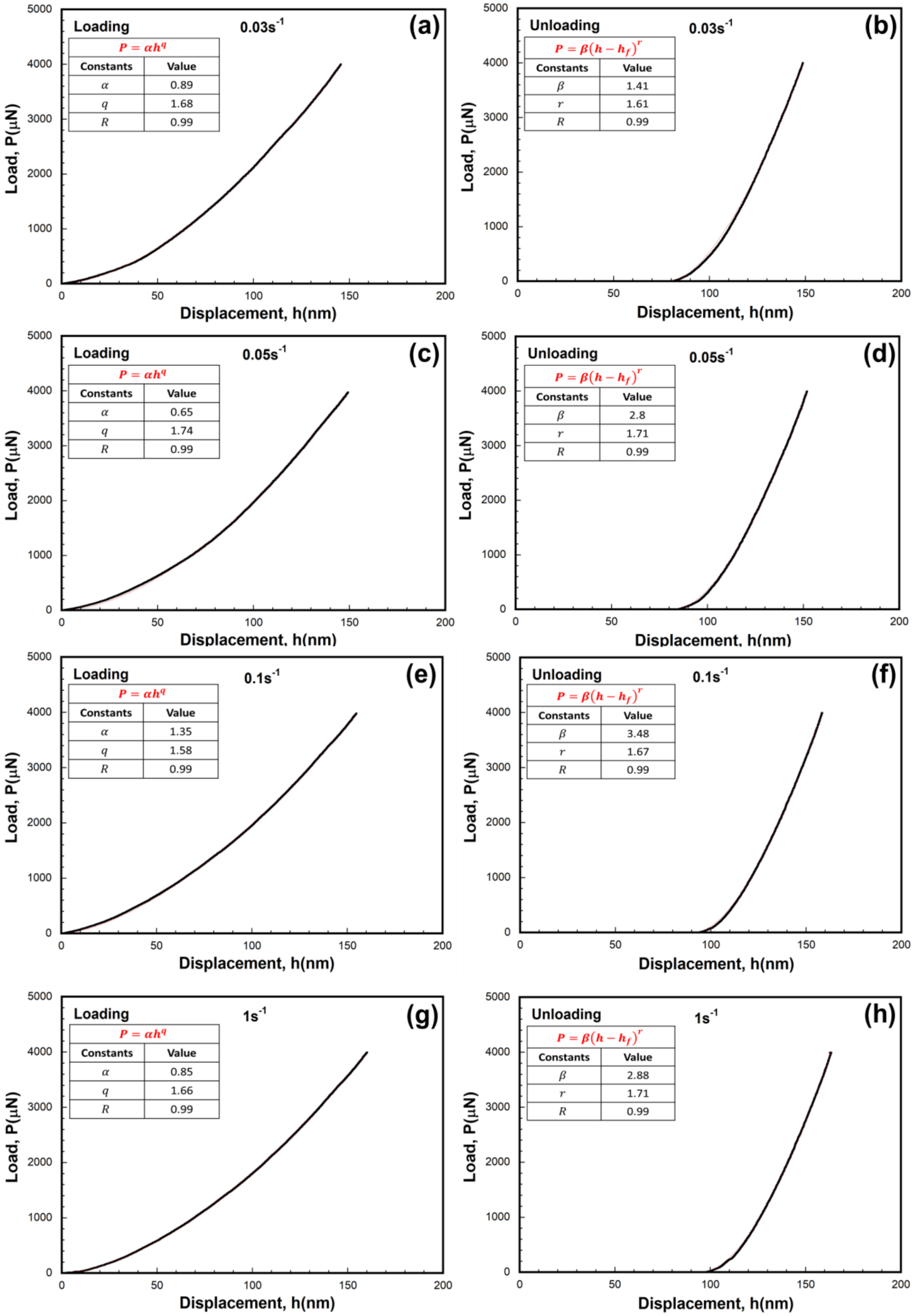

Figure A.5 Representative *P-h* curves of NG representing the loading a), c), e), f), and unloading b), d), f), h) portion fitted with the help of equation (4) and (5), respectively.

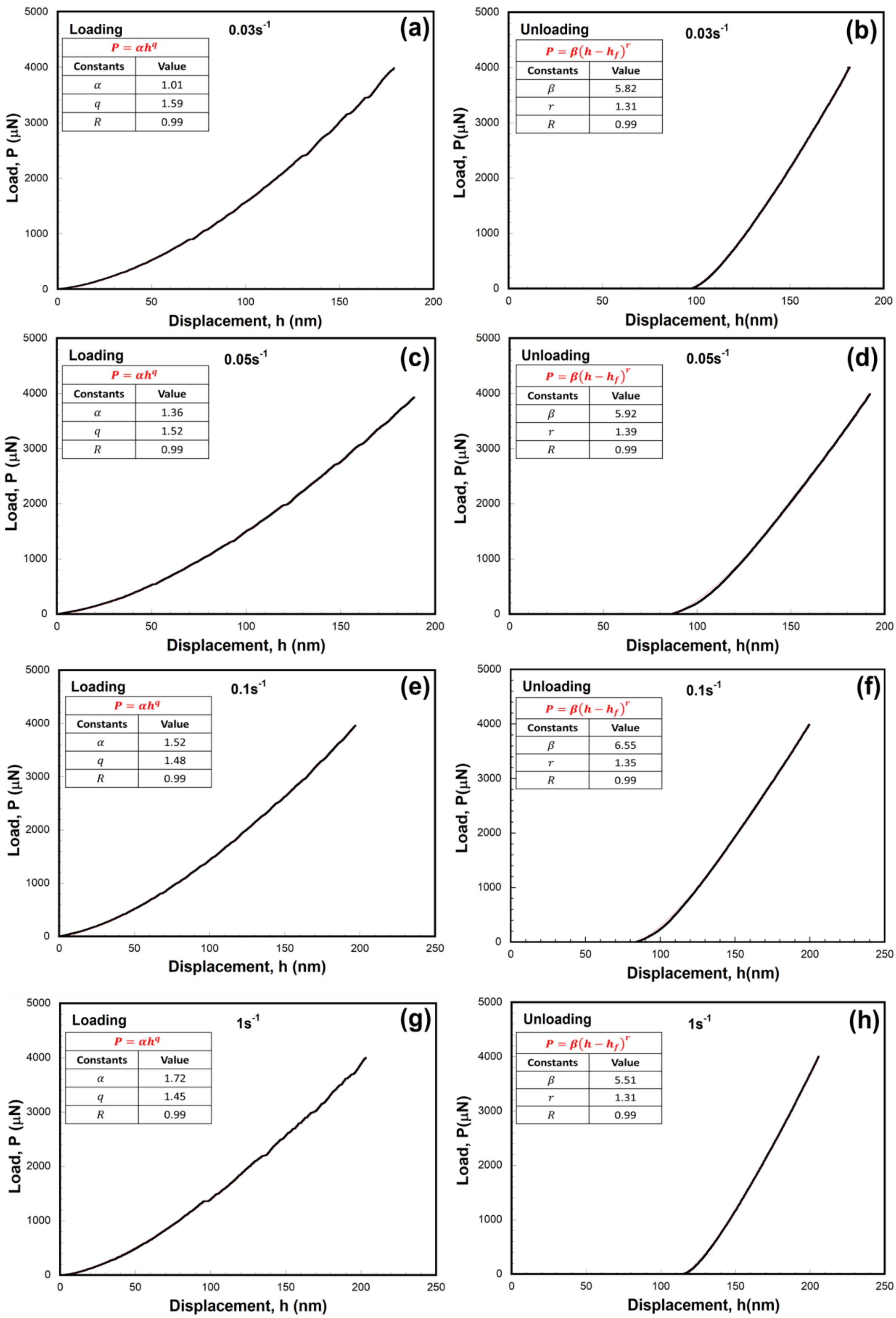

Figure A.6 Representative *P-h* curves of MG representing the loading a), c), e), f), and unloading b), d), f), h) portion fitted with the help of equations (4) and (5), respectively.

Table A.1 Values of the fitting constants obtained for NG from the load, P vs. displacement, h curves (Fig. A5) along with the regression co-efficient describing the goodness of the fit.

Strain rate, s^{-1}	**Fitting Constants (NG)**					
	Loading curve			**Unloading curve**		
	$\boldsymbol{\alpha}$	$\boldsymbol{q}$	$\mathbf{R^2}$	$\boldsymbol{\beta}$	$\boldsymbol{r}$	$\mathbf{R^2}$
0.03	0.89	1.68	0.99	1.41	1.61	0.99
0.05	0.65	1.74	0.99	2.8	1.71	0.99
0.1	1.35	1.58	0.99	3.48	1.67	0.99
1	0.85	1.66	0.99	2.88	1.71	0.99

Table A.2 Values of the fitting constants obtained for MG from the load, P vs. displacement, h curves (Fig. A6) along with the regression co-efficient describing the goodness of the fit.

Strain rate, s^{-1}	**Fitting Constants (MG)**					
	Loading curve			**Unloading curve**		
	$\boldsymbol{\alpha}$	$\boldsymbol{q}$	$\mathbf{R^2}$	$\boldsymbol{\beta}$	$\boldsymbol{r}$	$\mathbf{R^2}$
0.03	1.01	1.59	0.99	5.82	1.31	0.99
0.05	1.36	1.52	0.99	5.92	1.39	0.99
0.1	1.52	1.48	0.99	6.55	1.35	0.99
1	1.72	1.45	0.99	5.51	1.31	0.99

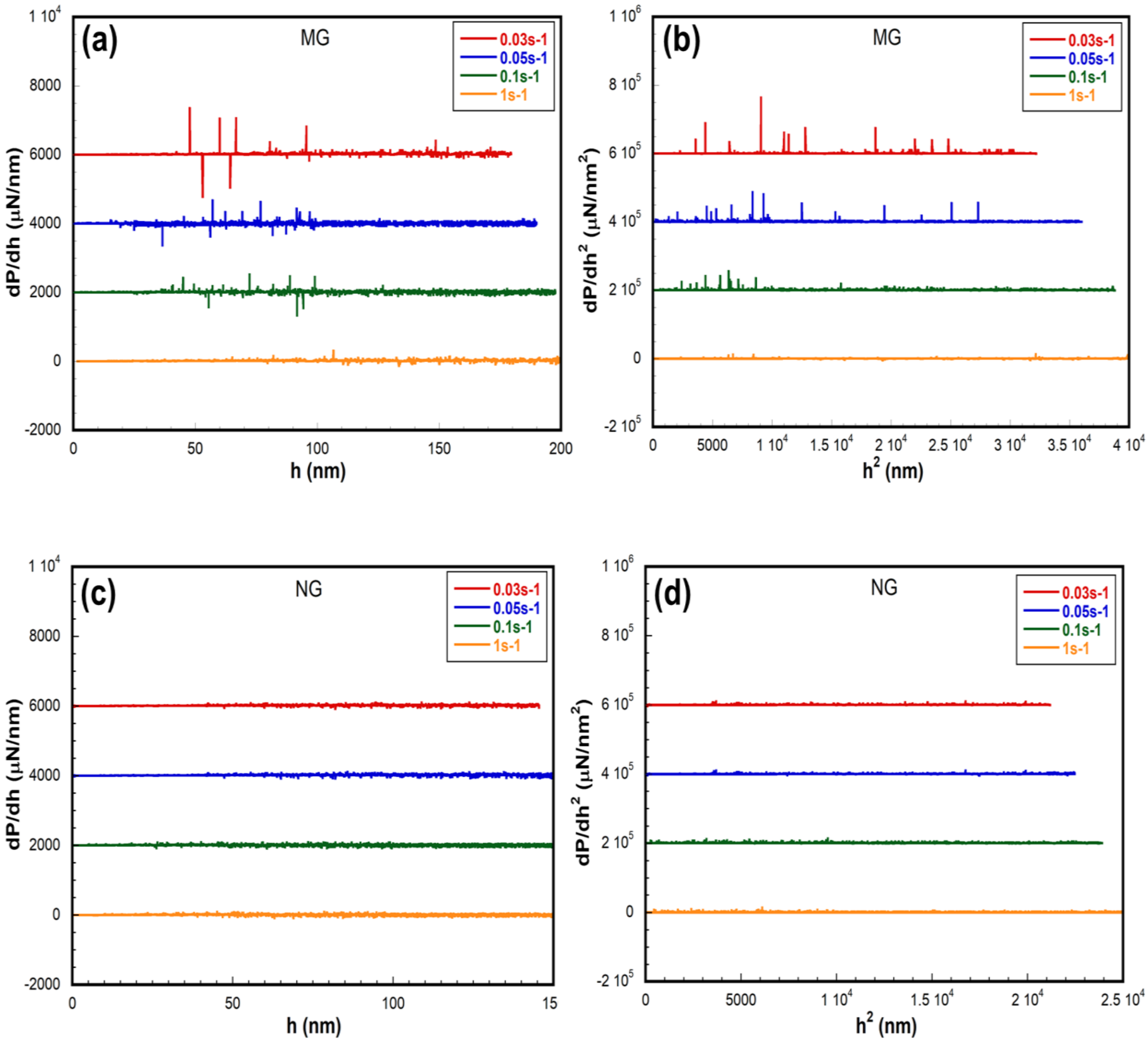

Figure A.7 Variation of dP/dh with h and $dP\ /\ dh^2$ with h^2 for MG is presented in (a) and (b), respectively, while the variation of NG in (c) and (d), respectively.

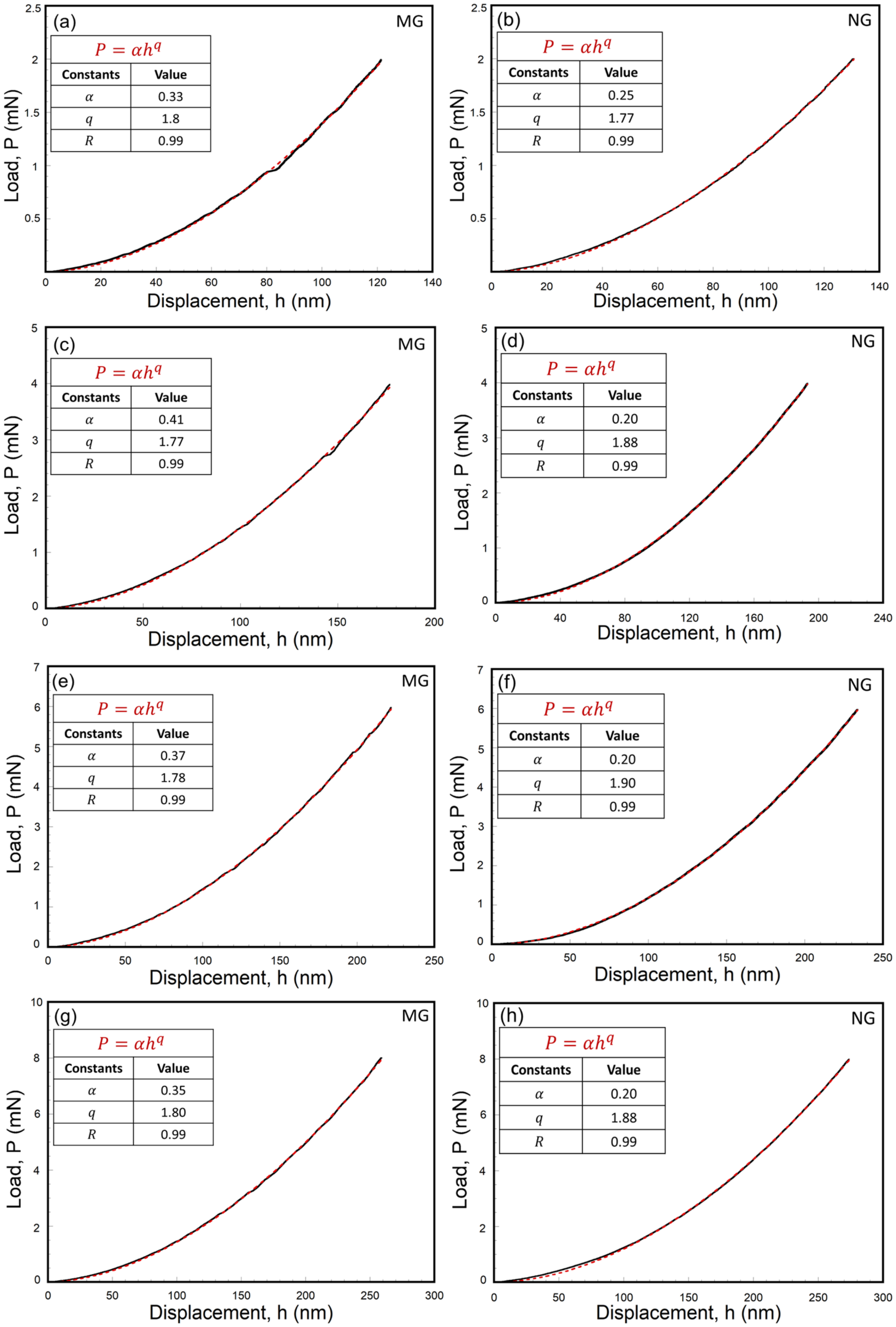

Figure A.8 Representative loading portion of the *P*-*h* curves obtained with the Berkovich indenter for MG a), c), e), g), and NG b), d), f), h) respectively

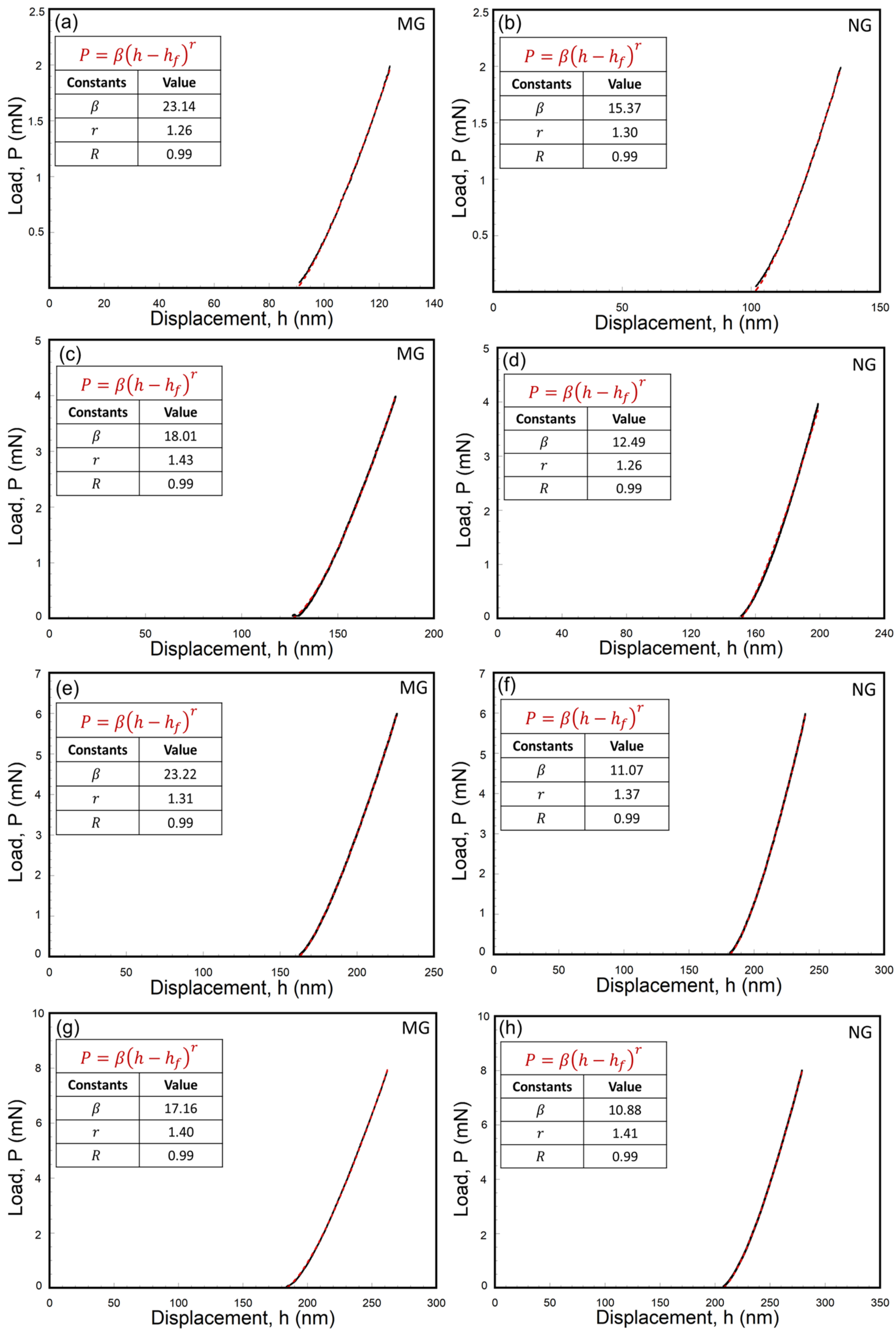

Figure A.9 Representative Unloading portion of the *P-h* curves obtained with the Berkovich indenter for MG a), c), e), g), and NG b), d), f), h) respectively.

Table A.3 Values of the fitting constants obtained from the loading portion of the load, *P* vs. displacement, *h* curves (Fig. A8) conducted with the Berkovich indenter along with the regression co-efficient describing the goodness of the fit

Load, P_{max} (*mN*)	**Loading curve fitting constants (Berkovich Indenter)**					
	MG			**NG**		
	$\boldsymbol{\alpha}$	$\boldsymbol{q}$	$\mathbf{R^2}$	$\boldsymbol{\alpha}$	$\boldsymbol{q}$	$\mathbf{R^2}$
2	0.33	1.80	0.99	0.35	1.77	0.99
4	0.41	1.77	0.99	0.20	1.88	0.99
6	0.37	1.78	0.99	0.20	1.90	0.99
8	0.35	1.80	0.99	0.20	1.88	0.99

Table A.4 Values of the fitting constants obtained from the unloading portion of the load, *P* vs. displacement, *h* curves (Fig. A9) conducted with the Berkovich indenter along with the regression co-efficient describing the goodness of the fit.

Load, P_{max} (*mN*)	**Unloading curve fitting constants (Berkovich Indenter)**					
	MG			**Unloading curve**		
	$\boldsymbol{\beta}$	$\boldsymbol{r}$	$\mathbf{R^2}$	$\boldsymbol{\beta}$	$\boldsymbol{r}$	$\mathbf{R^2}$
2	23.14	1.26	0.99	15.37	1.30	0.99
4	18.01	1.43	0.99	12.49	1.26	0.99
6	23.22	1.31	0.99	11.07	1.37	0.99
8	17.16	1.40	0.99	10.88	1.41	0.99

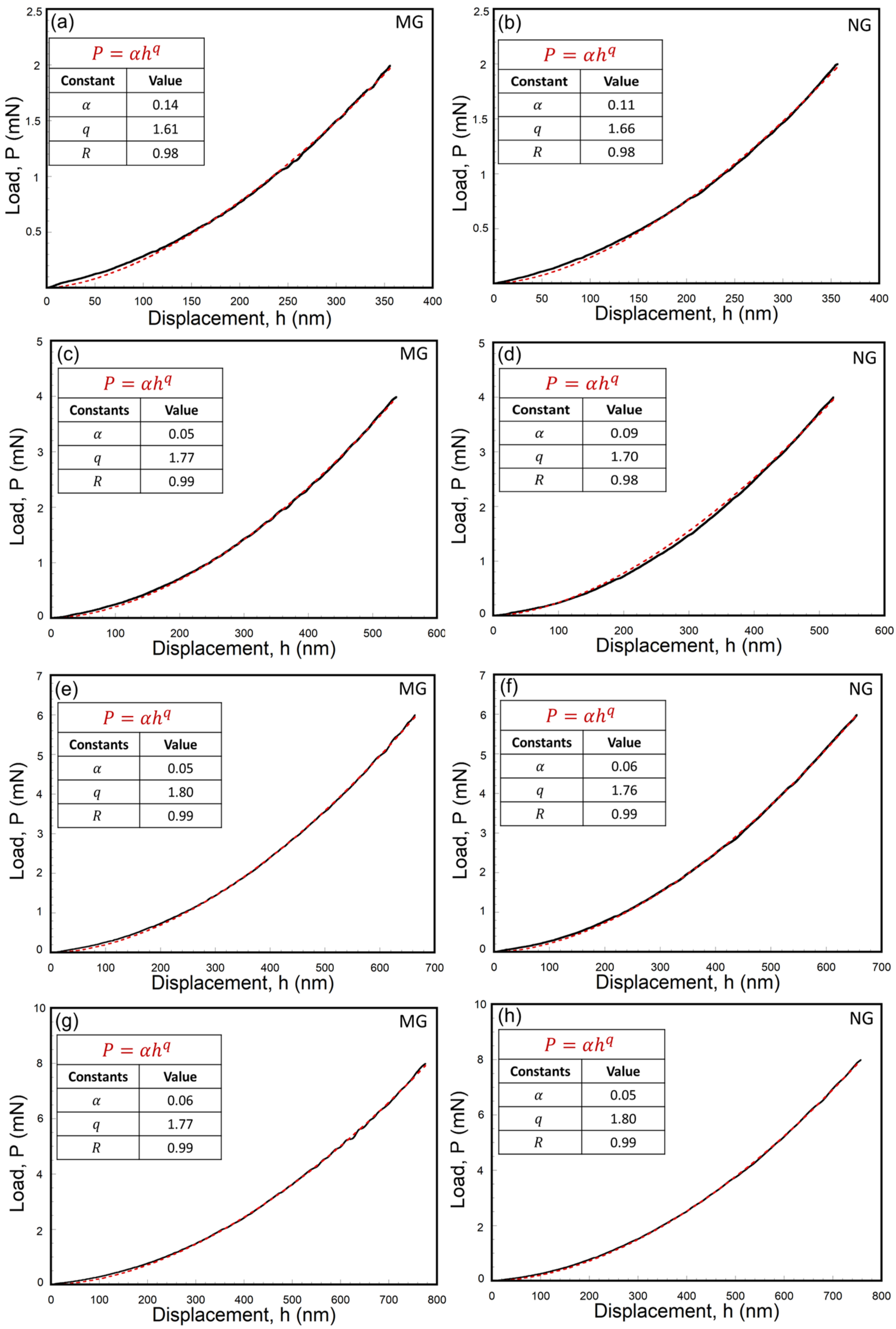

Figure A.10 Representative loading portion of the *P*-*h* curves obtained with the Cube-corner indenter for MG a), c), e), g), and NG b), d), f), h) respectively.

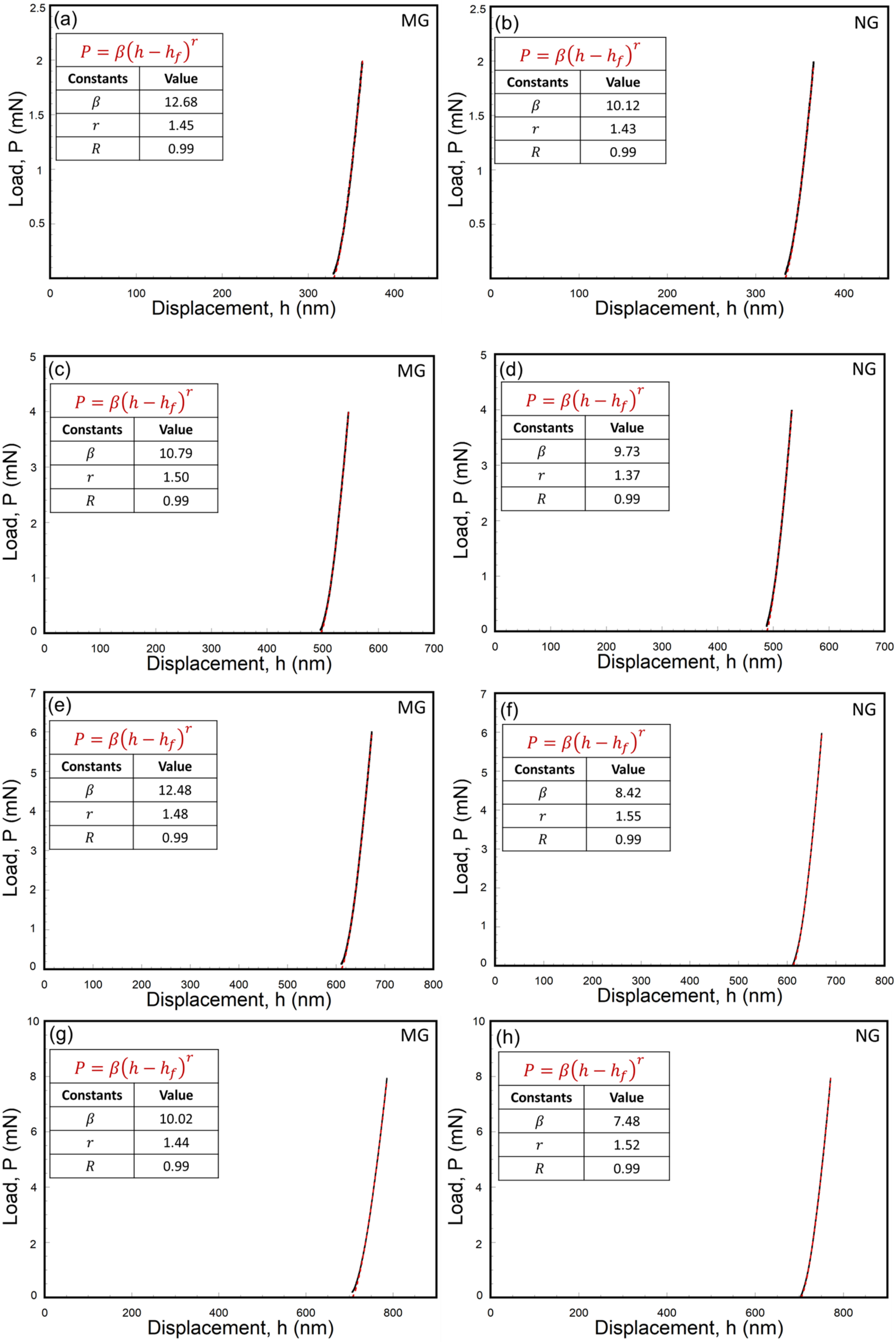

Figure A.11 Representative Unloading portion of the *P*-*h* curves obtained with the Cube-corner indenter for MG a), c), e), g), and NG b), d), f), h), respectively.

Table A.5 Values of the fitting constants obtained from the loading portion of the load, *P* vs. displacement, *h* curves (Fig. A10) conducted with the Cube-corner indenter along with the regression co-efficient describing the goodness of the fit.

Load, P_{max} (*mN*)	**Loading curve fitting constants (Cube-corner Indenter)**					
	MG			**NG**		
	$\boldsymbol{\alpha}$	$\boldsymbol{q}$	$\mathbf{R^2}$	$\boldsymbol{\alpha}$	$\boldsymbol{q}$	$\mathbf{R^2}$
2	0.14	1.61	0.98	0.11	1.66	0.98
4	0.05	1.77	0.99	0.09	1.70	0.98
6	0.05	1.80	0.99	0.06	1.76	0.99
8	0.06	1.77	0.99	0.05	1.80	0.99

Table A.6 Values of the fitting constants obtained from the unloading portion of the load, *P* vs. displacement, *h* curves (Fig. A11) conducted with the Cube-corner indenter along with the regression co-efficient describing the goodness of the fit.

Load, P_{max} (*mN*)	**Unloading curve fitting constants (Cube-corner Indenter)**					
	MG			**Unloading curve**		
	$\boldsymbol{\beta}$	$\boldsymbol{r}$	$\mathbf{R^2}$	$\boldsymbol{\beta}$	$\boldsymbol{r}$	$\mathbf{R^2}$
2	12.68	1.45	0.99	10.17	1.43	0.99
4	10.79	1.50	0.99	9.73	1.37	0.99
6	12.48	1.48	0.99	8.42	1.55	0.99
8	10.02	1.44	0.99	7.84	1.52	0.99

BIBLIOGRAPHY

- Adibi S., Branicio P. S., Zhang Y.W., Joshi S.P. (2014), Composition and grain size effects on the structural and mechanical properties of CuZr nanoglasses, *Journal of Applied Physics*, 116, 043522 (doi.org/10.1063/1.4891450).
- Adibi S., Sha Z. D., Branicio P. S., Joshi S. P., Liu Z. S., Zhang, Y. W. (2013), A Transition from Localized Shear Banding to Homogeneous Superplastic Flow in Nanoglass. *Applied Physics Letters*, 103, 211905 (doi:10.1063/1.4833018).
- Adjaoud O., Albe K. (2016), Interfaces and interphases in nanoglasses: Surface segregation effects and their implications on structural properties, *Acta Materialia*, 113, 284–292. (doi:10.1016/j.actamat.2016.05.002).
- Adjaoud O., Albe K. (2017), Microstructure formation of metallic nanoglasses: Insights from molecular dynamics simulations, *Acta Materialia*, 145, 322–330 (doi:10.1016/j.actamat.2017.12.014).
- Adjaoud O., Albe K. (2021), Nanoindentation of Nanoglasses Tested by Molecular Dynamics Simulations: Influence of Structural Relaxation and Chemical Segregation on the Mechanical Response. *Frontiers in Materials,* 8, 95 (doi:10.3389/fmats.2021.664220).
- Adjaoud O., Albe K. (2019), Influence of microstructural features on the plastic deformation behavior of metallic nanoglasses, *Acta Materialia,* 168, 393-400 (doi.org/10.1016/j.actamat.2019.02.033).
- Albe K., Ritter Y., Şopu D. (2013), Enhancing the plasticity of metallic glasses: Shear band formation, nanocomposites, and nanoglasses investigated by molecular dynamics simulations, *Mechanics of Materials*, 67, 94–103 (doi:10.1016/j.mechmat.2013.06.004).
- Argon A. S. (1979), Plastic deformation in metallic glasses, *Acta Metallurgica*, 27, 47-58 (doi.org/10.1016/0001-6160(79)90055-5).
- Arnold W., Birringer R., Braun C., Gleiter H., Hahn H., Nandam S. H., Singh S. P. (2020), Elastic Moduli of Nanoglasses and Melt-Spun Metallic Glasses by Ultrasonic Time-Of-Flight Measurements. *Transaction of the Indian Institute of Metals*, 73, 1363–1371 (doi:10.1007/s12666-020-01969-x).
- Ashby M. F., Greer A. L. (2006), Metallic glasses as structural materials, *Scripta Materialia,* 54, 321-326 (doi:10.1016/j.scriptamat.2005.09.051).
- Bag S., Baksi A., Wang D., Kruk R., Benel C., Chellali M.R., Hahn H. (2019), Combination of pulsed laser ablation and inert gas condensation for the synthesis of nanostructured

nanocrystalline, amorphous and composite materials, *Nanoscale Advances*, 1, 4513–4521 (doi:10.1039/c9na00533a).

- Bhattacharyya A., Singh G., Prasad K. E., Narasimhan R., Ramamurty U. (2015), On the strain rate sensitivity of plastic flow in metallic glasses, *Material Science and Engineering A*, 625, 245–251 (doi.org/10.1016/j.msea.2014.12.004).
- Bhowmick R., Raghavan R., Chattopadhyay K., Ramamurty U. (2006), Plastic flow softening in a bulk metallic glass, *Acta Materialia*, 54, 4221–4228 (doi:10.1016/j.actamat.2006.05.011).
- Boltynjuk E. V., Gunderov D. V., Ubyivovk E. V., Monclús M. A., Yang L.W., Molina-Aldareguia J.M., Tyurin A.I., Kilmametov A., Churakova A. A., Yu Churyumov A., Valiev R.Z. (2018), Enhanced strain rate sensitivity of Zr-based bulk metallic glasses subjected to high pressure torsion. *Journal of Alloys and Compounds*, 747, 595-602 (doi:10.1016/j.jallcom.2018.03.018).
- Brinell J. A. (1900), In: 2ieme Congres Internationale Me´thodes d’Essai. Paris.
- Chaudhri M. M. (1998), Subsurface strain distribution around vickers hardness indentations in annealed polycrystalline copper, Acta Materialia, 46, 3047. (doi.org/10.1016/S1359-6454(98)00010-X).
- Cheng B., and Trelewicz J. R. (2019), Interfacial Plasticity Governs Strain Delocalization in Metallic Nanoglasses. *Journal of Materials Research*, 34, 2325–2336 (doi:10.1557/JMR.2019.101).
- Chen K. W., Lin J. F. (2010), Investigation of the relationship between primary and secondary shear bands induced by indentation in bulk metallic glasses. *International Journal of Plasticity*, 26, 1645–1658 (doi.org/10.1016/j.ijplas.2010.03.003).
- Chen N., Yao K. F., Ruan. F (2007), Microstructural features of phase transformation in a binary Pd-Si metallic glass, *Philosophical Magazine Letters*, 87, 677–686 (doi:10.1080/09500830701441905).
- Chen N, Frank R., Asao N., Louzguine-Luzgin D. V., Sharma P., Wang J. Q., Xie G. Q., Ishikawa Y., Hatakeyama N., Lin Y. C., Esashi M., Yamamoto Y., Inoue A. (2011), Formation and properties of Au-based nanograined metallic glasses, *Acta Materialia* 59, 6433–6440. (doi:10.1016/j.actamat.2011.07.007).
- Chen N., Shi X., Witte R., Nakayama K. S., Ohmura K., Wu H., Takeuchi A., Hahn H., Esashi M., Gleiter H., Inoue A., Louzguine D. V. (2013), A novel Ti-based nanoglass

composite with submicron–nanometer-sized hierarchical structures to modulate osteoblast behaviors, *Journal of Materials Chemistry B*, 1, 2568. doi:10.1039/c3tb20153h.

- Cheng Y. Q., Cao A. J., Sheng H. W., Ma E. (2008), Local Order Influences Initiation of Plastic Flow in Metallic Glass: Effects of alloy Composition and Sample Cooling History. *Acta Materialia*, 56, 5263–5275 (doi:10.1016/j.actamat.2008.07.011).
- Chen Z., Datye A., Brooks P.A., Sprole M., Ketkaew J., Sohn S., Schroers J., Schwarz U. D. (2019), Dependence of Modulus and Hardness on the Annealing Conditions of $Pt_{57.5}Cu_{14.7}Ni_{5.3}P_{22.5}$ Bulk Metallic Glass, *MRS Advances*, 4, 73–79 (doi.org/10.1557/adv.2019.30).
- Choi I., Zhao Y., Kim Y., Yoo B. G., Suh J.Y., Ramamurty U., Jang J. (2012), Indentation size effect and shear transformation zone size in a bulk metallic glass in two different structural states, *Acta Materialia*, 60, 6862–6868 (doi.org/10.1016/j. actamat.2012.08.061).
- Dalla Torre F. H., Dubach A., Siegrist M. E., Löffler J. F. (2006), Negative strain rate sensitivity in bulk metallic glass and its similarities with the dynamic strain aging effect during deformation, *Applied Physics Letters*, 89, 091918 (doi.org/10.1063/1.2234309).
- Das J., Güth A., Klauß H.-J., Mickel C., Löser W., Eckert J., Roy S.K., Schultz L. (2003), Effect of casting conditions on microstructure and mechanical properties of high-strength $Zr_{73.5}Nb_9Cu_7Ni_1Al_{9.5}$ in situ composites, *Scripta Materialia*, 49(12), 1189–1195 (doi:10.1016/j.scriptamat.2003.08.015)
- Deng L., Kosiba K., Limbach R., Wondraczek L., Uhn U.K., Pauly S. (2021), Plastic deformation of a Zr-based bulk metallic glass fabricated by selective laser melting, *Journal of Materials Science and Technology*, 60, 139–146 (doi.org/10.1016/j.jmst.2020.06. 007).
- Dieter G.E. and Bacon D. (1986), Mechanical Metallurgy, Metric (Ed.), *McGraw-Hill*, New York.
- Doener M. F., Nix W. D. (1968), A method for interpreting the data from depth-sensing indentation instruments, Journal of Materials Research, 1, 601. (doi.org/10.1557/JMR.1986.0601).
- Dubach A., Dalla Torre F.H., Löffler J.F. (2009a), Constitutive model for inhomogeneous flow in bulk metallic glasses, *Acta Materialia*, 57, 881–892, (doi.org/10. 1016/j.actamat.2008.10.027).
- Dubach A., Raghavan R., Löffler J.F., Michler J., Ramamurty U. (2009), Micropillar compression studies on a bulk metallic glass in different structural states, *Scripta Materialia*, 60, 567–570 (doi.org/10.1016/j.scriptamat.2008.12.013).

- Eckert J., Das J., Pauly S., Duhamel, C. (2007), Mechanical properties of bulk metallic glasses and composites, *Journal of Materials Research*, 22(2), 285-301. (doi:10.1557/jmr.2007.0050).
- Falk M.L., Langer J.S. (1998), Dynamics of viscoplastic deformation in amorphous solids, *Physical Review E*, 57 (1998) 7192 (https://doi.org/10.1103/physreve.57.7192)
- Field J. S., Swain M. V., Dukino R. D. (2003), Determination of fracture toughness from the extra penetration produced by indentation-induced pop-in. *Journal of Materials Research*, 18, 1412. (doi.org/10.1557/JMR.2003.0194).
- Fang J. X., Vainio U., Puff W., Wurschum R., Wang X. L., Wang D., Ghafari M., Jiang F., Sun J., Hahn H., Gleiter H. (2012), Atomic structure and structural stability of $Sc_{75}Fe_{25}$ nanoglasses, *Nano Letters*, 12, 458-463 (doi.org/10.1021/nl2038216).
- Franke O., Leisen D., Gleiter H., Hahn H. (2014), Thermal and plastic behavior of nanoglasses, Journal of Materials research, 29, 1210-1216 (doi.org/10.1557/jmr.2014.101).
- Gleiter H. (2008), Our thoughts are ours, their ends none of our own: Are there ways to synthesize materials beyond the limitations of today? *Acta Materialia*, 56, 5875–5893 (doi:10.1016/j.actamat.2008.08.028).
- Glieter H. (2009). Are There Ways to Synthesize Materials beyond the Limits of Today? *Metallurgy and Materials Transactions A*, 40, 1499–1509 (doi:10.1007/s11661-009-9848-7)
- Gleiter H. (2013), Nanoglasses: a new kind of noncrystalline materials, *Beilstein Journal of Nanotechnology*, 4, 517-533 (doi.org/10.3762/bjnano.4.61).
- Gleiter H. (2016). Nanoglasses: a New Kind of Noncrystalline Material and the Way to an Age of New Technologies? *Small*, 12, 2225–2233 (doi:10.1002/smll.201500899).
- Golovin Y. I., Ivolgin V. I., Khonik V. A., Kitagawa K., Tyurin A. I. (2001), Serrated plastic flow during nanoindentation of a bulk metallic glass, *Scripta Materialia*, 45, 947-952 (doi.org/10.1016/S1359-6462(01)01116-2).
- Gonzalez S., Xie G.Q., Louzguine-Luzgin D.V., Perepezko J.H., Inoue A. (2011), Deformation and strain rate sensitivity of a Zr-Cu-Fe-Al metallic glass, *Material Science and Engineering A*, 528, 3506–3512 (doi.org/10.1016/j.msea.2011.01.049).
- Greer, A. L., Castellero, A., Madge, S. V., Walker, I. T., Wilde, J. R. (2004). Nanoindentation studies of shear banding in fully amorphous and partially devitrified metallic alloys. *Material Science and Engineering A*, 375-377, 1182-1185 (doi:10.1016/j.msea.2003.10.032).

- Greer A. L., Cheng Y. Q., Ma E. (2013), Shear bands in metallic glasses. *Material Science and Engineering: R: Reports*, 74(4), 71-132 (doi.org/10.1016/j.mser.2013.04.001).
- Gu J., Song M., Ni S., Guo S., He Y. (2013), Effects of annealing on the hardness and elastic modulus of a $Cu_{36}Zr_{48}Al_8Ag_8$ bulk metallic glass, *Materials & Design*, 47, 706–710 (doi:10.1016/j.matdes.2012.12.071).
- Gunti A., Das J. (2022), Effect of testing conditions on the nanomechanical behavior of surface and inner core of as-cast Zr-base bulk metallic glassy plates, *Material Science and Engineering A*, 845, 143206 (doi.org/10.1016/j.msea.2022.143206).
- Guo C., Fang Y., Chen F., Feng T. (2019), Nanoindentation creep behavior of electrodeposited Ni-P nanoglass films, Intermetallics, 110, 106480 (doi.org/10.1016/j.intermet.2019.106480).
- Guo H., Yan P. F., Wang Y. B., Tan J., Zhang Z. F., Sui M. L., Ma E., Tensile ductility and necking of metallic glass, *Nature Materials*, 6, 735–739 (doi:10.1038/nmat1984).
- Hays C. C., Kim C. P., Johnson W. L. (2000), Microstructure controlled shear band pattern formation and enhanced plasticity of bulk metallic glasses containing in situ formed ductile phase dendrite dispersions, *Physical Review Letters*, 84, 2901–2904 doi:10.1103/PhysRevLett.84.2901.
- Hahn H., Averback R. S. (1990), The production of nanocrystalline powders by magnetron sputtering, *Journal of Applied Physics*, 67, 1113–1115. (doi:10.1063/1.345798).
- Hajlaoui K., Yavari A.R., LeMoulec A., Botta W.J., Vaughan F.G., Das J., Greer A.L., Kvick A. (2007), Plasticity induced by nanoparticle dispersions in bulk metallic glasses, *Journal of Non-Crystalline Solids*, 353(3), 0–331 (doi:10.1016/j.jnoncrysol.2006.10.011).
- He J., Kaban I., Mattern N., Song K., Sun B., Zhao J., Kim D.H., Eckert J., Greer A. L. (2016), Local microstructure evolution at shear bands in metallic glasses with nanoscale phase separation, *Scientific Reports*, 6 (2016) 1–8 (doi:10.1038/srep25832).
- Hey P. D., Sietsma J., Beukel A. V. D. (1998), Structural Disordering in Amorphous $Pd_{40}Ni_{40}P_{20}$ Induced by High Temperature Deformation. *Acta Materialia*, 46, 5873–5882 (doi:10.1016/S1359-6454(98)00234-1).
- Hill R. (1950), The mathematical theory of plasticity. Oxford: Clarendon Press.
- Hill R., Lee E. H. (1947), The theory of wedge indentation of ductile materials. Tupper. Proc Roy Soc A, 188, 273-289.
- Hirmukhe, S. S., Prasad, K. E., and Singh, I. (2019), Finite Element Analysis of Tensile Deformation of Nanoglass-Metallic Glass Laminate Composites. *Computational Material Science*, 161, 83–92 (doi:10.1016/j.commatsci.2019.01.031).

- Hirmukhe S. S., Prasad K. E., Singh I. (2020), Investigation of pressure sensitive plastic flow in nanoglasses from finite element simulations, *Scripta Materialia*, 180, 45–50 (doi.org/10.1016/j.scriptamat.2020.01.022).
- Hirmukhe S.S., Sharma A., Nandam S. H., Hahn H., Prasad K.E., Singh I. (2022), Investigation of softening induced indentation size effect in Nanoglass and Metallic glass, *Journal of Non-Crystalline Solids*, 577, 121316 (doi.org/10. 1016/j.jnoncrysol.2021.121316).
- Hofmann D.C., Suh J. Y., Wiest A., Duan G., Lind M. L., Demetriou M. D., Johnson W. L. (2008), Designing metallic glass matrix composites with high toughness and tensile ductility, *Nature*, 451, 1085–1089 (doi:10.1038/nature06598).
- Huang Y., Shen J., Sun Y., Sun, J. (2010), Indentation Size Effect of Hardness of Metallic Glasses. *Material Design*, 31, 1563–1566 (doi:10.1016/j.matdes.2009.09.046).
- Huang L., Wang H. Y., Qiu F., Jiang Q. C. (2006), Synthesis of dense ceramic particulate reinforced composites from Ni–Ti–C, Ni–Ti–B, Ni–Ti–B4C and Ni–Ti–C–B systems via the SHS reaction, arc melting and suction casting. *Material Science and Engineering A*, 422, 309-315 (doi:10.1016/j.msea.2006.02.019).
- Huang Y., Shen J., Sun Y., Sun J. (2010), Indentation size effect of hardness of metallic glasses, *Materials & Design*, 31, 1563-1566 (doi.org/10.1016/j.matdes.2009.09.046).
- Hufnagel T. C., Deiry P. El., Vinci R. P. (2000), Development of shear band structure during deformation of a $Zr_{57}Ti_5Cu_{20}Ni_8Al_{10}$ bulk metallic glass. *Scripta Materialia*, 43(12), 1071–1075 (doi:10.1016/s1359-6462(00)00527-3)
- Inoue A. (1995), High Strength Bulk Amorphous Alloys with Low Critical Cooling Rates, *Material Transactions JIM*, 36, 866–875 (doi:10.2320/matertrans1989.36.866).
- Ivanisenko Y., Kubel C., Nandam S. H., Wang C., Mu X., Adjaoud O., Albe K., Hahn H. (2018), Structure and properties of nanoglasses, *Advanced Engineering Materials*, 20, 1800404 (doi.org/10.1002/adem.201800404).
- Jana S., Ramamurty U., Chattopadhyay K., Kawamura Y. (2004a), Subsurface deformation during Vickers indentation of bulk metallic glasses, *Material Science and Engineering A*, 375-377, 1191–1195 (doi.org/10.1016/j.msea.2003.10.068).
- Jana, S., Bhowmick, R., Kawamura, Y., Chattopadhyay, K., and Ramamurty, U. (2004b). Deformation Morphology Underneath the Vickers Indent in a Zr-Based Bulk Metallic Glass. *Intermetallics* 12, 1097–1102 (doi:10.1016/j.intermet.2004.04.018).

- Jiang J. I., Lance M. J., Wen S., Tsui T. Y., Pharr G. M. (2005), Indentation-induced phase transformations in silicon: influences of load, rate and indenter angle on the transformation behavior, *Acta Materialia*, 53, 1759-1770 (doi:10.1016/j.actamat.2004.12.025).
- Jiang J. I., Lance M. J., Wen S., Pharr G. M. (2005), Evidence for nanoindentation-induced phase transformations in germanium, *Applied Physics Letters*, 86, 131907 (doi: 10.1063/1.1894588).
- Jiang J. I., Pharr G. M. (2008), Influence of indenter angle on cracking in Si and Ge during nanoindentation, *Acta Materialia*, 56, 4458-4469. (doi:10.1016/j.actamat.2008.05.005)
- Jang J. I., Yoo B. G., Kim J.Y. (2007), Rate dependent inhomogeneous-to-homogeneous transition of plastic flows during nanoindentation of bulk metallic glasses: Fact or artifact? *Applied Physics Letters,* 90, 211906. (doi: 10.1063/1.2742286).
- Jiang W. H. and Atzmon M. (2003), Rate dependence of serrated flow in a metallic glass, *Journal of Material Research*, 18, 755-757 (doi:10.1557/JMR.2003.0103).
- Jiang W. H., Liu F. X., Choo H., Liaw P. K. (2007), Effect of Structural Relaxation on Mechanical Behavior of a Zr-Based Bulk-Metallic Glass. *Materials transactions*, 48(7), 1781–1784 (doi:10.2320/matertrans.mj200734)
- Jiang W.H., Liu F.X., Jiang F., Qiu K.Q., Choo H., Liaw P.K. (2007), Strain-rate dependence of hardening and softening in compression of a bulk-metallic glass, *Journal of Materials Research*, 22 (2007) 2655–2658 (10.1557/jmr.2007.0351).
- Jing J., Kramer A., Birringer R., Gleiter H., Gonser U. (1989), Modified atomic structure in Pd-Fe-Si nanoglass: a Mossbauer study, *Journal of Non Crystalline Solids*, 113, 167-170 (doi.org/10.1016/0022-3093(89)90007-0).
- Kauzmann W. (1948), The nature of the glassy state and the behaviour of liquids at low Temperatures, *Chemical Reviews*, 43, 219–256 (https://doi.org/10.1021/cr60135a002).
- Kathavate V. S., Praveen Kumar B., Singh I., Eswar Prasad K. (2021). Analysis of Indentation Size Effect (ISE) in Nanoindentation Hardness in Polycrystalline PMN-PT Piezoceramics with Different Domain Configurations. *Ceramics International*, 47, 11870–11877 (doi:10.1016/j.ceramint.2021.01.027).
- Katnagallu S., Wu G., Singh S. P., Nandam S. H., Xia W., Stephenson L. T., et al. (2020), Nanoglass-Nanocrystal Composite-A Novel Material Class for Enhanced Strength-Plasticity Synergy. *Small*, 16, 2004400 (doi:10.1002/smll.202004400).
- Klement W., Willens R. H., Duwez P. (1960), Non-crystalline Structure in Solidified Gold–Silicon Alloys, *Nature*, 187, 869–870 (doi:10.1038/187869b0).

- Kushima A., Liu X. H., Zhu G., Wang Z. L., Huang J. Y., Li J. (2011), Leapfrog Cracking and Nanoamorphization of ZnO Nanowires during In Situ Electrochemical Lithiation, *Nano Letters*, 11, 4535–4541 (doi.org/10.1021/nl201376j).
- Lam D. C. C., Chong A. C. M. (2001), Model and experiments on strain gradient hardening in metallic glass, *Materials Science and Engineering A*, 318, 313-319 (doi.org/10.1016/S0921-5093(01)01329-6).
- Li. F. C., Wang T. Y., He Q. F., Sun B. A., Guo C. Y., Feng T., Yang Y. (2018), Micromechanical mechanism of yielding in dual nano-phase metallic glass, *Scripta Materialia*, 154, 186-191 (doi.org/10.1016/j.scriptamat.2018.05.050).
- Li M. (2020), Effect of annealing on strain rate sensitivity of metallic glass under nanoindentation, *Metals*, 10, 1063 (doi.org/10.3390/met10081063).
- Li M. C., Jiang M. Q., Jiang F., He L., Sun J. (2017), Testing effects on hardness of a Zr-based metallic glass under nanoindentation, *Scripta Materialia*, 138, 120-123 (doi.org/10.1016/j.scriptamat.2017.05.046).
- Li N., Chan K. C., Liu L. (2008), The Indentation Size Effect in $Pd_{40}Cu_{30}Ni_{10}P_{20}$bulk Metallic Glass. *Journal of Applied Physics D*, 41, 155415 (doi:10.1088/0022-3727/41/15/155415).
- Li N., Liu L., Chan K. C., Chen Q., Pan, J. (2009a), Deformation Behavior and Indentation Size Effect of $Au_{49}Ag_{5.5}$Pd2.3Cu26.9$Si_{16.3}$ Bulk Metallic Glass at Elevated Temperatures. *Intermetallics*, 17, 227–230 (doi:10.1016/j.intermet.2008.07.018).
- Li, N., Liu, L., and Chan, K. C. (2009b). Deformation Behavior and Indentation Size Effect in Amorphous and Crystallized $Pd_{40}Cu_{30}Ni_{10}P_{20}$ alloy. *Journal of Materials Research*, 24, 1693–1699 (doi:10.1557/jmr.2009.0222).
- Ma C., Li S., Huang P., Wang F. (2020), Size dependent hidden serration behaviors of shear banding in metallic glass thin films, *Journal of Non-Crystalline Solids*, 534, 119953 (doi.org/10.1016/j.jnoncrysol.2020.119953).
- Malzbender J., With G. de. (2001), The use of the indentation loading curve to detect fracture of coatings, *Surface and Coatings Technology*, 137, 72–76 (doi.org/10. 1016/s0257-8972(00)01091-4).
- McGurk M., Page T. (1999), Using the P–δ^2 analysis to deconvolute the nanoindentation response of hard-coated systems, *Journal of Materials Research*, 14, 2283–2295 (doi. org/10.1557/JMR.1999.0305).

- Meagher P., O’ Cearbhaill E. D., Byrne J. H. Browne D. J. (2016), Bulk Metallic Glasses for Implantable Medical Devices and Surgical Tools, *Advanced Materials*, (doi:10.1002/adma.201505347).
- Meyer E. (1908), Z Ver Dtsch Ing, 52, 645.
- Mukai T., Nieh T.G., Kawamura Y., Inoue A., Higashi K. (2002), Effect of strain rate on compressive behavior of a $Pd_{40}Ni_{40}P_{20}$ bulk metallic glass, *Intermetallics*, 10, 1071 (doi.org/10.1016/s0966-9795(02)00137-1).
- Mulhearn T. O. (1959), The deformation of metals by vickers-type pyramidal indenters, *Journal of Mechanics and Physics of Solids*, 7, 85–88 (doi: 10.1016/0022-5096(59)90013-4).
- Murali P and Ramamurty U. (2005), Embrittlement of a bulk metallic glass due to sub-Tg annealing, *Acta Materialia* 53, 1467-1478 (doi:10.1016/j.actamat.2004.11.040).
- Nandam S. H., Ivanisenko Y., Schewaiger R., Snoadecki Z., Mu X., Wang D., Chellali R., Boll T., Kilmametov A., Bergfeldt T., Gleiter H., Hahn H. (2017), Cu-Zr nanoglasses: Atomic structure, thermal stability and indentation properties, *Acta Materialia*, 136, 181-189 (doi.org/10.1016/j.actamat.2017.07.001).
- Nandam S. H., Adjaoud O., Schwaiger R., Ivanisenko Y., Chellali M. R., Wang D., Albe K., Hahn H. (2020), Influence of topological structure and chemical segregation on the thermal and mechanical properties of Pd-Si nanoglasses, *Acta Materialia*, 193, 252-260 (doi.org/10.1016/j.actamat.2020.03.021)
- Nandam S.H., Schwaiger R., Kobler A., Kubel C., Wang C., Ivanisenko Y., Hahn H. (2021), Controlling shear band instability by nanoscale heterogeneties in metallic nanoglasses, *Journal of Materials Research*, 36, 2903–2914 (doi.org/10.1557/s43578- 021-00285-4).
- Narasimhan R. (2004), Analysis of indentation of pressure sensitive plastic solids using the expanding cavity model, *Mechanics of Materials*. 36, 633-645 (doi.org/10.1016/S01676636(03)00075-9).
- Narayan R. L., Singh P. S., Hofmann D. C., Hutchinson N., Flores K. M., Ramamurty U. (2012), On the microstructure-tensile property correlations in bulk metallic glass matrix composites with crystalline dendrites, *Acta Materialia*, 60, 5089-5100 (https://doi.org/10.1016/j.actamat.2012.06.032).
- Neill H. O. (1934), The hardness of metals and its measurement. London: Chapman and Hall.

- Nix W. D., and Gao H. (1998). Indentation Size Effects in Crystalline Materials: A Law for Strain Gradient Plasticity. *Journal of Mechanics and Physics of Solids*, 46, 411–425 (doi:10.1016/S0022-5096(97)00086-0).
- Oliver W. C., and Pharr G. M. (1992). An Improved Technique for Determining Hardness and Elastic Modulus Using Load and Displacement Sensing Indentation Experiments. *Journal of Materials Research*, 7, 1564–1583 (doi:10.1557/JMR.1992.1564).
- Oliver W. C., and Pharr G. M. (2004). Measurement of hardness and elastic modulus by instrumented indentation: Advances in understanding and refinements to methodology, *Journal of Materials Research*, 19, 3-20 (doi.org/10.1557/jmr.2004.19.1.3).
- Pan D., Inoue A., Sakurai T., Chen M. W. (2008), Experimental characterization of shear transformation zones for plastic flow of bulk metallic glasses. (2008) *Proceedings of the National Academy of Sciences*, 105, 14769-14772 (doi: 10.1073 / pnas.0806051105).
- Pang J. J., Tan M. J., Liew K. M., Shearwood C. (2012), Nanoindentation study of size effect and loading rate effect on mechanical properties of a thin film metallic glass $Cu_{49.3}Zr_{50.7}$, *Physica B: Condensed Matter*, 407, 340–346 (doi.org/10.1016/j.physb.2011.10.050).
- Park K. W., Jang J. I., Wakeda M., Shibutani Y., Lee, J. C. (2007), Atomic Packing Density and its Influence on the Properties of Cu-Zr Amorphous Alloys. *Scripta Materialia*, 57, 805–808 (doi:10.1016/j.scriptamat.2007.07.019).
- Patnaik M. N. M., Narasimhan R., Ramamurty U. (2004), Spherical indentation response of metallic glasses, *Acta Materialia*, 52, 3335-3345 (doi.org/10.1016/j.actamat.2004.03.028).
- Peker A., Johnson W.L. (1993), A highly processable metallic glass: $Zr_{41.2}Ti_{13.8}Cu_{12.5}Ni_{10.0}Be_{22.5}$, *Applied Physics Letters* 63, 2342–2344 (doi:10.1063/1.110520).
- Pharr G. M., Herbert E. G., Gao Y. (2010), The Indentation Size Effect: A Critical Examination of Experimental Observations and Mechanistic Interpretations. *Annual Review Materials Research*, 40, 271–292 (doi:10.1146/annurevmatsci-070909-104456).
- Prasad, K. E., and Ramamurty, U. (2012), Effect of Temperature on the Plastic Zone Size and the Shear Band Density in a Bulk Metallic Glass. *Materials Science and Engineering A*, 535, 48–52 (doi:10.1016/j.msea.2011.12.040).
- Prasad K. E., Raghavan R., Ramamurty U. (2007), Temperature dependence of pressure sensitivity in metallic glass, *Scripta Materialia*, 57, 121-124 (doi.org/10.1016/j.scriptamat.2007.03.033).

- Prasad K. E, Chollacoop N., Ramamurty U. (2011), Role of indenter angle on the plastic deformation underneath a sharp indenter and on representative strains: An experimental and numerical study, *Acta Materialia*, 59, 4343–4355 (doi.org/10.1016/j.actamat.2011.03.058).
- Prasad K. E., and Ramesh K. T. (2019), Hardness and Mechanical Anisotropy of Hexagonal SiC Single crystal Polytypes. *Journal of Alloys and Compounds*, 770, 158–165 (doi:10.1016/j.jallcom.2018.08.102).
- Qiao J., Jia H., Liaw P.K. (2016), Metallic glass matrix composites, *Materials Science and Engineering R: Reports,* 100, 1-69 (doi.org/10.1016/j.mser.2015.12.001).
- Raghavan R., Ayer R., Jin H.W., Marzinsky C.N., Ramamurty U. (2008), Effect of shot peening on the fatigue life of a Zr-based bulk metallic glass. *Scripta Materialia*, 59, 167–170 (doi: 10.1016/j.scriptamat.2008.03.009).
- Ramamurty, U., Jana, S., Kawamura, Y., Chattopadhyay, K. (2005), Hardness and plastic deformation in a bulk metallic glass. *Acta Materialia* 53, 705-717 (doi:10.1016/j.actamat.2004.10.023).
- Rauf A., Guo C. Y., Fang Y. N., Yu Z., Sun B. A., Feng T. (2018), Binary Cu-Zr thin film metallic glasses with tunable nanoscale structures and properties. *Journal of Non-Crystalline Solids*, 498, 95–102 (doi.org/10.1016/j.jnoncrysol.2018.06.015).
- Ritter Y., Sopu D., Gleiter H., Albe K. (2011), Structure, stability and mechanical properties of internal interface in $Cu_{64}Zr_{36}$ nanoglasses studied by MD simulations, *Acta Materialia*, 59, 6588-6593 (doi.org/10.1016/j.actamat.2011.07.013).
- Ritter, Y., and Albe, K. (2012), Chemical and Topological Order in Shear Bands of $Cu_{64}Zr_{36}$ and $Cu_{36}Zr_{64}$ Glasses. *Journal of Applied Physics*, 111, 103527. (doi:10.1063/1.471774810.1063/1.4717748).
- Rong C., Shen B. (2018), Nanocrystalline and nanocomposite permanent magnets by melt spinning technique. *Chinese Physics B*, 27(11), 117502 (doi:10.1088/1674-1056/27/11/117502).
- Sahu B.P., Dutta A., Mitra R. (2019), Mechanism of negative strain rate sensitivity in metallic glass film, *Journal of Alloys and Compounds*, 784, 488–499 (doi.org/10.1016/j.jallcom.2022.165991).
- Samuels L. E. and Mulhearn T. O. (1957), An experimental investigation of the deformed zone associated with indentation hardness impressions, *Journal of Mechanics and Physics of Solids*, 5, 125–134 (doi: 10.1016/0022-5096(57)90056-X).

- Schroers J., Hodges T. M., Kumar G.; Raman H., Barnes A. J., Pham Q., Waniuk T. A. (2011), Thermoplastic blow molding of metals, *Materials Today*, 14, 14–19 (doi:10.1016/s1369-7021(11)70018-9).
- Schuh C. A., Nieh T. G, Kawamura Y. (2002), Rate dependence of serrated flow during nanoindentation of bulk metallic glass. *Journal of Material Research*, 17, 1651-1654 (doi.org/10.1557/JMR.2002.0243)
- Schuh, C. A., Nieh, T. G. (2003), A nanoindentation study of serrated flow in bulk metallic glasses. *Acta Materialia* 51, 87-99 (doi: 10.1016/S 13 59 -6454(02)00303-8).
- Schuh C. A., Nieh T. G.(2004), A survey of instrumented indentation studies on metallic glasses. *Journal of Material Research*, 19, 46-57(doi: 10.1557/jmr.2004.19.1.46)
- Schuh, C. A., Lund, A. C., Nieh, T. G., (2004). New regime of homogeneous flow in the deformation map of metallic glasses: elevated temperature nanoindentation experiments and mechanistic modelling. *Acta Materialia* 52, 5879-5891 (doi:10.1016/j.actamat.2004.09.005).
- Schuh C. A., Hufnagel T. C., Ramamurty U. (2007), Mechanical behavior of amorphous alloy, *Acta Materialia*, 55, 4067-4109 (doi.org/10.1016/j.actamat.2007.01.052).
- Sharma A., Nandam S. H., Hahn H., and Prasad K. E. (2021a), On the Differences in Shear Band Characteristics between a Binary Pd-Si Metallic and Nanoglass. *Scripta Materialia,* 191, 17–22 (doi:10.1016/j.scriptamat.2020.09.009).
- Sharma A., Nandam S.H., Hahn H., Prasad K.E. (2021b), Effect of structural relaxation on the indentation size effect and deformation behavior of Cu-Zr-based nanoglasses. *Frontiers in Materials*, 8, 676764 (doi.org/10.3389/fmats.2021.676764).
- Shen Y. T., Xing L. Q., Kelton K. F. (2005), Formation and crystallization of ZrCuTi metallic glasses, *Philosophical Magazine* 85, 3673–3682 (doi:10.1080/14786430500156724).
- Shi, T., Huang L., Li S. (2021), Effects of Annealing on Enthalpy Recovery and Nanomechanical Behaviors of a La-Based Bulk Metallic Glass, *Metals*, 11, 579 (doi.org/10.3390/met11040579).
- Singh G., Narayan R. L., Asiri A. M., Ramamurty U. (2016), Discrete drops in the electrical contact resistance during nanoindentation of a bulk metallic glass. *Applied Physics Letters*, 108, 181903 (doi:10.1063/1.4948540).
- Singh P. S., Narayan R. L., Sen I., Hofmann D. C., and Ramamurty U. (2012). Effect of Strain Rate and Temperature on the Plastic Deformation Behaviour of a Bulk Metallic

Glass Composite. *Material Science and Engineering A*, 534, 476–484. (doi:10.1016/j.msea.2011.11.096).

- Singh S. P., Chellali M. R., Velasco L., Ivanisenko Y., Boltynjuk E., Gleiter H., et al. (2020a). Deformation-Induced Atomic Rearrangements and Crystallization in the Shear Bands of a Tb75Fe25 Nanoglass. *Journal of Alloys and Compounds*, 821, 153486 (doi:10.1021/acsanm.0c0167410.1016/j.jallcom.2019.153486).
- Singh S. P., Witte R., Clemens O., Sarkar A., Velasco L., Kruk R., Hahn H. (2020b), Magnetic $Tb_{75}Fe_{25}$ Nanoglass for Cryogenic Permanent Magnet Undulator, *ACS Applied Nano Materials*, 3(7), 7281-7290 (doi:10.1021/acsanm.0c01674).
- Slipenyuk A. and Eckert J. (2004), Correlation between enthalpy change and free volume reduction during structural relaxation of $Zr_{55}Cu_{30}Al_{10}Ni_5$ metallic glass, *Scripta Materialia*, 50, 39-44 (doi:10.1016/j.scriptamat.2003.09.038).
- Smith R. L., Sandland G. E. (1925), J Iron Steel Inst, 61, 285.
- Sneddon I. N. (1965), The relation between load and penetration in the axisymmetric boussinesq problem for a punch of arbitrary profile, *International Journal of Engineering Science*, 3, 47-57 (doi:10.1016/0020-7225(65)90019-4).
- Sniadecki Z., Wang D., Ivanisenko Y., Chakravadhanula V. S. K., Kübel C., Hahn H., et al. (2016), Nanoscale Morphology of $Ni_{50}Ti_{45}Cu_5$ Nanoglass. *Materials Characterization*, 113, 26–33 (doi:10.1016/j.matchar.2015.12.025).
- Song S.X., Lai Y.H., Huang J.C., Nieh T.G. (2009), Homogeneous deformation of Au-based metallic glass micropillars in compression at elevated temperatures, *Applied Physics Letters*, 94, 061911 (https://doi.org/10.1063/1.3081111).
- Sopu D., Albe K. (2015), Influence of grain size and composition, topology and excess free volume on the deformation behavior of Cu–Zr nanoglasses. *Beilstein Journal of Nanotechnology*, 6, 537–545 (doi.org/10.3762/bjnano.6.56).
- Sopu D., Albe K. Ritter Y., Gleiter H. (2009), From nanoglasses to bulk massive glasses, *Applied Physics Letters*, 94, 191911 (doi.org/10.1063/1.3130209).
- Şopu D., Ritter Y., Gleiter H., Albe K. (2011), Deformation behavior of bulk and nanostructured metallic glasses studied via molecular dynamics simulations, *Physical Review B*, 83, 1–4. (doi:10.1103/PhysRevB.83.100202).
- Sort J., Fornell J., Li W., Surinach S., Baro M.D. (2008), Influence of the loading rate on the indentation response of Ti-based metallic glass, *Journal of Materials Research*, 24, 918–925 (doi:10.1557/jmr.2009.0117).

- Steenberge N. V., Sort J., Concustell A., Das J., Scudino S., Surinach S., Eckert J., Baro M. D. (2007), Dynamic softening and indentation size effect in a Zr- based bulk glass-forming alloy, *Scripta Materialia*, 56, 605-608 (doi.org/10.1016/j.scriptamat.2006.12.014).
- Subhash G., Zhang H. (2007), Dynamic indentation response of ZrHf-based bulk metallic glasses, *Journal of Material Research*, 22, 478–485 (doi.org/10.1557/jmr.2007.0058).
- Suryanarayana C., Inoue A. (2000), Metallic Glasses, *Ullmann's Encyclopedia of Industrial Chemistry*, (doi:10.1002/14356007.a16_335.pub2).
- Sharma P., Inoue A. (2010), Metallic Glass, *Handbook of Silicon Based MEMS Materials and Technologies*, 447–472 (doi:10.1016/b978-0-8155-1594-4.00027-9).
- Spaepen F. (1977), A microscopic mechanism for steady state inhomogeneous flow in metallic glasses, *Acta Metallurgica*, 25,407-415 (doi.org/10.1016/0001-6160(77)90232-2).
- Tabor D. (1951), Hardness of metals. Oxford: Clarendon Press.
- Tabor D. (1970), Rev Physics Technology.
- Tao K., Qiao J.C., He Q.F., Song K.K., Yang Y. (2021), Revealing the structural heterogeneity of metallic glass: mechanical spectroscopy and nanoindentation experiments, *International Journal of Mechanical Sciences*, 201, 106469, (doi.org/10.1016/j. ijmecsci.2021.106469).
- Telford M. (2004), The case for bulk metallic glass, *Materials Today*, 7, 36-43 (doi.org/10.1016/S1369-7021(04)00124-5).
- Volker C. A., Donohue A., Spaepen F. (2008), Effect of sample size on deformation in amorphous metals. *Journal of Applied Physics*, 103, 083539 (doi:10.1063/1.2884584).
- Xie S., George X. P. (2008), Hardness and shear band evolution in bulk metallic glasses after plastic deformation and annealing. *Acta Materialia*, 56, 5202-5213 (doi:10.1016/j.actamat.2008.07.009).
- Wahlberg A. (1901), J Iron Steel Institute, 59, 243.
- Wang C., Guo X., Ivanisenko Y., Goel S., Nirschl H., Gleiter H., Hahn H. (2017), Atomic structure of $Fe_{90}Sc_{10}$ glassy nanoparticles and nanoglasses, *Scripta Materialia* 139, 9–12. (doi:10.1016/j.scriptamat.2017.06.007).
- Wang J. G., Choi B. W., Nieh T. G., Liu C. T. (2000), Crystallization and nanoindentation behavior of a bulk Zr–Al–Ti–Cu–Ni amorphous alloy, *Journal of Material Research*, 15(3), 798-807 (doi:10.1557/jmr.2000.0114).

- Wang J. Q., Chen N., Liu P., Wang Z., Louzguine-Luzgin D. V., Chen M. W., Perepezko J. H. (2014), The ultrastable kinetic behavior of an Au-based nanoglass, *Acta Materialia* 79, 30–36 (doi:10.1016/j.actamat.2014.07.015).
- Wang J. Q., Wang W. H., Liu Y. H., Bai H. Y. (2011), Characterization of Activation Energy for Flow in Metallic Glasses. *Physical Review B* 83, 012201 (doi:10.1103/PhysRevB.83.012201).
- Wang W. H., Dong C., Shek C. H. (2004), Bulk metallic glasses, *Materials Science and Engineering R*, 44, 45-89 (doi:10.1016/j.mser.2004.03.001).
- Wang X., Ren Z.Q., Xiong W., Liu S.N., Liu Y., Lan S., Wang J.T. (2021), Negative strain rate sensitivity induced by structure heterogeneity in $Zr_{64.13}Cu_{15.75}Ni_{10.12}Al_{10}$ bulk metallic glass, *Metals*, 11, 339 (doi.org/10.3390/met11020339).
- Wang X. L., Jiang F., Hahn H., Li J., Gleiter H., Sun J., Fang J. X. (2015), Plasticity of a scandium-based nanoglass, *Scripta Materialia*, 98, 40-43 (doi.org/10.1016/j.scriptamat.2014.11.010).
- Wang X.L., Jiang F., Hahn H., Li J., Gleiter H., Sun J., Fang J. X. (2016), Sample size effects on strength and deformation mechanism of $Sc_{75}Fe_{25}$ nanoglass and metallic glass, Scripta materialia, 116, 95–99 (doi.org/10.1016/j.scriptamat.2016.01.036).
- Wang Y. (2016), Effect of indenter angle and friction on the mechanical properties of film materials, *Results in Physics*, 6, 509–514 (doi:10.1016/j.rinp.2016.08.008).
- Wang Y.B., Qu D.D., Wang X.H., Cao Y., Liao X.Z., Kawasaki M., Ringer S.P., Shan Z.W., Langdon T.G., Shen J. (2012), Introducing a strain-hardening capability to improve the ductility of bulk metallic glasses via severe plastic deformation, *Acta Materialia* 60, 253–260 (doi:10.1016/j.actamat.2011.09.026).
- Witte R., Feng T., Fang J. X., Fischer A., Ghafari M., Kruk R., et al. (2013), Evidence for Enhanced Ferromagnetism in an Iron-Based Nanoglass. *Applied Physics Letters*, 103, 073106 (doi:10.1063/1.4818493).
- Wright W. J., Saha R., Nix W.D. (2001), Deformation mechanisms of the $Zr_{40}Ti_{14}Ni_{10}Cu_{12}Be_{24}$ Bulk metallic glass, *Materials Transactions Japan Institute of metals*, 42, 642-649 (doi.org/10.2320/matertrans.42.642).
- Xia L., Shan S. T., Ding D., Dong Y. D. (2007), Binary bulk metallic glass Ni62Nb38 with high compressive strength of 3100 MPa, *Intermetallics*, 15, 1046–1049.
- Xie S., George E. P. (2008), Hardness and shear band evolution in bulk metallic glasses after plastic deformation and annealing, *Acta Materialia*, 56, 5202–5213 (doi:10.1016/j.actamat.2008.07.009).

- Xu Y., Fang J., Gleiter. H, Hahn H., Li J. (2010), Quantitative determination of free volume in $Pd_{40}Ni_{40}P_{20}$ bulk metallic glass, *Scripta Materialia*, 62, 674–677. (doi:10.1016/j.scriptamat.2010.01.025).
- Xu F., Ding Y. H., Deng X. H., Zhang P., Long Z. L. (2014), Indentation size effect in the nano- and micro-hardness of Fe-based bulk metallic glass, *Physica B: Condensed Matter*, 450, 84-89 (doi.org/10.1016/j.physb.2014.05.057).
- Xue F., Wang F., Huang P., Lu T. J., Xu K. W. (2016), Structural inhomogeneity and strain rate dependent indentation size effect in Zr- based metallic glass, *Materials Science and Engineering A*, 655, 373-378 (doi.org/10.1016/j.msea.2015.12.083).
- Yang B., and Nieh T. (2007b). Effect of the Nanoindentation Rate on the Shear Band Formation in an Au-Based Bulk Metallic Glass. *Acta Materialia*, 55, 295–300 (doi:10.1016/j.actamat.2006.08.028).
- Yang F., Geng K., Liaw P. K., Fan G., Choo H. (2007), Deformation in a Zr_{57} $Ti_5Cu_{20}Ni_8Al_{10}$ bulk metallic glass during nanoindentation, Acta Materialia, 55, 321-327 (doi.org/10.1016/j.actamat.2006.06.063).
- Yang Q., Pei C. Q., Yu H. B., Feng T. (2021), Metallic Nanoglasses with Promoted *β*-Relaxation and Tensile Plasticity, *Nano Letters*, 21, 6051-6056 (doi.org/10.1021/acs.nanolett.1c01283).
- Yoo B. G., Kim J. Y., Jang J. I. (2007), Influence of indenter geometry on the deformation behavior of $Zr_{60}Cu_{30}Al_{10}$ bulk metallic glasses during nanoindentation. *Materials Transactions*, 48(7), 1765-1769 (doi.org/10.2320/matertrans.MJ200752).
- Zhang H., Jing X., Subhash G., Kecskes L. J., Dowding R. J. (2005), Investigation of shear band evolution in amorphous alloys beneath a Vickers indentation, *Acta Materialia*, 53, 3849–3859 (doi.org/10.1016/j.actamat.2005.04.036).
- Zhang Q.S., Zhang, W., Xie, G.Q., Louzguine-Luzgin, D.V., Inoue, A. (2010). Stable flowing of localized shear bands in soft bulk metallic glasses. *Acta Materialia*, 58, 904–909 (doi.org/10.1016/j.actamat.2009.10.005)
- Zhao M.S.Z., Long Z.L., Peng L. (2021), Nanoindentation studies of strain rate sensitivities in bulk metallic glasses, *Journal of Non-Crystalline Solids*, 565, 150852 (doi. org/10.1016/j.jnoncrysol.2021.120852).
- Zhou Q., Du Y., Han W., Ren Y., Zhai H., Wang H. (2019), Identifying the origin of strain rate sensitivity in a high entropy bulk metallic glass, *Scripta Materialia*, 164, 121-125 (doi.org/10.1016/j.scriptamat.2019.02.002).

- Zhang Z and Xie J. (2005), Influence of relaxation and crystallization on micro-hardness and deformation of bulk metallic glass, *Materials Science and Engineering A* , 407(1-2), 161–166 (doi:10.1016/j.msea.2005.07.020).